Core-Shell Materials as Positive Electrodes in Lithium-Ion Batteries

by

John Camardese

Submitted in partial fulfilment of the requirements
for the degree of Doctor of Philosophy

at

Dalhousie University
Halifax, Nova Scotia
April 2015

To everyone who pushed me forward, even when I thought they were guiding me in the opposite direction.

Table of Contents

List of Tables

List of Figures

Abstract

Electric vehicles with lithium-ion batteries as their energy storage technology have been sold by major automotive manufacturers for the past few years, but with limited sales. Sales are poor because of the high purchase price, short driving range and limited lifetime of the battery pack. Current electric vehicles have a driving range of 30 to 265 miles, battery warranty of 5 to 8 years and a price of 30,000 to 75,000 USD.

The choice of electrolyte and positive electrode materials impact cost, lifetime and energy density. In this work the synthesis and characterization of core-shell positive electrode materials were explored. Core-shell materials have a different composition at the surface of the particles, where oxidative degradation of the electrolyte occurs, than the bulk. This structure was previously purposed for increasing lifetime and energy density without significant cost.

Several core-shell and gradient composition materials were synthesized by first making a core-shell mixed transition metal hydroxide precursor in a continuously stirred tank reactor and then blending with Li_2CO_3 and sintering at high temperatures. It was necessary to use multiple characterization techniques (XRD, SEM and EDS) to verify that the precursors had the desired core-shell structure and that the core and shell had the proper compositions. It was demonstrated that the composition of the core and shell phases and the thickness of the shell could easily be controlled.

A technique using absorption in X-ray diffraction patterns was developed to estimate the thickness of the shell layer, which was validated with spatial EDS measurements and a constant growth model.

The core-shell structure was maintained after sintering except that cobalt diffused from the shell phase into the core creating an approximately homogeneous cobalt concentration throughout the particles. Lithium uptake into the core and shell phases during sintering was different than what was observed when those phases were synthesized as single-phases not as core-shell samples.

Electrochemical data was collected using ultra high precision chargers which showed that the core-shell materials had less charge endpoint capacity slippage than the core only material, suggesting less electrolyte oxidation at the positive electrode.

List of Symbols and Abbreviations Used

a, b, c	Unit cell lengths
AEC	Allyl Ethyl Carbonate
BMF	Blown Microfibre Separator
C	C as in C-rate
CAFE	Corporate Average Fuel Economy
CE	Coulombic Efficiency
CIE/h	Coulombic Inefficiency per hour
CSTR	Continuously Stirred Tank Reactor
d	Atomic plane spacing
DEC	Diethyl Carbonate
EC	1,3-dioxolan-2-one (Ethylene Carbonate)
EDS	Energy Dispersive Spectroscopy
EIS	Electrochemical Impedance Spectroscopy
EV	Electric Vehicle
f	Atomic scattering factor
f_n	Flow rate of solution n (mL/s)
FEC	4-Fluoro-1,3-dioxolan-2-one (Fluoroethylene carbonate)
FWHM	Full Width at Half Maximum
h	Hours
(h k l)	Miller indices
HPC	High Precision Charger
I	Current

ICP-OES	Inductively Coupled Plasma Optical Emission Spectroscopy
I_n	Intensity at time or position n
IRC	Irreversible Capacity
K	Constant from Thompson Equation (2.4)
l	Length of radiation absorbing media
M	Molarity (mol/l)
MSO_4	A mixed metal sulfate solution
NMC-abc	A compound with a molar ratio of Ni:Mn:Co of a:b:c
NMP	1-methyl-2-pyrrolidone
P_n	Partial Pressure of species n
ppm	Parts Per Million
PEF	Petroleum-Equivalency Factor
PVDF	Polyvinylidene fluoride
q	Capacity
R	Goodness of fit factor of Rietveld refinement
r	Radius
RPM	Rotations Per Minute
SEI	Solid Electrolyte Interphase
SEM	Scanning Electron Microscopy
SLPM	Standard Litres Per Minute
t	Time
V	Voltage, Volume (Chapter 5)
T	Transmission

TEY	Total Electron Yield Detector
TFEC	Bis(2,2,2-trifluoroethyl) carbonate
UHPC	Ultra High Precision Charger
USD	United States Dollars
US DOE	United States Department of Energy
w_i	Weighting factor in goodness of fit
wt%	Weight Percent
XANES	X-ray Absorption Near Edge Spectroscopy
XPS	X-ray Photoelectron Spectroscopy
XRD	X-ray Diffraction
%v	Volume Percent
VC	1,3-Dioxol-2-one (Vinylene Carbonate)
α, β, γ	Interior angles of unit cell
θ	Scattering angle in XRD
λ	Wavelength of radiation
μ/ρ	Mass absorption coefficient
ρ	Density
X_n	Molar fraction of species n

Acknowledgements

There are many people that I would like to thank for their support, assistance and guidance in completion of this work. First I would like to thank my research supervisor, Jeff Dahn. The opportunities I have had working in the "Dahn Lab" have been second to none. I would also like to thank my undergraduate research supervisor, Adam Timmons who got me in contact with Jeff. I would also like to thank my committee members Professors Andreas, Obrovac and Zhang for their useful instruction in the courses they taught and for taking time to read my work and provide useful feedback.

I would like to thank a few fellow students with whom I have collaborated with on many different projects. Eric McCalla, for many hours of discussion and for letting me teach him about the importance of oxidation states. Jing Li, for many hours of useful "arguments" about our research that has led to a deeper understanding. Dan Abarbanel, whose dedication and hard work assisted greatly in this work. I would also like to thank Tara Tovstiga for her assistance with grammar and editing.

I would also like to thank Robbie Sanderson for repairing broken equipment and sputter coating samples. I would also like to thank Simon Trussler for his assistance with manufacturing parts for the tank reactor. I would like to thank Patricia Scallion and Andy George for their support with SEM and EDS measurements. I would also like to thank Gisselle Andrews for her assistance in preparing documents for my thesis.

I would finally like to thank my family and friends for their support. Without their encouragement I may have missed out on the opportunity to complete this work.

Chapter 1. Introduction

1.1 Motivation to Study Lithium-Ion Batteries for Electric Vehicles

Lithium-ion batteries have seen widespread use in the electronics market. They are the current preferred energy storage solution for portable electronics due to their high energy density, low cost and useful service lifetime. For perspective, an 18650 cylindrical Li-ion cell manufactured by Panasonic will be used as an example. This cell is similar to those found in laptop computers built in the early 2000s and is the same style of cell used in the Tesla Model S. The energy density based on the cell dimensions, voltage and capacity was 0.733 kWh/L and the purchase price of the cell found on Amazon.com was 10.50 USD, a cost of 840 USD/kWh[1]. Quantitative lifetime testing of the cell was found from the manufacturer and reported as 80% capacity retention for
300 cycles; note that 80% capacity retention is considered the end of life for most cell use. A cell that lasts 300 cycles used daily in an application like a laptop computer or cell phone would yield a calendar life of about 1 year. While these metrics for a battery may seem to be excellent, the next target application for lithium-ion batteries, electric vehicles (EV), will require even better performance.

The United States Department of Energy (US DOE) targets for EVs produced in 2020 are 0.500 kWh/L, 125 USD/kWh and service lifetime of 1000+ cycles and 10 calendar years.[2] It is important to note that although the energy density requirements appear to be satisfied, the US DOE targets are accounting for the whole battery pack, not only a single cell. An EV battery pack requires additional equipment such as circuitry and controllers

for monitoring individual cells and active thermal management to regulate cell temperature.[3] All of this additional equipment adds volume and cost compared to a single 18650 cell which has passive thermal management and relatively simple circuitry to monitor the cell's electrical state. Meeting the US DOE requirements will require dramatic improvements in lithium-ion batteries.

EVs are desired by government, consumers and auto manufacturers for different reasons. Consumers are interested in EVs because of a desire to "go green" and the relatively low refueling price compared to petroleum fueled cars. Table 1.1 shows that gasoline has nearly doubled in its inflation-adjusted price while residential electricity has only increased by just over 7% in the past 18 years. For consumers, this is a major selling point for EVs. Economically, over the lifetime of the vehicle, an EV may be a better financial choice than a gasoline powered vehicle. This is known as the payback period, which is the amount of time required for the EV's fuel cost plus initial purchase price to equal that of a comparable gasoline vehicle.

Table 1.1 Price of gasoline and electricity in the United States adjusted for inflation[4–6]

	Price of Gasoline (2014 USD/Gallon)	Residential Electricity (2014 USD/kWh)
June 1996	1.96	0.121
June 2014	3.56	0.130
% Increase	81.0%	7.44%

EVs are attractive to auto manufacturers due to the government regulations such as the Corporate Average Fuel Economy (CAFE) standards used in the United States. CAFE is a US government regulation that lists the minimum weighted average fuel economy for

passenger vehicles that auto manufacturers must meet for their complete portfolio of vehicles.[7] In 2012 the CAFE standard was 36 miles per gallon; by 2025 this value will nearly double to 60 miles per gallon. Since EVs require no gasoline, their fuel economy could be considered to be infinity. This however is not the case, a calculation called a petroleum-equivalency factor (PEF) which determines how much petroleum fuel would be consumed at a power plant to move the vehicle is used as a substitute.[8] Electric vehicles are often weighted with bonuses in a corporation's CAFE calculation such as counting sales as double. By including electric vehicles into their vehicle portfolio auto manufacturers can continue to produce high profit margin luxury trucks with poor fuel economy, keeping investors happy.

While the allure of reduced fuel prices should be attracting consumers to EVs, they have not currently captured a substantial market share from traditional internal combustion gasoline or diesel fueled vehicles (ICEs). For example, in August 2014 General Motors' inventory reported 2,511 Chevrolet Volts (an EV), 79,493 mid and full size ICEs, and a total of 272,423 vehicles delivered to dealerships in the United States.[9] Tesla manufactured about 25,000 Model S (EV) and Nissan delivered only 22,610 Leafs (EV) in all of 2013. For reference the top 50 auto manufacturers in the world produced over 65 million cars in 2012.[10–12]

Table 1.2 summarizes some problems plaguing current EVs. Some of the major issues with electric vehicles are due to the technology being new. When gasoline powered vehicles were first being manufactured at the turn of the 20th century, mechanic shops, gas stations and other infrastructural necessities did not exist. As the technology grew, so did the infrastructure, and so will be the same with electric vehicles. Problems of scientific and

chemical interest in Table 1.2 are driving range (energy density), lifetime, cost and safety, all of which can be addressed through developing new materials.

Table 1.2 Current issues resulting in low EV sales

Challenge	Solution
Lack of Service Infrastructure	More charging stations
Vehicle Driving Range	Improve battery energy density
Battery Pack Lifetime	Improve battery lifetime
Vehicle Cost	Economy of scales & reduced materials cost in batteries
Safety	Advanced materials for batteries Overcharge/discharge protection electronics (Battery Managements Systems)

Table 1.3 highlights lifetime, cost and driving range for three well established EVs, based on the manufacturers' performance specifications. The initial purchase price and limited range are two of the hardest selling points for EVs. Comparing the Nissan Leaf to the Nissan Versa, a similarly sized gasoline powered vehicle to the Leaf, the payback time for the Leaf is 142,000 miles (payback time does not include any government tax rebates for purchasing an EV and assumes gasoline prices will not change over the payback period).[10,13,14] For the average consumer, the Nissan Leaf doesn't become an economically responsible choice until at minimum 5 years, at which time the battery is no longer protected by the manufacturer's warranty! Driving range limitations for the Volt and Leaf also limit their sales; while the Tesla Model S has an adequate driving range, its purchase price is extremely expensive which limits its target consumers.

Table 1.3 Vehicle specifics for three electric vehicles[11,15,16]

	2014 Chevrolet Volt	2014 Nissan Leaf	2014 Tesla Model S
Driving Range (miles)	38 (640)*	124	265
Purchase Price (USD)	34,995	29,860	69,990
Battery Cost (USD)	8,000	12,000	35,000
Battery Warranty (years)	8 (100,000 miles)	5 (60,000 miles)	8 (125,000 miles)

*The Chevrolet Volt has an electric generator fueled by gasoline which extends the driving range via the electric drivetrain to 640 miles on a 35 litre gas tank and a fully charge battery pack.

Figure 1.1 shows how far a Nissan Versa and Leaf could be driven round trip on a fully charged battery pack or fully filled fuel tank away from the city centre of Halifax. The range limit of the Leaf makes it an unattractive primary vehicle since it cannot be used for trips outside of the daily commute, without the need to charge the battery. Improvements must be made to the energy density, cost and lifetime of lithium-ion batteries for sales to increase. Various other alternative energy storage systems to lithium-ion do exist, but generally are limited in certain characteristics such that without incredible improvements could never function in a viable commercial product. For example, a lithium-air battery is reported to have an energy density up to triple that of lithium-ion, but to date no one has demonstrated these energy densities with a cycle life greater than 10s of cycles.[17] For that reason these alternative storage systems such as Li-air, Li-sulfur, Na-ion and hydrogen fuel cells will not be further discussed in this thesis.

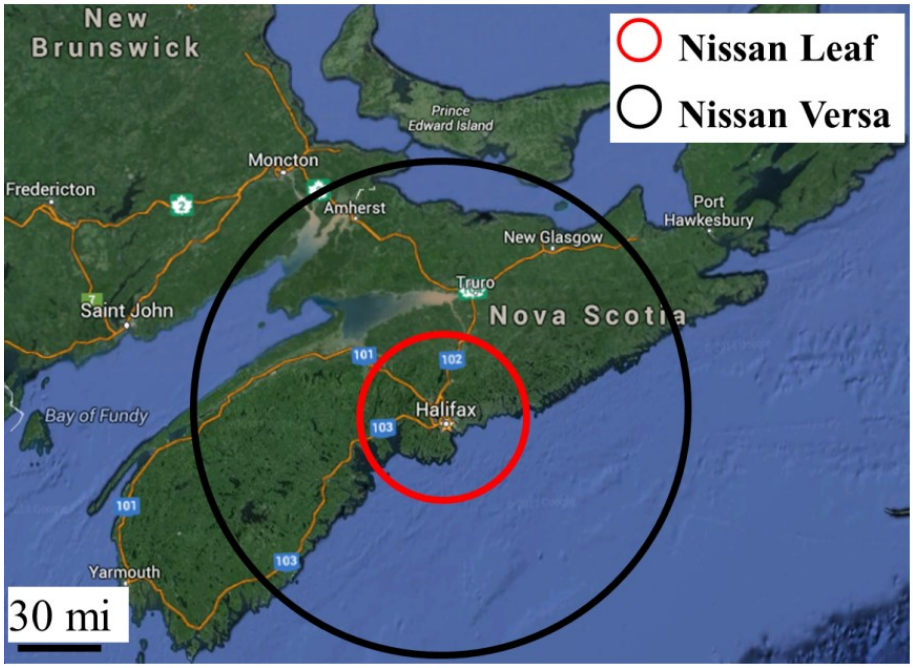

Figure 1.1 Roundtrip driving range limit of Nissan Versa and Leaf for a fully filled fuel tank or charged battery pack.[11,13,18]

Cost, safety, vehicle range and battery pack lifetime are all impacted by choice of materials used in lithium-ion batteries. Understanding how to improve lithium-ion batteries requires an understanding of the materials used in them and how the battery operates. The remainder of the introduction will discuss lithium-ion batteries and methods of research that may lead to developments that improve cost, safety, service life and energy density in a single solution.

1.2 Lithium-Ion Batteries

In its simplest form, a lithium-ion electrochemical cell is a "jelly roll" which is a positive electrode, separator and negative electrode tightly rolled or stacked together and placed into a housing. Electrolyte is then filled into the housing which wets the jelly roll

components. The housing is then hermetically sealed with electrical connections to the electrodes protruding from the sealed interior. Cells come in many different designs such as coin, cylindrical, prismatic or pouch cells.[3] The choice of cell form depends on the complexity of controlling equipment included in the battery pack, the power and energy demands on the cell and the dimensional and thermal limitations of the intended device. To avoid confusion, the words cell and battery should be defined for the scope of this thesis as the two words are often used interchangeably. A cell refers to a single electrochemical device which is described above. A battery will refer to a complete energy storage system which may include multiple cells in series and parallel circuits along with electronics and safety systems to manage the cells.

Figure 1.2 shows a cartoon schematic of the operation of a lithium-ion battery. During charging a current is applied to the cell which allows the non-spontaneous deintercalation of lithium ions from the positive host structure. In Figure 1.2, the positive electrode is lithium cobalt oxide, which has a layered structure with layers of lithium ions between slabs of cobalt oxide. Diffusion of lithium in lithium cobalt oxide is two-dimensional within the plane the lithium layer. Other possible structures do exist for the positive electrode and will be discussed later in this chapter. The separator is normally a polyolefin thin film. The separator is electronically insulating, and has micro-pores that allow lithium ions to diffuse through it. The electrolyte solution is normally a lithium salt such as lithium hexafluorophosphate dissolved in a mixture of linear or cyclic organic carbonates such as dimethyl carbonate and ethylene carbonate. During charging, lithium ions are removed from the positive electrode, travel through the electrolyte and separator and intercalate or alloy into the negative electrode active material. In Figure 1.2, graphite

is shown as the negative electrode, which can intercalate lithium between its graphene sheets. Silicon, which alloys with lithium, is also often used as a negative electrode. Discharging the cell results in this process occurring in reverse; lithium-ions are extracted from the negative electrode and intercalate back into the positive electrode. This spontaneous reaction results in usable electrical current which is utilized by an external load connected to the cell.

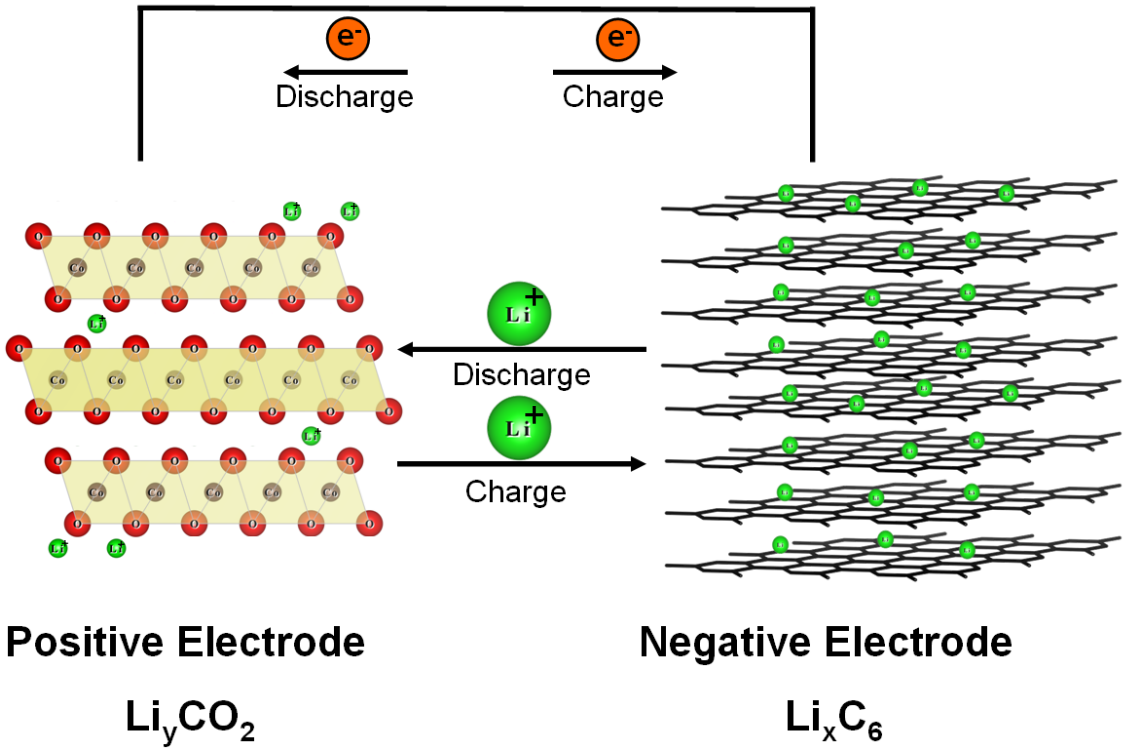

Figure 1.2. Schematic drawing of a lithium-ion cell with a $LiCoO_2$ positive electrode and graphitic carbon negative electrode. For clarity, the electrolyte and separator are not shown.

In addition to the positive and negative electrode active materials ($LiCoO_2$ & graphite), separator and electrolyte, a working cell has several other components such as metallic foil current collectors, conductive additives, binders and packaging. While these

components are not part of the classical definition of an electrochemical cell, without them the cell could not function and thus their cost and impact should be understood.

Table 1.4 shows the materials cost of an 18650 cylindrical lithium-ion cell, often found in laptop computers, and used as an example in Section 1.1. The positive electrode active material, electrolyte and separator represent the three largest contributors to the materials cost of a cell. Table 1.2 showed that in addition to cost, range limitations and cycle life were major concerns.

Table 1.4 Cost of components in a lithium-ion cell and their cost in 2010 USD.[19]

	Cost per Cell (USD)	% of Total Cost
Positive Electrode Active Material	0.2576	25.49
Aluminum (Current Collector Pos.)	0.0275	2.72
Separator	0.2092	20.70
Electrolyte	0.2186	21.63
Negative Electrode Active Material	0.0281	2.78
Copper (Current Collector Neg.)	0.0442	4.37
Binder	0.0289	2.86
Conductive Carbon	0.0032	0.32
Processing Materials	0.1394	13.79
Packaging	0.0540	5.34
Total	1.0107	100.00

The range of an EV is dependent on the energy density of the cells and the manufacturer's ability to minimize the volume and weight of the battery management system. Range improvements can also be made by advanced manufacturing of electric motors, and minimizing electric power wasted for ancillary services in the vehicle such as heaters and radios. The cell volumetric energy density (Wh/L) is

$$\frac{\int q\, dV}{Volume} \tag{1.1}$$

where q is the useable charge storage capacity in amp-hours (Ah), V is the voltage difference between the two electrodes and Volume is the total volume of the cell in litres.

The usable capacity of the cell is based on the choice of positive and negative electrode materials and the selected operating voltage window.

Figure 1.3 shows the voltage versus capacity of the charging process for a lithium-ion cell with a graphite negative electrode and lithium cobalt oxide positive electrode. The capacities of the lithium cobalt oxide positive electrode and graphite negative electrode are shown normalized to the full cell capacity.

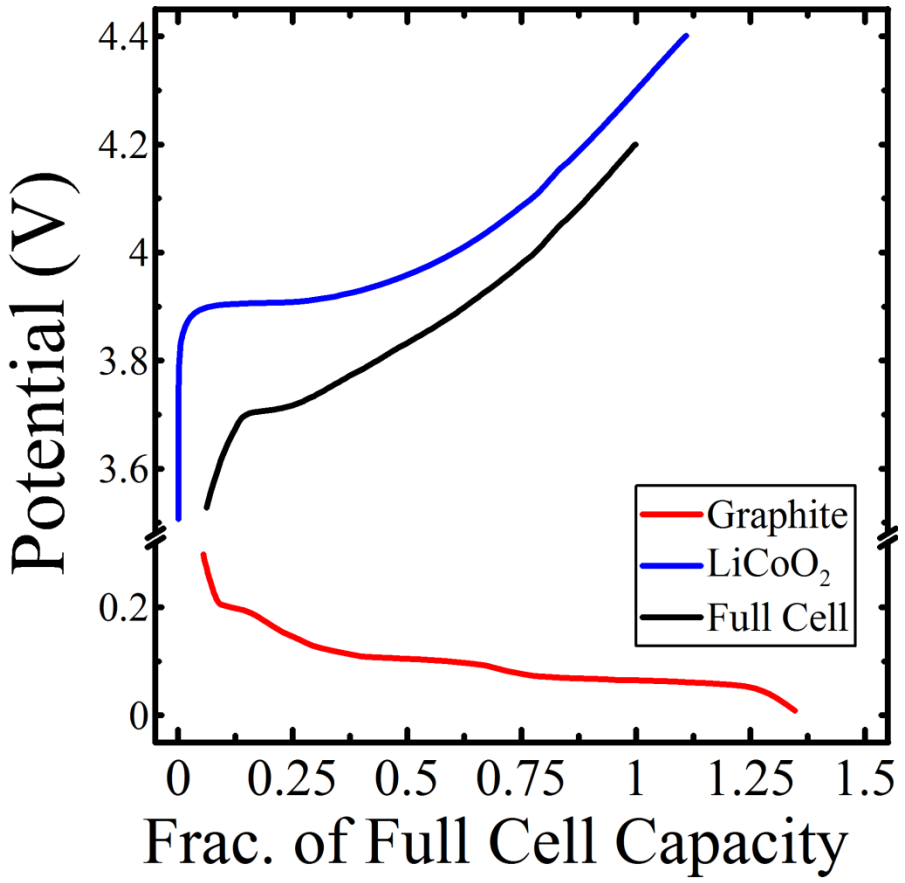

Figure 1.3 Schematic plot of potential versus capacity for $LiCoO_2$, graphite and a full cell composed of $LiCoO_2$ and graphite.

The cell shown in Figure 1.3 is a classic example of a cell used in a portable electronics; this cell is operated between 3.4 and 4.2 V. What is apparent from Figure 1.3

is that there is additional capacity available in both the positive and negative electrode, as the lithium cobalt oxide is shown having capacity up to 4.4 V and the graphite down to 0.01 V. The extra capacity is not utilized because it would result in significant loss in lifetime. Fathi *et al.* showed for the same lithium cobalt oxide/graphite cell chemistry cycled at 55ºC that when the upper cut-off voltage limit was raised from 4.075 V to 4.175 V the cycle at which 80% of the initial discharged capacity was achievable was reduced from 1100 cycles to only 550 cycles.[20] The reduction of capacity in Fathi's work was attributed to oxidation of the electrolyte at the positive electrode.

There are many reasons why a cell loses capacity with time and cycling. Early high precision charger (HPC) work by Smith *et al.*, that was expanded upon by Burns *et al.* discussed several common failure mechanisms in detail and methods to probe them. Smith reported four failure mechanisms that were the majority of the cause for cell failure:[21–23] The failure methods as reported were:

1. Li loss at the negative electrode through solid electrolyte interphase growth and repair;
2. Electrolyte oxidation at the positive electrode;
3. Transition metal dissolution at the positive electrode;
4. Positive electrode damage via Li trapping;

For failure mechanism number 1, the electrolyte and negative electrode composition are major contributors to the rate of failure via this mechanism. For mechanisms 2, 3 & 4 the electrolyte and positive electrode composition are major contributors to these failures. These failure mechanisms will be further discussed in the upcoming Sections 1.2.1 and 1.2.2. What is evident is that the positive electrode and electrolyte are important to lifetime.

The positive electrode and electrolyte are major components that impact lifetime, energy density and cost. These two components will be discussed in the next two sections.

1.2.1 Electrolytes

The electrolyte in a lithium-ion cell is usually a mixture of linear and cyclic organic carbonates and a lithium salt such as $LiPF_6$. Organic carbonates are the current choice solvent because they are kinetically stable at the operating potentials of a lithium-ion cell, have a high dielectric constant and are relatively inexpensive compared to alternatives such as ionic liquids.[24] While they are nominally stable at the operating potentials of a lithium-ion cell, the electrolyte should be completely inert to degradation if the cell is to last for thousands of cycles. As the electrolyte degrades the energy storage of the cell is reduced allowing the intended device to be operated for less time.

Electrolyte is degraded when it is consumed in unwanted "parasitic" reactions. A bulk of the consumption of the electrolyte occurs during the first charge of the cell. A passivation film called the solid electrolyte interphase (SEI) forms on the surface of the negative electrode when the cell is first assembled and current is applied. The exact chemical nature of the SEI is complex. Peled *et al.* described it as a film 30-50 nm thick composed of species such as Li_2O, LiF, Li_2CO_3 and various polyolefins.[24] The SEI passivates reactions between the graphite and the electrolyte preventing further consumption of the electrolyte.[25] Ideally, once the SEI film is formed it should be stable, but in a working lithium-ion cell this is not the case. The SEI is damaged via cracking due to lithium insertion and removal from the negative electrode.[22] Repairing the SEI results

in additional consumption of electrolyte and equally importantly lithium. Lithium in the SEI cannot be used in the reversible energy storage of the lithium-ion cell, decreasing the cell's energy density. As the SEI is repaired on subsequent cycles (failure mechanism #1 in Section 1.2) the cell gradually loses capacity as there is less lithium available in the active energy-storage lithium inventory for reversible intercalation. By modifying the electrolyte composition, the composition of the SEI may be modified. The modified SEI may have improved mechanical properties making it less susceptible to cracking, requiring fewer repairs and less lithium atoms required for intercalation lost.

At the positive electrode, the electrolyte is decomposed through oxidation (failure mechanism #2). The rate of oxidation of the electrolyte on the positive electrode is dependent on the electrolyte composition, positive electrode's surface composition, operating potential, temperature and other properties. Unlike the SEI which passivates additional reactions on the negative electrode, oxidation at the positive electrode is not as well passivated by surface films. This poor passivation results in additional oxidation every time the positive electrode is at high potential. Oxidation of the electrolyte removes active lithium from the electrolyte as reported by Smith.[26] This loss of lithium inventory in the electrolyte will hinder the electrolyte charge transport kinetics eventually resulting in cell failures; Burns classified this failure as a "roll-over" failure.[22] A cell will appear to being cycling normally for many cycles. Eventually the degraded electrolyte will no longer be able to move lithium ions effectively for the current being applied to the cell. This results in the cell losing much of its capacity in a relatively short time. In the work by Fathi discussed earlier, the cells charged to the higher 4.175 V cut-off experienced a roll-over failure at 550 cycles.[20] This roll-over failure was avoided by limiting the upper cut-off

voltage limit. However, if the electrolyte can be stabilized at high potential, more of the positive electrode's capacity can be utilized, increasing the cell's energy density.[27]

Researchers are looking for new electrolyte formulations that are suitable for high potential operations and that form a stable SEI. Electrolyte formulations are modified by introducing different solvent species referred to as additives. Additives are often added in 0.1-5 volume percent ($\%_v$) and are often thought to be sacrificial.[28,29] During the formation process additives are consumed or "sacrificed", to form highly stable passivation films on the electrode surfaces or the products of their oxidation or reduction minimize the continued consumption of electrolyte by blocking reaction pathways of the primary solvent (non-additive) and salt in the electrolyte. Vinylene carbonate is a common additive used in commercial cells and is often added at 2 $\%_v$. It is important that when additives are selected that their benefits at the positive electrode do not result in reduced performance at the negative electrode and vice versa.[30]

The choice for which additives to use and in what concentrations is often not a very scientific process.[27,31] Often, industrial researchers make many different cells with a large matrix of electrolyte formulations. Electrolyte formulations are then ranked solely on the capacity retained after hundreds or thousands of cycles done at charge and discharge rates faster than the cell would experience in normal operations. The formulation with the greatest capacity retention and acceptable cost is the one used in the commercial product. This method is highly ineffective in understanding how these additives function and leaves little scientific input into predicting additives that would perform better as only a single analysis, capacity retention was used. The accelerated test also makes the researcher blind

to degradation mechanisms that are time dependent. By cycling the cells at a fast rate the tests are simply "beating the clock".

The reason for brute force methods is that there are not many scientific probes that can easily study the electrolyte and its decomposition pathways in-situ or ex-situ. The primary reasons for the difficulties in probing electrolyte reactions are the complexity of materials in a working lithium-ion cell, the nanoscale thickness of the SEI and the organic and polymeric nature of the degradation products and surface films. This makes techniques such as X-ray diffraction (XRD), energy dispersive X-ray spectroscopy (EDS), scanning electron microscopy (SEM) and X-ray photoelectron spectroscopy (XPS) extremely challenging. Academic researchers have started to use techniques such as gas chromatography with mass spectrometry[32] or nuclear magnetic resonance spectroscopy[33] to probe the chemical structure and composition of the degradation products after a cell has been cycled. Other probes such as ultra-high precision cycling (UHPC), electrochemical impedance spectroscopy (EIS), differential capacity fitting and storage experiments can be used in tandem with chemical probes to develop a more complete understanding of the function of additives in lithium-ion cells.[34]

Figure 1.4 shows the structure of several additives commonly used in lithium-ion cells and two common solvent molecules, ethylene carbonate and dimethyl carbonate. The IUPAC name is listed first with common name and abbreviation given below. What is apparent from the few additives shown in Figure 1.3 is that additives are often derivative forms of EC or DEC, the bulk of the solvent molecules in the electrolyte. Other additives such as those containing sulfur and non-carbonate molecules have been explored.[35] The

derivation comes from the inclusion of fluorinated sites, conjugated rings or carbon-carbon double bonds.

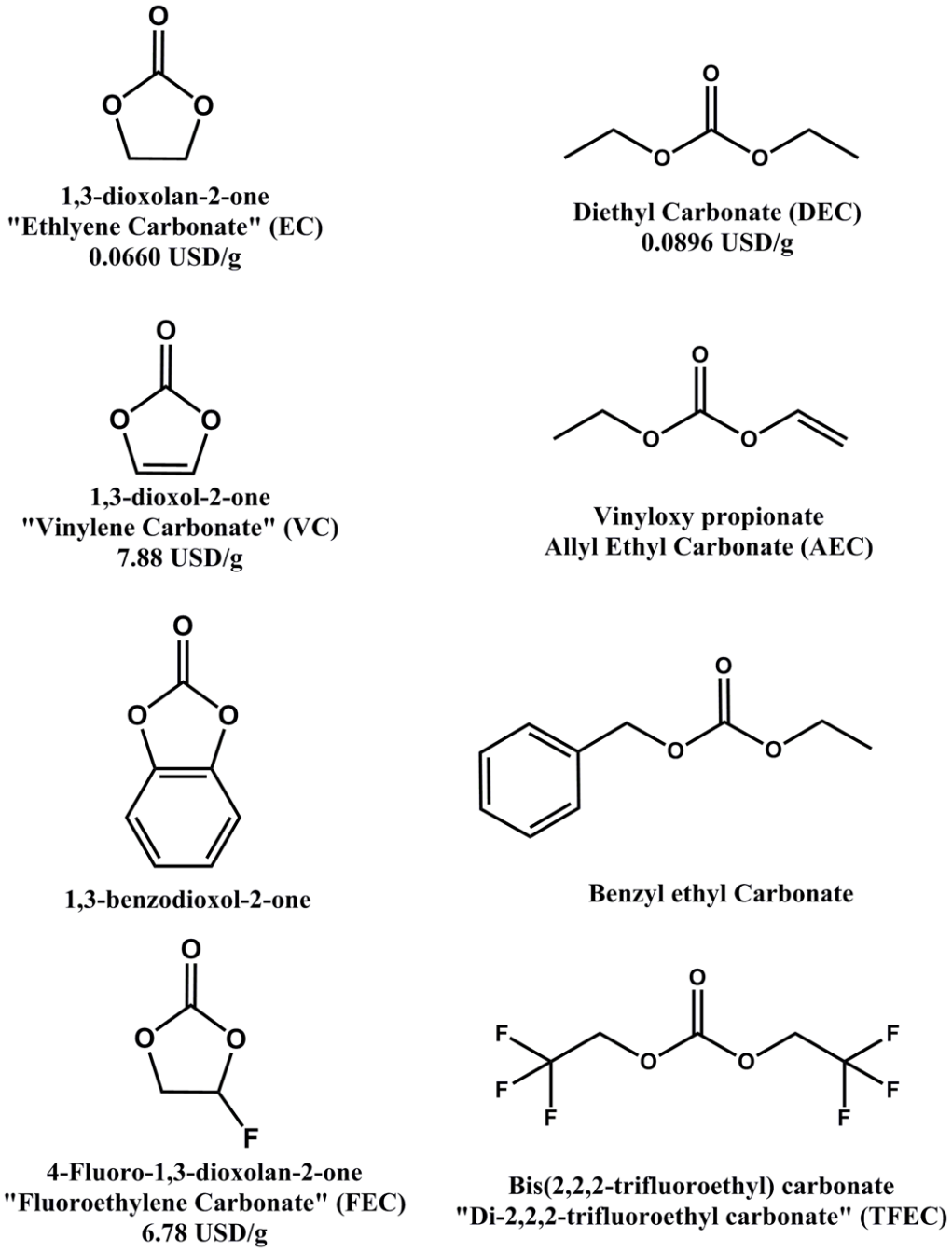

Figure 1.4. Structure drawings of several common linear and cyclic organic carbonates used as solvents or additives in lithium-ion batteries.[35–38]

Inclusion of these derivations requires additional synthesis and purification steps beyond what is required for EC and DEC, at a increased cost.[39] For example, to purchase EC, FEC or VC from a reputable chemical provider FEC and VC cost approximately 100 times more per gram than their precursor, EC. The solvent cost approximately triples when 2 $\%_v$ VC replaces EC; note EC and VC have relatively similar densities of 1.32 and 1.36 g/ml respectively. Without additives, the stability of the electrolyte solvent required to achieve the service lifetime required for EVs would be impossible. Current state of the art additives do not reduce the cost of a lithium-ion cell. Researchers are exploring additives that can provide the benefits of the molecules shown in Figure 1.4, but at a lower cost. The prices of the additives shown in Figure 1.4 is for small lab scale quantities (100 g max), economy of scales may significantly reduce the cost of additives.

In this thesis a complementary approach to electrolyte additives will be presented. As previously mentioned, the rate of oxidative degradation of the electrolyte on the surface of the positive electrode is affected by the electrolyte composition (additives), temperature, cell operation potential and the positive electrode surface composition. This thesis will focus on developing positive electrode materials that are of high energy density, low cost and promote long service lifetime by reducing the rate of oxidative degradation of the electrolyte on the positive electrode's surface. The remainder of the introduction will focus on the positive electrode and modification to its surface to increase service lifetime.

1.2.2 Lithium-Ion Positive Electrodes

The positive electrode of the lithium-ion battery can have different crystal structures; three of the most common structures are olivines, spinels and layered. Figure 1.5 shows the structure of three materials found in current commercial lithium-ion cells[40] Most lithium-ion positive electrode materials have a general formula of Li[Transition Metal]Anion. The transition metal can be a single metal such as $LiCoO_2$ or it can be a mixture of metals occupying the same crystallographic site in a solid solution such as $Li[Ni_{1/3}Mn_{1/3}Co_{1/3}]O_2$. Solid solutions exist for many different element combinations.

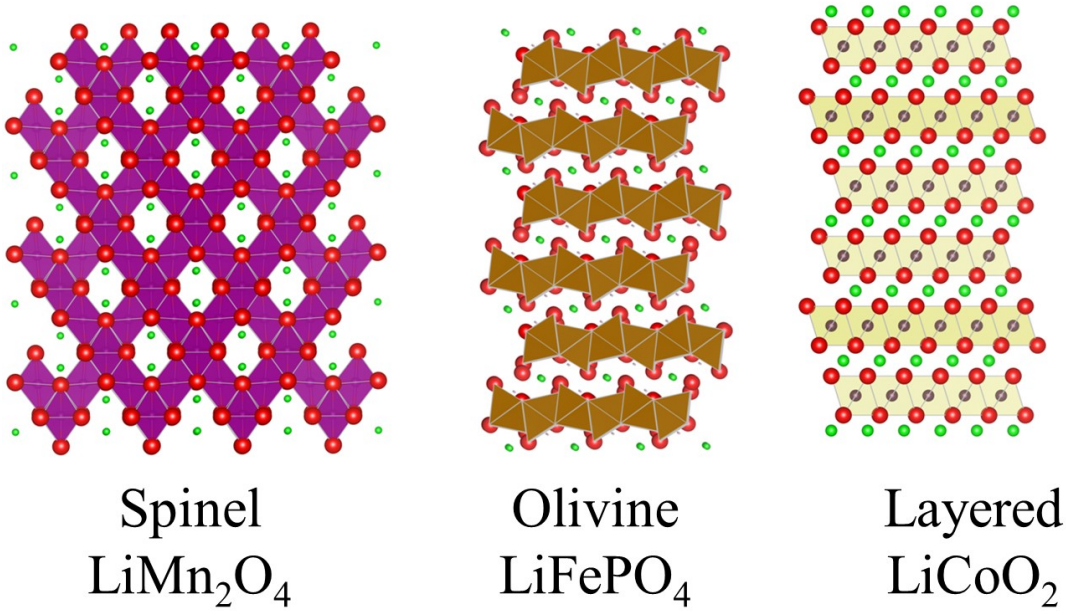

Figure 1.5. Structures of commonly used lithium-ion positive electrode materials, green spheres represent lithium atoms, red oxygen and transition metals as other colors located within polyhedra bonded to oxygen atoms.

McCalla developed a comprehensive phase diagram for the Li-Ni-Mn ternary oxide system using combinatorial studies which identified a large solid solution region of layered structures of which many compositions have been extensively studied.[41] Brown *et al.* with

the assistance of McCalla, expanded upon McCalla's work to the quaternary Li-Ni-Mn-Co oxide system.[42] Crystal structure and elemental composition have an impact on the performance of the material in a lithium-ion cell and should be carefully considered when designing new materials.

The energy density of a material is highly dependent on its composition and structure. The volumetric energy density, Wh/L, is determined by the density of the material and the amount of lithium that can be reversibly intercalated from the material within the desired voltage window. The achievable volumetric energy density is also dependent on the final electrode density which takes into account the packing efficiency of the secondary particles. Materials such as $LiFePO_4$ make use of a bulky phosphate polyanion for charge compensation. A phosphate, PO_4^{3-} and an oxide, O^{2-} anion have a mass to charge ratio of 32 and 8 g per negative charge respectively. A lower mass to charge ratio means less mass, so volume is "wasted" on inert structural anionic components. Comparing $LiMn_2O_4$ (spinel) to $LiCoO_2$ (layered) the theoretical gravimetric specific capacity of the spinel structure is 148 mAh/g and 274 mAh/g for the layered structure. It is important to realize that although $LiCoO_2$ has a theoretical capacity of 274 mAh/g, the achievable, nominal capacity in a working cell is about
150 mAh/g.[43] This is because if all of the lithium ions are removed from $LiCoO_2$, the structure will undergo an irreversible structural change which prevents the reintercalation of the lithium ions. For most layered structures the nominal capacity is between 140 and 240 mAh/g, which still exceeds the spinel's nominal capacity of about 90-120 mAh/g. $LiFePO_4$, an olivine structured commercialized material has a theoretical capacity of 170 mAh/g and a nominal capacity of about 150 mAh/g.[44] Compact structures that limit the

use of bulky polyanions and excessive structural components are an excellent framework for positive electrode materials. The olivine, spinel and layered frameworks are the most commonly studied in lithium-ion battery positive electrodes, of these structures the layered structure provides the opportunity for the greatest energy density and will be further discussed in Section 1.2.3.

Lithium diffusion is also important and crystal structure impacts the rate of diffusion. The positive electrode should have excellent diffusion of lithium to facilitate discharging and charging the cell quickly. Figure 1.4 showed the crystal structure of layered, spinel and olivine structures. For a layered structure diffusion is two dimensional. In a layered structure, lithium ions can be extracted parallel to layers of lithium atoms. In the spinel structure the tunnels of lithium ions form a three dimensional network allowing for diffusion in three dimensions. For the olivine structure the lithium channels are one-dimensional tubes. For olivine structured materials such as $LiFePO_4$, the crystallite and particle size must be minimized to facilitate reasonable charging and discharging rates.[45] Sizing $LiFePO_4$ is usually accomplished via a top-down approach with ball milling and the resulting nanoscale secondary particles are often irregular in shape. Packing efficiency of $LiFePO_4$ nanoparticles is low, reducing the overall volumetric energy density of the completed electrode. For layered and spinel structures the two and three dimensional networks allow for larger crystallite and particle sizes while still achieving facile lithium diffusion. These frameworks allow for more regular and higher packing efficiency microscale spherical particles.

As previously shown, the operating potential of the lithium-ion cell affects lifetime and energy density. The full cell voltage (cathode minus anode) is highly dependent on

the choice of positive electrode (cathode). Graphite is the current choice negative electrode material for lithium-ion batteries; the discharge curve of graphite was shown in Figure 1.3. For graphite, the average discharge potential is about 100 mV vs. Li/Li^+. The energy of a lithium ion cell is $\int q\, dV$ where q is the capacity discussed in the previous paragraphs and V, the voltage. If the potential is small the usable energy from the cell is limited. For the positive electrode, the lithium chemical potential depends on factors such as the atoms it is bonding to, the redox ability of host ions, structural geometry and other factors. For example, the olivine structure $LiFePO_4$ has an average lithium chemical potential of 3.5 V vs. Li/Li^+, while isostructural $LiCoPO_4$ has an average potential of 5.2 V vs. Li/Li^+.[45,46] Similarly, two spinel structures $LiMn_2O_4$ and $LiMn_{1.5}Ni_{0.5}O_4$ have an average lithium chemical potential of 3.8 and 4.7 V vs. Li/Li^+ respectively. Ceder *et al.* have used first-principle calculations to determine the average intercalation voltage for lithium in many different olivine, spinel and layered materials.[47]

Synthesis cost should also be considered when developing new materials. Synthesis cost has two major components, raw materials cost and processing cost. Raw materials costs are highly dependent on the choice of transition metals used. Cobalt, manganese and nickel are three of the most commonly used transition metals in lithium-ion batteries. The 2014 US mineral commodity summary listed the spot price of cobalt at 28.4 USD/kg, compared to nickel 15.0 USD/kg and manganese 0.0545USD/kg.[48]

Processing cost includes precursor synthesis, high temperature sintering and synthesis atmosphere. Precursors are template particles developed prior to the final olivine, layered or spinel structure. The precursor step serves two purposes. First, for samples that have mixed transition metals such as $Li(Ni_{1/3}Mn_{1/3}Co_{1/3})O_2$, the transition metals need to

be homogeneous throughout the particles to ensure a solid solution is synthesized. Secondly, the precursors serve to develop the particle size and morphology.[49] This process is usually done using a continuously stirred tank reactor (CSTR), sonication or sol-gel method where metal salts are dissolved in solvent and then precipitated in highly controlled reactions to form hydroxides, carbonates or other compounds. Additional details about precursor synthesis will be discussed in Chapter 2.

After a precursor is developed, a high temperature sintering step usually occurs. Prior to sintering, the precursor is mixed in a stoichiometric ratio with a lithium salt such as Li_2CO_3 or $LiOH \cdot H_2O$. A solid state reaction then occurs and the thermodynamically stable phase(s) form. The reaction atmosphere may also be controlled for some materials to ensure the desired product is synthesized. Inert atmospheres are used for material such as $LiFePO_4$ to prevent the oxidation of Fe^{2+} to Fe^{3+}.[45] The oxygen partial pressure may be controlled in the synthesis of layered or spinel structures to control lithium content in the solid due to an equilibrium between volatile lithium peroxide vapor and intercalated lithium at high temperature.[50] For most materials, sintering is the final step. Some materials may require additional steps such as coating to enhance conductivity or morphological modifications to optimize battery performance.[51] Modifying the synthesis by adding complicated or expensive processing should only be done when the added benefits of processing greatly enhance the material's performance.

It is also common for positive electrode materials such as $LiCoO_2$ to be coated with an inert coating of materials such as MgO, Al_2O_3 or SnO_2.[52–55] These coatings have been shown to improve lifetime, either by stabilizing the structure of the delithiated-$LiCoO_2$ or by passivating electrolyte oxidation at the particle surface. Coatings were applied by

suspending prepared $LiCO_2$ powder in a basic solution and adding a source of the desired metal such as $MgCl_2$. The product was then washed and fired at temperatures up to 600°C for several hours to produce the oxide coated particles.

Composition and structure of the positive electrode material will have lifetime implications.[56] Of the failure mechanisms listed at the end of section 1.2, mechanism 2, 3 & 4 are dependent on the composition of the positive electrode. Mechanism 2, electrolyte oxidation at the positive electrode, will be dependent on the surface composition and potential of the positive electrode. Gummow *et al.* described mechanism 3, transition metal dissolution via what is called a disproportionation reaction.[57] In this reaction two Mn^{3+} located in an octahedral environment can react together forming a Mn^{2+} in a tetrahedral site and an octahedral Mn^{4+}. The tetrahedral Mn^{2+} species are not tightly bound to the host structure and dissolve into the electrolyte. This reduces the available transition metals for oxidation and reduction during lithium intercalation and deintercalation, decreasing the cell capacity. Additionally, the dissolved manganese species can migrate to the negative electrode where they can damage the SEI.[58] Dissolution of manganese has also been reported in layered structures.[59] Mechanism 4, positive electrode damage, is also dependent on composition. Removal of lithium from the host structure results in changes in the lattice size of the positive electrode. These dimensional changes along with the structural defects in the lattice structure can lead to irreversible damage that can prevent intercalation of lithium back into the host.

Based on the analysis of the olivine, spinel and layered structures in this section the optimal structure for high energy density cells is the layered structure. The layered framework has the best theoretical energy density of the three structures due its use of an

efficient oxide anion for change balance and rudimentary structure. The layered structure also does not have any major disadvantages such as poor lithium diffusion or expensive processing cost as are present in the olivine family. Section 1.2.3 will discuss in detail discoveries of layered structured positive electrode materials and their use in next generation materials for lithium-ion batteries.

1.2.3 Layered Lithium-Ion Positive Electrodes

The layered material $LiCoO_2$ was the first positive electrode material used in commercial lithium-ion batteries developed by Sony in 1990.[60] $LiCoO_2$ was discovered as a useful lithium-ion positive electrode material by Goodenough *et al.* in 1980.[61] $LiCoO_2$ structure is of the space group, R-3m, commonly referred to as the α-$NaFeO_2$ type structure. In the late 1990s a new series of materials was developed independently and simultaneously by Lu *et al.* at Dalhousie University and Ohzuku *et al.* in Japan at Osaka City University.[62–64] These materials had a composition of $Li(Ni_xMn_xCo_{1-2x})O_2$ $0 \leq x \leq 0.5$. In these materials two Co^{3+} were replaced by a Ni^{2+} and a Mn^{4+}, and are commonly referred to as NMC materials due to their transition metal composition. One of the most successful NMC materials is NMC-111, which has a composition of $Li(Ni_{1/3}Mn_{1/3}Co_{1/3})O_2$. 111 refers to the ratio of Ni:Mn:Co. The NMC framework also allowed a new class of materials to be studied by Lu *et al.*, with a composition of $Li(Ni_xLi_{(1/3-2x/3)}Mn_{(2/3-x/3)})O_2$ $0 \leq x \leq 0.5$.[65] This class of materials were referred to as the "lithium-rich" series due to the presence of more than one lithium per formula unit. For the lithium-rich series, when $x = 0.5$, $Li(Ni_{0.5}Mn_{0.5})O_2$, there is no excess lithium. As x

decreases in this series, a substitution of three Ni^{2+} ions by two Li^{+} and one Mn^{4+} occurs. Figure 1.6 shows the transition metal layer for several layered materials with lithium ions shown in green, manganese in purple, nickel in green and cobalt in gray. In NMC-111 and the lithium–rich material shown, the transition metal layer is randomly occupied by Ni, Mn, Co or Li ions.[65] These samples are best described by the space group R-3m which has a single atomic position to describe all of the transition metal layer sites.

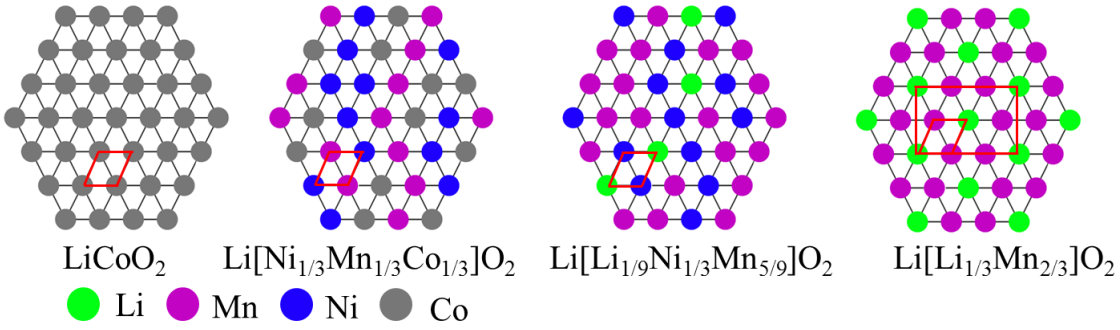

Figure 1.6 Top down view of the transition metal layer of $LiCoO_2$, NMC-111, $Li(Ni_{1/3}Li_{1/3}Mn_{5/9})O_2$ and $Li(Li_{1/3}Mn_{2/3})O_2$. A unit cell of R-3m is outlined in all 4 drawings in red. A C2/m unit cell (rectangle) is also outlined in the $Li[Li_{1/3}Mn_{2/3}]O_2$ drawing.

In $Li(Li_{1/3}Mn_{2/3})O_2$, the Li and Mn ions are ordered on the transition metal layer, which results in a compound being best described by the space group C2/m, although if the ordering within the transition metal layer is ignored, can also be described by R-3m. Removal of lithium from all of the layer structures shown requires compensation in charge in the host structure. For $LiCoO_2$, lithium extraction is associated with the redox couple, $Co^{+3/+4}$. In NMC materials Ni^{2+} and Co^{3+} are present and could be oxidized to the plus-four state as lithium is removed. For the excess lithium materials only Ni^{2+} is initially available for oxidation. For the material $Li[Ni_{1/3}Li_{1/9}Mn_{5/9}]O_2$, shown in Figure 1.6 there

is only $Ni^{2+/+4}$ oxidation which means a maximum of 2/3 of all the lithium atoms can be extracted if charge compensation is only achieved through the oxidation of nickel. This would limit the specific capacity of this material to 200 mAh/g. Surprisingly, MacNeil *et al.* reported a first charge capacity of nearly 300 mAh/g and a reversible capacity of about 220 mAh/g when the material was charged and discharged between 2.5 and 4.8 V versus a lithium metal counter-electrode.[64] The extra capacity and lithium extraction was suggested to be due to oxidation of the oxide anion. This oxidation process resulted in the evolution of O_2 gas and was noticeable by a long plateau in the voltage profile of this material when first charged.[66] After this process the material no longer had a plateau, but maintained a higher than expected capacity.

Figure 1.7 shows the voltage versus specific capacity plot of an excess lithium material for the first 2 cycles. The relatively flat plateau observed at 4.5 V vs. Li/Li^+ on the first charge (red) is what is commonly referred to as the oxygen release or activation plateau. It is clear from Figure 1.7 that during the second cycle (black) this plateau no longer occurs. This process results in some sort of activation that allows for reversible capacity on subsequent cycles to be obtained through a different charge compensation mechanism.

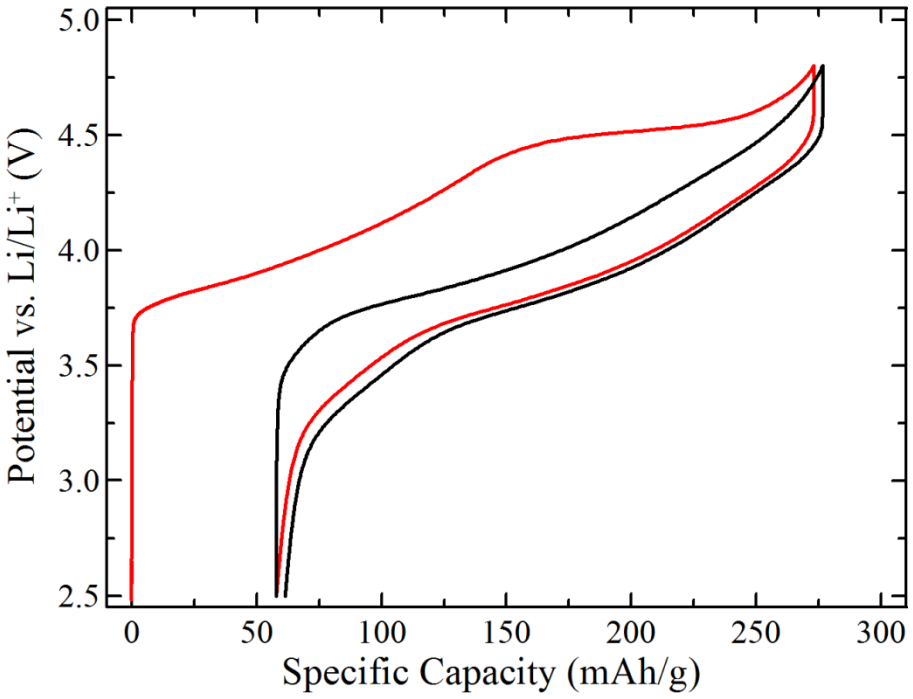

Figure 1.7. Plot of potential versus specific capacity for Li/Li[$Ni_{1/3}Li_{1/9}Mn_{5/9}$]O_2 cell with the first cycle shown in red and the second cycle shown in black.

As expected as the nickel content was lowered more lithium was extracted through this activation process instead of through conventional transition metal redox, leading to two issues with these materials.[65] Van Bommel *et al.* showed that as the length of the activation process plateau was increased, the irreversible capacity (difference in first charge and discharge capacity) increased.[67] Irreversible capacity presents a challenge to cell manufacturers as they must carefully balance the capacities of the positive and negative electrode. The large irreversible capacity requires extra negative electrode to compensate for the lithium extracted from the positive electrode and not replaced on discharge.

The second phenomenon observed in these materials is what is known as voltage decay. Voltage decay is the continual decrease in average discharge potential as the cell is charged and discharged for more cycles. Croy *et al.* showed with X-ray absorption data

that voltage decay is intrinsic to the manganese-rich materials and has nothing to do with interactions with the electrolyte as previously thought.[68,69] Koga *et al.* also proposed a mechanism that suggested that the voltage decay was due to a change in the composition near the surface of the particles.[70,71] Excess lithium materials show voltage decay for the first 20-50 cycles after which time the voltage stabilizes. Ideally if voltage decay could be avoided, it would be useful for energy density, but the work from Croy suggested that this is not possible.

There is a debate among researchers about the exact structure of the excess lithium materials. Some researchers believe these materials are a solid solution reported by Lu, $Li(Ni_xLi_{(1/3-2x/3)}Mn_{(2/3-x/3)})O_2$ $0 \leq x \leq 0.5$.[72] Other groups believes that these materials are not a solid solution but rather a "nano-composite" of the end members of Lu's series. The nano-composite has very small primary crystallites on the order of 10's of nm that are single phase. These small crystallites broaden the diffraction peaks in X-ray diffraction resulting in a pattern that is the weighted average of the two contributing phases. Neither description fails to explain the voltage decay and activation process. However, both descriptions are too primitive to understand reports by Li and McCalla that showed materials exist with lithium content in excess of Lu's solid series and the nano-composite limits.[73] For this reason these materials will be described as solid solutions of a composition $Li_{(1+x)}(Ni_yMn_{(1-y)})_{(1-x)}O_2$, of which the limits for x & y are determined by the reported single phase layered regions in the phase diagrams by Li and McCalla.[74] The McCalla/Li phase diagrams will be presented in Chapter 2.

1.3 Core-Shell Materials

The flexible framework of the layered structure allows for many different materials to be synthesized. While many materials are possible, the ones most extensively studied are $LiCoO_2$, NMCs and excess lithium materials. Figure 1.8 shows several datasets collected using high precision chargers on layered structured positive electrode materials.

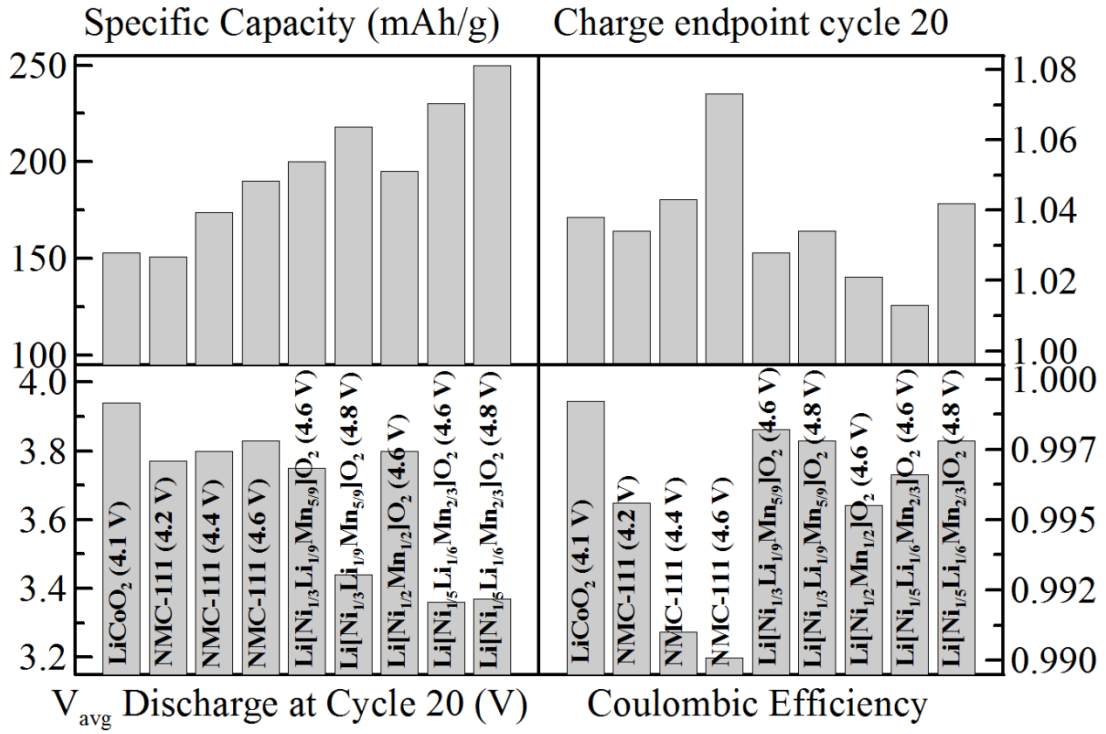

Figure 1.8 Specific capacity, coulombic efficiency, average discharge potential and charge endpoint slippage of several NMC and lithium rich materials.[75,76] All cells shown were cycled at a rate of approximately C/20 at 30.0°C in half cell configurations with 1 M $LiPF_6$ in an ethylene carbonate and dimethyl or diethyl carbonate solvent blend without electrolyte additives. Each panel's vertical axis label is shown above or below its respective horizontal axis.

To maximize energy density, materials with high capacity and high discharge voltages should be selected for the positive electrode. The right two panels show coulombic efficiency (CE) and charge endpoint capacity slippage, which are lifetime

indicators. The closer the value of CE is to $1.\bar{0}$, the longer lifetime the cell should have as side-reactions during charge and discharge are minimized. Charge endpoint capacity slippage is an indicator of the rate of electrolyte oxidation. In Figure 1.8, the charge end point has been normalized to the 2nd charge capacity of the materials shown, less slippage is desired for longer lifetime. Figure 1.8 is only a small sampling of layered structures studied in literature. Many materials have yet to be analyzed using high precision chargers which are the most effective way to measure coulombic efficiency and charge endpoint capacity slippage. In Figure 1.8 there is not a single material that is the best for all four metrics shown.

As shown at the end of Section 1.2, most of the lifetime limitations are due to interactions of the electrolyte at the surface of the positive electrode. Oxidative degradation requires the electrolyte molecules to be at the surface of the positive electrode to react. Examining all the cells charged to 4.6 V in Figure 1.8, the rate at which the electrolyte oxidizes differs from material to material. Materials of particular interest are $Li[Ni_{1/5}Li_{1/6}Mn_{2/3}]O_2$ and $Li[Ni_{1/2}Mn_{1/2}]O_2$. The manganese-rich $Li[Ni_{1/5}Li_{1/6}Mn_{2/3}]O_2$ showed extremely low charge endpoint slippage, but due to its manganese-rich composition was reported to show voltage fade resulting in a low average discharge voltage.[56] The composition $Li[Ni_{1/2}Mn_{1/2}]O_2$, has an adequate capacity and does not show voltage fading like the excess lithium materials resulting in an excellent energy density. $Li[Ni_{1/2}Mn_{1/2}]O_2$ does show a lower CE and higher charge endpoint capacity slippage than the manganese rich composition. It would be useful if the beneficial properties of these two compositions could be exploited to develop a long-lasting high energy density material.

Exploiting the benefits of multiple compositions was proposed by Sun and Amine in reports on what they described as core-shell materials several years ago.[77,78] These materials aimed to exploit two compositions by placing one composition at the surface for long lifetime and another in the core, accounting for the bulk of the particle, for high energy density. Figure 1.9 shows a schematic drawing of a core-shell particle.

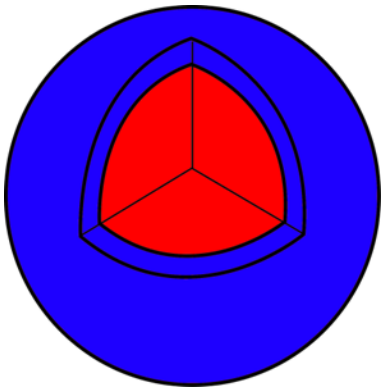

Figure 1.9 schematic drawing of a core-shell particle with a cutaway showing a red composition core with high energy density and a blue shell for long lifetime.

In Figure 1.9 a "red" core composition is encapsulated with a "blue" shell composition. The core is a composition with high energy density and the shell is a composition which excellent lifetime performance. The shell limits interactions between the core and the electrolyte and the core provides the bulk of the energy storage. The core-shell could also be developed with gradient compositions in the shell or throughout the particle. The gradient composition concept was suggested to minimize strain at the interface between the core and shell due to a drastic compositional change.[79]

Sun and Amine reported on core-shell materials that showed improved capacity retention and better thermal stability in comparison to their core-only counterparts.[78,80] In

the report the authors justified their choice of core and shell material based on differential scanning calorimetry results that showed that their selected shell phase was more thermally stable than their selected core phase. In their report, the diffraction pattern of the hydroxide precursor clearly showed two hydroxide phases present at the end of the synthesis. The diffraction patterns of the lithiated and sintered product were also reported. In the diffraction pattern of the final products it was unclear if the samples were two phases or a single phase. The authors reported a single set of lattice parameters for this sample which was intermediate of the core and shell single phase lattice parameters. To convince the readers that the sample was core-shell the author used energy dispersive spectroscopy (EDS) to report on the composition across a cross-sectioned particle. The EDS results showed that the transition metal composition varied across the particle suggesting multiple phases but, due to the noise in the data, this method was not quantitative. While Sun and Amine reported that the core-shell structures showed lifetime benefits while maintaining energy density, their reports left many questions about synthesis and characterization these core-shell structures. Their reports also did not include high precision charger results which would be useful in determining more specifically how the core-shell materials improved lifetime.

1.4 Scope of Thesis

Based on previous reports on core-shell materials, several questions in the synthesis, characterization and performance of core-shell materials still existed.

1. During precursor synthesis how can one ensure that the shell is forming a closed coating around the core particles?
2. What methods can be used to determine the ratio of the core and shell phases and the thickness of the shell coating?
3. Do transition metals diffuse during the sintering process?
4. Lithium cannot be detected with EDS methods so how can the lithium content in the core and shell phases be individually determined?
5. Is the core-shell structure maintained during charging and discharging of the material in a cell?
6. Does the core-shell material provide a lifetime benefit in coulombic efficiency and charge endpoint capacity slippage?

This thesis aims to answer the above listed questions. Chapter 2 will discuss the experimental techniques used to synthesize and characterize core-shell materials. Chapter 3 will discuss several single phase, materials studied with high precision chargers. Chapter 4 will primarily discuss core-shell precursor synthesis with the goal of addressing question 1. Chapter 5 will discuss a novel technique to measure the thickness of the shell. Chapter 6 will discuss the sintering process and characterization of the lithiated product. Chapter 7 will show high precision charger results of the core-shell materials and discuss their possible lifetime benefits.

Chapter 2. Experimental

2.1 Experimental Scope of Research

The motivation of this research was to study novel compositions of lithium-ion positive electrode materials with a core-shell microstructure and to develop robust and comprehensive characterization methods for them. These core-shell materials were developed using a two-step synthesis, which will be described in detail in this chapter. Synthesized materials were then tested in coin-cells which provided electrochemical performance data.

Materials were characterized throughout the synthesis process. Techniques such as X-ray diffraction (XRD), scanning electron microscopy (SEM) and Inductively Coupled Plasma Optical Emission Spectroscopy (ICP-OES) were used to characterize the synthesized powders. The details of these techniques will be presented later in this chapter. Electrochemical performance was tested in galvanostatic charge-discharge cycling using classical battery cyclers and ultra-high precision (UHPC) systems. This chapter will describe the synthesis and characterizations steps individually and in detail.

2.2 Research Landscape of Interest

The layered structure positive electrode materials studied in this work contained the elements lithium, nickel, manganese and oxygen. This system can be described as a pseudo-ternary oxide system when the only anion allowed is an oxide as is the case in this work. A Gibbs triangle can be used to describe the relationship between composition and structure for this pseudo-ternary system. Figure 2.1 shows a Gibbs triangle for the Li-Ni-

Mn pseudo-ternary oxide system when samples are prepared at 900 ºC in air and then slowly cooled to room temperature after 10 hours of heating. This diagram was prepared based on the results of McCalla, Li, Rowe and co-workers.[74,76,81]

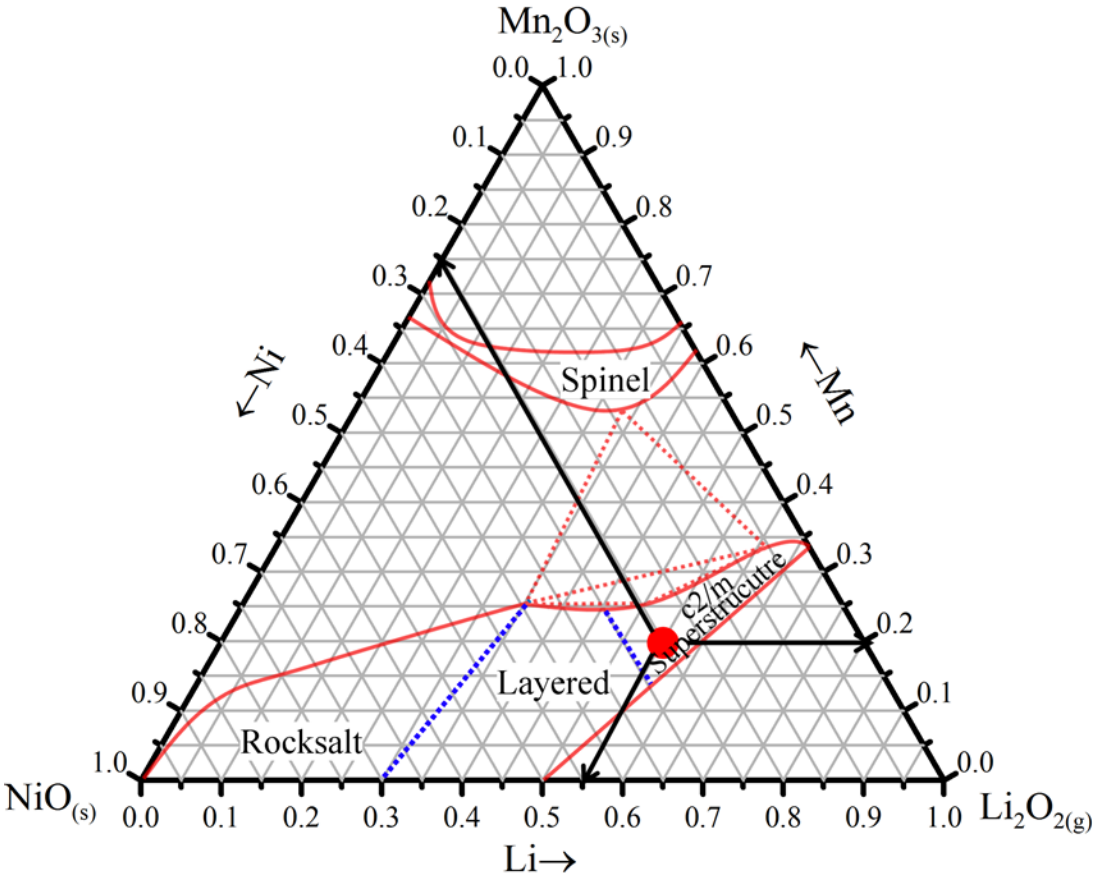

Figure 2.1 Gibb's triangle of the Li-Ni-Mn oxide pseudo ternary system for synthesis in air at 900 ºC with slow cooling to room temperature.[73,74,76] Single phase regions observed at room temperature are within solid red lines, two phase regions are between a dashed red line a solid line and three phase regions are outlined exclusively by dashed red lines. Dashed blue lines represent order-disorder transition disordered rocksalt to layered and layered to layered with c2/m superstructure. Solid black arrows indicate how to read the composition of the red circle at Li, Ni, Mn (0.55, 0.25, 0.20).

The Li, Ni and Mn atomic fractions at any given point in the ternary diagram are determined by the intersection of the point and the three axes. Oxygen content is allowed to vary based on the phases present. All samples in Figure 2.1 were synthesized using air

as the synthesis atmosphere (P_{O2} of 0.21 atm)[82], thus the nomenclature of "pseudo-ternary" system. The large red circle in Figure 2.1 intersects the base of the triangle at 0.55, the left side at 0.25 and the right side at 0.2 and black arrows show how to read the three axes. The axes labels in Figure 2.1 show that the base represents Li, the left side represents Ni and the right side represents Mn so the red point has a (Li, Ni, Mn) atomic fraction composition of (0.55, 0.25, 0.20). Since the atomic fraction of Li, Ni and Mn must sum to 1, any point in this diagram need only be described by a pair of coordinates. For clarity, compositions will be expressed as the ratio of the 3 elements. The large red circle lies within a single phase region (outlined by solid red lines) and the phase is the hexagonal layered phase, space group R-3m[83] This sample would have a composition of $Li[Li_{0.1}Ni_{0.5}Mn_{0.4}]O_2$, one of the lithium-rich samples described in Chapter 1. If a sample is a core-shell sample it will be described by a pair of coordinates on the phase diagram, one for the core phase and one for the shell phase. The ratio of phases and their compositions for samples within multiphase regions can be determined using the lever rule and tie lies, which are reported by McCalla, but not displayed in Figure 2.1.[41]

This thesis will exclusively examine samples within or near the borders of the single phase layered region. This structure-composition ternary diagram represents samples synthesized at 900ºC in air that are slowly cooled and is only applicable when the synthesis is under the same conditions. McCalla *et al.* have also published diagrams for the Li-Ni-Mn pseudo ternary system for other temperatures when samples are quenched or slow cooled and using variable oxygen partial pressures in the reaction atmosphere.[74] These alternative diagrams will not be discussed in this document. There are composition and phase combinations that are only synthetically achievable with conditions other than 900ºC

and slow cooling. These alternative materials may show promising performance for use in Li-ion batteries and should be explored by future researchers. The scope of this thesis is in characterization of core-shell materials, and is not necessarily pursuing the optimized material for commercial batteries. Without a complete understanding of the composition space one is working in, it becomes challenging to fully interpret the data. The structure-composition diagram of the samples at 900ºC in air is the most comprehensive diagram published for the Li-Ni-Mn pseudo ternary oxide system. A few samples which are part of the pseudo quaternary Li-Ni-Mn-Co oxide system will also be discussed in later chapters. Brown *et al.* have developed a rudimentary understanding of this composition space which can be visualized as on a "Gibb's Tetrahedron".[42,84] A comprehensive complete quaternary diagram would require tens of thousands of samples to develop with similar resolution to the diagram in Figure 2.1, which McCalla, Rowe and Li developed from less than one-thousand samples.[41,42,85] Due to the 2D printing limitations of this paper document, the quaternary diagram will not be shown. Figure 2.1 is one of the faces on the Li-Ni-Mn-Co tetrahedron diagram.

McCalla developed the first iteration of the Li-Ni-Mn oxide structure-composition diagram using combinatorial methods.[86] This allowed for a high throughput of samples, but because of the synthesis method, questions were raised as to if what was found was also true for synthesis that mimicked industrial processes. Li and Rowe developed many samples in bulk (1-10 g) scale that confirmed McCalla's results were accurate.[76,85]

2.3 Precursor Synthesis

Industrial synthesis of Li-Ni-Mn-Co layered positive electrode materials is usually accomplished using one of two methods.[87] The first method is purely a solid-state reaction in which oxides, carbonates or other salts of Li, Ni, Mn or Co are mechanically mixed in stoichiometric amounts and then sintered. The resulting particles from this methodology are irregular due to the lack of template precursor particles resulting in poor packing efficiency and low volumetric energy density. Samples prepared using this method also generally require higher temperatures or longer sintering time to ensure complete atom mixing required to develop solid solutions. Extending the heating time decreases throughput, increases cost and can cause extended crystallite growth which may inhibit lithium solid state diffusion.

Many have reported on mixed transition metal hydroxide co-precipitation as a method to synthesize template particles for lithium-ion positive electrode materials.[49,79,88,89] To synthesize the final positive electrode product, the precursor particles are mixed with lithium carbonate or lithium hydroxide and sintered to yield the desired lithiated solid solution.[49] Zhou showed that when the synthesis of the hydroxide was carefully controlled, potato-shaped 1-20 μm particles could be synthesized. These particles have a more desirable packing efficiency than materials prepared with only solid-state methods described in the previous paragraph. Since the transition metals were already well mixed, the sintering time and temperature could be milder and still yield the desired solid solution products with excellent electrochemical performance. From Zhou's work the most important parameters of the hydroxide precursor synthesis to monitor were temperature, synthesis atmosphere, stir rate, pH and the use of ammonium-ions.

Van Bommel expanded on Zhou's work using a continuously stirred tank reactor (CSTR).[90] Figure 2.2 shows a schematic of a tank reactor. This schematic is just one example of a reactor setup; the number of inputted solutions or probes can easily be modified depending on the desired synthesis controls. CSTRs are ideal for use in battery research as the methods are scalable from a small lab system of hundreds of millilitres to large industrial systems of thousands of litres. Systems can also be operated in a batch process, where the product is collected from the main tank after a specific amount of time and then the process is restarted after cleaning. Alternatively the reactor can be a continuous process in which a sizing mechanism expels particles of a desired size from the main tank and filters undersized particles back into the system for continued growth.

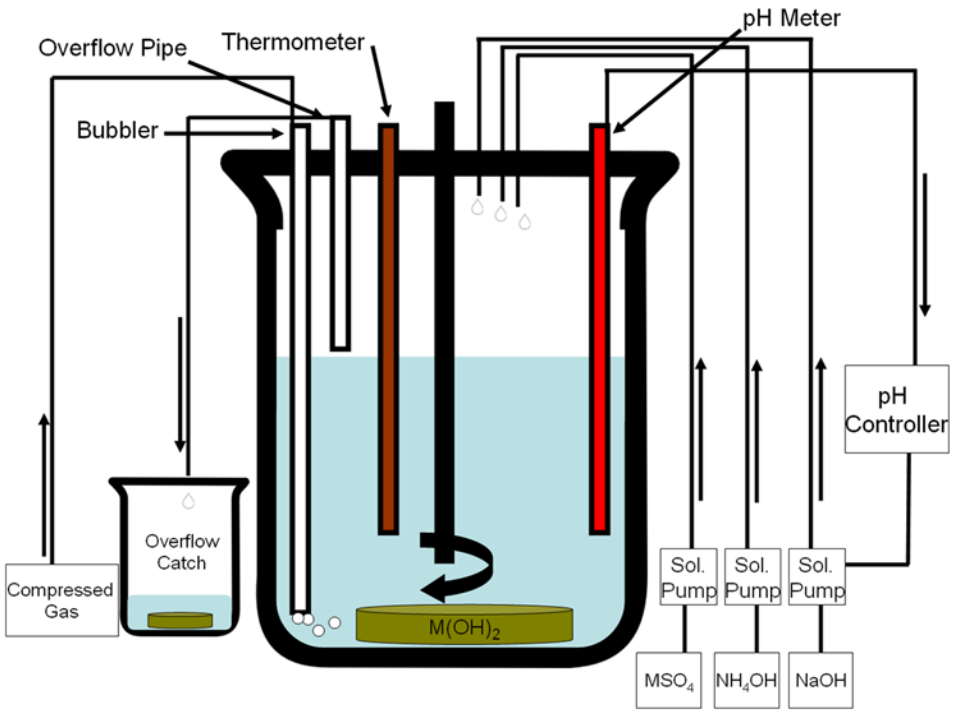

Figure 2.2 A schematic drawing of a CSTR during synthesis of a $M(OH)_2$ precursor. This reactor is setup to run under quasi-steady-state with the tank volume maintained at a constant level due to the position of the overflow pipe. M = Ni, Mn or Co.

2.3.1 Influence of Ammonia and pH on Morphology and Composition

Van Bommel used what he described as a quasi-steady-state method in his synthesis of Ni-Mn-Co hydroxides.[90] To initiate his reaction, 1 L of 1 M NH_4OH was poured into the tank and heated to 60 ºC. Nitrogen gas was then bubbled into the reactor to purge oxygen. The justification of an inert atmosphere was to minimize the oxidation of manganese-hydroxide which resulted in undesired morphologies. Once the reactor was warmed and purged, the reaction was started by slowly dripping MSO_4 solution into the tank (M = Ni, Mn or Co). A pH probe monitored the solution pH and maintained it at a fixed value by adding sodium hydroxide as required. As the volume of the solution increased some of the suspension was expelled from the main tank into an overflow catch. Van Bommel discarded the overflow product; however, in an industrial process overflow would be recycled to minimize product loss, via a more complicated system. Due to the loss of some solution via the overflow, NH_4OH was slowly added to the tank to maintain a fixed 1 M concentration of ammonia species.

Van Bommel synthesized many different Ni, Mn and Co hydroxides and explored the impact of pH, time and dispensing rate on the product synthesis. Van Bommel's best results were accomplished when the synthesis and dispensing of reactants occurred over 20 hours, dispensing 500 ml of 2 M MSO_4 and maintaining the pH between 9 and 11 with 1 M NH_4OH.[90] For Van Bommel's work, "best" was considered particles with high tap density due to excellent primary particle packing and uniformity in the shape and size of secondary particles. Morphology was highly dependent on metal composition and pH. This can be understood by the equilibrium that exists between free M^{2+} species, NH_3, OH^- and solid and soluble $M(OH)_2$ species. Ammonia will coordinate to Ni, Mn and Co in

solution and the concentration and number of coordinating ligands, $M(NH_3)_n$, $n \leq 6$, is dependent on pH and the transition metal as shown in Figure 2.3. Other parameters such as temperature and concentration also impacted the coordinating.

Figure 2.3 shows the concentration as a function of pH for $M(NH_3)_n$, $n \leq 6$, M = Ni, Mn or Co, generated using software (Medusa).[91] Each metal was calculated individually at a concentration of 1 M M^{2+} with a solution temperature of 25ºC and the total NH_3 concentration was 1 M. Temperature could not be varied with this software package. Coordinating the transition metals with ammonia in solution was shown by Van Bommel to improve the morphology significantly. The explanation for this process was that the presence of ammonia results in a thermodynamically favorable reaction of small particles with high surface area dissolving back into solution and coordinating to ammonia. Precipitation and dissolution would continue to occur until spherical, large particles with small surfaces areas were formed. The resulting products were roughly spherical with diameters of 2 to 15 μm. Size, shape and surface morphology were highly dependent on transition metal compositions even when the pH was optimized.

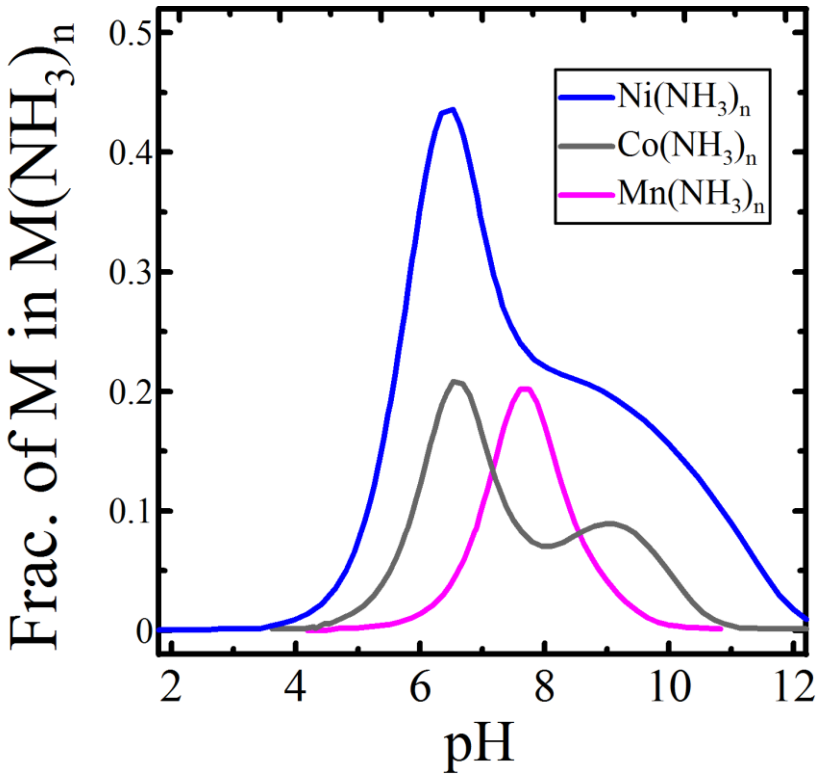

Figure 2.3 Plot of fraction of metallic species coordinated to NH_3. Diagram produced using Medusa with 1 M total NH_3, 1 M M^{2+} at 25ºC. Each metal curve is calculated free of other metals thus ignoring common-ion effects.[91,92]

All of these processes need to be carefully considered to synthesize the desired product with optimized morphology. If the pH is too high, morphology will suffer. If the pH is too low, then the differences in solubility of Mn, Ni and Co in the presence of NH_3 will result in the precipitated product having a composition different than that inputted and oversized particles. In slightly basic conditions (pH 7 to 9) and high ammonia concentrations, the dissolution-precipitation process results in particles of sizes too large for use in batteries. Large particles (over 30 μm) on the positive electrode are problematic because of sluggish mass transport, large void space in monodisperse distributions, and ease of delamination from the current collector.

Slightly basic conditions cause issues due to nickel's affinity for ammonia. The high affinity results in a significant portion of the nickel staying in solution, altering the final product stoichiometry. In highly basic conditions (pH above 11) manganese and cobalt will not coordinate to NH_3 which results in poor particle morphology. For materials in this thesis, samples were synthesized with pH values between 9 and 11. It is also important to note that the solubility curves shown in Figure 2.3 are at 25 °C and for only a single metal at a time. In a real reaction all the metals are present in a stoichiometric ratio which can result in common-ion effects. In principle, the work by Van Bommel and solubility curves were used as a starting point for each unique composition. Based on SEM and XRD results of the first attempt at a synthesis, the pH was adjusted to improve morphology and composition.

2.3.2 CSTR Operation

For most of the materials presented in this thesis a BioFlo 310 fermenter (New Brunswick Scientific) was used as the CSTR apparatus. Figure 2.4 shows a photograph of the setup with the system turned off.

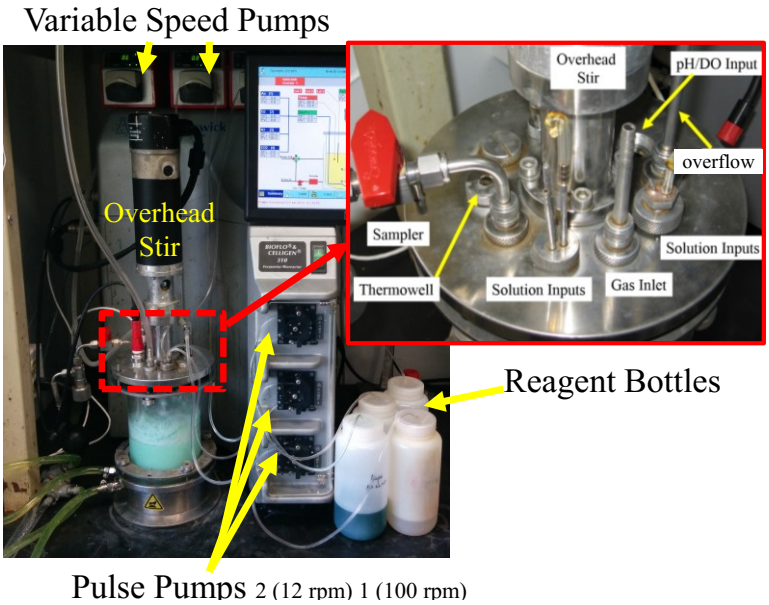

Figure 2.3 Photograph of Bioflo 310 Fermenter, insert shows the head-plate inputs.

The BioFlo 310 is programmable via simple graphical programming software. The flow rates of the pumps and gases, stir rate and temperature can all be programmed to adjust with time or with detectable changes in the reaction conditions such as pH or dissolved oxygen. The programming functions of the BioFlo 310 made development of core-shell and gradient composition samples possible. General parameters to the synthesis methods with this CSTR will be described in this section, with specifics for each synthesis presented in conjunction with the data in future chapters.

For each reaction, the reactor was filled 1 L of 1 M of NH_4OH and then the head-plate was sealed onto the glass vessel. The vessel was then heated to 60.0°C and

0.5 standard litres per minute (SLPM) of nitrogen gas (Praxair 99.999%) was bubbled through the solution. To the overflow inlet in Figure 2.3 a piece of Tygon tubing (Masterflex E-Lab 3603) was connected into a bottle filled with water to serve as an exhaust for the overpressure of nitrogen. The overflow tube was then positioned at the top

of the solution height (constant volume, CSTR mode) or pulled all the way to the top of the glass vessel (batch process). Any solution or product expelled into the overflow was discarded in either mode.

The pH of the solution was monitored using a pH electrode connected to the BioFlo 310. A Mettler-Toledo InGold DPAS-SC-K8 S was used as the pH probe. Prior to using the reactor the pH electrode was calibrated with buffered solutions of pH 7 and 12 (BDH Reference Standards) at room temperature using the internal 2 point calibration system on the BioFlo 310. Whenever the pH was 0.05 pH units below the desired set-point a solution of 10 M NaOH (Sigma Aldrich 99.9%) was dispensed via one of the pulse pumps. This resulted in a few drops of NaOH being added at a time until the pH value returned to at least the set-point.

Mixed metal sulfate solutions were prepared from stoichiometric mixtures of cobalt(II) sulfate heptahydrate, manganese(II) sulfate monohydrate or nickel(II) sulfate hexahydrate (Sigma Aldrich or Fisher Scientific >98%). Powders were dissolved in deionized water that had been previously boiled and capped while warm. All solutions stored in reagent bottles were prepared in this method to minimize oxygen introduction into the active reaction. The flow rate of metal sulfate solutions was 0.00694 mL/s via a variable speed peristaltic pump (Watson-Marlow). This flow rate resulted in 500 mL of solution being dispensed into the vessel in 20 hours.

After 20 hours the reaction was allowed to come to equilibrium by maintaining pH, stir, temperature and atmosphere for at least 1 additional hour. After the aging process, the reaction product was processed by first cooling the suspension to room temperature. The suspension was then filtered in a Büchner funnel and the product rinsed with at least four

times the suspension volume of deaerated deionized water. Samples of about 40 mL were also removed periodically during the reaction to monitor the morphology and composition, especially for core-shell samples. These samples were cooled in an ice-water bath and then filtered in a similar fashion. Powder X-ray diffraction patterns were collected on any products immediately after filtering, as decomposition would limit the usefulness of the collected pattern. The product was then dried at 80ºC in a forced air oven overnight before lithation.

Single phase, core-shell and continuous gradient composition samples were all prepared in a similar fashion using a CSTR. Single phase materials used a single mixed metal sulfate input solution which contained the stoichiometric ratios of Ni, Mn or Co desired in the final product. Core-shell samples used two mixed-metal sulfate solutions on individual pumps. A mixed-metal sulfate solution of the core's desired transition metal composition was first pumped into the reactor. After some time, a second mixed-metal sulfate solution of the shell's transition metal composition was then pumped into the reactor. Continuous gradient samples of a Ni core to a Mn shell and vice versa were synthesized using two pumps and two solutions. A solution of 2 M $NiSO_4$ was on pump 1 and a solution of 2 M $MnSO_4$ was on pump 2. The flow rate of the two pumps in mL/s was determined using

$$0.00694 = f_1(t) + f_2(t) \quad 0 \leq t \leq 36000\ s \tag{2.1}$$

$$f_1(t) = -1.928x10^{-7}t + 0.00694 \quad 0 \leq t \leq 36000\ s, \tag{2.2}$$

where f_1 and f_2 represent the flow rate of $NiSO_4$ or $MnSO_4$, with f_1 being the metal at the centre of the particle and f_2 being the metal at the particle surface.

The peristaltic variable speed pumps were calibrated before each run by measuring the volume of solution dispensed in 30 seconds when the pump was operated at its maximum flow rate. This calibration was excellent for single phase and core-shell samples which ran at a single, moderate flow rate. The pumps in gradient samples ran over a range of flow rates from 0 to 0.00694 ml/s. At very small flow rates the single point calibration methods were not accurate, resulting in variations in the composition from the expected composition at the particle centre and surface.

2.4 Lithiation of Precursors

To develop layered lithium transition metal oxide structures to use as the positive electrodes in cells, lithium must be mixed with the precursor and sintered to allow the solid state reaction shown in equation 2.3 to occur.

$$4Ni(OH)_{2\,(s)} + 2Li_2CO_{3\,(s)} + O_{2\,(g)} \rightarrow 4LiNiO_{2\,(s)} + 2CO_{2\,(g)} + 4H_2O_{\,(g)} \qquad (2.3)^{76}$$

Note in equation 2.3 the precursor is shown as a hydroxide, but due to oxidation of the manganese-containing hydroxide it is more likely an oxyhydroxide. This results in a small difference in molar mass of the precursors: $Mn(OH)_2$ 72.95 g/mol, MnOOH 71.94 g/mol. The reaction still proceeds in a similar method as both hydroxides and oxyhydroxides will decompose to oxides at temperatures below the formation of the product.

For samples that are lithium-rich (greater than 1 Li per formula unit) the reaction is similar to 2.1 with a difference in stoichiometric balance. Lithium hydroxide can also be used in lieu of lithium carbonate. The benefit of lithium hydroxide is its low melting point

of 471ºC, which allows the lithium to easily diffuse into the pores of the precursor particle.[93] Fusion and decomposition of Li_2CO_3 to $LiOCO_3$ occurs at 720°C.[93,94] All sintering in this thesis was done at 800°C or higher making lithium carbonate a suitable lithium precursor. The caustic nature of lithium hydroxide made it undesirable to work with on the bench top and thus it was omitted from experiments as it was found to have no discernable impact on the products. Lithium hydroxide may be of interest in lower temperature sintering of other materials, or if it is more readily available than carbonate salts.

Samples of between 0.5 and 10 g of precursor powder were mixed with a stoichiometric mass of lithium carbonate using a mortar and pestle. Many different ratios of lithium to transition metal were used to explore the impact on structure and performance. Using the phase diagram in Figure 2.1 as a reference point, samples with lithium contents slightly above the boundary for single layered phase and slightly below the two-phase region of layered and Li_2O were explored to ensure the full single phase composition space was characterized. Powders were ground together until the white Li_2CO_3 could not be observed in the mortar. After grinding, the powder was loosely packed into alumina heating dishes and then transferred to a box oven (Vulcan 3-550). The box oven could be programmed with a ramp rate, dwell time and cooling ramp rate. For most samples, the heating rate was 20ºC/min, followed by a dwell of 10 h at temperature and then a cooling rate of 10ºC/min. For quenched samples, the alumina boat was removed from the oven at high temperature after the dwell step. A sheet of copper foil was placed on a large copper plate. The content of the crucible was quickly transferred to the copper sheet and then the

hot powder was covered with another sheet of Cu foil and a top Cu plate and pressed for 30 seconds to rapidly dissipate the heat.

After recovery, the powders were lightly ground in a mortar to break up aggregates. It was observed that when the lithium content of samples was too great, the powders were quite hard. This was attributed to freezing of residual lithium salts during cooling. Excessive mechanical force was used to break up these hard aggregates. SEM measurements confirmed that the extra force required to break up lithium saturated samples did not cause appreciable damage to the secondary particles.

2.5 Electrode Preparation

Electrochemical testing was performed in coin cells. The working electrode contained a synthesized lithiated transition metal oxide as the active material. Marks *et al.* performed a large number of experiments on laboratory-scale electrode fabrication to optimize porosity, density and overall quality of the coating process.[95] Marks' work was used as a guide for optimized parameters such as active material, carbon black and binder ratios, spread thickness, calendaring pressure and drying temperature. Unless otherwise noted electrodes were made with a mass ratio of 90:5:5 active material, Super-S carbon black (Timcal), polyvinylidene fluoride, PVDF, binder (Kynar 301F-Elf-Atochem). A total powder mass of 1 g was lightly mixed in a mortar and pestle and then transferred to a polycarbonate container with 2 zirconium dioxide milling beads. 1-methyl-2-pyrrolidone, NMP, (Sigma-Aldrich 99.5% anhydrous) was added to the container. The total mass of NMP, ~1.3 g, varied depending on composition and was adjusted from sample to sample

depending on viscosity. The slurry mixture was then placed in a dual-motion planetary mixer (KK-250 S Mazerustar, Kurabo) for 3 mixing cycles of
100 seconds each. A sheet of 160 μm thick aluminum foil was cut to a length of 3-7 inches. This foil was wicked flat to a quartz glass plate using ethanol. Immediately after the mixing cycles were complete, the slurry mixture was spooned 1 cm from one end of the aluminum foil in a crescent shape. A 150 μm notch bar was then evenly pulled from one end of the aluminum foil to the other, spreading the slurry to an even thickness. The coated aluminum foil was then transferred to a 120ºC evaporating oven for several hours to evaporate the NMP. After drying the electrode was calendared using a roller press with a pressure of approximately 1000 atm.

Electrodes were generally used within a few days of fabrication. If electrodes were to be tested using ultra high precision chargers (UHPC), or had been stored for over a week, the electrodes were dried after punching to size. Drying was accomplished in a heated antechamber of a glovebox under vacuum at 120ºC overnight. After drying, the electrodes were transferred into the glovebox without air exposure.

2.6 Coin Cell Fabrication

Electrodes were used in laboratory coin cells to test the electrochemical performance. Prior to use in a coin cell, a 1.27 cm^2 disk of electrode was punched from the electrode sheet. These disks were then weighed using an ultra-microbalance with a resolution of 0.1 μg (Sartorius SE2). The mass of the disks were between 12 - 20 mg. Subtracting the mass of the aluminum foil current collector and accounting for the ratio of

active material, there was 7 - 12 mg of active material per disk. The mass of active material on the disk was used to determine the current applied during charging and discharging so each cell was exposed to the same gravimetric specific current.

Figure 2.4 shows a schematic of the components of a coin cell in an exploded view. The working electrode in Figure 2.4 would be the 1.27 cm^2 disk electrode described above. This coin cell is known as a 2325-sized cell, meaning it has a diameter of 23 mm and a height of 2.5 mm. For UHPC work, the casing bottom was sputter coated with 3 μm of aluminum to minimize currents due to corrosion of the stainless steel casing bottom which adds noise to the data.[96]

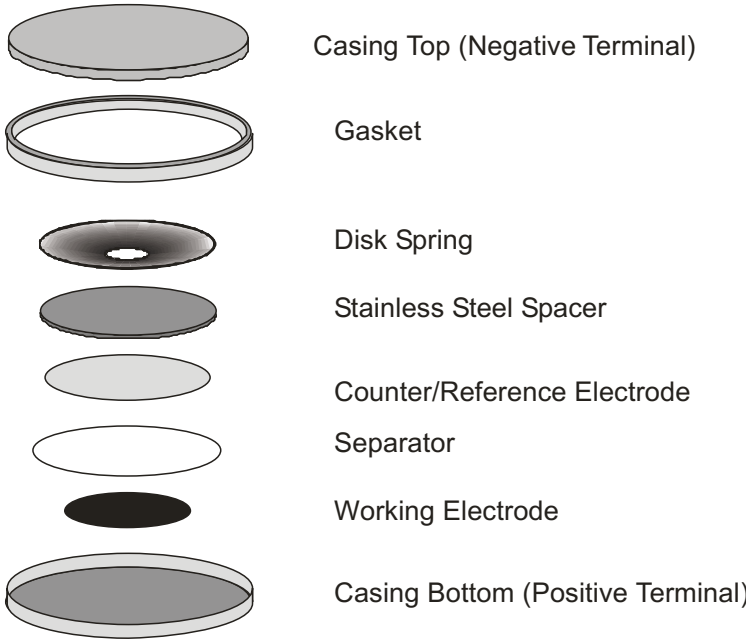

Figure 2.4 Exploded view of a 2325 sized coin cell's components.[97,98]

Assembly of coin cells took place in an argon-filled glovebox (Innovative Technologies) which was maintained to have an oxygen content less than 1 ppm and water

content less than 0.1 ppm. Oxygen and water content in the cells should be minimized as both are reactive with the lithium metal counter electrode. Hydrolysis and decomposition of the organic carbonates and reactions between the hexafluorophosphate and water can degrade the electrolyte.[99–101] For most studies in this document the electrolyte was 1 M $LiPF_6$ dissolved in a 1:2 mixture of 1,3-dioxolan-2-one (EC) and dimethyl carbonate (DMC) (BASF 99.9%) Cells were assembled by stacking components as shown in Figure 2.4. After the working electrode was centered on the casing bottom, 3 drops of electrolyte were placed on it using a syringe with a 21 gauge needle (20 µl/drop). Either a blown microfibre "BMF" (3M) or a Celgard 2400 thin film polypropylene (Celgard LLC) separator was then centered above the electrode. When a BMF separator was used, 10 drops of electrolyte were placed onto this separator to wet the separator. If a Celgard separator was used then only 1 drop was necessary to wet the separator. The BMF separators are thicker, providing more even stack pressure than the Celgard, but requiring additional electrolyte to ensure they are wet for good ionic conductivity. A second separator, a Celgard 2400, was placed above the first separator followed by 1 drop of electrolyte. A lithium foil (Chemetal >99.99%) disk 150 µm thick, 1.39 cm^2 in area was then centered on the stack. The separator and spring and casing top were then placed on the stack which was transferred to a pneumatic press where two custom jigs (DPM Solutions) were used to seal the cell by crimping the casing top and bottom together around a polypropylene gasket.

After assembly, the cells were removed from the glovebox and were further sealed using an epoxy (Torr Seal, Varian) to ensure no electrolyte loss during long term testing.

Stainless steel tabs were then spot-welded to the top and bottom of the assembled cells after which the cells were ready for analysis on a battery cycler.

2.7 Powder Characterization Techniques

This section will discuss the characterization techniques used to characterize the powders synthesized throughout this thesis. The general methods described in this chapter will be supplemented by specific information when necessary in later chapters.

2.7.1 Interactions of X-rays with Materials

X-rays are a useful type of electromagnetic radiation because their wavelengths (λ) are of the correct size to provide structural and composition insight into samples when they interact with materials. When an X-ray beam lands on an atom it can result in absorption or scattering events. Both absorption and scattering will be used in this thesis to gain insight into the structure and composition of samples.

Scattering of an X-ray beam from an atom can be elastic or inelastic Compton scattering. The elastic component is of interest to probe structure.[102] In the classical view, an electromagnetic wave with an electric field causes a force to be applied to the electrons in an atom. This force accelerates the electrons which results in radiation of X-rays of the same wavelength of the incident X-ray beam. This can be quantified as

$$I_p = I_0 \frac{K}{r^2}\left(\frac{1+\cos^2 2\theta}{2}\right) \quad (2.4)$$

which is the Thompson equation.[102] In 2.4, I_P is the absolute intensity of the elastically scattered beam at distance r, I_0 is the absolute intensity of the incident beam, $K = 7.94 \times 10^{-30}$ m^2 and θ is the Bragg angle.[103]

Equation 2.4 can be summed over all electrons in an atom to determine absolute scattering intensity from an atom. The observed scattering of atoms deviates from a simple summation of Equation 2.4 at scattering angles other than $\theta = 0$. This is due to the electrons surrounding the nucleus being located in different locations resulting in partial interference. The atomic scattering factor, *f,* is the ratio of the observed scattered intensity to the expected intensity due to the electrons in an atom as a function of the scattering angle and λ. Tables of atomic scattering factors are reported in literature and used in data fitting routines.[103]

Lithium-ion positive electrode materials and many other materials have repeating ordered arrangements of atoms, which can be defined using a unit cell. X-rays scatter off all the atoms in the sample. When the scattered X-rays are in phase, constructive interference occurs, otherwise the interference is destructive. The constructive interference is of interest for structure probing and is known as Bragg diffraction defined by the Bragg Law,

$$\lambda = 2d \sin(\theta) \qquad (2.5)$$

which relates the Bragg angle (θ) to the X-ray wavelength (λ) and the spacing between the atomic planes (d). Figure 2.5 is a schematic representation of a first order diffraction occurring due to ordered planes of atoms.

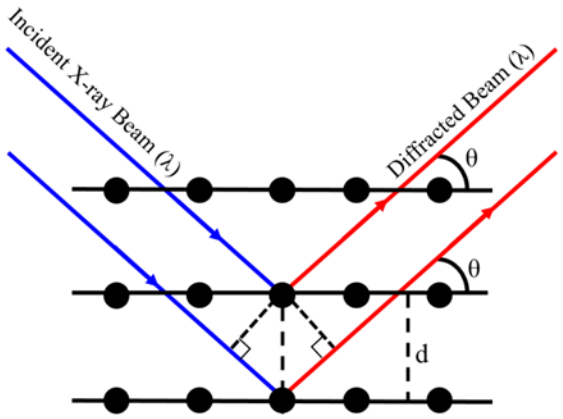

Figure 2.5 Schematic drawing of Bragg diffraction due to ordered planes in a crystalline sample.

In crystalline samples there are many different atomic planes that result in constructive interference, satisfying the Bragg Law. Allowed spacings are well known for common crystal structures based on a series of selection rules.[102] Using Equation 2.5, the scattering angles can be converted into the atomic plane spacings (d). By applying systematic absences, the observed diffraction peaks can be used to determine the arrangement of atoms and assign a space group to the structure. Once a space group has been assigned, the observed diffraction peaks can be assigned Miller indices (*h,k,l*). With the geometry of the unit cell and several planes now known, the unit cell lengths (a, b & c) and angles (α, β & γ) can be determined. The relative integrated intensity of the diffraction peaks give insight to which atoms are located on which sites in the unit cell. The relative integrated intensity of each diffraction peak can be determined by summing for all of the scattering atoms along the path and accounting for factors such as scattering angle, multiplicity, temperature and preferential orientation.[102] Fitting algorithms such as Rietveld refinement have been developed to fit diffraction patterns and will be discussed in Section 2.7.3.[104]

Databases such as PDF-4+ by the International Centre for Diffraction Data contain thousands of well indexed diffraction patterns.[105] Software can be used to find similarities in experimental patterns and those in the database to assist in identification.[106] This can be useful if a sample contains multiple phases which make applying selection rules difficult. For samples in this thesis, indexing peaks was trivial thanks to the understanding of the relationship between structure and composition for samples of interest shown in Figure 2.1.

In addition to scattering, X-rays interacting with atoms can result in absorption processes. Absorption occurs when the X-ray interacting with the atoms is of sufficient energy to eject a core electron as a photoelectron. Figure 2.6 shows the mass absorption coefficient (μ/ρ) in units of (cm^2/g) for nickel and manganese versus the wavelength of the X-rays.[107] The blue dashed line in Figure 2.6 marks the energy of Cu-Kα radiation which was used in all diffraction experiments in this thesis.

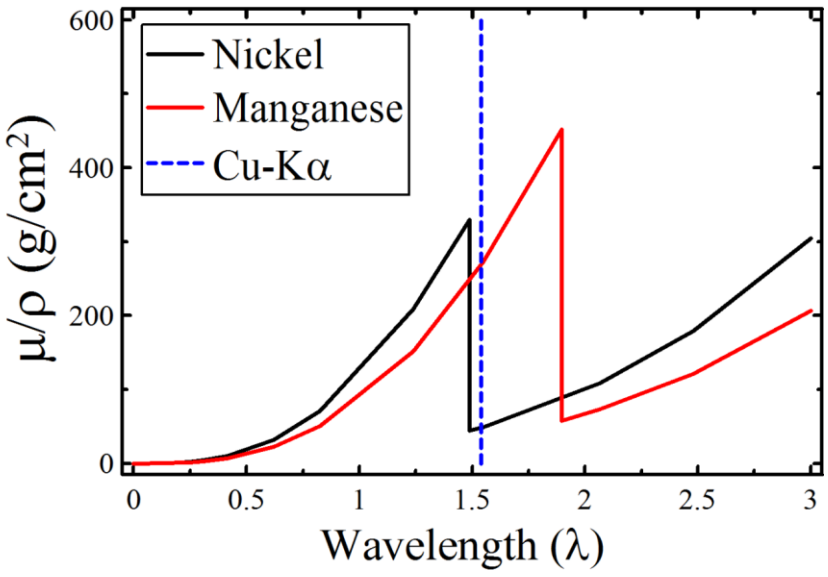

Figure 2.6 Mass absorption coefficients as a function of wavelength for nickel and manganese. Blue dashed vertical line shows the wavelength of the Cu-Kα X-rays used in the diffractometers employed in this thesis.[107]

A sharp change in absorption is observed for nickel at 1.5 Å and at 1.8 Å for manganese. These peaks are the K-absorption edges for these nuclei. At wavelengths greater than the absorption edge, (softer X-rays) the photon's energy is too small to expel the core 1s electron from the respective nuclei, thus absorption is weak. At wavelengths smaller than the absorption edge, (harder X-rays) core 1s electrons can expelled from the nuclei and absorption is strong. At 1.54 Å the wavelength of Cu-Kα X-rays is hard enough to eject manganese 1s electrons, but not nickel 1s electron thus making manganese a much stronger absorber than nickel of Cu-Kα radiation.

X-ray absorption was used in this thesis to estimate the thickness of the shell in core-shell samples. The mass absorption for a sample such as $Ni_{0.5}Mn_{0.5}(OH)_2$ is a linear combination of the absorbers in the sample. The attenuation of a beam is described by:

$$\frac{I}{I_o} = e^{-\left(\Sigma\left(\mu/\rho\right)l\right)} \qquad (2.6)^{108}$$

where the fraction of transmitted X-rays, (I/I_0) is can be determined based on the summation of mass absorption coefficients (μ/ρ) for all absorbers along the beam's path, l. Details about how Equation 2.6 was used to model absorption observed in diffraction patterns will be discussed in Chapter 5.

2.7.2 X-ray Diffractometers

In this specific work, two diffractometers were used to collect data, a system assembled from parts called the JD-2000 and a Siemens D-5000. The JD-2000 consists of a Phillips PW 1720 4-window X-ray generator, forward reflection Bragg-Brentano goniometer and a scintillation point detector. In the generator, electrons are generated via

thermionic emission and accelerated towards a copper or other transition metal anode due to a bias of 20 - 40 kV. Most of the electrons bombarding the anode result in heat, which is dissipated by water cooling the X-ray tube assembly. A small portion of the electrons result in the expulsion of core 1s electrons from the copper anode. Allowed electron transitions occur, filling the 1s hole resulting in Cu-Kα (1.541 Å) and Kβ (1.392 Å) X-rays being generated.[107] X-rays pass through a window in the tube then through a divergent slit which defines the spread of the X-ray beam. The X-ray beam now interacts with the sample and events described in Section 2.7.1 occur. The diffracted beam then passes through anti-scatter slits followed by a receiving slit and then a diffracted beam monochromator to filter out Cu-Kβ and fluorescence radiation before the scintillator detector.[109] After signal amplification, the computer software, which controls the goniometer positions, records the intensity of diffracted beam as a function of scattering angle. In the JD-2000, the slit configurations cannot be dynamically altered.

The D-5000 instrument is a similar forward-reflection Bragg-Brentano goniometer with a Cu-Kα X-ray source. The D-5000 provides the advantage of higher resolution due to dynamic control over divergent and anti-scatter slits and several various receiving slits that can be manually changed between samples. Improvements to resolution result in a decreased flux and diffracted intensity. Optimization of X-ray scanning parameters will be discussed in later chapters.

To measure a sample on either of the instruments, a well in a stainless steel holder is filled with the powder to be analyzed. The powder is compacted and excess is removed from the surface so the powder is flush with the holder and then mounted in the diffractometer. Figure 2.7 shows a schematic drawing of a Bragg-Brentano goniometer

with the sample mounted at the center of the focusing circle. Figure 2.7 shows a general schematic for a Bragg-Brentano goniometer, but additional components such as Söller slits may also be present along the path in some setups. A computer controller adjusts parameters such as divergent slit angle and moves the detector and X-ray source around the focusing circle to the desired smallest scattering angle. The goniometer remains at this point for a specified dwell time and the computer controller records the intensity at that specific scattering angle. The X-ray source and detector then step forward to a new scattering angle and again intensity is measured; this process repeats until the desired upper limit of the scattering angles is measured. For most samples diffraction patterns were collected between scattering angles of 15 - 90°. The dwell time was 3 - 30 seconds and the step size was either 0.02 or 0.05°. There is an obvious trade-off between data quality and sample throughput depending on the scanning parameters used.

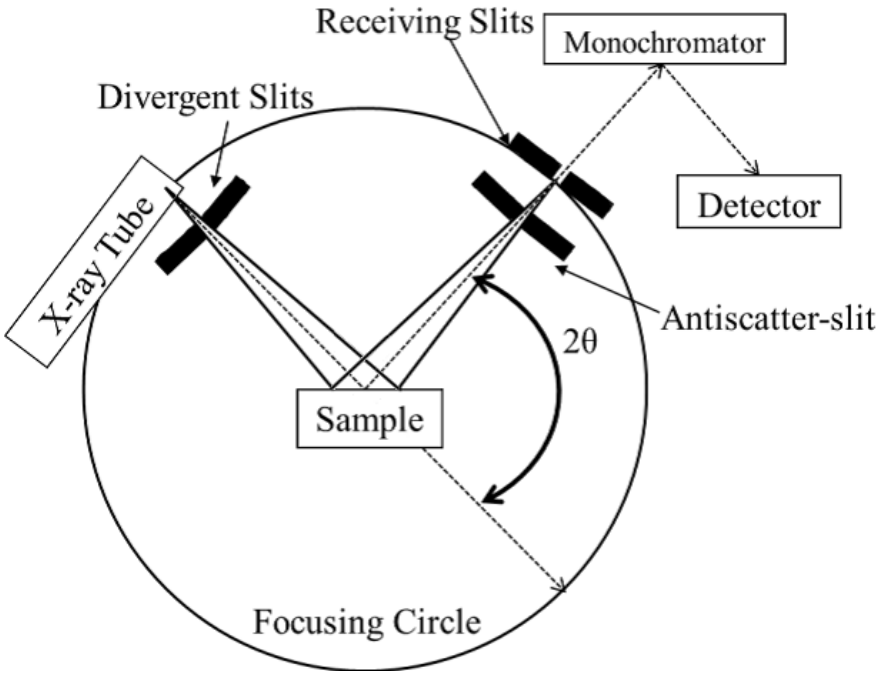

Figure 2.7 Schematic of forward-reflection Bragg-Brentano goniometer, shown with divergent slits, antiscatter slits and receiving slits.

2.7.3 Interpreting X-ray Diffraction Data

The collected diffraction patterns from a XRD experiment can provide a plethora of information when it is properly analyzed. Rietveld refinement was used in this thesis to extract meaningful information from the diffraction patterns.[104] Rietveld refinement is a least squares fitting method that minimizes the difference between the observed data and a calculated pattern. This refinement adjusts parameters such as lattice parameters, site occupations, background and peak shape. Rietica 2.1 for Windows was used for Rietveld refinement.[110] Rietveld refinement requires a basic understanding of the sample to start a pattern refinement. The basic model of the sample is used to determine the position and relative intensities of diffraction peaks. Required starting parameters include the space group, atomic positions, site occupations and lattice parameters. The atomic positions, site occupations and lattice parameters need only to be an estimate as these values will be refined through the fitting routine. There are additional parameters that can be adjusted such as background, peak shapes and phase intensities.

When performing a Rietveld refinement, the refinement that results in the smallest residual value may not necessarily be the best fit. It is important that the values of the parameters are physically meaningful. For example, a series of parameters are used to describe the peak shape of the diffraction peaks. The parameter, γ describes the ratio of Lorentzian to Gaussian in the pseudo-Voigt peak shape. The only acceptable values of γ are $0 \leq \gamma \leq 1$. The residual, known as the R-factor, is

$$R = \sum_i w_i [I_i(obs) - I_i(calc)]^2 \qquad (2.7)$$

where w is a weighting term and I(obs) and I(calc) are the observed and calculated intensities at data point i.[111] Specific weighting terms for various R-factors will be discussed in Chapter 4 with refined data.

A few parameters of interest to discuss are those associated with peak shapes and those associated with lattice parameters and site occupations. Based on the description of Bragg diffraction given so far in this chapter one may expect the diffracted intensity to be observed exclusively at the Bragg angle. Diffraction is not observed at discrete points, but as peaks. The breadth of diffraction peaks depends on scattering angle, experimental setup and sample morphology and composition. In general, peak broadening generally increases as the size of the crystallites decreases. Strain can also modify the peak width due to the crystallites being distorted.

Instrumentation limitations also broaden peaks. Instrumentation broadening is due limitations on focusing, slit width and penetration depth. For example, in a Bragg-Brentano setup, interactions between sample and X-rays are meant to occur at the sample holder's surface. In reality, some powder is located above or below the intended sample height and still participates in Bragg diffraction. These scattering events not at the expected height are satisfying the Bragg law, but due to the samples location are being recorded not at the true diffraction angle as they are not aligned with the intended geometry.

While deconvolution of all the individual contributions to peak broadening may provide useful insight, it is rather difficult, if not impossible, with standard experiments. The broadened diffraction peaks can be fit with a pseudo-Voigt peak shape. Peak broadening and careful consideration of fitting parameters will be discussed in the fitting routines for core-shell materials. For the core-shell materials examined in this thesis, the

core and shell are of the same space group and of similar composition resulting in similar lattice parameters. The extreme similarity of the two phases resulted in the diffraction peaks of the core and shell somewhat overlapping.

Lattice constants and site occupations are the primary information extracted from the refinement. The hydroxide precursors, $Ni_xMn_{(1-x)}(OH)_2$ are a solid solution for $0 \leq x \leq 1$. This means Ni and Mn are mixed at the atomic level and are randomly distributed on the same sites in the lattice. As the ratio of Ni to Mn changes, the lattice expands or contracts to accommodate the change in composition. Zhou *et al.* fit the change of lattice constants with respect to composition with a linear line of best fit.[112] This allows the value of x to be determined from the lattice constants instead of using a spectroscopic method such as ICP-OES. This concept will be discussed in detail in Chapter 6 as this approach was used to characterize core-shell samples in which bulk techniques could not provide the elemental composition of the core and shell phases individually.

2.7.4 Scanning Electron Microscopy & Energy Dispersive Spectroscopy

Scanning electron microscopy (SEM) was used to characterize the microstructure of powders. A focused electron beam is rastered across a sample in vacuum. The electrons are then scattered off the sample and detected. A computer then associates the intensity of the scattered electrons at a specific point with a grayscale intensity which is then displayed as an image. Two types of detectors are most often used, secondary and backscattered electron detectors.[113] A backscattered detector detects elastically scattered electrons. Alternatively a secondary electron detector can be used which detects low energy core

electrons ejected from the samples. Backscattered detectors have the advantage of offering contrast between different elements, but due to the high energy, probes deeper into the sample. Secondary detectors lose elemental contrast due to their ease of absorbance, resulting in a smaller interaction volume allowing for enhanced surface imaging.

Two instruments were used in this study. The first is a desktop system installed in the Dalhousie James Dunn Physics Building (Nano Science Instruments-Phenom Pro Desktop SEM) equipped with a backscatter detector. This was used for the bulk of SEM imaging due to its ease of use and access. A second instrument (Hitachi S-4700) was accessible at the Dalhousie engineering campus. This instrument has improved electronics which allowed for improved resolution and higher magnification. Samples were primarily imaged with a secondary detector on the Hitachi instrument.

The Hitachi instrument is also equipped with an Oxford Instruments 80 mm^2 silicon drift X-ray detector. This detector allowed for energy dispersive spectroscopy analysis (EDS). EDS detects X-rays that are released when a vacancy in a core electron orbital is filled by an electron falling into the vacant orbital. Due to the unique properties of each element the X-ray energies are element specific. EDS analysis was used to determine the composition at different points across a particle. EDS was used to map the composition of the entire SEM window. EDS is usually limited to detecting elements with more protons than boron. This is due to the low energy of X-rays of light elements being easily absorbed before reaching the detector.

For core-shell samples, EDS was used to examine the contrast in transition metal composition across a particle that was cut in half. Particles were prepared for this analysis by melting a small pool of epoxy, CrystalBond 555 (SPI, Supply/Structure Probe Inc.) and

placing approximately 1 mg of powder into the epoxy. The powder was allowed to sink in the viscous epoxy before it was removed from heat. After cooling and hardening, the epoxy powder suspension was then polished with 550 grit sandpaper until it was evident that particles were being cut. After this point a finer 50 μm alumina paste was used for polishing followed by 5, 1 and 0.05 μm alumina paste (Buehler Ltd.) resulting in a mirror finish. The prepared stubs were then coated with a conductive coating, 40 nm of amorphous carbon, using magnetron sputtering.[114] The sputtering table was water cooled during operations to prevent melting of the epoxy.

EDS data was collected on a single cut particle at a time. The whole SEM window range was sampled over a time of 300 seconds. The collected grayscale maps were then processed using image software (GIMP 2.8.10).[115] The gray-scale intensity images for nickel and manganese were converted to blue and red scale images respectively and then layered on top of each other. Care was taken so that the processing method was similar for each sample.

For this thesis EDS was used as mostly a qualitative technique to prove the existence of a shell phase with a different transition metal composition than the core phase. EDS can be a quantitative technique, but only when experiments are carefully executed. Figure 2.8 shows two possible reasons why EDS in these experiments should not be used for quantitative results. In the left panel of Figure 2.8 the beam interaction within the sample was simulated using the program Casino.[116,117] These simulations show that the X-ray beam interacts with a large volume of the sample both radially and in depth. This makes it challenging in deconvoluting the exact composition at a specific point. Based on the simulations shown in Figure 2.8, characteristic X-rays in a quantifiable quantity are being

generated from about 0.1 μm^3 of sample. Although the beam interaction volume is large, for the particle size and shell thicknesses examined in this thesis it is sufficient to qualitatively show there is a core and shell of contrasting transition metal composition. The right panel of Figure 2.8 shows experimental errors of the sample preparation. Due to the polishing technique used it is impossible to know if a sample was polished perfectly to the midpoint or if it is at an angle. The qualitative EDS results were used to prove that a shell phase existed and then X-ray diffraction was used to determine the composition.

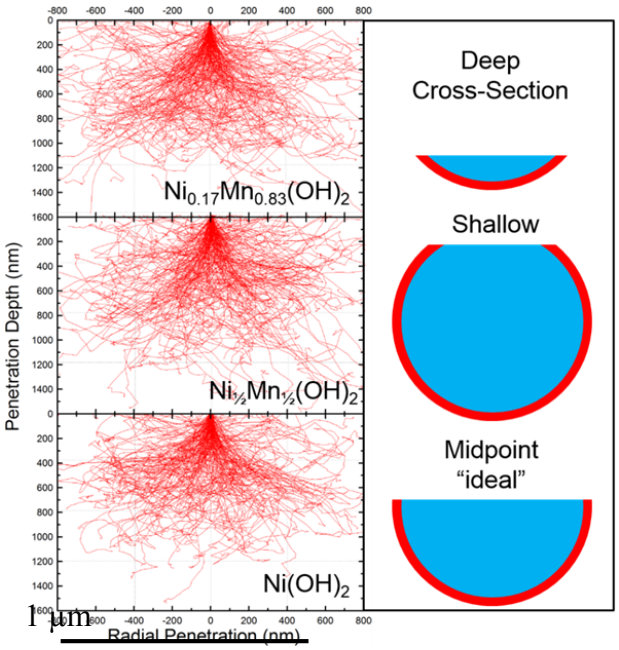

Figure 2.8 (Left). Simulated electron beam interactions for various Ni and Mn hydroxide samples. Simulations were performed by Casino using 10,000 electrons at an accelerating voltage of 20 kV onto an infinitely thick substrate of the given hydroxide. (Right). Three possibly polishing results of the EDS sample preparation. Reproduced from the Journal of the Electrochemical Society, open-source article.[118]

2.7.5 Tap Density

Tap density of powders was measured using a Vander Kamp tap density tester (VanKel). This system tapped a graduated-cylinder filled with powder 1000 times. The powder was then shaken and mounted in the system for 2 more 1000-tap cycles, after which

time the volume of the compacted powder was measured and used with its mass to determine the tap density. Volumetric energy density of a sample is dependent on the tap density of the powder; a higher tap density is desired for higher volumetric energy density. Poor tap density resulted from excessive porosity in the secondary particles and poor particle packing efficiency due to shape and size of the secondary particles.

2.7.6 Bulk Spectroscopic Elemental Analysis

Two systems were used to determine the bulk metallic composition (including Li) of powder samples: a Perkin-Elmer Optima 8300 Inductively Coupled Plasma Optical Emission Spectrometer (ICP-OES) in the Dalhousie Dentistry department and a Teledyne Leeman Labs Prodigy ICP-OES at the Dalhousie Geochemical Analysis lab. Powders were prepared for analysis for both systems by dissolving ~1 mg of powder into 5 ml of a 2:1 $HCl:HNO_3$ (Sigma Aldrich Reagent Grade) Aqua Regia solution. After a few hours of digestion, a 100 µl aliquot of this solution was diluted to 20 ml using NanoPure water (Barnstead Thermo Scientific 18.2 MΩ·cm). Standard solutions for the Perkin-Elmer instrument were made in 1 and 2 ppm concentrations by diluting 1000 ppm standards of Li, Ni and Mn (Ultra Scientific Analytics Solutions) in NanoPure water. The Dalhousie Geochemical Analysis used a similar standard and repeated each measurement 3 times with a reported uncertainty of 2%. Data was processed to determine the atomic ratio of Li:Ni:Mn which could be used to position a sample on the Gibb's triangle presented in Figure 2.1.

2.8 Electrochemical Measurements

Electrochemical performance of materials was measured using two types of battery cyclers, standard charger systems built by E-One Moli Energy Limited Canada and Ultra High Precision Charger systems built in-house at Dalhousie.[75] For both systems coin cells described in Section 2.6 were mounted in mounts called boats, shown in Figure 2.9. The boat was then placed in a temperature controlled box that maintained the desired temperature with a precision of 0.1°C throughout testing. Cells were then run through a protocol of steps which charged and discharged the cells with specific current between an upper and lower potential limit. This methodology is known as galvanostatic or constant current cycling. The protocol contained multiple steps which tested the cells at different specific currents or between different potential limits. Cells were also occasionally examined for performance at different temperatures.

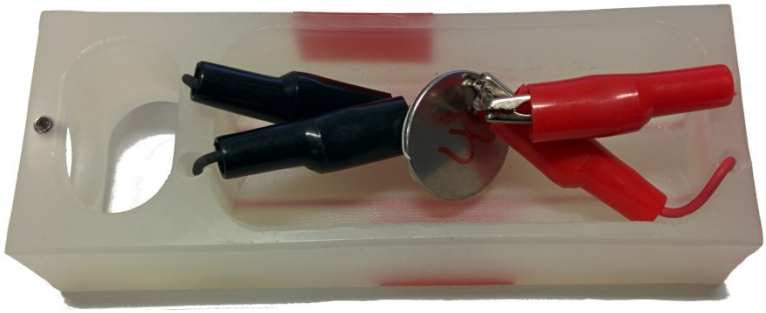

Figure 2.9 Image of a boat with a 2325 coin cell connected to it.

2.8.1 Standard Battery Chargers

Standard battery chargers are used primarily to examine the specific capacity and capacity retention with cycling. This data was used in conjunction with structural and compositional studies from X-ray diffraction to better understand the impact on

performance that structure and composition have. Galvanostatic charge and discharge cycling was used to analyze coin cells. Cell voltage (V) and current (I) are recorded regular time intervals. This data can then be processed to generate plots such as voltage curves (V vs. q), differential capacity (dq/dV vs. q) or cyclic data such as discharge or charge cycle capacity, and average discharge voltage.

Standard battery chargers provided sufficient precision to make measurements described in the previous paragraph, but lack the precision and accuracy to make other measurements such as coulombic efficiency (CE) and charge endpoint capacity slippage. CE and charge endpoint capacity slippage are metrics of cell lifetime and require better precision and accuracy than most standard battery chargers offer to make meaningful measurements. A source of noise in battery chargers is in the way the system measures and records current. The Moli battery cyclers operate by attempting to charge a cell at a set current inputted by the users. A current source is used to deliver a constant current as the potential is allowed to vary based on the state of charge of the cell and other variables. The capacity of the cell is simply calculated by multiplying the requested current by the time of charging or discharging. A constant current is not perfectly maintained due to the changing potential of the cell and variable temperature of the electronics in the current source. Secondly there is no guarantee that the calibration in the charger system is perfect and the error in the requested current is the same in the forward and reverse direction. For example, consider a cell that was designed to be charged and discharged between fixed voltage limits at 5 mA. The current source was not properly calibrated and the actual charge current was 5.05 mA and the discharge, 4.95 mA. This would mean if the charge process took 10 hours the cell would have a capacity of 50.5 mAh of capacity, but would

be measured as 50.0 mAh. If the cell was a perfect cell with no difference in capacity or parasitic side reactions between charge and discharge, the discharge process would take 10.2 hours, which would be accounted as 51.0 mAh of capacity. The difference between the measured charge and discharge capacity would be about 1%.

A 1% error in the measured cycle capacity seems small, but it is quite large when features due to electrolyte decomposition are to be examined. Downie *et al.* showed through isothermal microcalorimetry measurements that the heat flow due to electrolyte decomposition was on the order of 100 nW when a lithium cobalt oxide/graphite 200 mAh pouch cell was being charged above 4.1 V.[119] Smith also showed for similar cell chemistry with high precision chargers that the rate of charge endpoint capacity slippage, an indicator of electrolyte oxidation, was approximately 0.1 % of the cycle capacity each cycle.[26] Core-shell materials are designed to limit the electrolyte oxidation on the positive electrode surface. To gain any insight in the protecting ability of the shell, high precision and accuracy measurements must be made.

Thermal variations in the cell are also a source of noise. The Nernst relationship shows that the potential of a specific chemical reaction is dependent not only on the concentration and activity of oxidized and reduced species, but on the temperature of the system.[120] When a cell is charged and discharged between fixed potential limits the capacity achieved between these limits will change on each cycle if the temperature is not held constant.

While many of the issues with standard chargers are addressable, the financial cost of implementing advanced thermal controls and current sources is counterproductive for large-scale systems. Standard chargers do provide useful information, and are an excellent

first diagnostic tool as they can screen out cell configurations that would be of little interest to study with more advance tools.

2.8.2 Ultra High Precision Battery Chargers

Smith *et al.* attempted to overcome the limitations of standard battery chargers by building a system at Dalhousie aimed at fixing the limitations described in Section 2.8.1.[23] In the first model of their system they overcame current measuring limitations by using an advanced current source. A Keithley 220 programmable current source was used and carefully calibrated regularly. The manufacturer's specification for noise in current is less than 100 ppm when the requested current is in the range of 10^{-7} to 10^{-1} A.[121] Cell voltage was monitored and recorded at a frequency of 1 Hz using a Keithley 2000 scanning multimeter. Cells were also stored in temperature-controlled chambers which maintained the cell within 0.1°C of the setpoint. Smith's first system was able to demonstrate that coulombic efficiency of Li-ion cells could be measured with a precision of 100 ppm. Smith's design was upgraded by Bond *et al.* by making a few modifications. Bond's major modification to Smith's system was in the current measuring system.[122] Bond's modification included a high precision resistor in series with the cell in a thermally controlled box. The voltage across the resistor was measured to determine the instantaneous current and recorded. As a result, the capacity of the cycle was no longer a simple multiplication, but instead current was integrated throughout each cycle to determine the capacity. The ultra-high precision system (UHPC) was determined to measure coulombic efficiency to a precision of better than 10 ppm and an accuracy of 30

ppm, compared to a Maccor 4000, an industry standard battery charger system which has a precision of 100 ppm and accuracy of 2000 ppm.

2.8.3 Interpreting UHPC data

The high precision of the UHPC system allowed for careful electrochemical measurements to be made on cells which could provide more insights into what was occurring during operations. Coulombic efficiency (CE) provides a measurement of total parasitic processes in a cell. CE is the ratio of discharge capacity to charge capacity (q_d/q_c). If the only process occurring during operation was fully reversible lithium insertion and removal from the electrodes then the CE would be exactly 1. Any deviation from 1 is due to some of the capacity during charge or discharge being lost due to irreversible processes.[123] These processes could be irreversible intercalation due to material damage such as delamination or crystallographic damage, SEI building and repairing, electrolyte oxidation or other side reactions. While CE is reported as a numerical value, these numbers cannot be used to provide a specific cycle or calendar life. Instead, the data is best used to compare the impact modifications to the cell configurations make. The reason for this is because CE is a measurement of many different processes, it is difficult to separate it into its principle components. Two cells of different chemistries could show the same CE, but in cell A the deviation from 1 is due to electrolyte oxidation and in cell B the deviation is due to transition metal dissolution from the cathode. The total lifetime of these cells would most likely not be the same as these two processes impact cell performance in different ways.

Another measurement UHPC provides is charge endpoint capacity slippage. It is well known that the electrolyte will oxidize when exposed to high potential at the positive electrode surface.[31] This oxidation results in each charge cycle being slightly longer then discharge process. When each charge cycle is slightly longer due to electrolyte oxidation the voltage curve shifts to the right as shown in Figure 2.10. A faster charge endpoint slippage to the right implies more electrolyte oxidation. This metric is extremely useful for core-shell cells as it can be used to directly measure the impact shell coatings have on electrolyte oxidation.

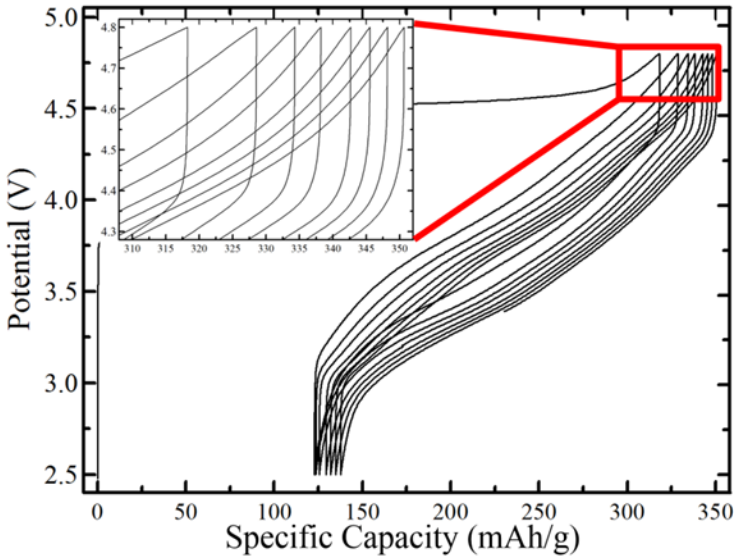

Figure 2.10 Voltage versus specific capacity (cycles 2-10) for a $Li[Li_{1/9}Ni_{1/3}Mn_{5/9}]O_2/Li$ coin cell cycled between 2.5-4.6 V, electrolyte was 1 M $LiPF_6$ in 1:2 EC:DEC, insert panel shows charge endpoint slippage.

Another useful data stream from UHPC is differential capacity measurements. The high precision of the current and voltage measurements allows for a low noise voltage curve and differential capacity plot. Differential capacity data can be plotted for many cycles for a cell and the changes from cycle to cycle can provide insight into changes

occurring. Figure 2.11 shows the differential capacity plot of various cycles for the same cell shown in Figure 2.10.

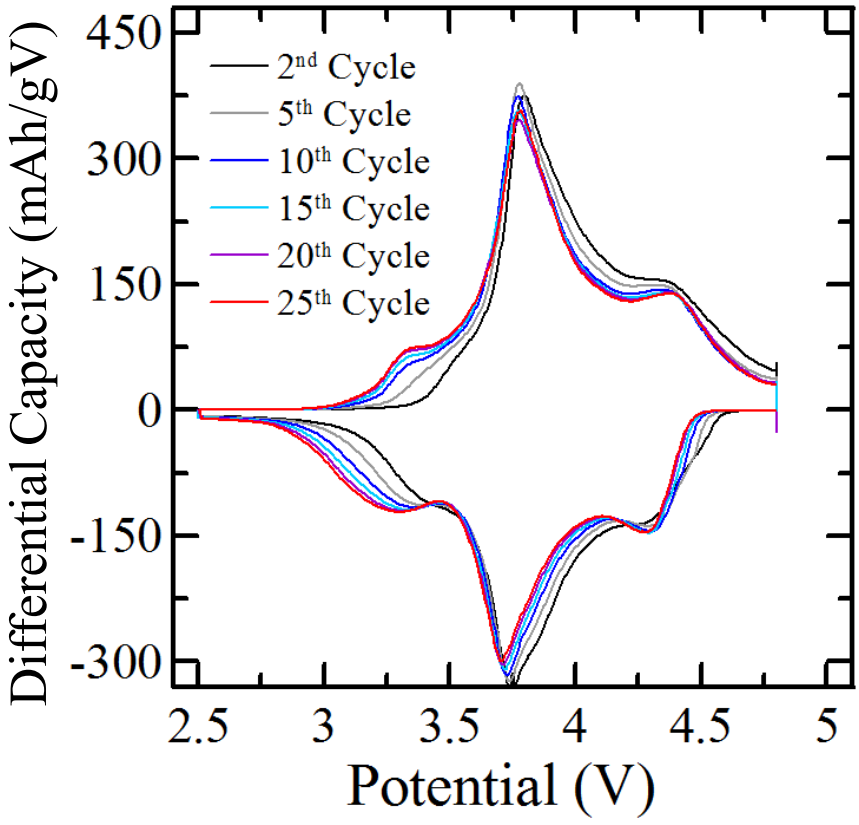

Figure 2.11 Differential capacity plot collected using UHPC with cycles 2, 5, 10, 15, 20 and 25 shown in various colours. Cell configuration was the same as that in Figure 2.10.

Figure 2.11 shows that as this particular cell configuration was cycled, more capacity was observed in the 3-3.5 V region and less in the 3.5-4 V region. This resulted in the energy density of this material decreasing with cycling. Differential capacity data can also be collected on the standard charger systems, with increased noise that may mask some features. Another advantage to differential capacity plotting is that it can provide insight into composition. For example, materials which have a spinel phase and a layered

phase show additional peaks as lithium is deintercalated from the spinel phase at a different potential then the layered phase. When the amount of spinel phase is very small it may be difficult to detect with X-ray diffraction due to the structural similarities to the layered phase resulting in overlap of diffraction peaks. Differential capacity can provide a second measurement to confirm samples are multiphase.

UHPC is an excellent tool for material diagnostics but on its own the technique does not fully characterize a material. It must be used in tandem with the other techniques described in this section. The goal of characterizing a material is to understand the impact that structure and composition have on performance. With a better understanding of this relationship, materials can continue to be improved. For this thesis specifically, UHPC was used to find materials of interest for shell coatings and to determine if specific core-shell materials showed improved lifetime metrics in comparison to bare core materials.

Another challenge to UHPC studies is cell to cell reproducibility. For cells manufactured on an industrial scale, cells are highly reproducible. For this thesis a majority of the research was conducted on coin cells with electrodes that were fabricated by hand. Figure 1.8 showed that the differences in CE for target core and shell materials is as small as 0.003. UHPC studies often required analysis of at least five coin cells to verify the CE measurements. The major sources of poor cell reproducibility are misalignment in the cell components stack, variable electrolyte loadings, inhomogeneity in the electrode composition and impurities present on cell components. The bulk of these errors are absent in well manufactured commercial cells.

Chapter 3. Study of Single Phase Materials with UHPC

3.1 Desired Traits of a Shell Material

While there are many materials that have been studied using standard chargers there are few materials that have been characterized using UHPC. Without UHPC characterization, it is difficult to know the impact that a material may make as a shell material. Sun *et al.* used differential scanning calorimetry to show that their choice of shell material was thermally more stable than their core, which they claimed implied improved lifetime.[77,124] This approach is an indirect method and their final core-shell product was not characterized with UHPC, instead capacity retention in half-cells was used as a lifetime indicator. Capacity retention in a half-cell is not a good metric for lifetime. In a half-cell the lithium metal counter electrode is grossly oversized in capacity compared to the working electrode being studied. This virtually infinite supply of lithium in the cell can mask degradation pathways that consume lithium. In a conventional cell with a lithium transition metal oxide or phosphate positive electrode and graphite negative electrode there is a limited supply of lithium for intercalation. Parasitic reactions that remove lithium from the active intercalation process decrease the lifetime in a conventional full cell while they are masked in a half cell.[26]

Several lithium-rich materials were studied with UHPC for CE and charge endpoint capacity slippage. It is important when selecting a pair of materials that they are synthetically compatible and the potential window of electrolyte stability is acceptable for the choice of shell material. Synthetic compatibility will be discussed in Chapters 4 and 6. When using metrics like charge endpoint capacity slippage to compare electrolyte

oxidation of various materials it is important that the charge endpoint capacity slippage is measured at an appropriate potential. For example if a core material has capacity up to 4.6 V vs. Li/Li^+, the selected shell material for this core should show the least charge endpoint capacity slippage when charged up to 4.6 V vs. Li/Li^+. For most of the lithium-rich materials 4.6 V vs. Li/Li^+ is the normal upper cut-off potential. This requirement would exclude many current commercial NMC materials, such as NMC-111 or NMC-442 for being shell materials as they show poor lifetime performance at such a high potential.

3.2 Shell Materials Examined

Table 3.1 shows the composition and lattice parameters, derived from X-ray diffraction data, of materials studied in this chapter as candidate shell materials. The measured compositions shown are based on the results from ICP-OES analysis while normalizing the metallic fractions so they accommodate a layered notation. Some of the materials studied in this chapter were synthesized and characterized by Aaron Rowe in a complementary study that examined materials which contained vacancies in their transition metal layers.[56] Vacancies were confirmed by redox titrations, helium pycnometry and supported by Monte Carlo simulations.[125] The results of the UHPC study and vacancies were published in two manuscripts, one in the Journal of the Electrochemical Society[56] and one in Chemistry of Materials.[125]

Table 3.1 Composition and lattice parameters of studied single phase shell materials

Precursor	Measured Composition (ICP-OES)	a_{hex} (Å)	c_{hex} (Å)
$Ni_{0.5}Mn_{0.5}(OH)_2$	$Li(Li_{0.09}Ni_{0.46}Mn_{0.45})O_2$	2.8810(1)	14.283(3)
$Ni_{0.36}Mn_{0.64}(OH)_2$	$Li(Li_{0.12}Ni_{0.32}Mn_{0.56})O_2$	2.8732(1)	14.275(3)
$Ni_{0.16}Mn_{0.84}(OH)_2$	$Li(Li_{0.16}Ni_{0.12}Mn_{0.65}\square_{0.17})O_2$	2.8564(1)	14.261(1)

□ Denotes a vacancy

The materials in Table 3.1 span the transition metal range of the excess lithium layer materials of the pseudo ternary-phase diagram for Li-Ni-Mn at 900°C (Figure 2.1). The manganese-rich material $Li(Li_{0.16}Ni_{0.12}Mn_{0.65}\square_{0.17})O_2$ was synthesized at 900°C, but quenched. The other materials shown in Table 3.1 were synthesized by heating to 950°C and then slowly cooled to room temperature. For all three materials a CSTR apparatus was used for the precursor synthesis. Each precursor was synthesized using the experimental description in chapter 2. Precursors were synthesized in a Biostat M fermentor (MBraun) which is similar to the BioFlo 310 described in chapter 2, except for computer controls.

Figure 3.1 shows the diffraction pattern of $Li(Li_{0.09}Ni_{0.46}Mn_{0.45})O_2$ and the fit from Rietveld refinement. Data was collected using the D-5000 with a dwell time of 30 seconds, a step size of 0.05°, anti-scatter and divergent slits of 1° and a receiving slit of 0.2 mm.

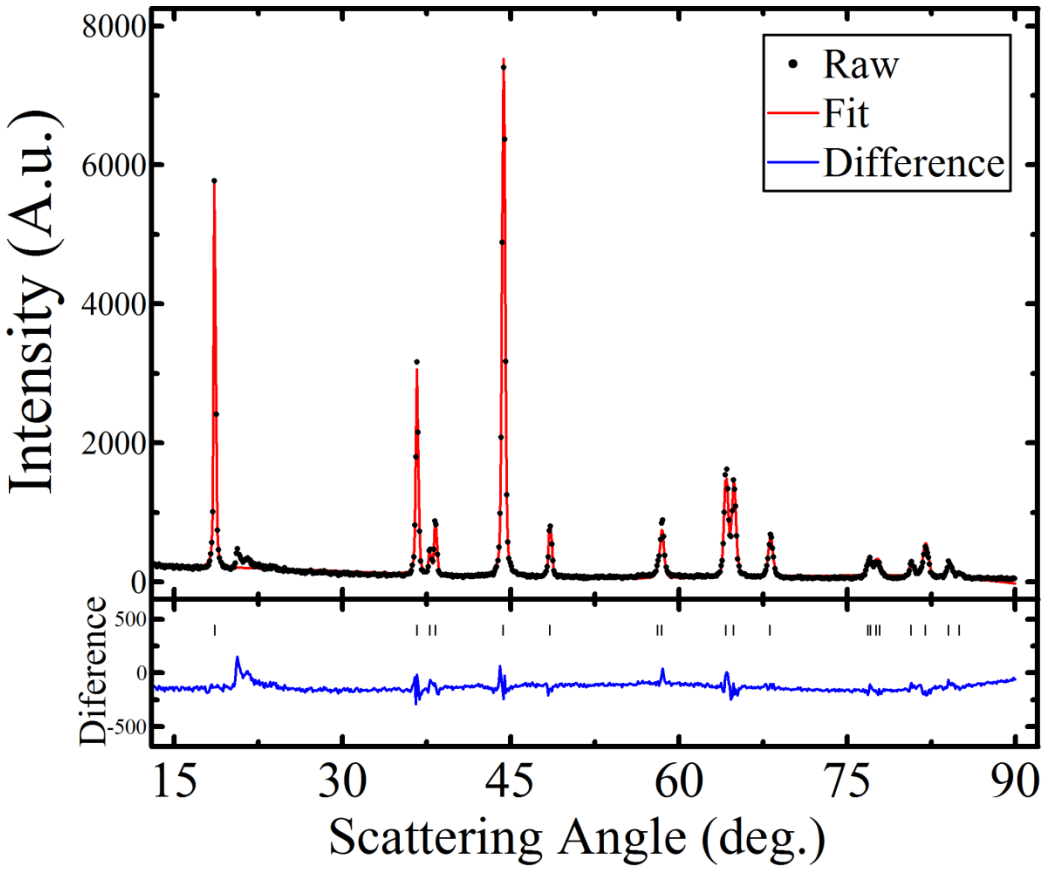

Figure 3.1 X-ray diffraction pattern of sample $Li(Li_{0.12}Ni_{0.32}Mn_{0.56})O_2$ (black symbols) with Rietveld refinement shown in red and difference plot in blue.

To fit this pattern with Rietveld refinement a single phase of space group R-3m was used with lithium atoms on 1a sites (0, 0, 0), transition metals and excess lithium located on 3b sites (0, 0, ½) and oxygen on 6c sites (0, 0, ¼). It had been previously shown by Dahn *et al.* that nickel will substitute for lithium on 1a sites due to similarities in ionic radius.[126] This was included in the fit with a constraint on the refinement that allowed for a one for one substitution of lithium located on 1a, for nickel on a 3b site. For the sample shown in Figure 3.1 the refinement converged when 3.5% of the 1a sites were occupied by nickel. The z parameter of the oxygen position was allowed to vary and converged at a value of 0.256. Small features were observed in the scattering angle range of 20-25° which

do not agree with the atom arrangement for the R-3m space group and lattice parameters. These features were due to the ordering of Li^{+}, Ni^{2+} and Mn^{4+} on the 3b sites resulting in a monoclinic superstructure.[125] These reflections are weak and broad because this ordering is short range for this sample. These ordering peaks were observed in greater clarity for the sample at $Li(Li_{0.16}Ni_{0.12}Mn_{0.65}\square_{0.17})O_2$ and were virtually absent for $Li(Li_{0.09}Ni_{0.46}Mn_{0.45})O_2$ as shown in Figure 3.2.

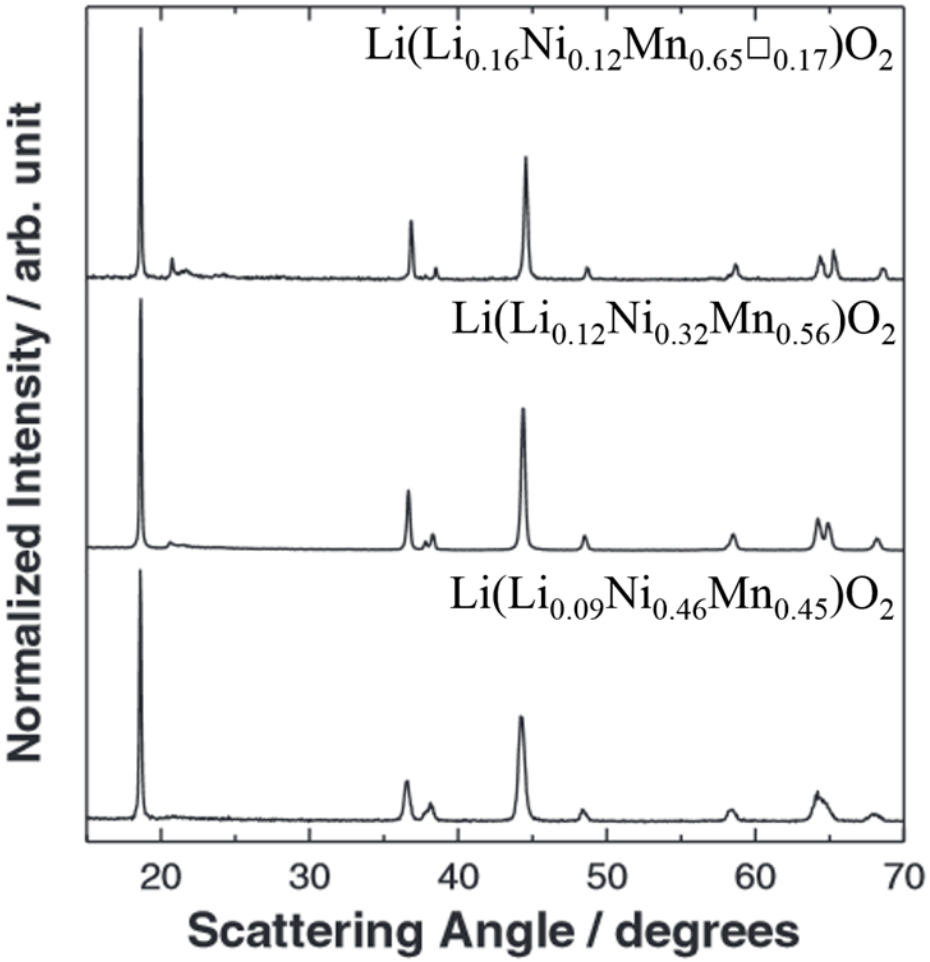

Figure 3.2 Diffraction patterns of the three layered transition metal oxide samples examined in Chapter 3. Reproduced with permission from *J. Electrochem. Soc.*, **161**, A1189 (2014). Copyright 2015, The Electrochemical Society.[56]

3.3 Electrochemical Results for Shell Materials

Half-cells were made of the three materials and examined using high precision coulometry. For the materials $Li(Li_{0.09}Ni_{0.46}Mn_{0.45})O_2$ and $Li(Li_{0.12}Ni_{0.32}Mn_{0.56})O_2$, cells were cycled at 15 mA/g at 30°C. The first charge was to 4.8 V so to complete the activation process of the excess-lithium positive electrode in the cell. After the activation step, cycling between 2.5 and 4.6 V occurred for at least 30 cycles. The material $Li(Li_{0.16}Ni_{0.12}Mn_{0.65}\square_{0.17})O_2$, which was originally designated for Rowe's vacancy study, was only charged between 2.5 and 4.6 V with no 4.8 V first charge activation. Figure 3.3 shows the voltage curves of these 3 materials for at least 30 cycles for each material. The first cycle, after the activation process was complete is shown in blue for each cell and the last full cycle is shown in red with all other cycles shown in black. For the vacancy material, activation at 4.6 V took 9 cycles. For the other two materials activation appeared complete after the first charge to 4.8 V occurred.

Comparing the three voltage curves in Figure 3.3, as the manganese content of the materials increased, the average discharge voltage decreased with each cycle for the first 20 or so cycles. Voltage fade is commonly observed in these excess lithium materials and is thought to be attributed to manganese becoming an active species in the redox associated with lithium intercalation and deintercalation.[127] The exact mechanism of this is debated, but the trend of more voltage fade with increased manganese content is generally accepted. Although the vacancy rich material showed the highest specific capacity, the voltage fade reduced its energy density and made it a poor choice for the core of a core-shell material. The manganese rich composition also had the largest irreversible capacity which is undesirable.

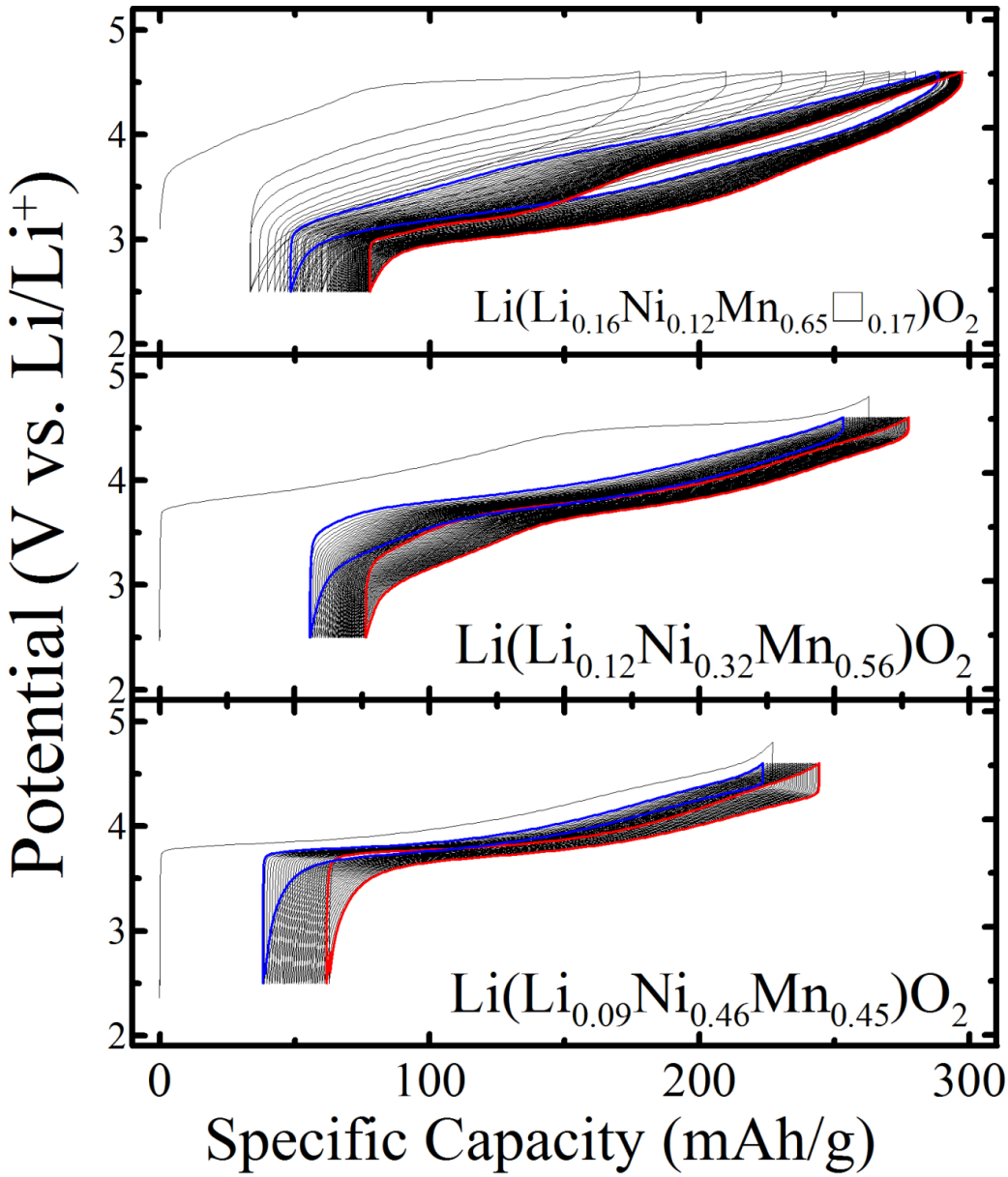

Figure 3.3 Voltage curves of materials studied in chapter 3. First cycle after activation was complete is shown in blue, final cycle is shown in red with all other cycles shown in black. Adapted with permission from *J. Electrochem. Soc.*, **161**, A1189 (2014). Copyright 2015, The Electrochemical Society.[56]

3.3.1 Voltage Fade in $Li(Li_{0.12}Ni_{0.32}Mn_{0.56})O_2$

Voltage fade is commonly observed in excess-lithium materials. The quality of high precision charger data allows for careful observation of voltage fade. $Li(Li_{0.12}Ni_{0.32}Mn_{0.56})O_2$ was used in half cells that were charged to 4.6 V or 4.8 V to examine if the upper cut-off potential had any impact on the voltage fade. 2 *wt*% vinylene carbonate was also used as an additive in the electrolyte for cells charged to 4.6 V to see if it had an impact on voltage fade. Cells were tested at 30, 40 and 50°C to also investigate if temperature impacted the rate of voltage fade. Figure 3.4 shows the differential capacity plots for these cells. In Figure 3.4, the first cycle after 4.8 V activation, the 10^{th} cycle, and the final cycle collected on the high precision charger are shown for each panel. Examining the first column of plots for the 4.8 V cut-off VC-free cells, there appears to be the characteristic voltage fade noticeable by the increase in capacity in the 2.5 - 3.5 V region of each panel. It is evident that the amount of voltage fade was dependent on temperature as the 50°C cells showed the largest changes in their differential capacity plots. Increasing the cut-off potential from 4.6 V to 4.8 V did not result in dramatic change in the low voltage capacity, but decreased capacity significantly in the 3.5 to 4.1 V region compared to the cells without VC charged to 4.6 V.

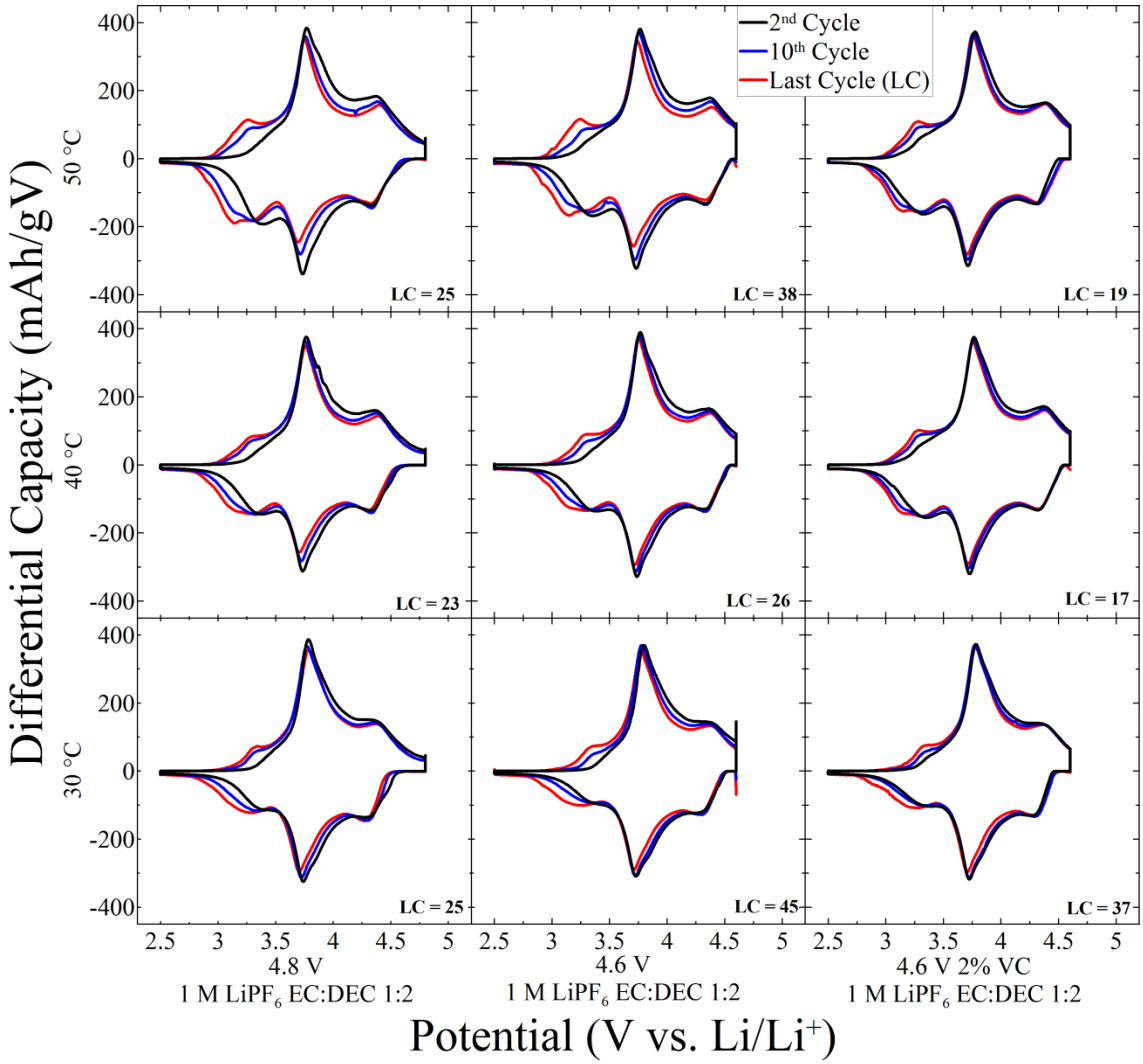

Figure 3.4 Plots of differential capacity versus potential for various half-cells with a positive electrode of $Li(Li_{0.12}Ni_{0.32}Mn_{0.56})O_2$ cycled at different temperatures, cut-off potentials and electrolyte formulations. LC represents the last full cycle collected on high precision chargers.

The most common hypothesis for voltage fade is a conversion of the material from a layered structure to a spinel structure.[71,128] It is thought that this conversion occurs near the surface of the primary particles slowly growing inward with continued cycling. This conversion to spinel allows manganese, which is exclusively in the +4 oxidation state after synthesis to reduce to the +3 state and become electrochemically active. The reduction of

manganese has been confirmed using X-ray absorption near edge spectroscopy (XANES). The position of the manganese K-edge shifted in materials that had been cycled suggesting a change in the manganese oxidation state. Carroll *et al.* collected XANES spectra using two detectors, a total electron yield detector (TEY) and transmission mode detector.[128] By collecting spectra in both modes they could get a better understanding of difference in the bulk and surface of the particles as TEY is more surface sensitive than transmission mode. They observed that the shift in the Mn-Kedge position for the same sample was greater in TEY-collected data than transmission confirming that this reduction in manganese occurs more at the surface.

Similar studies have been completed by Croy *et al.*, who collected X-ray absorption spectra that support a structural change.[68,69] Croy's data was only collected in transmission mode which prevents an understanding of the differences in the bulk and surface of the sample. Croy's work proposed a mechanism that suggested the lithium extraction mechanism during charge was not the same as the lithium insertion pathway on discharge.

Figure 3.5 shows the fractional capacity between various voltage limits for the cells cycled at 50°C in Figure 3.4. The regions in Figure 3.5 were defined as 2.5 to 3.5 V, the region of low voltage capacity growth; 3.5 to 4.1 V, the principle peak observed in the differential capacity plot and 4.1 V to the upper cut-off potential. In Figure 3.5 it is clear that the capacity observed during charge in one region was not equal to the amount of capacity recovered during discharge in the same region. More capacity was observed in the high voltage region during charge and recovered at low potential during the discharge. This approximately 1 V hysteresis is too large to be attributed to polarization, but instead is due to a difference in lithium insertion and removal pathways. Figure 3.5 shows that

most of the decrease in average discharge voltage is due to a decrease in capacity in the 3.5-4.1 V region and an increase in the 2.5-3.5 V region. The top row of Figure 3.5 shows the full cycle capacity in mAh/g, which shows that although there were changes in the voltage that lithium was inserted and removed with cycling, the materials showed very little capacity fade in the first 30 cycles except for the cells charged to 4.8 V.

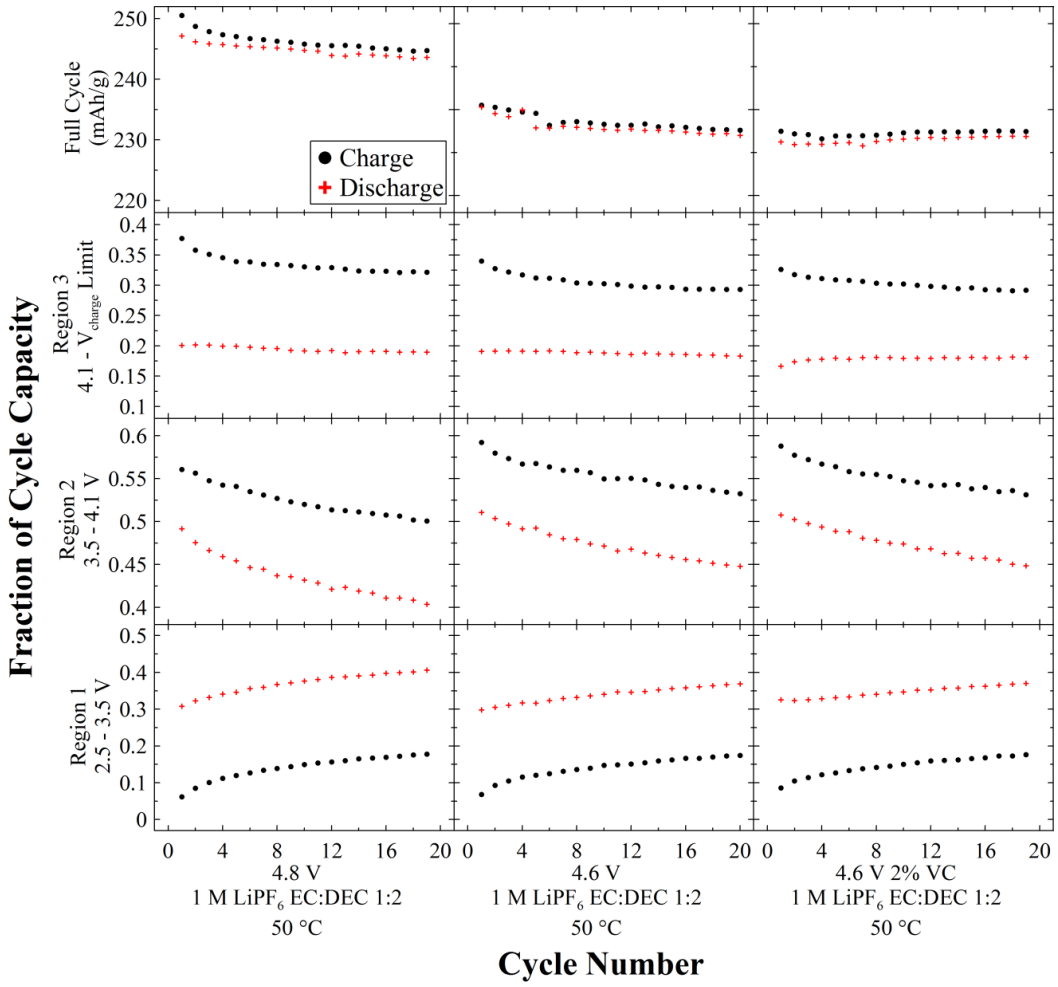

Figure 3.5 Fractional capacity versus cycle number for cells cycled at 50°C shown in Figure 3.4. Fractional capacity was defined as capacity during charge or discharge within the voltage limits shown on each panel's vertical axis. The top row of each panel shows the full cycle charge and discharge capacity versus cycle number.

Figure 3.5 shows that in the high voltage region there was almost no capacity fading with cycling even when half-cells were charged to 4.8 V. It was clear in Figure 3.4 that

the cells cycled to 4.8 V at 50°C showed the largest voltage fade, but the material was quite stable in the high voltage region. For the VC-containing cell more capacity was observed in the middle 3.5 to 4.1 V region and less in the 2.5 to 3.5 V region. This may be due to an interaction between VC and the positive electrode.

Carroll's study using TEY and transmission XANES proposed a mechanism for the conversion to spinel near the particle surface, which was support with XPS and electron energy loss spectroscopy data. Carroll's model is shown in Figure 3.6, this model showed the process that occurs during the first charge activation process.[128] This study lacked longer cycling, but it is not unreasonable to suspect that this process can continue to occur beyond the first cycle. In this model a complex bilayer is formed on the surface of the positive electrode due to the release of oxygen from the positive electrode during the activation process. According to Carrol *et al.* the outer layer was an amorphous mixture of superoxide and Mn^{4+} species. The inner layer which was called oxygen defect spinel was responsible for the voltage fade. The outer layer's interaction with the electrolyte and inner layer is responsible for the conversion to the spinel phase. Laoire *et al.* showed that the stability and lifetime of superoxides in non-aqueous environments was dependent on the electrolyte composition in lithium-air cells.[129] By including VC in the electrolyte or charging to 4.6 V instead of 4.8 V, superoxides may suppress the formation of the oxygen defect spinel via recombination of oxygen into the lattice.

Activation and participation of the oxygen species in the lithium extraction and insertion process was also suggested by Koga *et al.*[70,71] Koga's model also suggest that changes were occurring at the particle surface. Sathiya *et al.* examined a structurally similar solid-solution series $Li(Li_{1/3}Ru_{2/3-y}Sn_y)O_2$, $0 \leq y \leq ⅔$.[130] In this study the authors

showed with XPS that oxygen oxidation was occurring reversibly during cycling. The bulky Ru and Sn cations prevented migration and spinel formation, but supported the electrochemical active nature of oxygen in these structures. This study was interesting as the material was of high capacity and didn't show voltage fade. The inclusion of the 4d ruthenium cation is not economically feasible in a commercial product. The mechanism for lithium intercalation and deintercalation may be different for 4d ruthenium compared to nickel, manganese and cobalt due to differences in the overlap between the transition metal valence orbitals and the oxygen 2p valence orbitals.

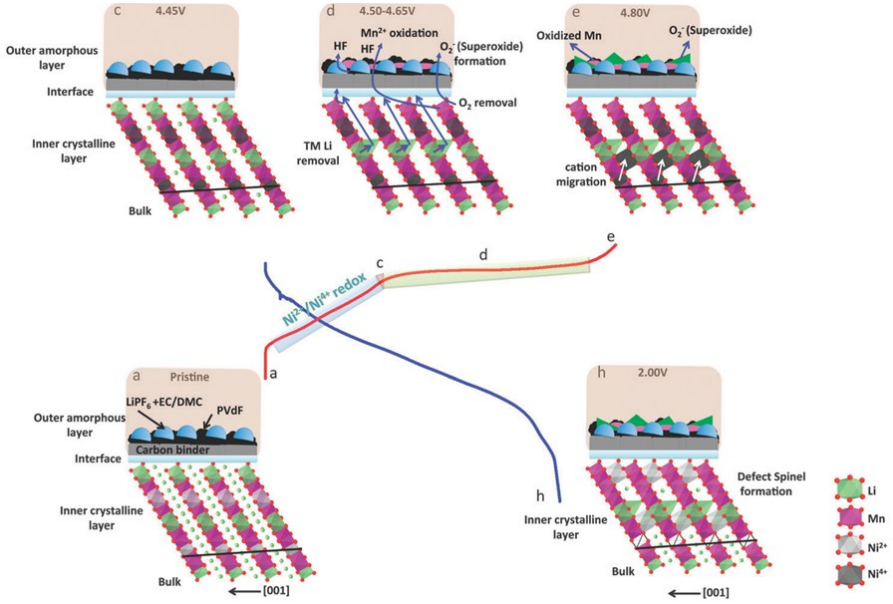

Figure 3.6 Proposed mechanism of defect spinel formation during activation process of excess lithium materials. Reproduced with permission from the PCCP Owner Societies.[128]

Voltage fade is an issue with these materials that reduces energy density. While this is a problem that should be examined it can be minimized by selecting proper materials or by using a core-shell material. When the core of the particle is composed of a material which doesn't show a lot of voltage fade, such as $Li(Ni_{0.5}Mn_{0.5})O_2$, and the shell is a thin layer of a material which shows voltage fade, the voltage fade can be limited to an

acceptable amount. This will be further explored in Chapter 6 which explored such a case with a variable shell thickness.

3.3.2 Lifetime Metrics from High Precision Charger

Figure 3.7 shows some of the cyclic electrochemical performance data for the materials discussed in this chapter charged to 4.6 V at 30°C with no VC. CE and charge endpoint capacity slippage are the two metrics of interest for shell materials qualifications. The charge endpoint capacity slippage was calculated by normalizing the charge endpoint capacity slippage to the endpoint of cycle 10. This was done because the vacancy containing material did not complete the activation process until after cycle 9 due to the lack of a 4.8 V first charge. The 4.8 V first charged was sufficient to activate the other materials in just one charge cycle.

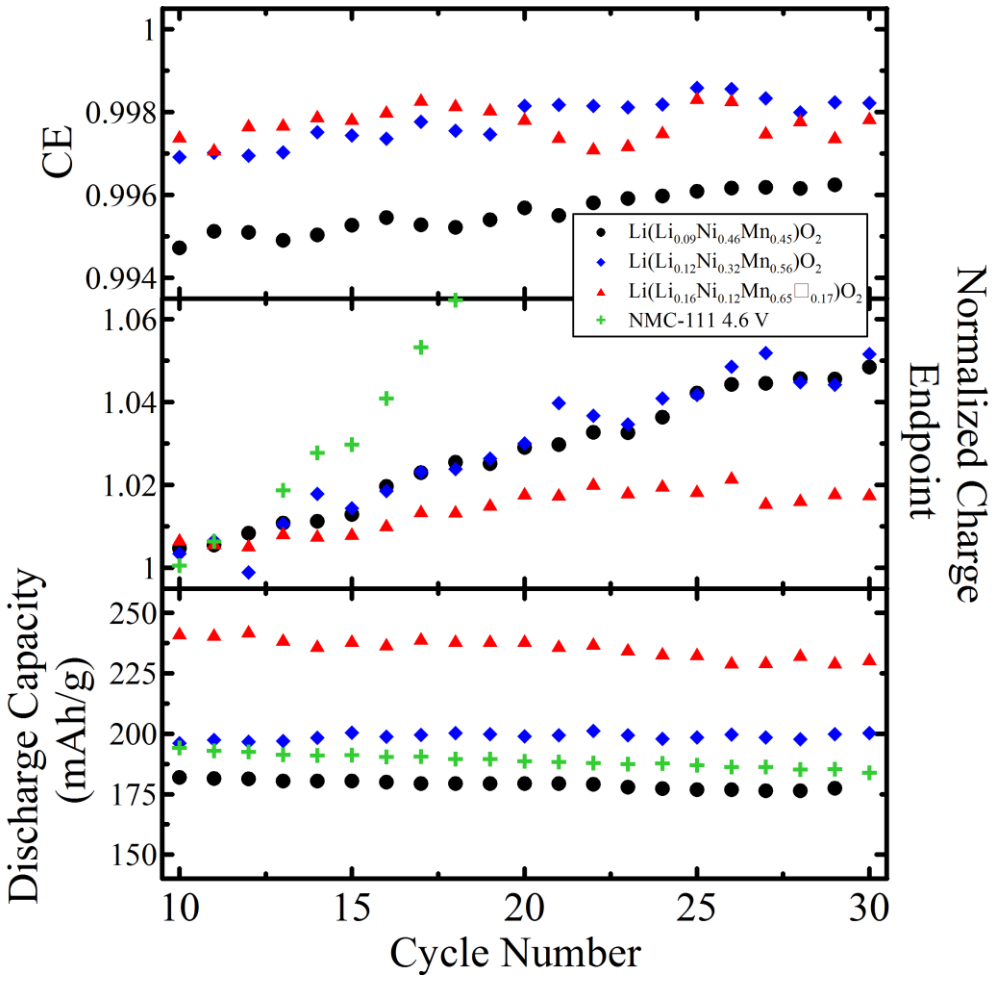

Figure 3.7 Plot of discharge specific capacity, normalized charge endpoint slippage and coulombic efficiency versus cycle number for materials discussed in Chapter 3 and NMC-111.[131]

High quality shell materials display minimum electrolyte oxidation via a small charge endpoint capacity slippage. In Figures 3.7 and 3.3, the manganese-rich vacancy containing material showed the smallest charge endpoint slippage. Although this material also showed the highest reversible capacity for the first 30 cycles it is of little interest for the core material due to massive voltage fade. Rowe's study also showed with extended cycling that the capacity started to fade after 30 cycles.[76] The small charge endpoint slippage of the vacancy-containing material makes it an excellent candidate for a shell

material. For comparison, the charge endpoint capacity slippage and discharge capacity are shown for NMC-111 charged to 4.6 V are shown in Figure 3.7. For cells that show capacity fade, charge endpoint capacity slippage must be carefully understood. It can be difficult to separate slippage and capacity fade, since capacity fade may result in negative charge endpoint capacity slippage. In Figure 3.7 NMC-111 has a substantially larger charge endpoint capacity slippage, but similar discharge capacity fade rate compared to the other materials. This suggest that at 4.6 V the excess-lithium materials are less reactive with the electrolyte compared to NMC-111, and should be explored as possible shell coating compositions.

Carroll's model shown in Figure 3.6 can be used to propose why Rowe's material showed a small charge endpoint slippage. In Rowe's sample there was a lot of voltage fade and a very small charge endpoint slippage. The increased voltage fade may have been associated with an increase in the formation of superoxides at the particle surface. During the first few cycles these superoxides may aid in the formation of a surface film composed of the products of reactions between the electrolyte, positive electrode and the superoxides. This surface film might inhibit the oxidation of additional electrolytes during cycling, thus the small charge endpoint capacity slippage. This model was not further explored in this thesis work, but should be pursued by future researchers by studying many different compositions with UHPC and various spectroscopic techniques.

3.4 Chapter 3 Conclusions

Three materials that spanned the excess lithium materials single phase region $Li(Li_{0.09}Ni_{0.46}Mn_{0.45})O_2$, $Li(Li_{0.12}Ni_{0.32}Mn_{0.56})O_2$ and $Li(Li_{0.16}Ni_{0.12}Mn_{0.65}\square_{0.17})O_2$ were studied with high precision coulometry. What was determined from this study was that the charge endpoint capacity slippage was very small for $Li(Li_{0.16}Ni_{0.12}Mn_{0.65}\square_{0.17})O_2$. This material showed a smaller charge endpoint capacity slippage compared to NMC-111 and $LiCoO_2$, two materials commonly used in commercial cells today. Voltage fade in $Li(Li_{0.12}Ni_{0.32}Mn_{0.56})O_2$ was carefully examined using differential capacity plots and it was shown that lithium insertion and removal must have a different pathway on charge and discharge as independently confirmed by Croy *et al.*. The model of superoxide and defect spinel formation at the particle surface purposed by Carroll and supported by the work of Croy and Koga also provided a plausible explanation for the excellent charge endpoint slippage of the vacancy rich material.

It is unclear from this work if the vacancy-rich material was special because it is rich in manganese, the lack of a high voltage formation or the inclusion of vacancies. Shunmugasundaram *et al.* have continued the vacancy studies of Rowe with cobalt containing excess-lithium materials.[132] His results may shed light onto the impact vacancies have on electrochemical performance.

A second study to also consider for future work is the impact of electrolyte composition, cut-off potential and cathode composition on electrolyte stability. In this study 1 M $LiPF_6$ EC:DEC 1:2 with and without 2 *wt*% VC were examined. It was shown that the inclusion of VC at 50°C slowed the rate of voltage fade. It should be of interest to those who study electrolyte to better understand the impact composition, vacancies,

activation protocol and electrolyte formulation have on voltage fade, charge endpoint slippage and other properties of these excess lithium materials.

Rowe's composition was used as a shell material in this thesis work. The development of the composite core-shell precursors will be discussed in Chapter 4 and the lithiation process will be discussed in Chapter 6.

Chapter 4. Core-Shell Precursor Materials

4.1 Precursor Materials Studied

As discussed in Chapter 2, the core-shell structure is formed during the synthesis of the hydroxide precursor particles. In this chapter the synthesis and characterization of core-shell precursor materials will be discussed. Table 4.1 lists core-shell precursors that were synthesized and will be discussed in this thesis. Table 4.1 shows the core and shell precipitation times, the target composition of the core and shell and the pH set points for the core and shell. The precipitation time is proportional to the molar ratio and nearly proportional to the mass ratio of core to shell. Table 4.1 does not include other CSTR parameters such as gas flow rate, stir rate or tank mode. Specific parameters will be discussed as necessary throughout this chapter.

Single-phase, not core-shell, samples of the various core and shell compositions were also synthesized for comparison to the core-shell materials. Some of these core-shell and single-phase samples were studied as lithium-ion positive electrode materials by following the lithiation and sintering procedure outlined in Section 2.4. Discussion of the products recovered after sintering and their electrochemical performance will be presented in Chapters 6 and 7. Results from the synthesis of some of the core-shell precursors of this chapter were prepared into two manuscripts that were published in the Journal of the Electrochemical Society.[118,133]

Table 4.1 List of core-shell precursor materials synthesized.

Sample	Core (Ni,Mn)	Shell (Ni,Mn)	Core Time (h)	Shell Time (h)	Core pH	Shell pH
S4-1	1, 0	0.5, 0.5	16	4	10.3	10.3
S4-2	1, 0	0.5, 0.5	16	4	10.3	9.5
S4-3*	1, 0	0.5, 0.5	12	4	10.3	10.3
S4-4	Continuous gradient Ni→Mn 10 h total				9.5	9.5
S4-5	Continuous gradient Ni→Mn 10 h total				9.5	9.5
S4-6	0.6, 0.4	0.2, 0.8	13.33	6.67	9.8	9.5
S4-7	0.6, 0.4	0.2, 0.8	16	4	10	9.5
S5-1	0.5, 0.5	0.17, 0.83	10	10	10.3	9.5

*In S4-3 a gradient composition from $Ni(OH)_2$ to $Ni_{0.5}Mn_{0.5}(OH)_2$ was precipitated over 4 hours between the core and shell

4.2 Core Shell Precursors S4-1 and S4-2

Figure 4.1 shows several SEM micrographs of powders recovered at different times during the synthesis of S4-1. The first micrograph in Figure 4.1 shows the core of the particles measured after 16 hours of precipitation. At this point in time the pump which dispensed the solution of 2 M $Ni(SO)_4$ was turned off and another pump dispensing 2 M $Ni_{0.5}Mn_{0.5}(SO)_4$ turned on. Examining the 17 to 20 hour micrographs in Figure 4.1 it is clear that new particles were formed as the shell composition was being dispensed into the reaction vessel.

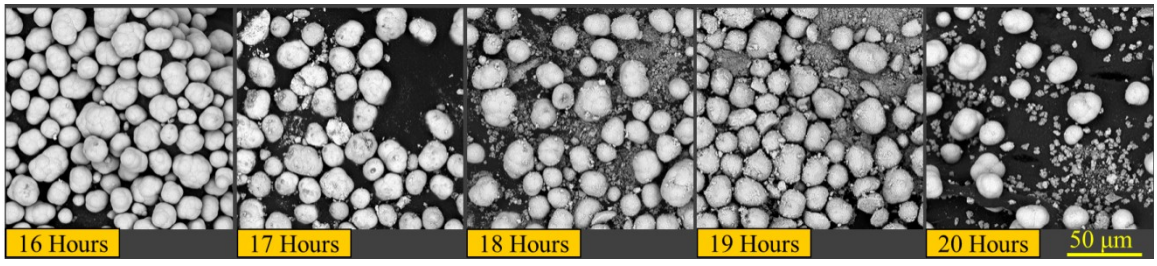

Figure 4.1 SEM micrographs of powders recovered from the tank reactor of various times during the synthesis of S4-1. All micrographs were taken at the same magnification with a common scale bar shown in the bottom right corner of the figure.

Figure 4.2 shows SEM micrographs at a higher magnification of the 16 hour "core" and 20 hour products. The right micrograph in Figure 4.2 shows that the newly formed small particles differ in surface morphology compared to the larger particles. Comparing the surfaces of the large particles in the left and right micrographs in Figure 4.2 there is little change in the surface morphology. The formation of new particles of different surface morphology and the lack of significant change in the surface morphology of the larger particles suggests that under these reaction conditions the shell composition primarily produced new particles and did not form a coating on the existing $Ni(OH)_2$ particles.

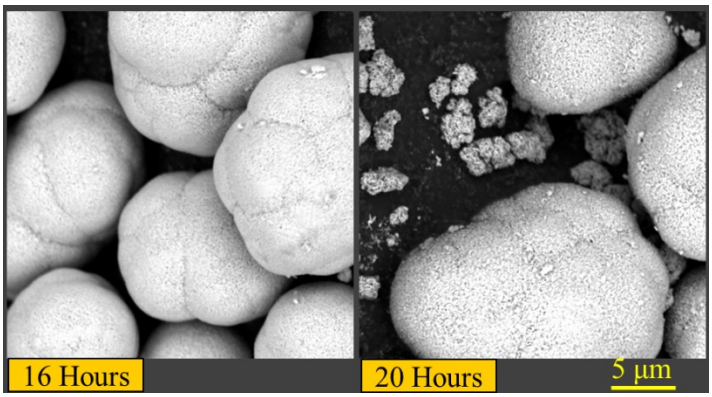

Figure 4.2 SEM micrographs of S4-1 16 and 20 hour products.

The products shown in Figures 4.1 and 4.2 were not the desired core-shell structure. There are many possible reasons why the new composition preferred new particle formation over coating. One possible reason is lattice mismatch between the core and shell due to the differences in composition; $Ni(OH)_2$ a = 3.126 Å, c = 4.605 Å and $Ni_{0.5}Mn_{0.5}(OH)_2$ a = 3.220 Å, c = 4.697 Å.[112,134] The resulting strain in freshly formed shell coatings coupled with gas agitation (1.5 SLPM) and stirring motion (1000 RPMs) may have caused the shell coatings to easily fall off the core particles. The dissolution-precipitation mechanism involving NH_3 described in Chapter 2 may also have caused a

lack of coating. For sample S4-1 the pH was maintained at 10.3 for the core and shell dispensing. Figure 2.3 shows that at this pH the concentration of manganese present as soluble $Mn(NH_3)_n$ species is virtually zero. At this pH new particle formation for the shell composition should be favored over precipitation-dissolution. This caused the freshly dispense solution to precipitate as new particles. Lowering the pH when the shell process begins would allow for more manganese to coordinate to NH_3 in solution, allowing dissolution-precipitation to occur. All of these issues were investigated with sample S4-2. In S4-2 the core and shell compositions and ratio of phases was the same as S4-1. For S4-2 the stir rate was reduced from 1000 RPM to 500 RPM, the flow of nitrogen was reduced from 1.5 SLPM to 0.5 SLPM and at 16 hours, the start of the shell, the pH was lowered to 9.5.

Figure 4.3 shows the SEM micrographs of samples removed at 16, 17, 18, 19 and 20 hours from the synthesis run, S4-2. Similar to sample S4-1, the cores of the particles, shown in the 16 hour micrograph, were potato shaped particles with a densely packed surface. Examining the rest of the micrographs in Figure 4.3, very few if any, new small particles were being formed. The higher magnification micrographs in the bottom of Figure 4.3 show that the surface of the particles was more porous in the 20 hour sample than the 16 hour sample suggesting the surface composition had changed.

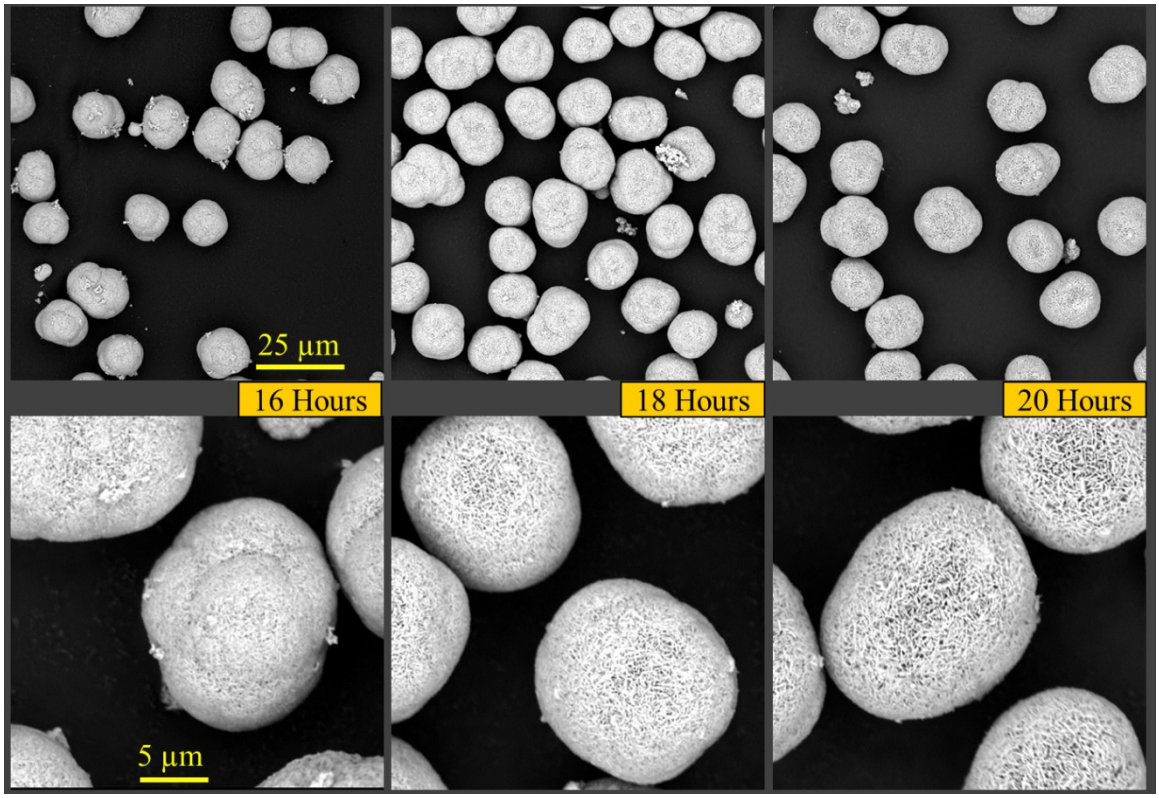

Figure 4.3 SEM micrographs of particles from S4-2 removed from the CSTR at different times shown at 2 different magnifications.

Figure 4.3 shows that new particles were not appreciably forming, but it may be possible that the composition of the core and shell were not the desired transition metal composition. Figure 4.4 shows a series of X-ray diffraction patterns collected on the JD-2000 of samples removed during the synthesis of S4-2 at various times. The diffraction patterns were collected while the samples were still wet, but after filtering and rinsing. Patterns were collected on wet samples because the manganese containing hydroxides decompose on exposure to air and the rate of decomposition is accelerated at higher temperatures.[90] Scans were collected between 15-65° 2θ with a step size of 0.05° and a dwell time of 3 s on the JD-2000.

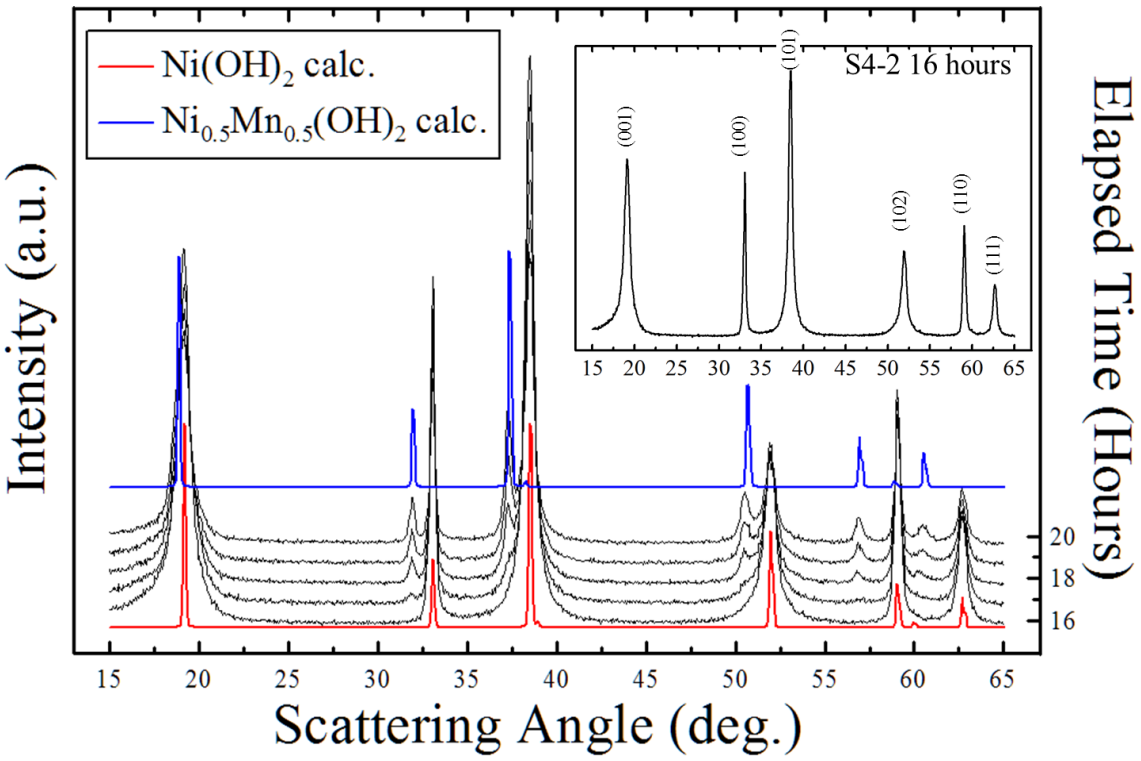

Figure 4.4 Diffraction patterns of samples from S4-2 collected at various times (right axis). Red plot shows the calculated pattern for $Ni(OH)_2$ and blue plot shows the calculated pattern for $Ni_{0.5}Mn_{0.5}(OH)$.[112,135] Insert shows diffraction pattern of sample collected after 16 hours.

The diffraction pattern of the 16 hour S4-2 sample in Figure 4.4 showed a single set of diffraction peaks that are in excellent agreement with the peak positions for the calculated peaks of $Ni(OH)_2$. Examining the diffraction patterns of samples from 18 hours or longer, a second set of diffraction peaks appeared, such as those at 32 and 51°. The second set of diffraction peaks are in excellent agreement with the calculated $Ni_{0.5}Mn_{0.5}(OH)_2$ calculated pattern. The inset in Figure 4.4 shows the diffraction pattern of the S4-2 16 hour sample in which broadening of the (101) and (102) diffraction lines were observed. Delmas *et al.* reported on this selective broadening and concluded it was due to stacking faults in $Ni(OH)_2$.[136,137]

Figure 4.4 along with Figure 4.3 confirms the existence of a two phase sample of the desired $Ni(OH)_2$ core and $Ni_{0.5}Mn_{0.5}(OH)_2$ shell. These figures do not show if the shell coating is uniform around the core or explain how thick the shell may be. To examine the homogeneity and thickness of the shell, EDS was used to examine cross-sectioned particles using the procedure outlined in Section 2.7.4. Figure 4.5 shows a cross-sectioned particle of the final product of S4-2 in the top panel with yellow spots showing where the composition was probed. The bottom panel of Figure 4.5 shows the ratio of nickel to manganese from the EDS measurement as a function of each yellow spots linear distance from the nearest edge position. Constant, horizontal error bars in the spot position were calculated based on the electron beam interaction-volume simulations shown in Figure 2.8. Figure 4.5 shows that near the particle edges the composition is close to the expected $Ni_{0.5}Mn_{0.5}(OH)_2$ composition. Moving away from the particle edges, the nickel concentration increases. Unexpectedly a region of sloping composition change instead of the expected step transition of a discrete core and shell composition was observed a few microns in from the edge. This sloping region was due to the EDS measurement method, not a true representation of the sample composition. If this gradient composition existed for a few microns in from the particle edge it should be noticeable in the diffraction experiments. Gradient samples will be discussed in this chapter and they are easily observed with X-ray diffraction. The gradient is most likely an artifact of the sampling method as described in section 2.7.4.

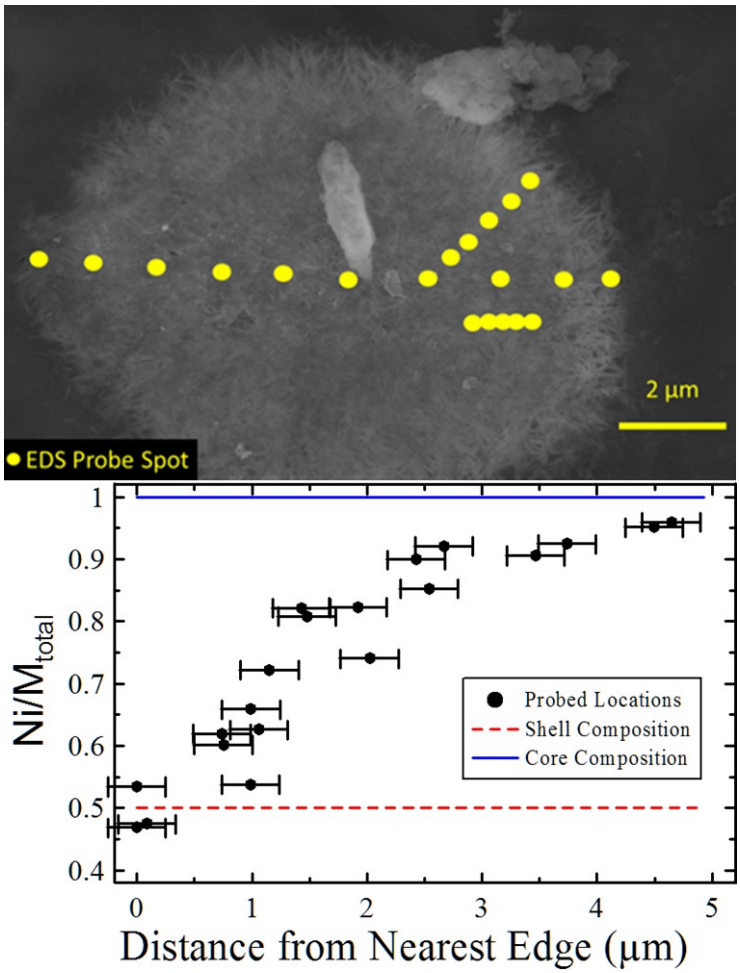

Figure 4.5 (Top). SEM micrograph of cross-sectioned particle of S4-2 final product. Yellow circles show where composition as probed with EDS. (Bottom). Atomic ratio of Ni to total metal versus linear distance from nearest edge of probed spot for spots in top panel. Reproduced from the Journal of the Electrochemical Society, open-source article.[118]

The cross-sectioned particle micrograph in the top panel of Figure 4.5 shows that the bulk of the particle is composed of densely packed metal hydroxide primary particles. Towards the surface of the particle the metal hydroxide primary particles are more loosely packed. This was also observed in the high magnification micrographs shown in Figure 4.3. The increased porosity in the shell is likely due to the decreased rate of dissolution-precipitation in the more manganese-rich surface morphology, $Ni_{0.5}Mn_{0.5}(OH)_2$, compared

to the core. Recalling that, the reason for the core-shell structure is to limit core-electrolyte interactions, the porosity and thickness of the shell should be considered in designing new materials. If the shell precipitation results in a porous coating then a thicker coating may be necessary to minimize the area of unprotected core surface. Changing the shell composition may require a thicker or thinner shell to achieve the best lifetime and energy density.

4.3. Core Shell Precursor with a Gradient

Section 4.2 showed that without careful consideration of pH and stir rate the shell composition could form new particles instead of forming a closed coating around the existing core particles. Sample S4-3 was made with a gradient between the core and shell. Sun *et al.* previously reported on samples with a similar, core-gradient-shell radial composition in which the intermediate gradient was claimed to reduce interfacial stress between the chemically different core and shell.[124] It was thought that by implementing a gradient, lattice mismatch would not be an issue. Sample S4-3 (Ni, Mn) = (1, 0) was precipitated for the first 12 hours at a pH of 10.3. At 12 hours the flow rate on the (1, 0) pump slowly decreased as the flow rate on another pump dispensing (0.5, 0.5) increased at the same rate with the pH maintained at 10.3. This gradient mixture was dispensed over 4 hours after which time the (0.5, 0.5) pump continued to dispense for 4 more hours to apply the shell composition again maintaining the pH at 10.3.

Figure 4.6 shows a series of diffraction patterns for run S4-3 collected at various times during the synthesis. Similar to the diffraction patterns shown Figure 4.4 for S4-2,

the peaks are in agreement with the calculated core $Ni(OH)_2$ phase. In the 20 hour diffraction pattern a second set of hydroxide diffraction peaks in agreement with the shell targeted composition, $Ni_{0.5}Mn_{0.5}(OH)_2$, appeared. Examining the patterns for the samples at 13, 14, 15 and 16 hours in the 50-52° range the diffraction peaks appear to become broad and asymmetric on the lower scattering angle side. The inset in Figure 4.6 shows the diffraction pattern at the end of the gradient process, 16 hours, which shows a distinct asymmetry in all diffraction peaks. This asymmetry is due to the presences of compositions intermediate between $Ni(OH)_2$ and $Ni_{0.5}Mn_{0.5}(OH)_2$. The lattice parameters "a" in $Ni_xMn_{(1-x)}(OH)_2$ $0 \leq x \leq 1$, vary with x according to

$$a(x) = 0.203(x) + 3.118 \text{ Å} \quad (4.1)$$

and c,

$$c(x) = 0.088(x) + 4.653 \text{ Å}.^{112} \quad (4.2)$$

As the manganese content in the mixed hydroxide increased, the "a" and "c" lattice parameters both increase and diffraction peaks shifted to lower scattering angles. This area of diffraction is direct evidence of the solid solution gradient and will be explored over a larger composition range later in this chapter.

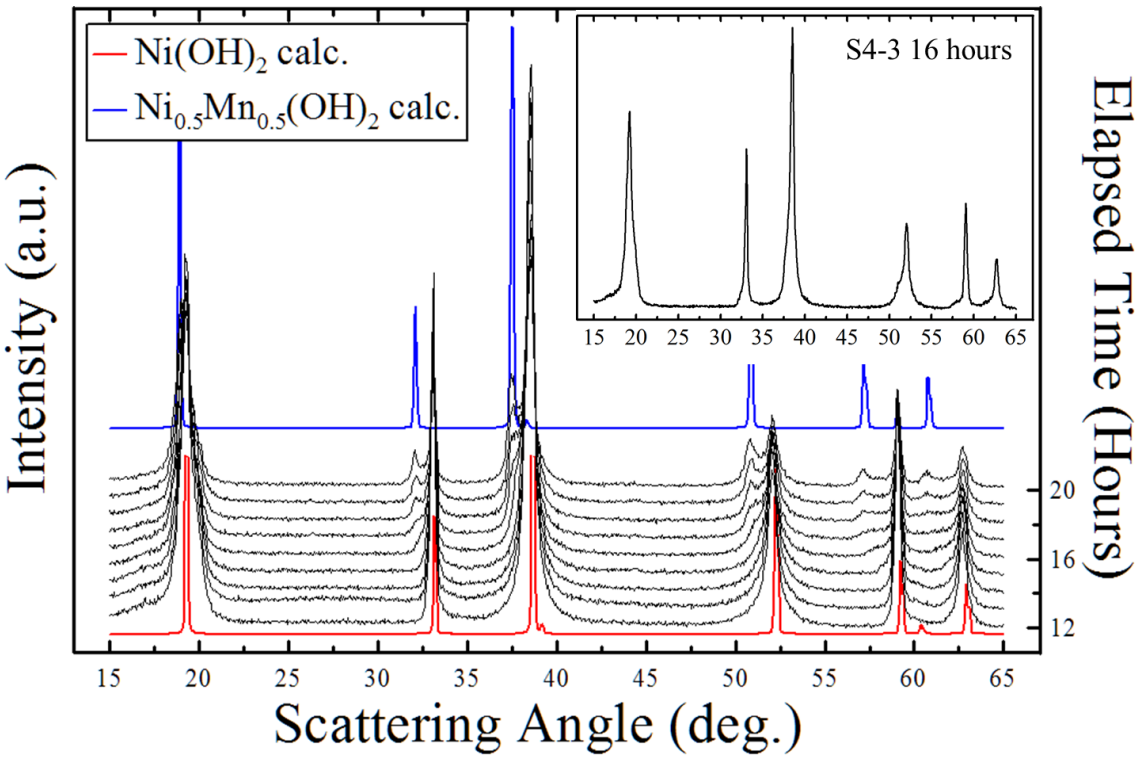

Figure 4.6 Diffraction patterns of samples collected hourly from 12-20 hours for run S4-3. Insert panel shows diffraction pattern of the sample collected at 16 hours, the end of the gradient precipitation process.

The XRD results shown in Figure 4.6 confirm the presence of a core, gradient and shell phases, but fail to confirm if coating was occurring or if new particles were forming. Figure 4.7 shows micrographs of the hourly collected samples of S4-3. The 12 hour micrograph in Figure 4.7 shows core particles of similar morphology to those shown in Figures 4.1 and 4.3. In the micrographs showing products from 13-15 hours there appears to be very few new particles suggesting that the core particles are being coated with the dispensing gradient composition. The 16 hour micrograph shows new particle formation which continues as the shell composition was dispensed until 20 hours. This shows that the gradient composition was not able to prevent the shell from forming new particles without any other synthesis modifications such as pH or stir rates.

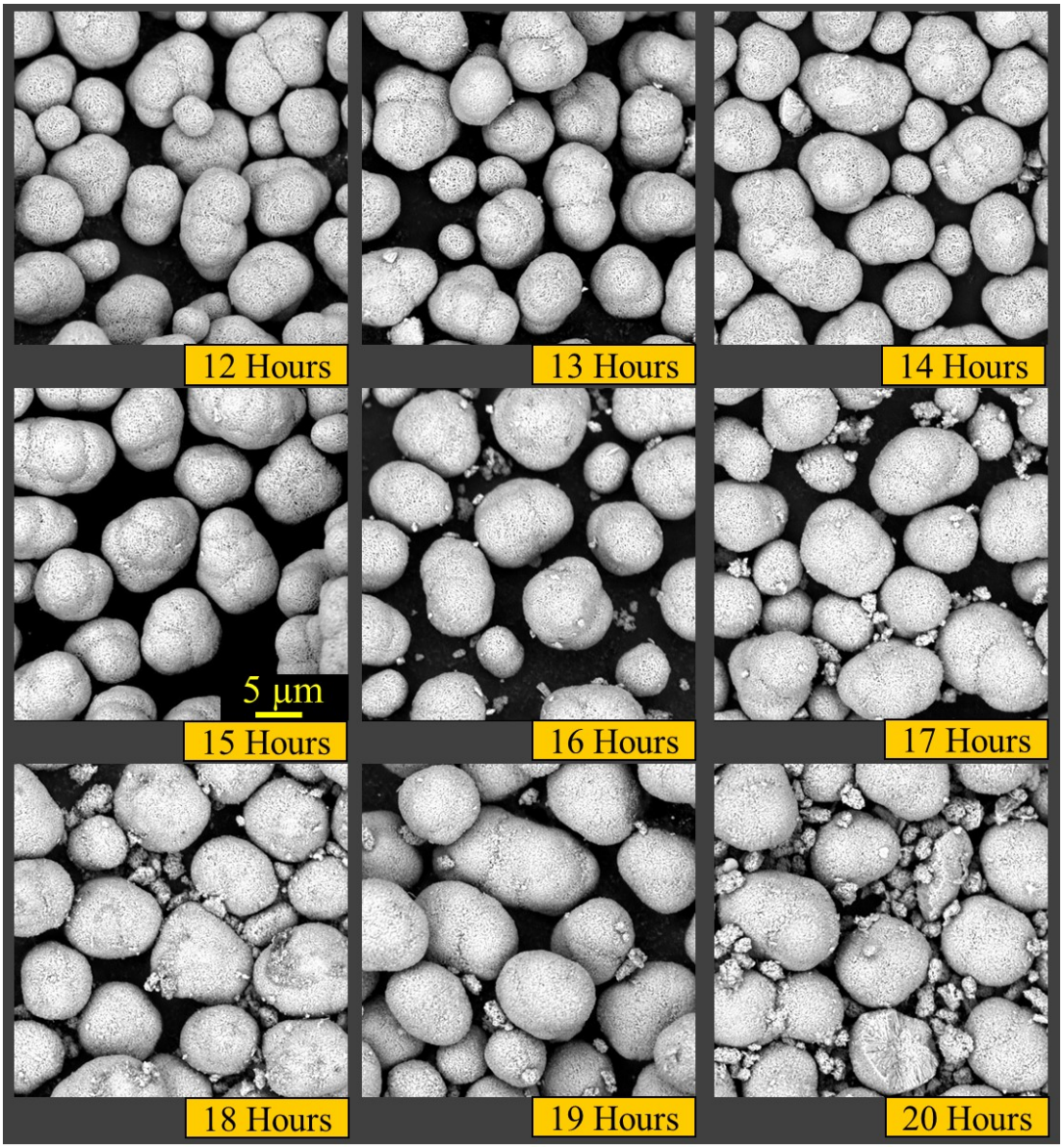

Figure 4.7 SEM micrographs taken at 7500x magnification of powders from run S4-3 at times shown below each micrograph.

4.4 Full Gradient Composition Particles

The diffraction patterns and micrographs of S4-3 with the gradient were interesting because they showed evidence of a gradient solid solution. The micrographs presented in Figure 4.7 also showed that the gradient would form on the existing particles until the

manganese content was too great favoring new particle formation over dissolution-precipitation. The previously reported hydroxide gradients by Sun *et al.* did not show evidence of a gradient in their diffraction patterns, only through EDS measurements.[80,124]

To further explore gradients, two more gradients were made. One had a gradient from $Ni(OH)_2$ to $Mn(OH)_2$ (S4-4) and the other with the inverse, $Mn(OH)_2$ at the centre and $Ni(OH)_2$ on the surface (S4-5). For these gradient samples the total dispensing time was 10 h instead of 20 h and the total dispensed volume of metal sulfates was the same as a 20 h run. Shorter runs were required due to the limited resolution and minimum flow rate of the variable speed peristaltic pumps and the desire to sample the gradient regularly throughout the precipitation process. The pH was maintained at 9.5 throughout the run to accommodate the manganese rich compositions.

Figure 4.8 shows the diffraction patterns of samples removed hourly from 2 to 10 hours from run S4-4; a sample was not collected at 1 hour as there was too little product formed at this point to recover an adequate sample for diffraction measurement. Guidelines in the inset of Figure 4.8 show that scattering angle range of $I_{max\text{-}101}$ $Mn(OH)_2$ to $I_{max\text{-}101}$ $Ni(OH)_2$. Diffracted intensity from the 10 h sample is observed within this area and has more of a saw-toothed shape rather than the predicted pseudo-Voigt shape of single diffraction lines. This is due to the addition of many diffraction peaks between scattering angles of the end members $Mn(OH)_2$ and $Ni(OH)_2$. This supports that the sample is a gradient of compositions ranging from $Mn(OH)_2$ to $Ni(OH)_2$.

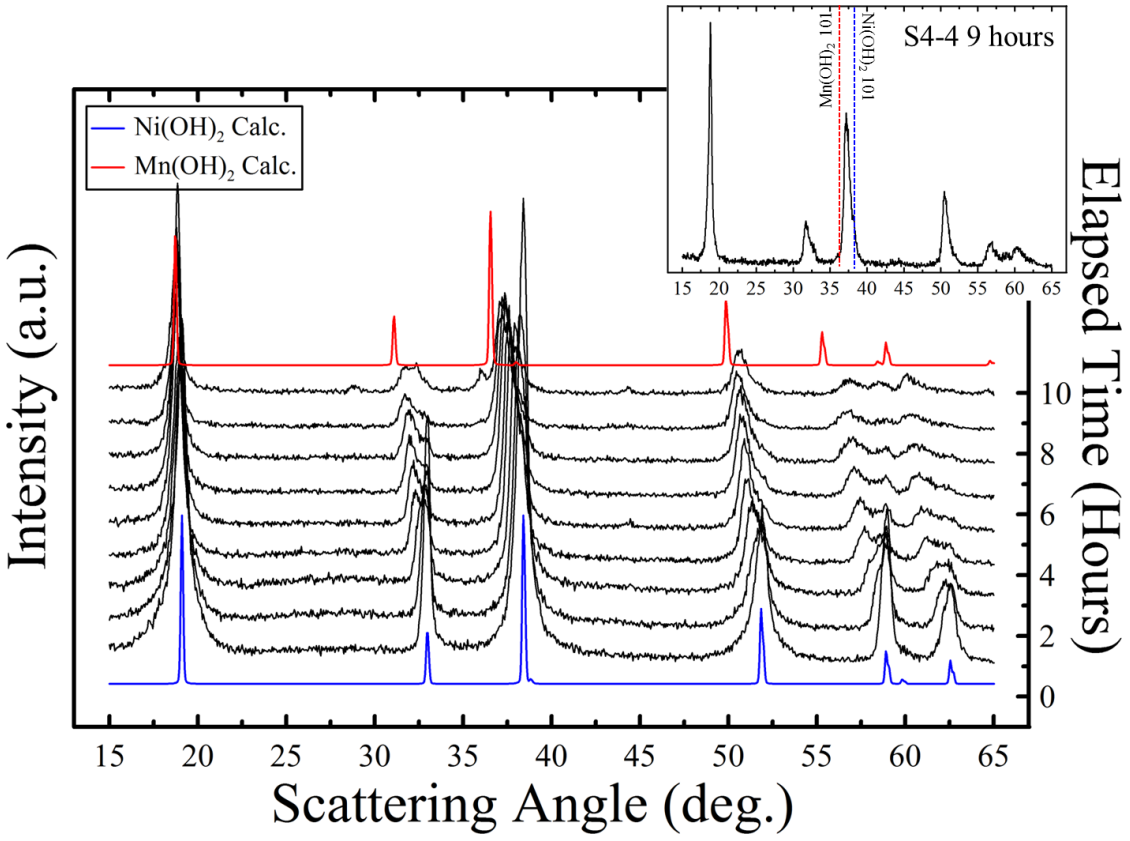

Figure 4.8 Diffraction patterns of samples removed from S4-4 (gradient Ni→Mn) hourly from 2-10 hours. Insert shows diffraction pattern of sample removed at 9 hours. Vertical dashed lines in insert mark the position $I_{max\text{-}101}$ for $Mn(OH)_2$ and $Ni(OH)_2$

Sample S4-4 is a linear gradient, assuming that individual crystallites exist as discrete compositions it would be expected that there is an equal distribution of all possible crystallites from $Ni(OH)_2$ to $Mn(OH)_2$ present in the final product, ignoring any product removed via sampling or overflow. The integrated intensity of diffraction lines for $Ni(OH)_2$, $Mn(OH)_2$ and any of the solid solution between should be quite similar since the scattering power of the atoms present are similar. Examining the feature between 50-54° in Figure 4.8, the intensity is higher on the lower scattering angle side of the peak system; this is also observed in the (100) system at 31-34°. The asymmetry towards the lower

scattering angle is due to absorption. This absorption results from the radial composition of the secondary particles. The absorbing medium along the path for crystallites near the surface of the particle is different than those near the centre of the particles. Manganese has a shorter absorption length for Cu-Kα than nickel, and since it is in greater concentration near the surface the diffraction peaks are asymmetric.

Sample S4-5 was developed with the inverse gradient of S4-4, manganese-rich near the centre and nickel-rich near the surface. Figure 4.9 shows the diffraction patterns of samples removed during the synthesis of S4-5 between 1-10 hours. Similar to S4-4, the inset panel in Figure 4.9 shows samples covering the full solid solution range of the $Ni_xMn_{(1-x)}(OH)_2$, $0 \leq x \leq 1$ system. What was different in the diffraction patterns of S4-5 compared to S4-4 was the diffraction peaks of the manganese-rich core were less attenuated than the nickel-rich core peaks were in S4-4. This was due to the differences in the absorbing species near the surface of the particles. Manganese has an absorption length that is 10 times shorter than that of nickel. The contrast in mass absorption coefficients in Ni and Mn was exploited to estimate the shell thickness and will be described in Chapter 5.

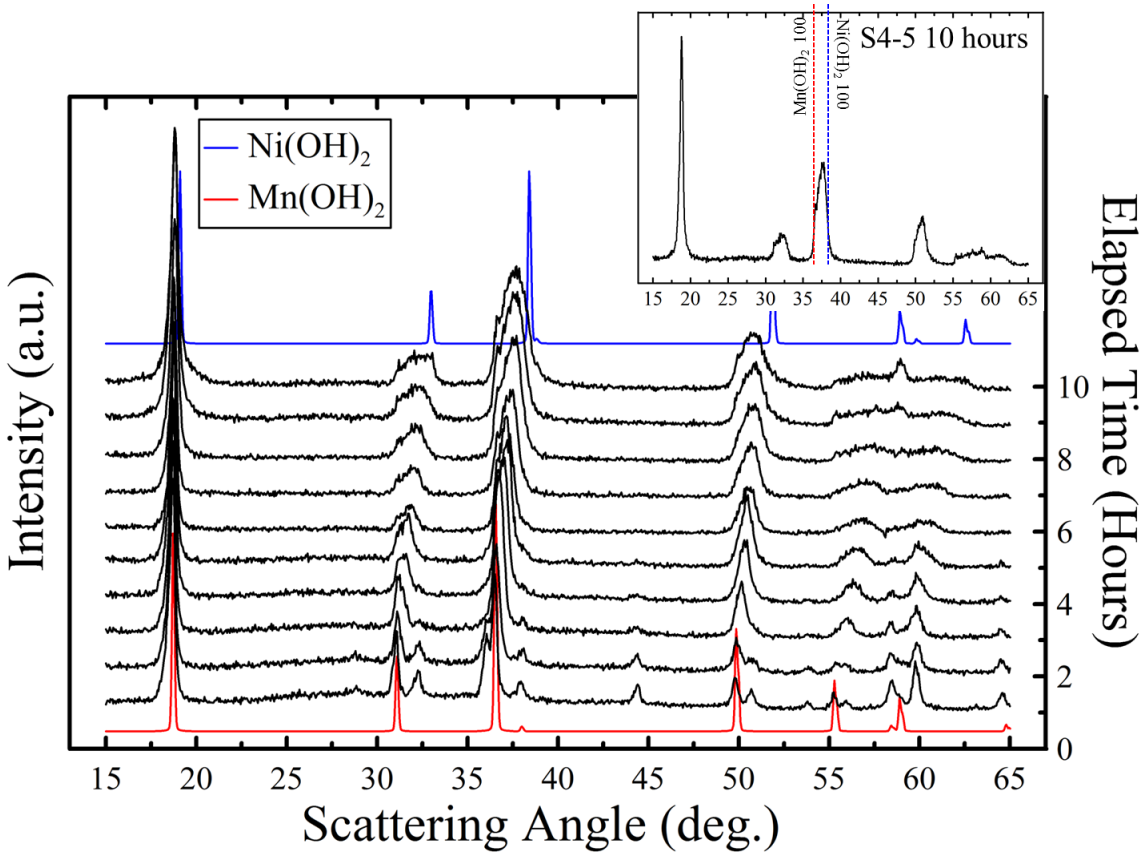

Figure 4.9 Diffraction patterns of samples removed from S4-5 (gradient Mn→Ni) hourly from 1-10 hours. Insert shows diffraction pattern of sample removed at 10 hours. Vertical dashed lines in insert mark the position $I_{max\text{-}100}$ for $Mn(OH)_2$ and $Ni(OH)_2$

The 1 and 2 hour diffraction patterns in Figure 4.9 show additional diffraction peaks, for example at 44°, that do not index to a P-3m1 hydroxide space group.[138] These peaks are no longer evident in the 3 hour or later samples. These peaks were attributed to Mn_3O_4 (PDF-16-154) which formed on the exposure of the manganese-rich hydroxide samples to air during the work up and diffraction data collection.[138] Samples were exposed to air for 1.5-2 hours before the whole diffraction pattern was collected. The disappearance of these peaks in the 3 hour or later scans may be due to the surface of the particles

containing a more air stable nickel-rich composition which limited oxidation of the manganese-rich core. Spinel formation could also be seen in the 10 hour scan of S4-4.

Figure 4.10 shows the diffraction patterns of the 10 hour samples from S4-4 and S4-5 between 30 and 55°. The overall composition and distribution of crystallites in S4-4 and S4-5 10 hour samples should be identical with the radial composition the inverse of each other. Examining the peaks at 35-40°, S4-5 shows a square wave like shape compared to S4-4 which is much more slanted showing more intensity towards smaller scattering angle, larger d-spacings, manganese-rich. This slanting was due to the X-ray path being different for the two samples and supports that the gradient composition was distributed across the radius of secondary particles.

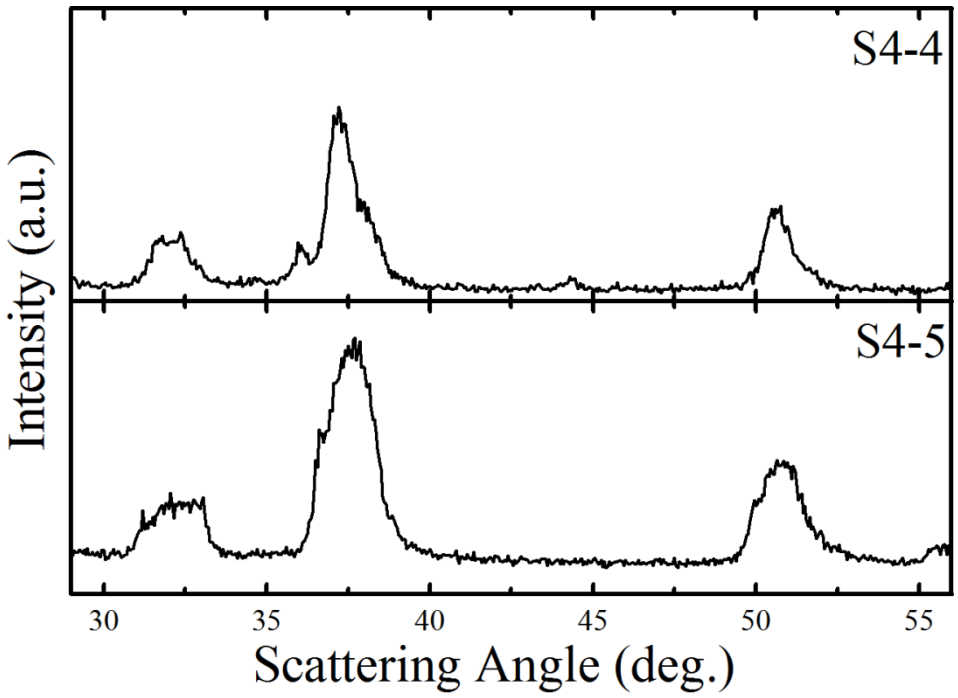

Figure 4.10 Diffraction patterns of samples removed at 10 hours from samples S4-4 and S5-5 collected on the JD-2000. For both panels the vertical axes length is 900 counts.

The diffractometers in this thesis all used a Cu-Kα X-ray tube as the X-ray source. Chapter 2 showed that at this wavelength, manganese has a shorter absorption length than nickel. The relative absorption length of nickel and manganese can be modified by using an X-ray source other than Cu-Kα. A synchrotron facility can produce X-rays for diffraction experiments at virtually any X-ray photon energy.[108] By using harder X-rays such as 0.5 Å, the absorption lengths would be very long, thus "turning off" absorption. If a softer X-ray, such as 2.0 Å, was used nickel would have a longer absorption length than manganese. Synchrotron experiments were never conducted, but may be of interest for future researchers. Using multiple photon energies and comparing diffraction patterns of the same sample may provide a better understanding of radial composition.

Figure 4.11 shows micrographs of the various gradient samples removed during run S4-4 and the final products of runs S4-4 and S5-5. The synthesis of these gradient samples was completed in only 10 hours which limited the growth of the particles. The pH was held fixed during the whole reaction which resulted in very porous particles. It is difficult to tell from the micrographs in Figure 4.11 if the gradients are exclusively forming a coating on existing particles instead of new particles. Unlike the core-shell materials where the core was allowed to develop over several hours, the full gradient samples are changing composition from the start of dispensing. This did not allow seed particles of appreciable size of a single composition to serve as the core to coat. Evidence of coating was present in the diffraction patterns shown in Figure 4.9 and in the micrographs of the first row of Figure 4.11. In the early diffraction patterns, the product was decomposing to Mn_3O_4 before the pattern could be fully collected, after 3 hours of dispensing this was no longer

observed. This suggests that a barrier between the manganese rich core and the oxygen atmosphere existed.

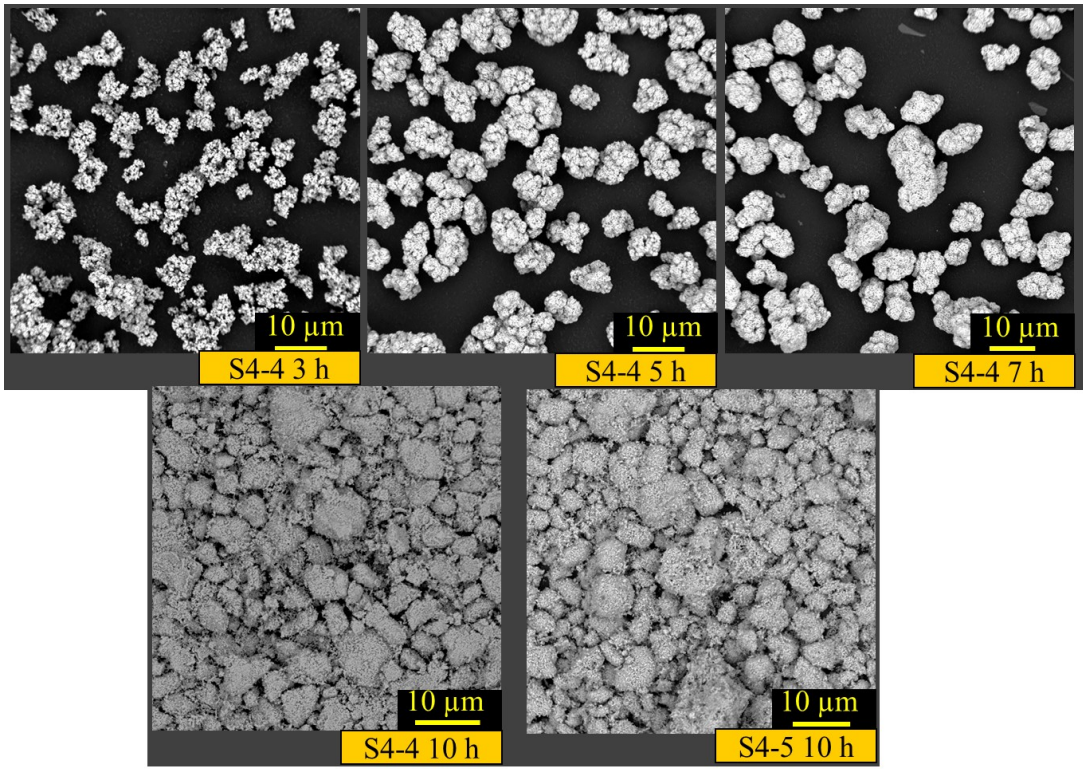

Figure 4.11 SEM micrographs of samples extracted from S4-4 and S4-5 at various times.

While the gradient samples are interesting from a scientific standpoint they do not seem like the logical choice for a lithium-ion battery positive electrode material. The reason for using a core-shell was to select the best lifetime material for the shell and the best energy density material of a similar composition for the core. A gradient is a mixture of many different compositions instead of just the best known materials. Gradient precursors were not further examined in this thesis, but from a fundamental standpoint should be further investigated.

4.5 Core-Shell Hydroxide Precursors for Positive Electrode Synthesis (S4-6, S4-7)

In Chapter 3 several single phase Li-Ni-Mn oxide materials were studied using ultra high precision chargers to find materials of interest to use in core-shell materials. For that study a material found by Aaron Rowe showed minimum charge endpoint capacity slippage, useful for a shell material.[131] It was also shown and supported by literature that as the manganese content of the material decreases, voltage fade decreases. For these reason samples S4-6 and S4-7 were synthesized with a nickel-rich core.

The choice of the core composition of $Ni_{0.6}Mn_{0.4}(OH)_2$ was to have a significant enough difference in composition from the $Ni_{0.2}Mn_{0.8}(OH)_2$ shell. The selected composition would be different enough to resolve core and shell diffraction peaks in the lithated products. It would seem that it would have made sense to use even more nickel in the core, however extremely nickel rich materials are difficult to synthesize properly.[139] Nickel and lithium will easily substitute for each other on 1a sites (lithium layer) or 3b (transition metal layer) sites. When the nickel content is high and the synthesis performed at incorrect temperatures, mixing of the cations occurs leading to poor electrochemical performance. While there are established methods that can minimize cation mixing it would have resulted in different heating methods then those used by McCalla and co-workers. This would have hindered the usefulness of their structure composition diagram which was essential to understanding the lithated products developed from S4-6 and S4-7.

Figure 4.12 shows the diffraction patterns of the final products from S4-6, S4-7 and synthesized single phase samples of the target core, $Ni_{0.6}Mn_{0.4}(OH)_2$ and target shell, $Ni_{0.2}Mn_{0.8}(OH)_2$. Single phase samples were made in the CSTR with a dispensing time of 20 h and pH of 10.3 for $Ni_{0.6}Mn_{0.4}(OH)_2$ and 9.5 for $Ni_{0.2}Mn_{0.8}(OH)_2$. Examining the pair

of (100) diffraction peaks for S4-6 and S4-7 at 30-35° there are clearly two phases present. The ratio of intensity of the core peaks compared to the shell peaks was greater in S4-6 compared to S4-7, as expected since the shell precipitation time was longer in S4-6 than S4-7. It was interesting to notice that the preferential broadening of diffraction peaks due to stacking faults present in $Ni(OH)_2$ was less in the samples shown in Figure 4-12 with a greater manganese content.

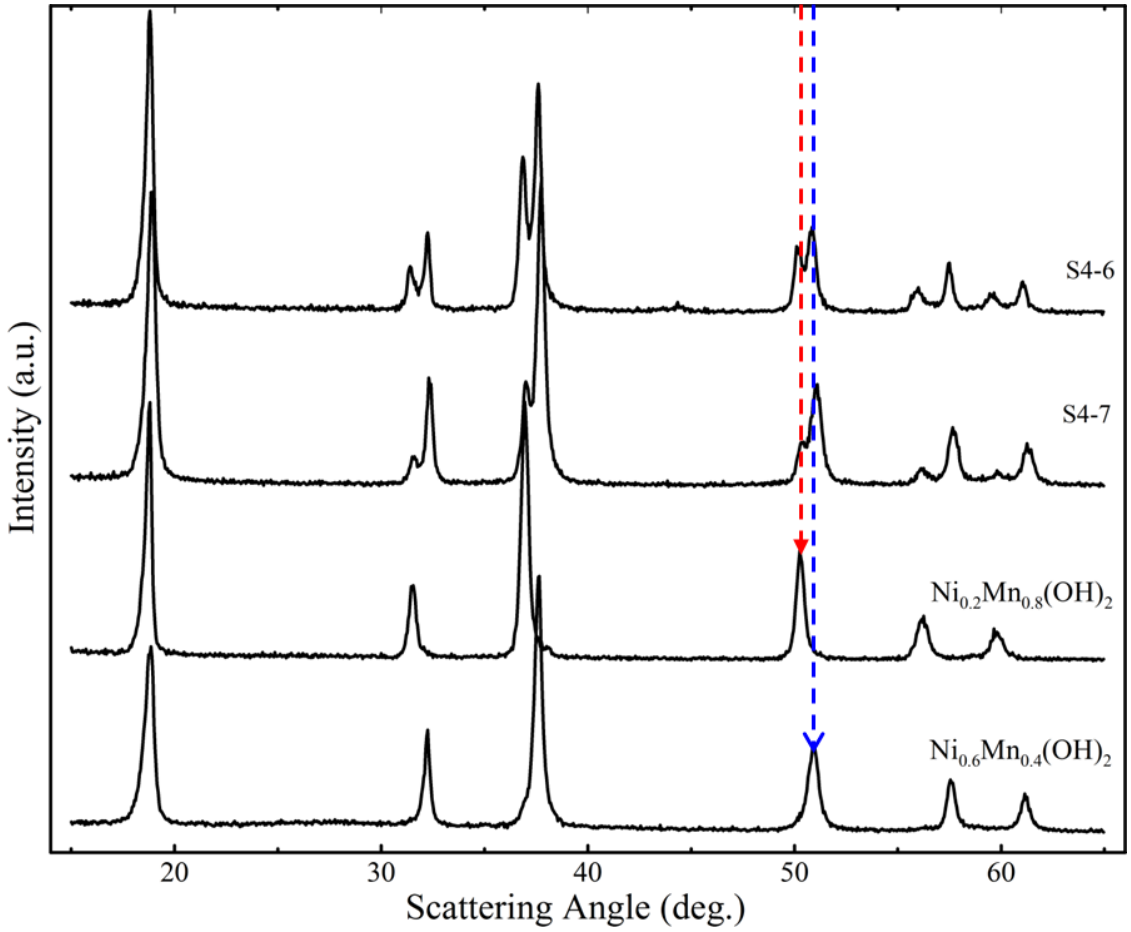

Figure 4.12 Diffraction patterns of samples S4-5, S4-6, $Ni_{0.2}Mn_{0.8}(OH)_2$ and $Ni_{0.6}Mn_{0.4}(OH)_2$. Reproduced from the Journal of the Electrochemical Society, open-source article.[140]

Rietveld refinement was performed on all of the diffraction patterns shown in Figure 4.12. For the single phase samples, a single P-3m1 phase was used to fit the pattern and for the core-shell samples, two P-3m1 phases with the target transition metal compositions for the core and shell phases were used to fit the diffraction patterns. In samples S4-6 and S4-7, the core and shell peaks are clearly separated except for the (001) diffraction peak at 18°. Separation of diffraction peaks increases with scattering angle due to the sin(θ) term in the Bragg equation. The (001) diffraction peaks could also not be used in the Rietveld refinement due to asymmetry associated with axial divergence in the JD-2000.[102] The D-5000 contains Söller slits, which limits axial divergences aberrations, but the JD-2000 does not. The diffraction patterns were fit between 25-65° where diffraction peaks capable of being fit with the Rietveld algorithm were present.

The following parameters were used to start the fitting routine; phase ratio core:shell (dispensing time), site occupations (target composition), a and c lattice constants (Equations 4.1 and 4.2), third-order polynomial background and zero offset. Hydrogen atoms were not included in the fit as their X-ray scattering intensity is effectively zero compared to the other elements and their position in the unit cell is not well defined.[83] After defining these terms, the refinement started by allowing phase scales, lattice parameters a and c and zero offset to be refined. The phase scales were constrained so they maintained the target ratio. This is a poor estimate of phase scales as it assumes absorption to be negligible which has already been established to not be the case. After these parameters were refined to stable values the peak shapes were fitted. Both the core and shell were fit as individual pseudo-Voigt shaped peaks. The lattice constants were fixed at this time and the constraint on phase scales removed. After refinement of the peak shape and phase

scale, the parameters for peak shape were verified to be physically meaningful. When satisfactory peak shapes were obtained the lattice parameters were again allowed to be refined along with the z coordinate of oxygen. After refinement, the fit was again checked to verify all parameters were physically meaningful after which the refinement was considered complete. Table 4.2 lists the fitting results of refinements of the samples shown in Figure 4.12.

Table 4.2 Rietveld refinement results of samples discussed in section 4.5.

Sample	a_{core} (Å)	c_{core} (Å)	a_{shell} (Å)	c_{shell} (Å)	Phase Scale core/shell	R_{wp}	X_{Ni}*
S4-6	3.205(6)	4.707(8)	3.274(6)	4.726(8)	1.39	9.22	0.367
S4-7	3.195(6)	4.687(6)	3.267(6)	4.718(8)	3.13	8.65	0.508
$Ni_{0.6}Mn_{0.4}(OH)_2$	3.193(6)	4.690(8)				9.89	0.579
$Ni_{0.2}Mn_{0.8}(OH)_2$			3.269(6)	4.715(8)		9.93	0.226

**Results from ICP-OES, S4-6 target 0.467, S4-7 0.520.*

$R_{wp,}$ a weighted profile goodness of fit was used to compare the quality of the Rietveld refinements with the weighting factor $w_i = \sigma_i^2$.[141] This was selected over the more commonly used R_{Bragg} which only accounts for differences between the observed integrated intensities and calculated. Since absorption in core shell particles is not equal at all scattering angles and unaccounted for in the Rietveld model used, there would be an error in the R_{bragg} values that would vary from sample to sample. R_{wp} values are best used to compare data collected using the same instrument and scanning conditions as it is highly sensitive to the signal to noise ratio. Table 4.2 shows that for each sample the R_{wp} values are fairly similar and below the accepted value of 10 for a quality fit.[111]

Table 4.2 shows that for sample S4-7, the core and shell lattice parameters are in excellent agreement with the single phase core and shell parameters. For S4-6, there is a greater difference compared to the lattice parameters of the single phase reference materials. For S4-6, both the core and shell have lattice parameters larger than the reference which suggest the phases are richer in manganese, which is supported by the ICP-OES analysis. Assuming that S4-6 and S4-7 were made exactly to the target and absorption was not present, the phase scales ratio should be 4 and 2 respectively, Table 4.2 shows that the phase scales ratios are less. If absorption was considered, the core peaks will be attenuated more than the shell resulting in the phase ratios decreasing.

Figure 4.13 shows the Rietveld refinement of samples S4-5 showing the histogram fit and the calculated core and shell contributions. Each panel in Figure 4.13 was scaled to maximize the data. Peak markers show only the contribution for Cu-$K\alpha_1$, but the fit was completed using both Cu-$K\alpha_1$ and Cu-$K\alpha_2$ in the expected 2:1 ratio. The right panel of Figure 4.13 shows some of the challenges to fitting these samples. In this panel there are 6 total diffraction peaks and separating these peaks which had relatively small integrated intensities was difficult.

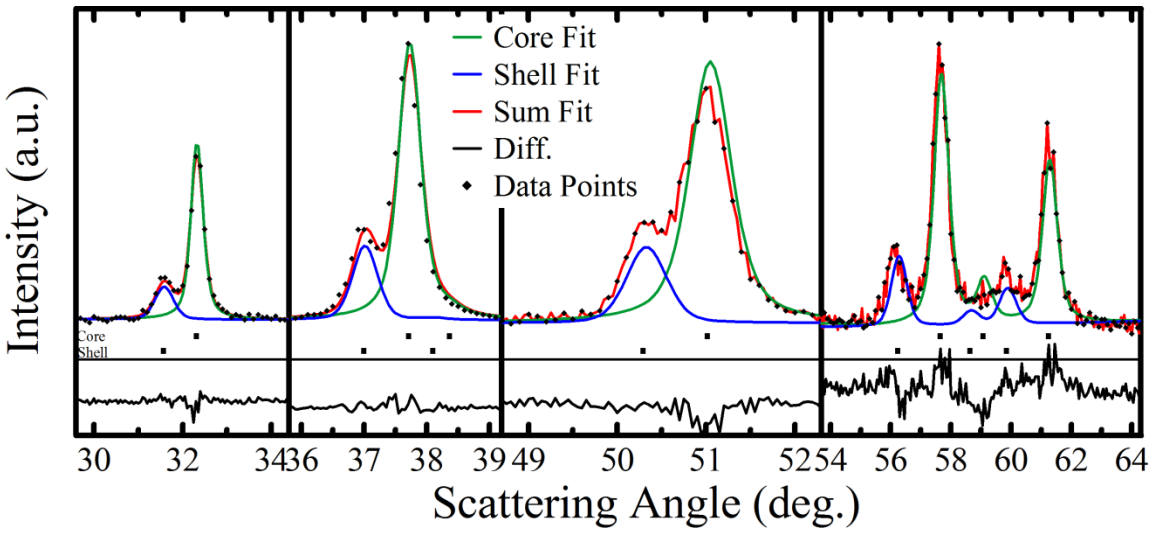

Figure 4.13 X-ray diffraction pattern and Rietveld refinement for S4-5 with individual contributions of core (green) and shell (blue) shown. Each panel is scaled vertically to fill the panel with the difference plot shown on the same scale as each panel.

Figure 4.14 shows micrographs of the samples discussed in this section. The first column of Figure 4.13 is the core or single phase core analog and the second column is the core-shell 20 hour product or shell analog. The right two columns of Figure 4.14 are of the same samples as the left two columns at higher magnifications. As with other samples in this chapter, the micrographs of the core only and coated core-shell products combined with the diffraction results verify a shell of desired (or close to) composition formed around existing core particles.

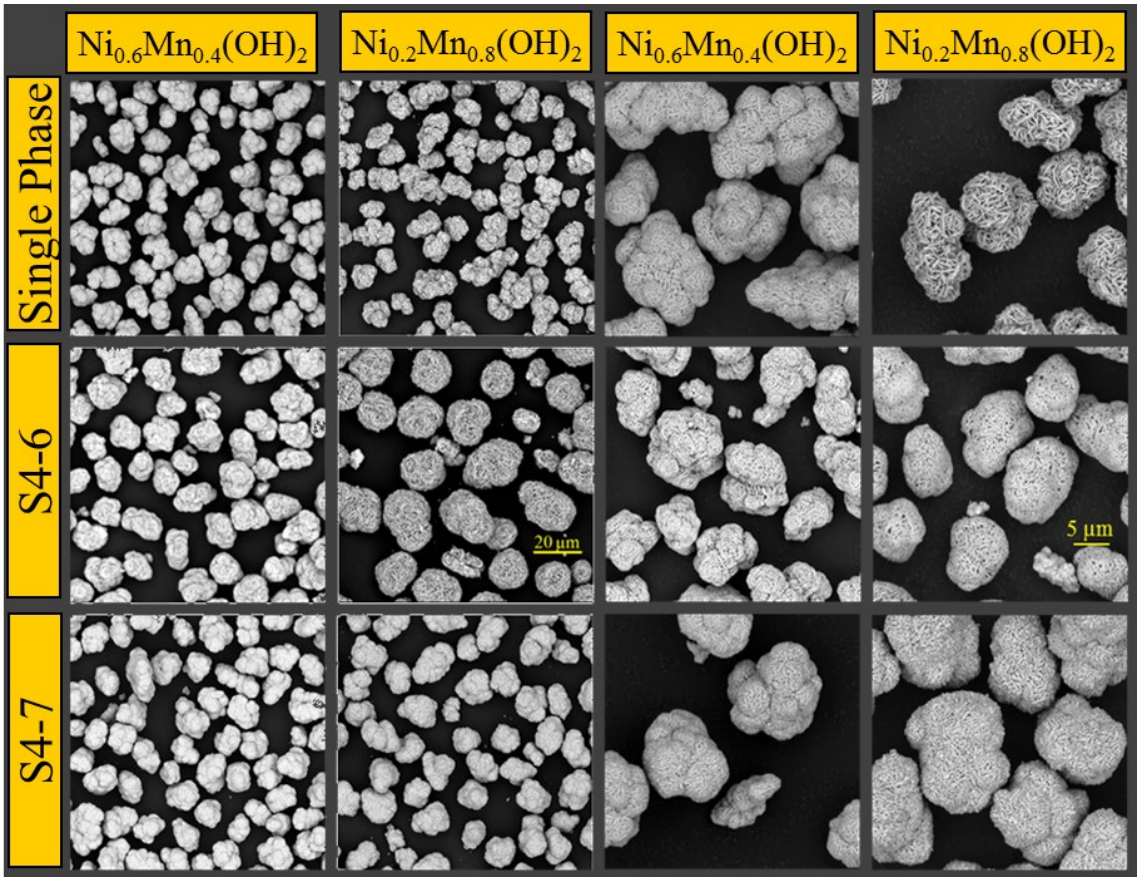

Figure 4.14 SEM micrographs of the core (first column), shell (second column) at low (left two columns) and higher magnification (right two columns). The top row of micrographs shows the analog single phase materials for the respective core and shell. Text labels at the top of each column denote the composition located at the surface of the imaged particles. Reproduced from the Journal of the Electrochemical Society, open-source article.[140]

Figure 4.15 shows the qualitative EDS composition false-colour images of particles from S4-6 and S4-7. Unlike the EDS analysis shown in Figure 4.5, this data was collected as the electron beam was rastered across the entire window instead of focusing at selected points. The data collection method is identical to the description of SEM given in Chapter 2, except instead of counting secondary or back-scattered electrons at each point the intensity of characteristic X-rays were quantified into an element concentration at each

raster point of the electron beam. This data is best used as a qualitative measurement instead of a quantitative measurement. EDS measurements in this thesis originally were collected like those in 4.5, but after it was apparent that quantification was not straightforward this more qualitative method was employed.

Figure 4.15 shows that there was a manganese (red) rich shell around a blue-red core of the cross sectioned particles. In the particle imaged from S4-7, the coating around the particle looks to be uniform and the coverage complete. In the particle imaged from S4-6, the coating appears to be less uniform with a thicker coating on the top of the particle than the bottom. The thicker top side shell versus the bottom may be due to the particle moving during data collection. In Figure 4.15 small dark circles are visible in the substrate; these circles were damage to the epoxy substrate due to melting. Electrons striking the insulating epoxy heat up the substrate and can cause melting. A conductive carbon coating was used to improve charge dissipation, but melting was still evident. As the substrate heated and melted, the imaged particle may have shifted in time relative to the fixed imaging window. Over the 300 seconds of collection, the particle imaged may have shifted down and to the right. This is supported by the evidence of many charging circles in the top and left of the micrograph of S4-6.

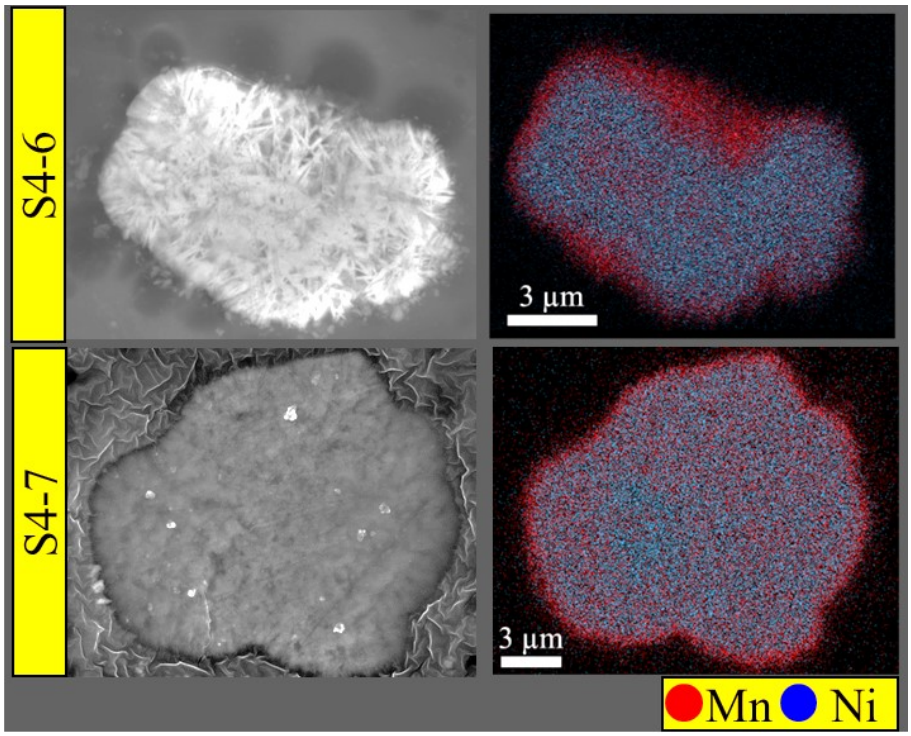

Figure 4.15 SEM micrographs (left column) and false-colour EDS maps of same cross-sectioned particle of S4-6 and S4-7 showing the concentration of Mn (red) and Ni (blue).

4.6 Chapter 4 Conclusions

In this chapter several core-shell precursors were discussed. It was shown that stir rate, gas flow rate and pH are important factors to monitor when trying to improve the shell coating process. It was determined that the pH should be changed between the core and the shell to improve the shell coating with a general trend of decreasing pH with manganese concentration. It was also shown in this chapter that SEM or XRD alone are insufficient to characterize the core-shell particles. Both XRD and SEM must be used to verify the core and shell composition and that new particle formation is minimized. For all core shell materials a sample of the suspension should be analyzed at the end of the core process and several samples should be taken during the shell dispensing process to monitor the reaction.

EDS is an excellent tool for qualitative analysis and showed that a uniform shell could be precipitated onto particles. Many previous reports relied solely on EDS to verify the shell coating and this single method should be avoided. The sample size in EDS is one or a few particles, which is not a valid representation of a sample with millions of particles. All three techniques used together provide better insight into radial composition distribution, homogeneity of particles and core and shell composition.

The samples presented in section 4.5 will be discussed as lithiated and sintered products in Chapter 6. Chapter 5 will focus on estimating the shell thickness of the nickel-rich compositions discussed in section 4.2.

Chapter 5. Shell Thickness Estimation via Absorption Modeling

Chapter 4 showed many different core-shell and gradient hydroxide materials synthesized for this thesis. The linear gradient samples S4-4 and S4-5, which have the same overall composition, but the reversed radial composition, showed different diffracted intensities. The differences in these diffraction patterns were attributed to absorption of X-rays by the shell phase which should also be observed in core-shell samples. This chapter will discuss methods used to quantify absorption to estimate the thickness of the shell layer. Prior to this model the only reported method to measure the shell thickness was using EDS.[124,142] The model presented in this chapter was a joint effort with Eric McCalla who assisted with the numerical integration and spherical absorption model and the writing of a numerical integration calculator in Yorick.[143] The results of the absorption modeling were prepared in a manuscript published in the Journal of the Electrochemical Society.[118]

5.1 Samples for Absorption Modeling

Sample S4-2 from Chapter 2 was used for the absorption modeling. A second sample, S5-1 with a $Ni_{0.50}Mn_{0.50}(OH)_2$ core and $Ni_{0.17}Mn_{0.83}(OH)_2$ shell with a dispensing time ratio of 1:1, was made to test the robustness of the model. The other samples discussed in Chapter 4 were not analyzed because the samples were inhomogeneous due to precipitation problems, or the diffraction data originally collected was of inferior quality to use with the model.

Figure 5.1 shows the fraction of transmitted Cu-Kα X-rays (I/I_0) through a block of various hydroxides of length, *l*, determined using

$$\frac{I}{I_0} = e^{-\left(\Sigma\left(\mu/\rho\right)l\right)}. \qquad (2.6)$$

Figure 4.5 showed that for a particle of S4-2 with a radius of 5.4 μm, the $Ni_{0.5}Mn_{0.5}(OH)_2$ shell was approximately 1 μm thick. X-rays would have to travel through a total of 2 μm of $Ni_{0.5}Mn_{0.5}(OH)_2$ going in the shell, diffracting and exiting back out the shell on the other side of the particle, the transmission through 2 μm of $Ni_{0.5}Mn_{0.5}(OH)_2$ would be about 93%.

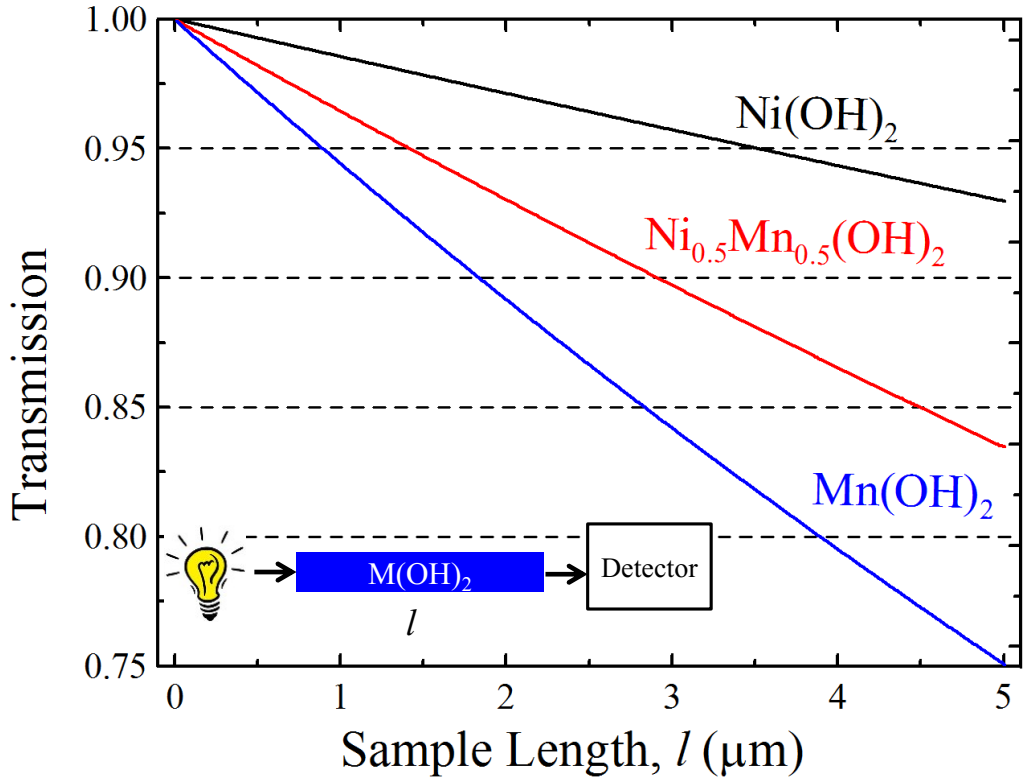

Figure 5.1 Transmission of Cu-Kα X-rays through hydroxide media calculated using Equation 2.6 with linear absorption coefficients of the hydroxides shown.[107]

To make the best measurement possible of a reference material (I_0) and the sample (I), several precautions were taken in sample preparations. A sample of the core-only (16 h in S4-2, 10 h in S5-1), an aliquot of the final product and reference single-phase materials of the target core and shell composition were freeze-dried to remove water without

degrading the sample, prior to collecting diffraction patterns. Freeze-drying was accomplished by quickly removing the powder after filtration and freezing in liquid nitrogen in a scintillation vial. This scintillation vial was then transferred to a vacuum apparatus fitted with a cold trap. Vacuum was drawn on the frozen wet powder. As the vials warmed to room temperature water in the sample evaporated and was collected in a cold trap. Samples were dried overnight and remained under vacuum until ready for diffraction measurements.

Water removal was important for two reasons. First, water absorbs X-rays; 1 mm of water results in about 40% transmission of Cu-Kα X-rays.[144] If water content differed from sample to sample then separation of absorption due to the shell and from water would be difficult. Secondly, variable water content would result in a variable amount of sample in the well and diffracted intensity.

To be consistent from sample to sample, the same sample holder was used for diffraction pattern collection. S4-2 and its reference analog samples were collected on the JD-2000 from 15-65° with a 3 s dwell time and 0.05° per step. The same parameters were used for S5-1 and its relevant standards except the D-5000 was used for measurements with anti-scatter and divergent slit angles of 1° and a receiving slit of 0.10 mm. Figure 5.2 shows diffraction patterns and micrographs of samples of S5-2 collected at various times during the synthesis. Similar to the results in Chapter 4, the use of both SEM and XRD confirm the final product does not contain many shell-only particles and that the core and shell compositions were in agreement with the targets.

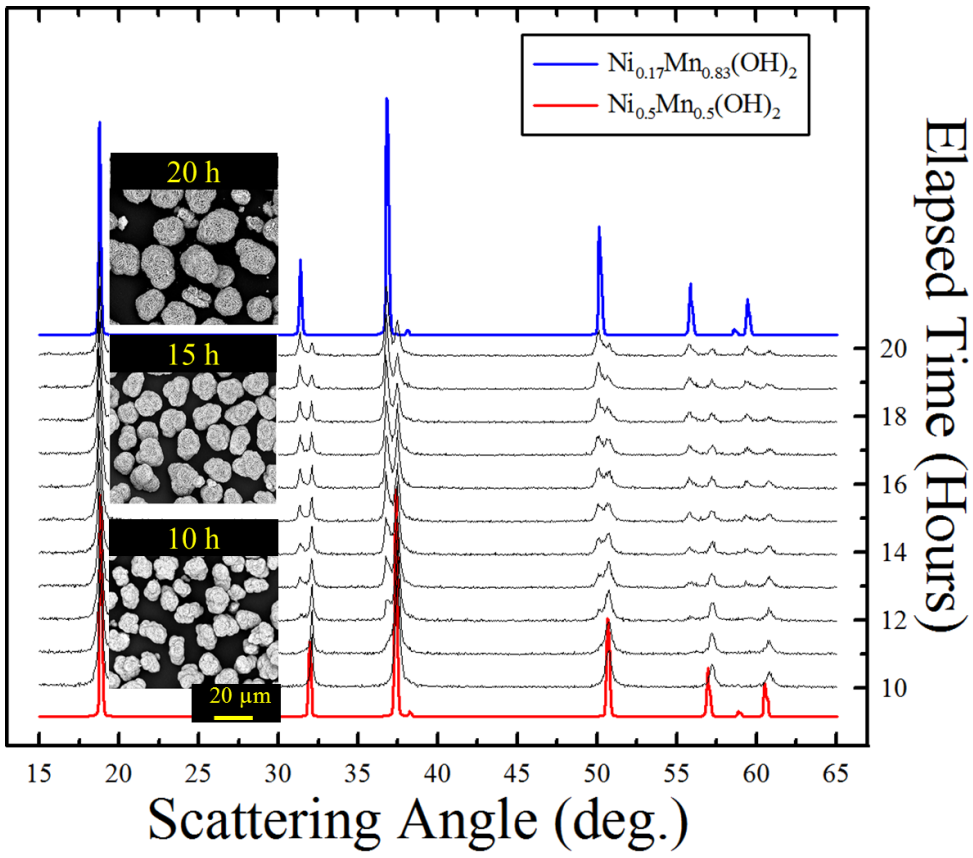

Figure 5.2 SEM Micrographs and diffraction patterns of samples collected during the synthesis of S5-1. Reproduced from the Journal of the Electrochemical Society, open-source article.[140]

The micrographs in Figure 5.2 showed that the shell coating was quite porous, an inherent trait of manganese-rich compositions. Examining the diffraction patterns of the sample from 18 hours or longer, the peak area of diffraction peaks related to the shell composition are more intense than those of the core. The decrease in intensity of the core peaks was due not only to absorbance but also due to the reduced mass fraction of core crystallites in the core-shell product.

5.2 Accounting for Absorption in Diffraction Patterns

Figure 5.3 shows the (012) diffraction peaks of the 20 h products (core-shell) of S4-2 and S5-1 along with the core only (10 or 16 h) and a mixed reference sample made by mixing powders of single phase core and shell in the targeted weight ratio. The vertical axis in both panels is intensity, in counts. When the scan of S5-1 was collected on the D-5000, the X-ray tube and detector were nearing the end of their useful service life and thus the counts are considerably less than the S4-2 series from the JD-2000. The signal to noise ratio, $I_{max}/I_{background}$, of the smallest Bragg peak was 10 for S5-1 and 7 for S4-2.

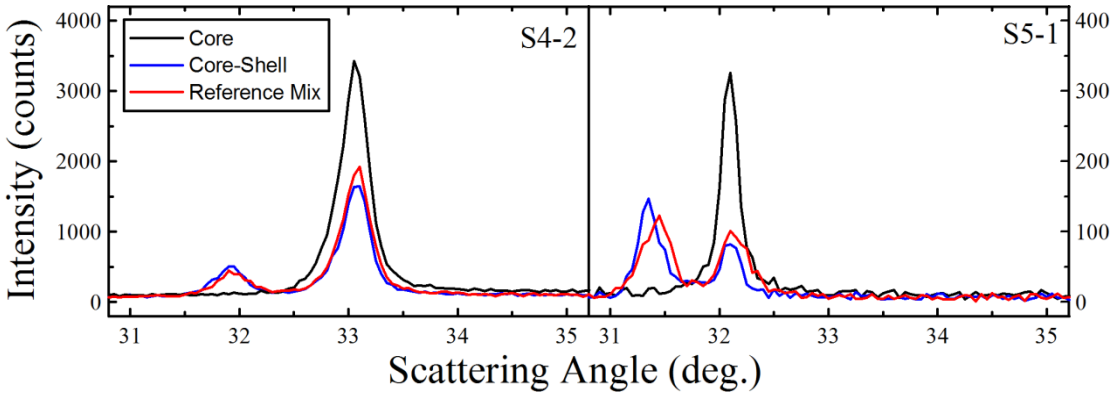

Figure 5.3 (012) Diffraction peaks of core, core-shell samples S4-2 and S5-1 and reference mix. Reference mix was made by blending in the target mass ratio single-phase samples of the target core and shell composition. S4-2 collected using the JD-2000 and S5-1 collected using the D-5000. Reproduced from the Journal of the Electrochemical Society, open-source article.[140]

Comparing the red reference mix and blue core-shell diffraction peaks in S4-2 (Figure 5.3), the breadth of the peaks for both core and shell are nearly identical in the reference mix and core-shell sample; however the integrated intensities of the core peaks were visibly less. For the (012) peaks of the shell composition, the areas were virtually the same in the reference mix and core-shell sample. Reduced integrated intensity was

similarly observed for S5-1, but there was a clear shift in peak position which was due to slight differences in the reference material compositions compared to the core-shell.

To quantify absorption it was necessary to accurately determine the peak area, which can only be accomplished if the core and shell peaks were well separated. Figure 4.4 showed a $Ni(OH)_2$ diffraction pattern with the peaks indexed. All of the peaks labeled in Figure 4.4 except the (001) and (002) peaks were used for absorption modeling. To quantify the integrated peak intensity, Fityk 0.9.8 was used to perform a least squares fitting to determine peak areas.[145] The background was fit with a 6^{th} order polynomial and a pseudoVogitA peak shape was used to fit each Bragg peak. Integrated peak areas could also be found using Rietica, after performing a Rietveld refinement. The Rietveld refinement results were not used because in the Rietveld refinement model, the peak shapes of all the peaks are constrained to a common set of parameters. Fityk allowed each peak shape to be independent. This allows for a more accurate integration of the peak areas than Rietica provided. The Rietveld algorithm used did not model aberrations such as axial divergence or stacking faults which would result in an error in the integrated peak intensity. The integrated intensities of the shell phase diffraction peaks were not used in the model.

5.3 Simple Slab Model of X-ray Absorption in Powder Diffraction

The first model used to quantify the absorption due to the shell coating was a simple slab model. In Figure 5.4 an X-ray beam enters the sample, simplified to an infinitely thick substrate of core below a layer of shell. In this model, diffraction from the core was assumed to occur close to the core-shell interface, so core dimensions and absorption were

ignored. The right panel of Figure 5.4 shows a simplified model of diffraction in the mixed reference sample. In the middle panel of Figure 5.4, the X-ray beam does not have to penetrate the shell to reach the core and diffract. The core-shell model assumes the X-ray path before it enters the particle and exits back out was the same for the core-shell sample and reference material. The transmission ratio of core to the reference mix was used to solve for the absorption length which can be converted to a linear shell thickness using trigonometry.

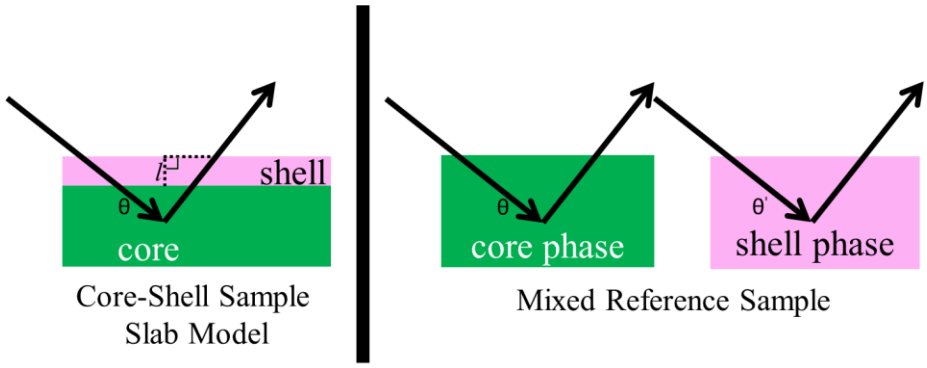

Figure 5.4 Left. Schematic drawing of diffraction from the core in a core-shell modeled as a slab. Right. Schematic of diffraction from a mixed reference sample. Volume ratio of core to shell in both panels not drawn to scale.

The shell thickness (*l*) was obtained using,

$$l = -\frac{\sin\theta}{2}\frac{\ln\frac{I_{cs}}{I_{ref}}}{\sum \mu/\rho} \qquad (5.1)$$

θ is half the scattering angle of a Bragg peak with integrated intensity I_{cs}, in the core-shell sample and I_{ref} in the reference mix. Composition of the shell phase and crystallographic density were used to determine the shell linear absorption coefficient, Σ(μ/ρ). Table 5.1 list the mass absorption coefficients of Cu-Kα X-rays of the elements of interest in this thesis.

Table 5.1 Mass absorption coefficients for Cu-Kα X-rays.[108]

Element	μ/ρ (cm^2/g)
Hydrogen	0.39
Oxygen	11.03
Manganese	272.50
Nickel	48.83
Cobalt	338.6
Lithium	0.4770

Equation 5.1 was applied to all resolvable diffraction peaks. Table 5.2 shows the fitting results for S4-2 using the mixed reference sample as the reference integrated peak intensity. The average thickness calculated using 5 peaks was 0.55(20) μm. For this model, as the scattering angle increased, the calculated shell thickness also increased which may be an artifact of the simplicity of this model.

Table 5.2 Slab model shell thickness calculations for S4-2.

Bragg Peak	Scattering Angle I_{max} (° 2θ)	I/I_{ref}	l (μm)
(010)	33.1	0.85	0.45
(011)	38.5	0.86	0.49
(012)	52.0	0.91	0.41
(110)	59.0	0.90	0.51
(003)	62.7	0.84	0.89
			0.55(20)

The calculated shell thickness of 0.55 μm did not disagree with the EDS results shown in Figure 4.5, but the large standard deviation suggested that a more precise model should be investigated. This model was thought too simplistic as it fails to account for absorption from the powder matrix or the core of the particle. It also required the mixed reference sample, which was tedious to make.

5.4 Spherical Model of X-ray Absorption in Powder Diffraction

Through discussion with Eric McCalla, a new model was proposed treating the sample as series of layers of spherical core-shell particles in a matrix, "jelly", of the average composition, a better representation of the diffraction experiments. Figure 5.4 shows a schematic of the spherical model with various points along the incident and diffracted beam path given letter labels. The absorption length of the shell was from B to C and E to F, absorption due to the matrix occurred from A to B and F to G. Particles were assumed to have a face centred cubic packing density of 74%. The core was also responsible for absorption which is the path from C to E.

The spherical model was a much closer approximation to the actual experimental conditions than the slab model. Since a term for absorption due to the sample matrix was now included in the model, the core only sample could be used as a reference material instead of the mixed reference material used in the slab model. Using the core-only as the reference was far simpler since it was already necessary to sample the core for SEM and XRD to verify coating and composition.

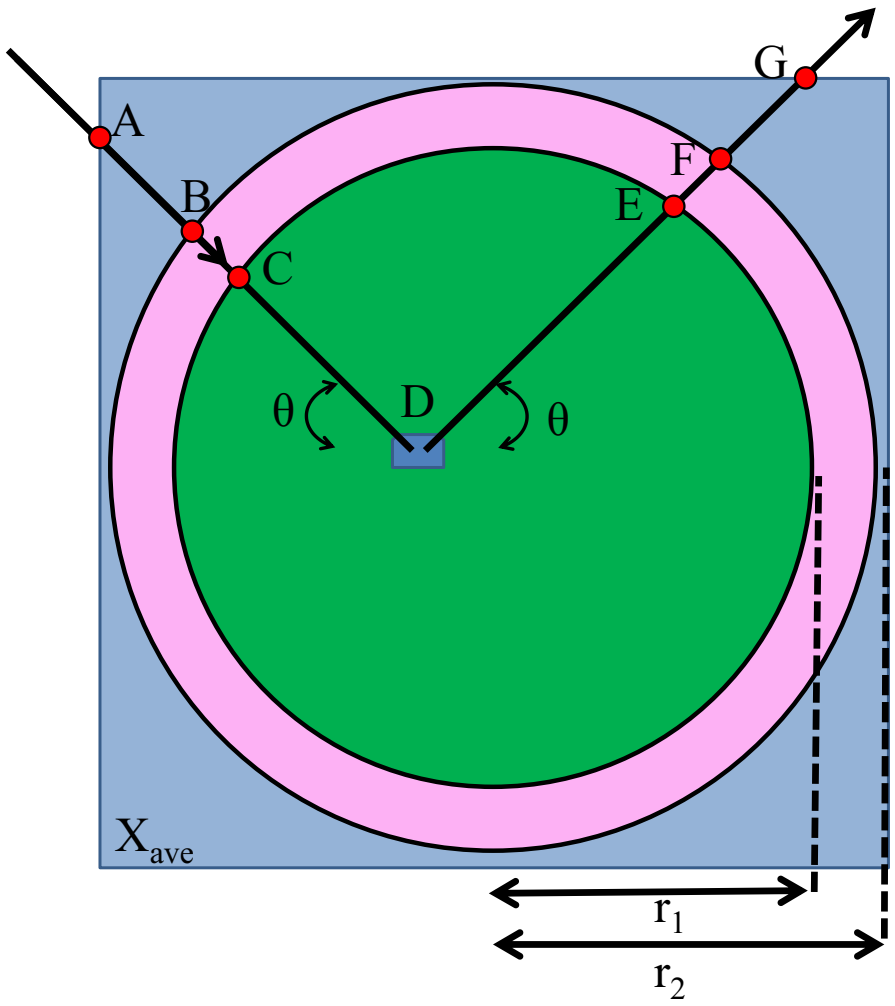

Figure 5.5 Schematic drawing of the spherical absorption model used to estimate the thickness of the shell (r_2-r_1). Calculation determined the transmission of diffracted X-rays from crystallite, D along the path A to G. θ is half of the scattering angle. Reproduced from the Journal of the Electrochemical Society, open-source article.[118]

The fraction of transmitted X-rays, T(r, θ) scattering from element D is

$$T(r,\theta) = e^{-\int\left(\frac{\mu}{\rho}\right)\rho dl} \tag{5.2}$$

where r is a vector from the particle centre to point D in Figure 5.5, θ is half the scattering angle, and l is the X-ray path from A to G. The integral in Equation 5.2 can be broken down into the different components along the path, A to G:

$$\int \left(\frac{\mu}{\rho}\right)\rho dl = \left[\left(\frac{\mu}{\rho}\right)_{Ni} \cdot \rho_{Ni,1} + \left(\frac{\mu}{\rho}\right)_{Mn} \cdot \rho_{Mn,1} + \left(\frac{\mu}{\rho}\right)_{O} \cdot \rho_{O,1}\right](d_{CD} + d_{DE}) + \left[\left(\frac{\mu}{\rho}\right)_{Ni} \cdot \rho_{Ni,2} + \left(\frac{\mu}{\rho}\right)_{Mn} \cdot \rho_{Mn,2} + \left(\frac{\mu}{\rho}\right)_{O} \cdot \rho_{O,2}\right](d_{BC} + d_{EF}) + \left[\left(\frac{\mu}{\rho}\right)_{Ni} \cdot \rho_{Ni,ave} + \left(\frac{\mu}{\rho}\right)_{Mn} \cdot \rho_{Mn,ave} + \left(\frac{\mu}{\rho}\right)_{O} \cdot \rho_{O,ave}\right](d_{AB} + d_{FG}) \quad (5.3)$$

The first row of Equation 5.3 is the absorption length from C-D and D-E, the core. (μ/ρ) values for each element were shown in Table 5.1 and the density of each element in that phase, ρ, was determined using the target composition and the crystallographic density. The second row is similar to the first accounting for the absorption lengths B-C and E-F, the shell. The last row is the sample average composition, the matrix, which accounts for absorption from A-B and F-G. Hydrogen was not included as an absorbing species since its absorption length was negligible. Integrating over the entire core volume (V),

$$T = 1/V \int T(r,\theta)dV \quad (5.4)$$

the fraction of X-rays transmitted, (T), can be determined.

Equation 5.4 was repeated to sum over multiple monolayers of particles in the matrix with each successively lower layer including absorption from all layers above it, convergence of transmission was observed at 10 monolayers. The Yorick calculator developed for this calculation required the particle radius, shell thickness, scattering angles, core composition, shell composition and matrix average composition to begin, the output was the integrated intensity ratio of the core-shell diffraction peak to a reference material, either the mixed reference ($I/I_{mixed\text{-}ref}$) or core sample ($I/I_{core\text{-}ref}$). The particle radius was selected to match the radii of the cross-sectioned particles from EDS analysis. If the integrated intensity ratios outputted by the calculator differed from the observed, the

calculation was repeated, adjusting the shell thickness. The results of the spherical model for S4-2 are shown in Table 5.3. Table 5.3 shows the calculated shell thickness using both the core ($l_{core\text{-}ref}$) and mixed reference material ($l_{mixed\text{-}\mathrm{ref}}$) as the reference integrated intensity.

Table 5.3 Spherical model shell thickness calculations for S4-2, 5.5 μm radius.

Bragg Peak	Scattering Angle I_{max} (° 2θ)	$I/I_{mixed\text{-}ref}$	$l_{mixed\text{-}ref}$ (μm)	$I/I_{core\text{-}ref}$	$l_{core\text{-}ref}$ (μm)
010	33.1	0.85	0.46	0.49	0.45
011	38.5	0.86	0.46	0.49	0.47
012	52.0	0.91	0.42	0.46	0.55
110	59.0	0.90	0.43	0.49	0.52
003	62.7	0.84	0.49	0.49	0.52
			0.45(3)		0.50(4)

The results in Table 5.3 are within a standard deviation of the value reported using the slab model and angular dependence is no longer evident. There was only a small difference in the shell thickness using the core or mixed material as the reference intensity, suggesting both are excellent references.

The spherical model was also applied to sample S5-1. In S5-1, the shell was thicker and contains more manganese so more attenuation was expected. The results of modeling S5-1 are shown in Table 5.4 using both the mixed reference material and core as reference intensities. A particle with a radius of 7.9 μm was modeled which was selected to match the longer radii of the ellipsoidal shaped particle measured with EDS.

Table 5.4 Spherical model shell thickness calculations for S5-1, 7.9 μm radius.

Bragg Peak	Scattering Angle I_{max} (° 2θ)	$I/I_{mixed\text{-}ref}$	$l_{mixed\text{-}ref}$ (μm)	$I/I_{core\text{-}ref}$	$l_{core\text{-}ref}$ (μm)
010	32.1	0.72	1.66	0.33	1.57
011	37.5	0.72	1.74	0.36	1.52
012	50.9	0.72	1.84	0.33	1.75
110	57.3	0.73	1.85	0.36	1.65
003	59.7	0.65	2.04	0.28	2.05
			1.83(14)		1.71(21)

As expected, the shell for S5-1 was thicker than S4-2. The shell thickness determined using the two different reference materials were again within their standard deviations. Figure 5.6 shows a S5-1 particle cross-sectioned and the composition measured with EDS with a vertical dashed line showing the shell thickness from the spherical model and horizontal solid guidelines showing the target core and shell composition. The shell thickness determined with the spherical model was in agreement with the EDS measurements. The data point collected at 2.5 μm from the edge starts to show the sloping region, due to the end of the shell. Closer to the edge from this spot the composition was close to the targeted $Ni_{0.17}Mn_{0.83}(OH)_2$ shell. The cross-sectioned particle micrograph shows that the shell primary particles had a preferred orientation. The needle-like primary particles are orientated in such a manner that provides minimal area coverage. Ideally the thin primary particles would be orientated in a manner that provides a higher areal coverage.

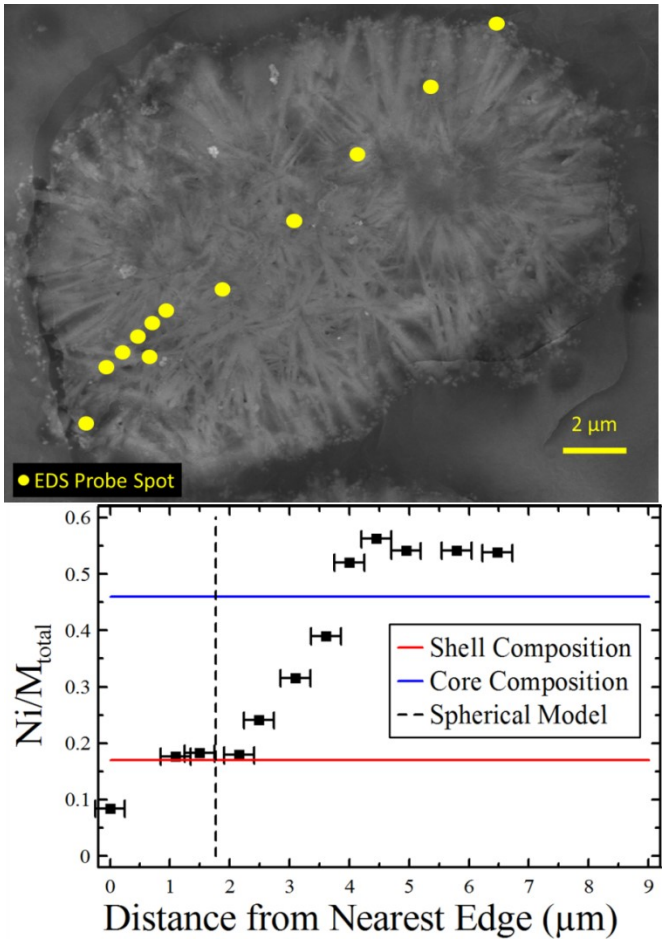

Figure 5.6 (Top). SEM micrograph of cross-sectioned particle of S5-1 final product. Yellow circles show where composition was probed with EDS. (Bottom). Atomic ratio of Ni to total metal versus linear distance from nearest edge of probed spot in top panel. Vertical guideline shows calculated shell thickness using spherical model and horizontal lines show target core and shell composition. Horizontal error bars show approximate electron beam interaction volume. Reproduced from the Journal of the Electrochemical Society, open-source article.[118]

5.5 Shell Thickness Estimate from ICP-OES Data

As an alternative to estimating the shell thickness using absorption modeling, the shell thickness can be estimated knowing the core and shell composition and the overall particle composition. ICP-OES was used to determine the bulk metallic composition of S4-2 and S5-1. The mass fraction of core (a) was determined using,

$$X_{Ni,overall} = a\left(X_{Ni,core}\right) + (1-a)\left(X_{Ni,shell}\right) \tag{5.5}$$

$X_{Ni,overall}$ was the ICP-OES reported metallic composition and $X_{Ni,core}$ and $X_{Ni,shell}$ the target compositions for the core and shell in S4-2 and S5-1. For sample S4-2, a = 0.72 and for sample S5-1, a = 0.30. The relative volume of the core and shell phases based on the value of a and crystallographic density are,

$$V_{core} = {}^{a}/_{\rho_{core}} \qquad V_{shell} = {}^{(1-a)}/_{\rho_{shell}}\,. \tag{5.6}$$

Equation 5.6 can be combined with the volume of a sphere and hollow sphere to determine the core radius, r_1, of a particle with overall radius r_2:

$$\frac{V_{core}}{V_{Shell}} = \frac{{}^{4}/_{3}\pi {r_1}^3}{{}^{4}/_{3}\pi {r_2}^3 - {}^{4}/_{3}\pi {r_1}^3} = \frac{a\cdot\rho_{shell}}{(1-a)\rho_{core}}\,. \tag{5.7}$$

Equation 5.7 simplifies to:

$$r_1 = r_2 \sqrt[3]{\frac{b}{1+b}} \quad with\ b = \frac{a\cdot\rho_{shell}}{(1-a)\rho_{core}} \tag{5.8}$$

which was used to determine the shell thickness l,

$$l = r_2 - r_1. \tag{5.9}$$

Figure 5.7 shows the shell thickness as a function of particle radius determined using the calculation above for S4-2 and S5-1. Vertical dashed lines in Figure 5.7 show the radius of the particles cross-sectioned with EDS in Figures 5.6 and 4.5.

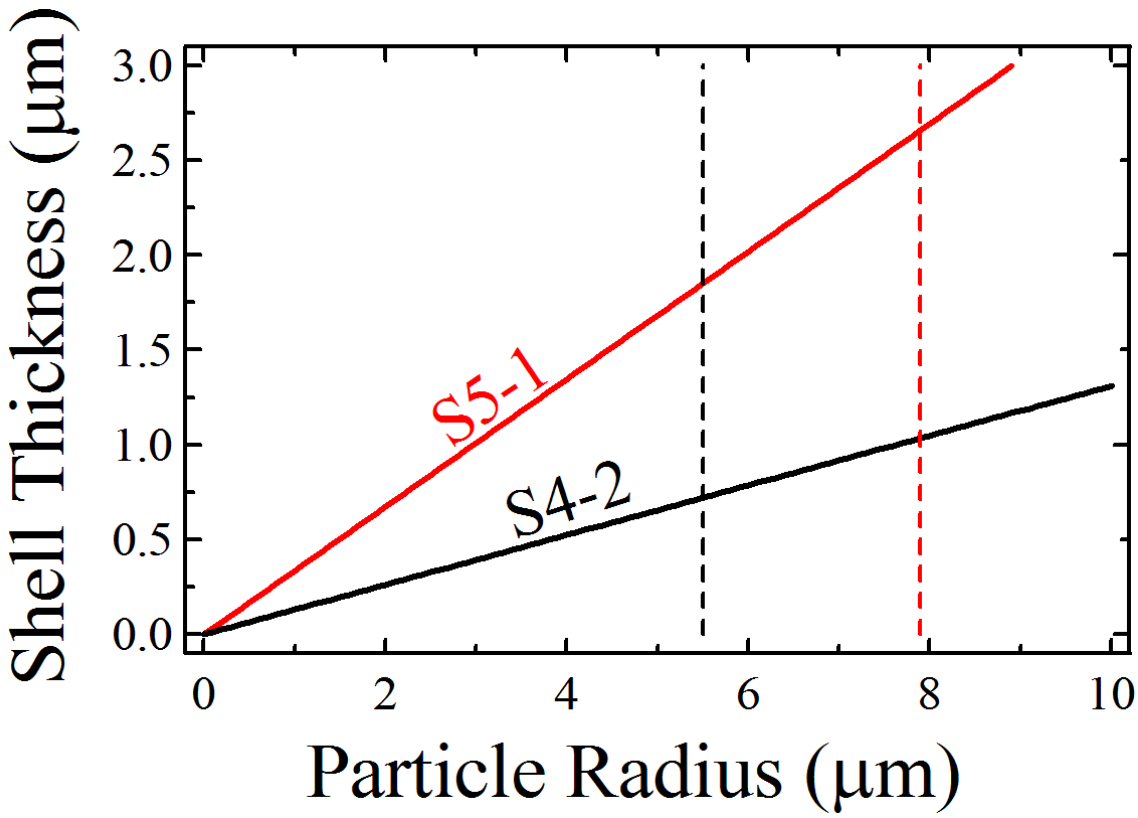

Figure 5.7 Shell thickness estimations for S5-1 and S4-2 determined from ICP-OES bulk composition.

For a 5.5 μm particle from S4-2, the thickness estimation using ICP-OES was 0.72 μm, slightly larger than the spherical absorption model, 0.47 μm. For a 7.9 μm particle of S5-1, the growth model predicted a shell thickness of 2.66 μm, significantly larger than the spherical model 1.78 μm and EDS 2.2 μm. The discrepancy in S5-1 was most likely due to the error in the target core and shell phases composition. The calculated line in Figure 5.7 used the target compositions instead of the actual composition. Since it was known the core and shell were manganese-rich compared to the target composition from the diffraction patterns, there would be an error in the value of *a* in Equation 5.5 resulting in a thicker shell than the actual. The micrographs of S5-1 shown in Figure 5.2 showed some

small shell only particles. The shell only particles are counted as shell coating in the bulk ICP-OES measurement, but they are not accounted for properly in the spherical model or EDS measurements.

The tank reactor was operated with constant volume conditions which resulted in a steady loss of material via the overflow. The loss of material via the overflow resulted in a deviation from the dispensing ratio of core to shell since more core material was lost to the overflow than shell. If S4-2 and S5-1 were exactly their dispensing ratio and target composition, *a* in Equation 5.5 would have been 0.8 and 0.5 for S4-2 and S5-1, larger than the experimental values meaning the samples were shell-rich compared to the dispensing ratio.

Figure 5.7 assumes that particles simply grow forever; this is an oversimplification of what really occurs in the tank reactor. There is a critical diameter at which new particles formation will be favored. Many people have studied particle growth in precipitation reactions with very sophisticated models.[146,147] The ICP-OES shell thickness estimation was a decent estimate of the shell thickness. It may be a useful technique for other compositions which do not produce such beautiful diffraction data.

5.6 Chapter 5 Conclusions

In this chapter the shell thickness was estimated for two different core-shell hydroxide samples that varied in composition and shell thickness. The spherical absorption model agreed well with the EDS results and ICP-OES bulks sampling. The spherical model using the sampled core as the reference material is experimentally simple to use. It also

requires no additional data collection as Chapter 4 showed the necessity of collecting diffraction patterns and micrographs of the core only and coated shell product. If the freeze drying step could be avoided or accelerated, the model could be used *ex-situ* during precipitation so the shell precipitation could continue until the desired thickness was achieved. This model may also be of use to others in material science looking at similar bilayer composite samples.[148] The range of coating thicknesses that could be examined could be increased by using a synchrotron to increase or decrease attenuation by changing X-ray energy.

While scientifically the spherical shell thickness model was interesting, in practice it is not extensively useful for lithium-ion battery positive electrode materials. The optimal thickness will vary with the shell composition since the porosity and primary particle morphology are composition and tank reactor condition dependent. The model reports on the shell thickness for a given particle radius, in reality, the particles are of a distribution of sizes that will have a variable shell thickness. Small particles should have a larger shell radius than large particles. In a real sample, with a distribution of particle sizes, large particles with incomplete shell coatings may exist. In a numerical distribution, these large particles are a small fraction, but volumetrically, and gravimetrically, they can be a significant portion of the sample. These poorly coated particles should have poorer lifetime performance than the smaller thicker coated particles.

The optimized thickness is not just a simple number, but rather needs to consider factors like porosity and size distribution. In reality the optimized shell thickness is not simple to predict, but can be determined from experimental electrochemical results from a UHPC. Examining the charge endpoint capacity slippage for various shell thicknesses with

the same core and shell composition would show at which thickness the shell fails to provide any additional lifetime benefits.

Chapter 6. Lithiation and Sintering of Core-Shell Materials

6.1 Experimental Design for Sintering with Lithium Carbonate

Samples S4-6 and S4-7 were used as precursors for the synthesis of positive electrode materials for lithium-ion batteries. The core and shell compositions in S4-6 and S4-7 are the same, the dispensing time ratio for the core to shell was 2:1 in S4-6 and 4:1 in S4-7. Samples were "lithiated" by blending the precursors with the target amount of lithium carbonate, followed by sintering at high temperature. The structural and electrochemical analysis of these samples was incorporated in a manuscript published in the Journal of the Electrochemical Society.[140]

In another study of $Li_{(1+x)}[Ni_yMn_{(1-y)}]_{(1-x)}O_2$ $0 \leq y \leq 1$, $-0.2 \leq x \leq 1$ materials with Jing Li, it was shown that the value of x where the maximum capacity was achieved depended on the value of y.[81] When the samples were nickel-rich, $y \geq 0.5$, cation disordering was the major limitation on capacity, so the value of x must be large enough to minimize cation disorder.[81] When samples were manganese-rich, $y < 0.5$, the value of x should be just large enough that the sample was in the layered single phase region shown in Figure 2.1. Adding additional lithium, increasing x, resulted in oxidation of nickel. A higher average oxidation state of nickel in the starting material reduced the amount of nickel that can be oxidized during lithium extraction, thus reducing capacity.

For S4-6 and S4-7, the core was nickel-rich and the shell manganese-rich. Chapter 3 showed that for lifetime considerations, lithium content and vacancies may be important. For the core, the selected lithium content should maximize capacity; for the shell, the lithium content should be optimized for the smallest charge endpoint capacity slippage.

Since the core-shell structure was developed during the precursor process, the core and shell phases are physically inseparable after this step. Any processing or reagents added to the particles after the core-shell is formed will happen simultaneous to both the core and shell phases. For example, one cannot add n moles of lithium to the core phase and m moles of lithium to the shell phase; instead x moles of lithium are added to the core-shell sample. Thermodynamics and kinetics will determine the distribution of x moles of lithium into the core and shell phases. To better understand how lithium uptake occurs in the two phases, several different lithium contents were examined using S4-6 and S4-7 as the precursors. Table 6.1 shows sample targeted overall composition, precursor used and the sample labels for the materials studied.

Table 6.1 Target composition of lithiated samples from S4-6 and S4-7.

Sample	Precursor	Li	Ni	Mn
S6-46A		0.42	0.28	0.30
S6-46B		0.53	0.23	0.27
S6-46C		0.54	0.22	0.24
S6-46D	S4-6	0.56	0.21	0.23
S6-46E		0.58	0.20	0.22
S6-46F		0.60	0.19	0.21
S6-46G		0.61	0.18	0.21
S6-47A		0.41	0.31	0.28
S6-47B		0.52	0.26	0.22
S6-47C		0.53	0.25	0.22
S6-47D	S4-7	0.55	0.24	0.21
S6-47E		0.57	0.23	0.20
S6-47F		0.59	0.22	0.19
S6-47G		0.61	0.21	0.18

The target compositions in Table 6.1 were selected to span the length of the single phase region for the core and shell; see Figure 2.1. Samples S6-46A and S6-47A were

purposely made to be lithium deficient for both the core and shell to be single phases. Samples S6-46G and S6-47G were also synthesized with lithium beyond the lower single phase boundary. All samples were prepared by mixing the precursor with lithium carbonate as described in Chapter 2. The heating time was 10 h at which time the oven was cooled to room temperature at a programmed rate 20 °C/min. Figure 6.1 shows the layered region of the structure-composition diagram shown in Figure 2.1. Black-dashed lines in Figure 6.1 tie the lithium corner to the precursor's core and shell phase transition-metal compositions on the Ni-Mn edge of the diagram.

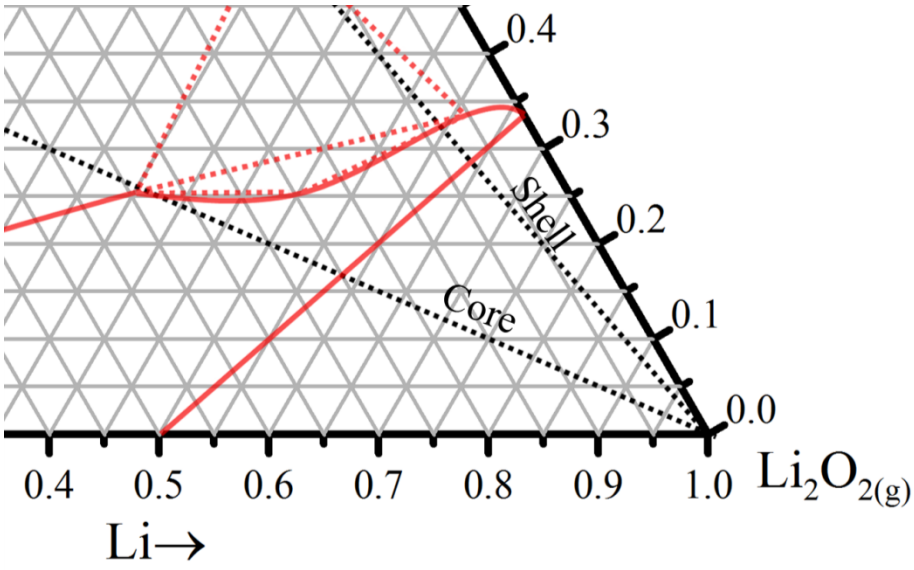

Figure 6.1 Section of the structure-composition diagram shown in Figure 2.1. Black-dashed lines connecting the lithium corner to the precursor's core and shell target transition metal compositions on the Ni-Mn edge.

The goal of lithiation and sintering was to synthesize a material with both the core and shell phases on their respective dashed lines and in-between the red solid lines in Figure 6.1, the single-phase layered region. Beyond being in the single-phase region, it would be preferred if both the core and shell were at their optimized lithium concentration. It is also

desired that the volume changes that occur in the core and shell during the phase change (Equation 2.3) are small enough that particles do not break apart.

Diffusion should also be considered with core-shell materials. It is desired that decomposed, liquid lithium carbonate will diffuse quickly at 900°C, allowing the lithium transition metal oxide to form in both the core and shell. At the same time, transition metal diffusion between the core and shell phases should be extremely slow. Diffusion of transition metals was studied by subjecting samples of the same composition, S6-46F, to various temperatures and dwell times, and then mapping the composition with EDS.

6.2 SEM and EDS Results of Lithiation and Sintering of S4-6 and S5-7

Figure 6.2 shows the SEM micrographs of the recovered powders S6-46A to S6-46G with a higher magnification of S6-46A shown in the bottom left micrograph. The particles for S6-46B to S6-46F look extremely similar. For sample S6-46A the primary particles appear to be more crystalline. These large crystallites may be due to spinel which forms large crystallites at temperatures above 800°C.[149]

In the micrograph of S6-46G, black spots appear on the particles, such as the one circled in red. The black spots were attributed to lithium carbonate. The intensity of backscattered electrons increases with the electron density of the sample, thus lithium carbonate appeared darker compared to the lithium transition metal oxide. The product for S6-46G was very hard compared to the other products which would break up upon shaking the alumina heating vessel. The hardness was due to unreacted lithium carbonate freezing during cooling, effectively gluing secondary particles together. The micrographs

of S6-46A to S6-46G do not show damage to the core-shell structure such as separated particles, suggesting that volume expansion during sintering with Li_2CO_3 was not destroying the core-shell structure.

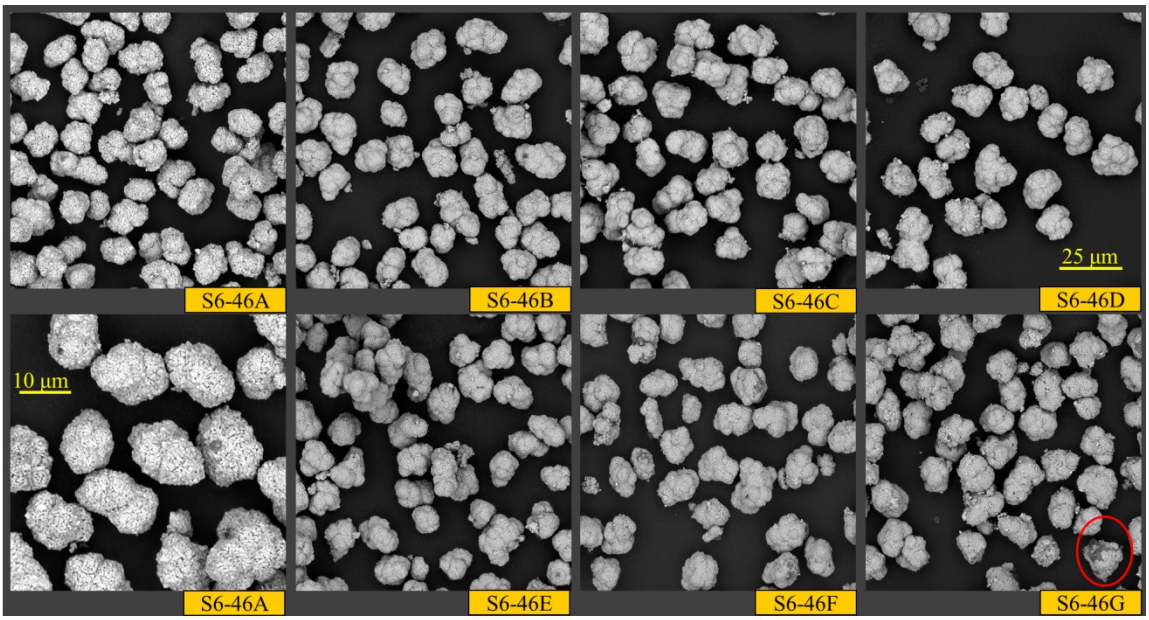

Figure 6.2 SEM micrographs of powders recovered from S6-46A to S6-46G. Bottom-left micrograph of S6-46A was captured at a higher magnification. Red circle in bottom right micrograph indicates presence of lithium residue on a particle.

Figure 6.3 shows SEM micrographs of selected samples from the series S6-47. Similar to S6-46A, S6-47A showed spinel present such as the large octahedra in the bottom-left micrograph of Figure 6.3. Upon increasing the lithium fraction by 0.11 in sample S7-47B, the large octahedra of spinel were no longer observed. Similar to S6-46G, S6-47G showed many dark spots on the particles thought to be excess lithium carbonate. Sintering of the primary particles was also evident. The impact sintering has on the shell coating needs to be better understood. Sintering should seal small gaps between primary particles, but may form larger voids between the sintered primary particles.

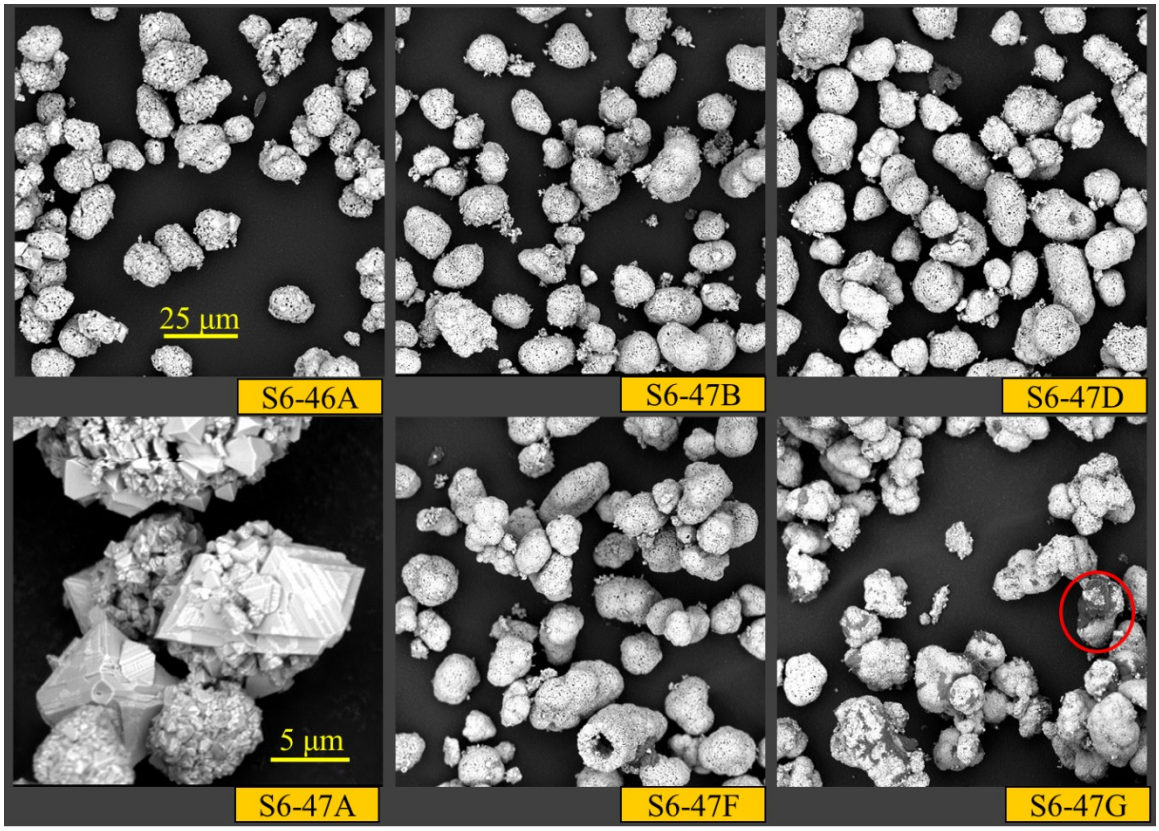

Figure 6.3 SEM micrographs of powders of S6-47A, B, D, F & G. Red circle in bottom right micrograph indicate presence of residual lithium carbonate.

The micrograph of S6-47F shows a large tube-shaped secondary particle with a void in the middle. It was suspected that the core fell out of this particle during synthesis. A morphological change during heating, damaging the core-shell structure, was also evident in another sample. A sample that was the same core and shell composition of S4-7 but with the core and shell reversed, a manganese-rich core and nickel-rich shell, was made. Figure 6.4 shows a cross-sectioned particle from the precursor and the lithiated product for this sample. Similar to that shown in Chapter 4, a clear contrast between the core and shell in nickel and manganese composition was present in both the precursor and

the lithiated product. A void between the core and shell are evident in the false-colour map on the bottom-left of the sintered particle.

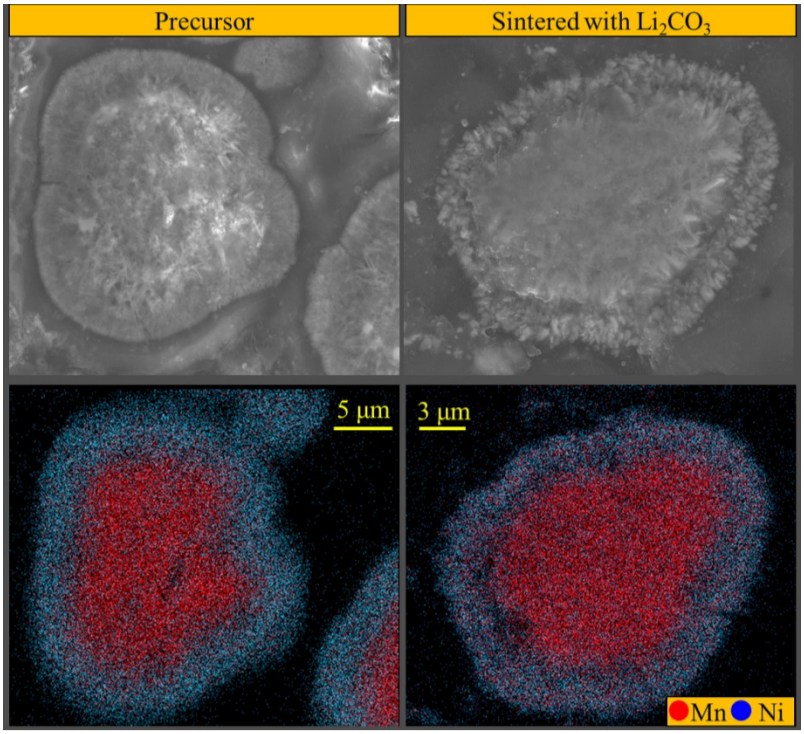

Figure 6.4 SEM and EDS of cross-section precursor and sintered particles; (Ni, Mn) Core 16 h precipitation (0.2, 0.8), Shell 4 h precipitation (0.6, 0.4).

The precursor SEM in Figure 6.4 shows that the shell coating was very dense compared to the core. A clear transition between the core and shell can be seen in the micrograph. After heating the shell appears more crystalline than the core phase. The large crystallites of the shell composition may reduce the contact area between the core and shell. Crystallite size can be reduced by using milder conditions, as is does when it is desired to make spinels.[150]

Figure 6.5 shows the SEM and EDS of S4-6, S4-7, S6-46F and S6-47C. In the SEM micrograph of S6-46F, the core and shell phases can easily be seen. The EDS false-

colour map of S6-46F shows that the diffusion has not resulted in complete mixing of transition metal diffusion as a "red", manganese-rich shell was observed surrounding a blueish-red nickel-rich core.

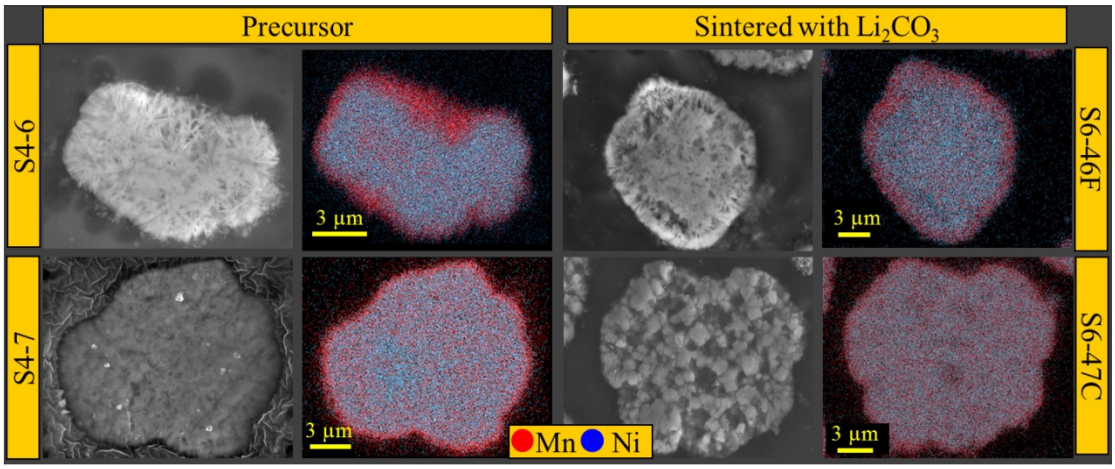

Figure 6.5 Micrographs and false-colour EDS composition map of precursors S4-6 and S4-7 and products made from them, S6-46F and S6-47C.

In the micrograph of sample S6-47C in Figure 6.5, the primary particles are far larger than those in S6-46F. This may be due to the lower lithium content of this sample resulting in the core phase being a disordered rocksalt structure forming large cubic primary particles.[151] The disordered rocksalt structure was supported by diffraction results which showed 12% of the lithium sites were occupied with nickel. Similar to S6-47F, S6-47C also has a clear, manganese-rich shell surrounding the nickel-rich core.

Figure 6.5 showed that the core-shell structure was maintained at 900°C for 10 h. Diffusion of nickel and manganese at this temperature was slow enough that complete mixing of transition metals did not occur. Figure 6.6 shows a "table" of false-colour composition maps for samples synthesized with the same target composition as S6-46F,

with the reaction temperature shown above each column and the dwell time shown next to each row.

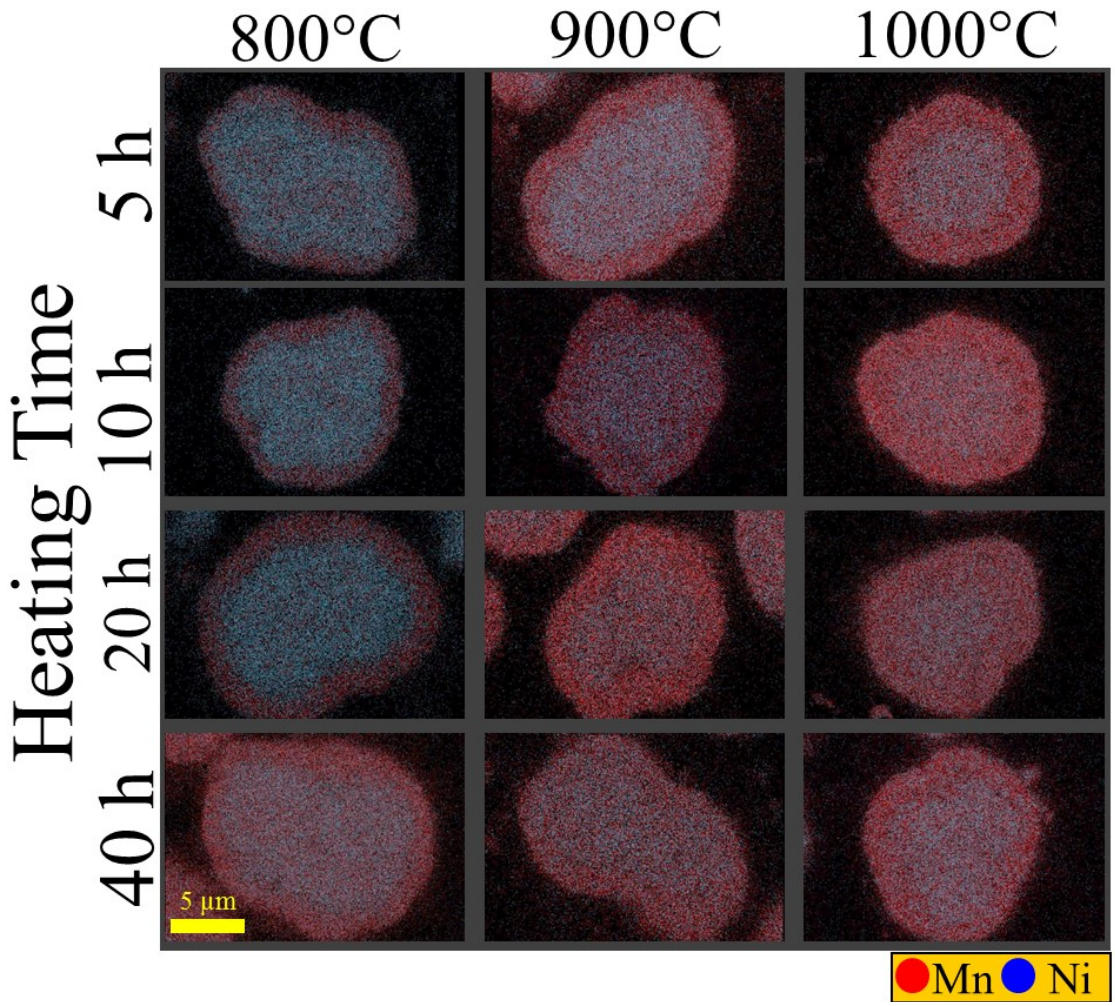

Figure 6.6 EDS false-colour maps of samples of the target composition S6-46F. Temperature above each row shows the dwell temperature, labels left of each column show the dwell time.

In Figure 6.6, the 3 samples heated to 800°C for up to 20 hours have a contrast in composition between the core and shell similar to that observed for their precursor in Figure 6.5. At higher temperatures or longer dwell times there is less contrast between the core and shell, but in all images there was still a bluer core surrounded by a red shell. For

industrial processes temperatures range from 850 to 950°C and heating times are generally less than 10 h.[40] For industrial processing conditions, a core-shell morphology remained.

6.3 X-ray Diffraction of Sintered and Lithiated Products

Section 6.2 showed that the core-shell structure was maintained after sintering. It was thought that the core-shell structure would also be observed in X-ray diffraction experiments as was the case with the precursors shown in Chapter 4. Figure 6.7 shows the diffraction patterns collected for samples derived from S4-7 using the JD-2000 with a dwell time of 3 seconds and a step size of 0.05°. The diffraction patterns in Figure 6.7 appear to show a single set of diffraction peaks in agreement with the expected layered R-3m space group. The peak at 43° in sample S6-47A shows an asymmetry which may be due to spinel impurities, as supported by the micrographs in Figure 6.2.

EDS false-colour mapping showed that these samples had core and shell phases with different transition metal compositions. The diffraction patterns appeared single phase because for the lithiated products the relative difference in lattice constants was much smaller than for the hydroxide precursors. Instrumentation broadening may have made the core and shell phases appear as one set of diffraction peaks. To determine if a second phase could be observed the scanning parameters on the D-5000 diffractometer were optimized using a reference standard material.

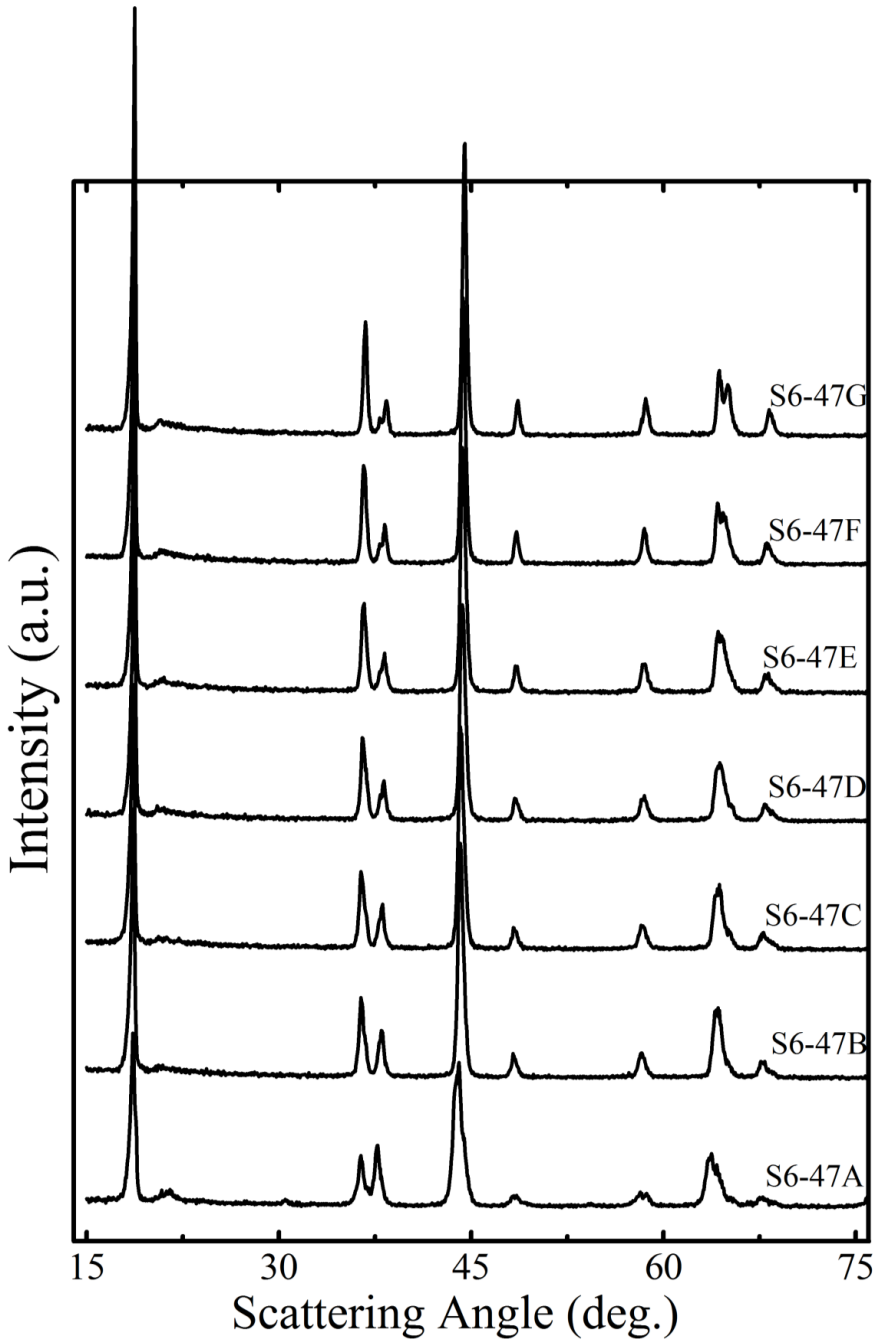

Figure 6.7 X-ray diffraction patterns of samples S6-47A-G made from precursor S4-7. Reproduced from the Journal of the Electrochemical Society, open-source article.[140]

A corundum, Al_2O_3, standard (NIST SRM 1976 Instrument Sensitivity, Alumina Plate) was analyzed on the D-5000 using a variety of divergent, anti-scatter slit and

receiving slit sizes. Figure 6.8 shows the (104) diffraction peak of corundum collected on the D-5000 with a variety of slit settings. Table 6.2 shows the fitting results from Fityk for the peak area, full width at half max (FWHM) for the Cu-Kα_1 (104) diffraction peak.

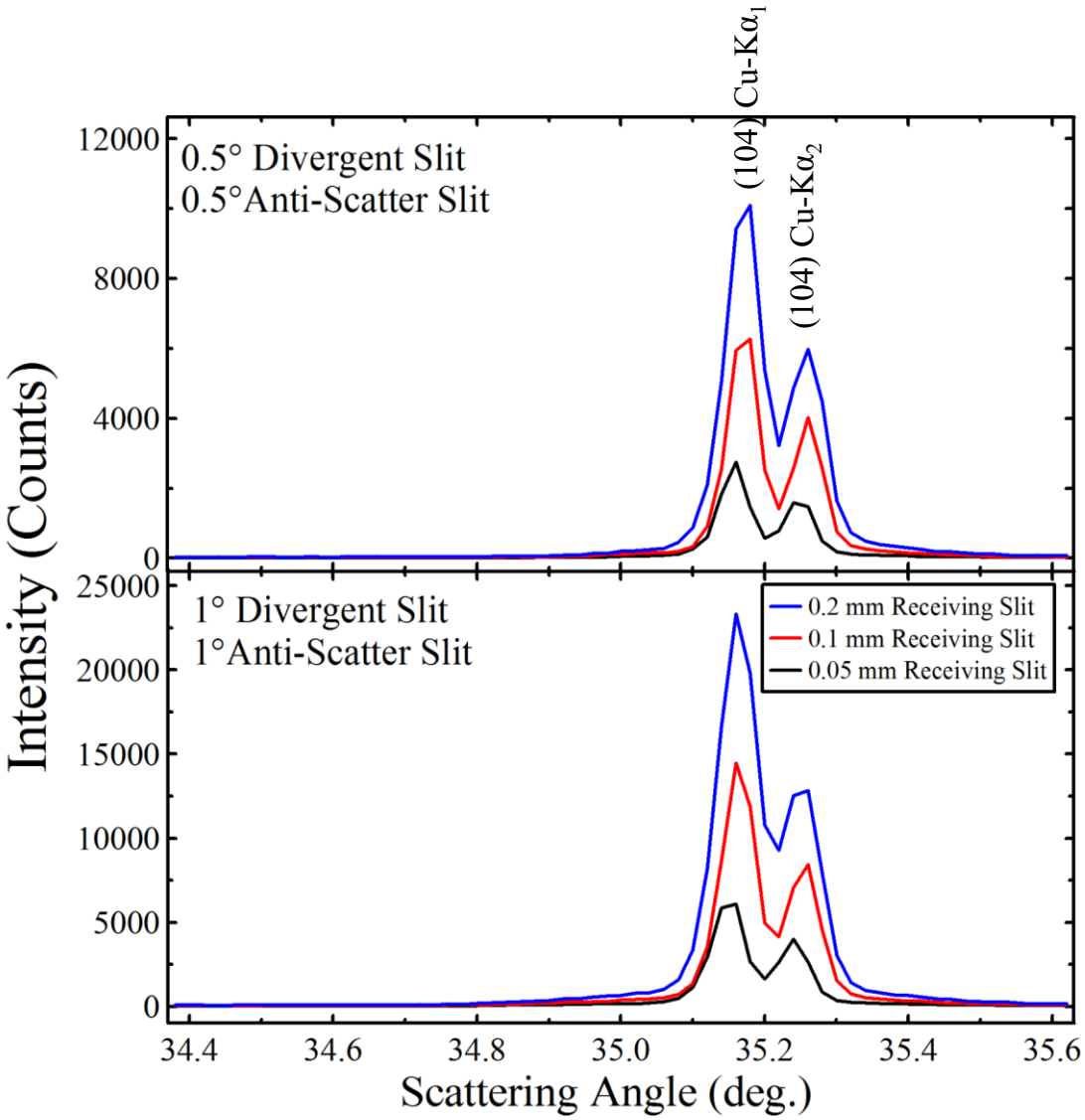

Figure 6.8 Corundum flat plate standard (104) diffraction peak from D-5000 diffractometer with various slit settings, 10 s dwell and 0.02°/step. Vertical scale of top panel is exactly half of the bottom panel.

Table 6.2 Corundum flat plate standard (104)-Cu-Kα_1 peak fittings results.

Divergent & Anti-Scatter Slits (°)	Receiving slit (mm)	Integrated Intensity (°2θ)	FWHM (° 2θ)
1.0	0.05	452	0.0507
1.0	0.1	1030	0.0529
1.0	0.2	1930	0.0637
0.5	0.05	162	0.0446
0.5	0.1	413	0.0469
0.5	0.2	750.	0.0573

Based on the fitting results in Table 6.2, high resolution diffraction patterns of samples in Table 6.1 were collected using divergent and anti-scatter slits of 0.5° and a receiving slit of 0.1 mm. Although the FWHM of the corundum standard was better using the narrower 0.05 mm receiving slit, the improvement was small enough that it was considered a poor trade-off of intensity to resolution. 0.02°/step and 7 second dwell times were used, which resulted in 6 hours of instrument time to collect a diffraction pattern from 15-75°.

Diffraction patterns collected using the optimized parameters resulted in patterns of enough quality to perform Rietveld refinements with a two-phase sample model. Figure 6.9 shows the high resolution diffraction pattern and Rietveld fit for sample S6-47C. The procedure for fitting these patterns was similar to that for precursors. The core composition was fixed as $Li_{1.04}[Ni_{0.6}Mn_{0.4}]_{0.48}O_2$, and the shell as $Li_{1.24}[Ni_{0.6}Mn_{0.4}]_{0.38}O_2$, equal distance from the single phase boundary on the core and shell tie-lines in Figure 6.1. Lattice parameters and background for the two phases were first refined. The lattice parameters were then fixed, and peak shapes were refined for both phases. Lattice parameters and all other parameters were then again allowed to be refined. A 1 for 1 substitution of lithium ions on 1a sites for nickel on 3b was allowed to occur after peak shapes were determined.

All parameters were verified for to be a plausible representation of the sample before the refinement was considered complete. Peak markers in Figure 6.9 are shown for only the Cu-Kα_1 core and shell contribution for clarity, but the Rietveld refinement accounted for both Cu-Kα_1 and Kα_2 contributions.

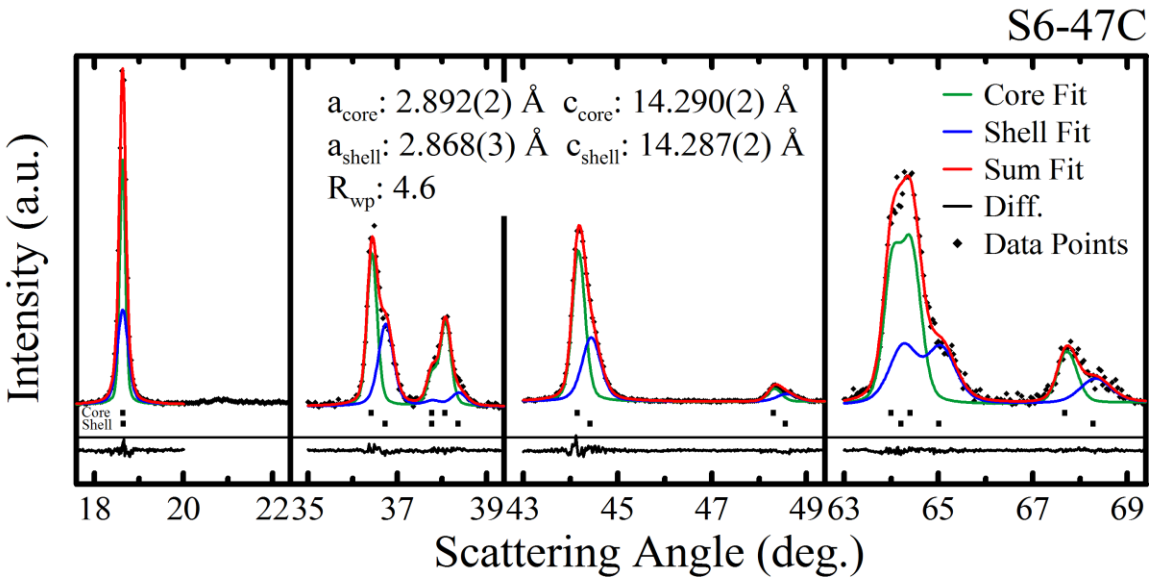

Figure 6.9. Diffraction pattern and Rietveld refinement fit of pattern for S6-47C. Diffraction pattern collected using optimized scanning parameters for D-5000. Reproduced from the Journal of the Electrochemical Society, open-source article.[140]

Examining the (104) peaks at 44° or the (101) peaks at 36°, asymmetry is evident supporting that the sample is indeed two-phase. Most other diffraction peaks are significantly overlapped with other peaks. The absorption model was not attempted on these samples due to the complexity of determining the peak area of individual diffraction peaks due to overlap. The lithium content of the core and shell could not be directly measured making determinations of the linear absorption coefficients for the core and shell phases difficult. Two-phase fits were completed on samples S6-47C to S6-47F. Samples A and B could not be well fit, most likely due to the presence of spinel impurities. Similar

to the series S6-47A-G, diffraction patterns of the series S6-46A to S6-46H were measured originally on the JD-2000 with 3 s dwell times and 0.05°/step and are shown below in Figure 6.10.

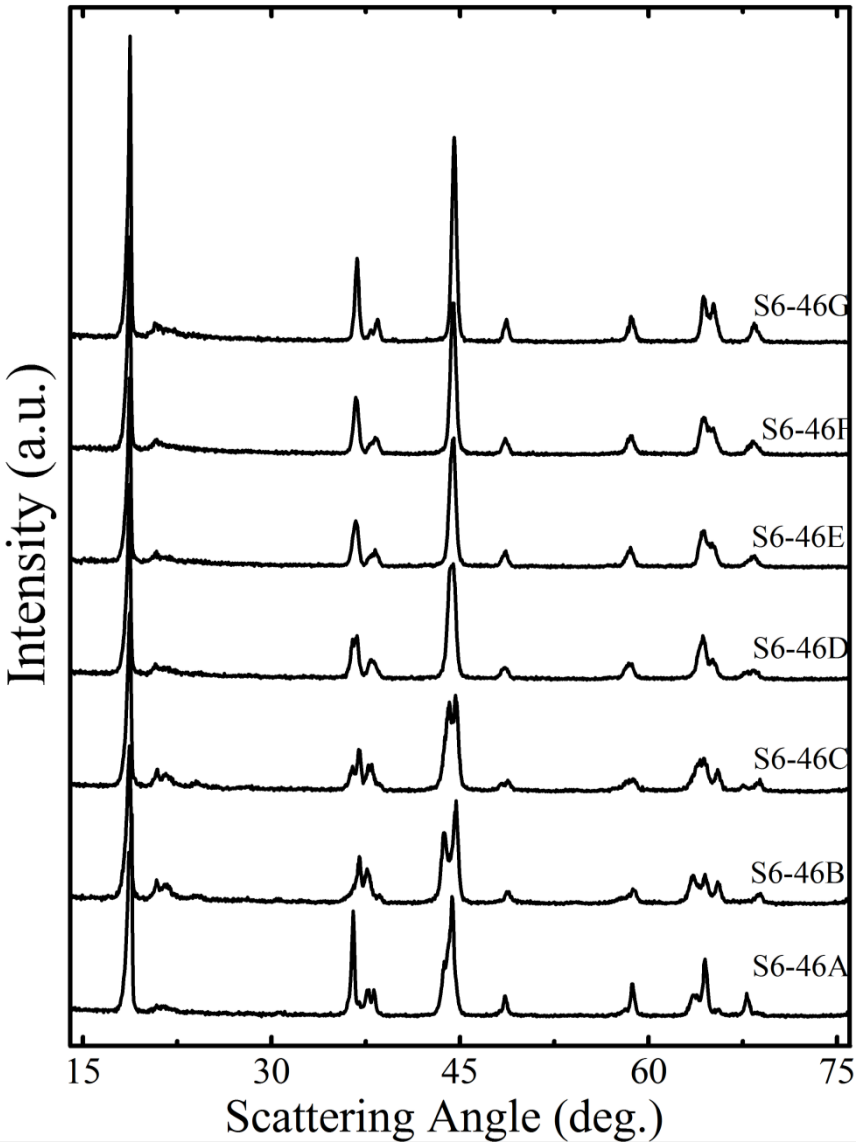

Figure 6.10 X-ray diffraction patterns of samples made from precursors S4-6. Reproduced from the Journal of the Electrochemical Society, open-source article.[140]

The diffraction patterns for S6-46B & C clearly show more than one phase present. For diffraction patterns of samples with more lithium than S6-46C, the splitting of the core

and shell phases (104) peaks in the 43-45° range was less evident and the patterns appear more like single-phase samples, although EDS had confirmed that S6-46F was two-phased. Optimized scanning parameters were used to collect higher resolution diffraction patterns of samples from the series S6-46A to S6-46G. Figure 6.11 shows the Rietveld refinement and high resolution diffraction pattern of S46-E, which in Figure 6.10 was difficult to visually tell if it was one or two phases.

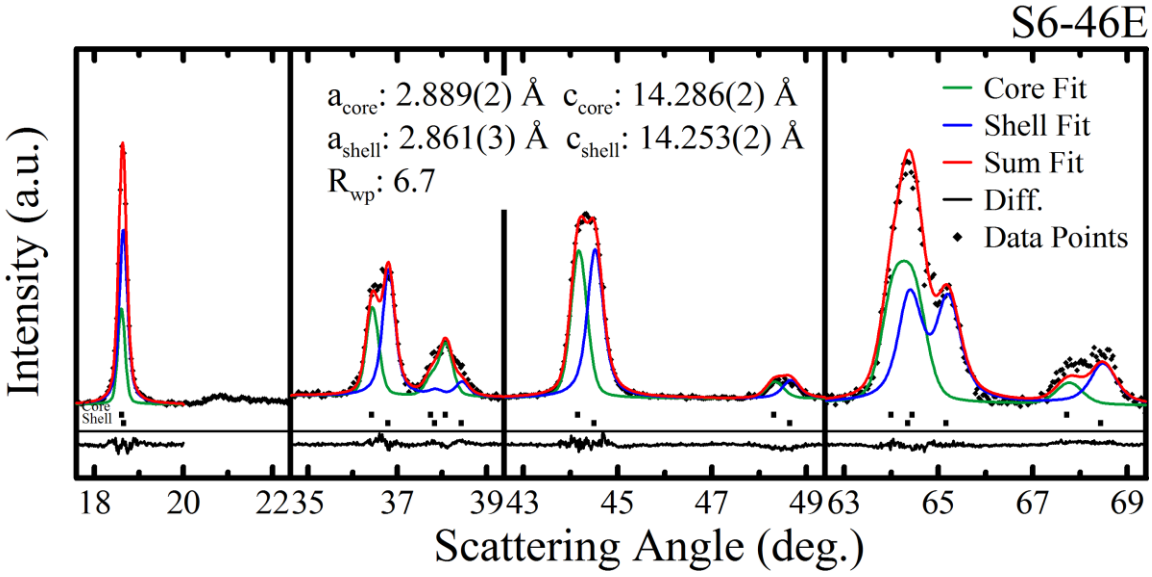

Figure 6.11. Diffraction pattern and Rietveld refinement fit of pattern for S6-46E. Diffraction pattern collected using optimized scanning parameters for D-5000. Reproduced from the Journal of the Electrochemical Society, open-source article.[140]

In Figure 6.11, the (104) peaks of the core and shell at 44-45° are of similar integrated intensity and if not carefully examined may appear as a single broad diffraction peak. Visually comparing the high resolution scan of S6-46E and S6-47C, S6-47C was far easier to discern that it was two phases due to the asymmetry in the overlapping (104) peaks of the core and shell phases. Although S6-47C was visually easier to see, the difference in the lattice parameters in S6-46E was greater. It is important that both EDS and XRD are

used to generate a clear understanding of the sample nature so the model used in Rietveld refinement accurately describes the sample.

Rietveld refinement was performed on all samples that did not show evidence of spinel. The Rietveld refinement results are shown in Table 6.3. All fits were performed on diffraction patterns collected with the optimized settings.

Table 6.3 Lattice parameters and R_{wp} of Rietveld refinements of series S6-46 and S6-47

Sample	a_{core} (Å)*	c_{core} (Å)*	a_{shell} (Å)*	c_{shell} (Å)*	R_{wp}
S6-46C	2.899	14.309	2.856	14.254	5.8
S6-46D	2.893	14.295	2.856	14.255	6.1
S6-46E	2.887	14.285	2.855	14.247	6.7
S6-46F	2.882	14.272	2.855	14.255	6.5
S6-46G	2.873	14.263	2.855	14.257	4.5
S6-47C	2.890	14.285	2.863	14.269	5.4
S6-47D	2.888	14.283	2.865	14.270	5.6
S6-47E	2.884	14.269	2.865	14.279	7.9
S6-47F	2.879	14.263	2.863	14.280	5.6
S6-47G	2.873	14.239	2.863	14.278	5.5

**Accuracy of lattice parameters: a = 0.002 Å, c = 0.004 Å*

The lattice parameters for the shell phase in both series do not appreciably change as more lithium was blended with the samples. As lithium content increased, the core lattice parameters steadily decreased. The shell phase appears to be saturated with lithium at the concentration of samples "C". Figure 2.1 showed that there should be a range of lithium concentrations with the shell phase transition metal composition that would lie within the single phase region. It may be thermodynamically favourable for the lithium to over-lithiate the core phase over the shell phase. In this sense, over-lithiate means to incorporate excess lithium beyond what was necessary for the core or shell to lie in the single phase region.

Alluded to earlier in this chapter, the lithium concentration in the core and the shell have optimal targets. Lithium cannot be detected with EDS and bulk sampling techniques such as ICP-OES would only provide the overall lithium content which was expected to be similar to the target. In a separate project with Jing Li on single phase materials, a series of contour plots which described the relationship between the lattice parameters and composition in the single phase layered region were developed.[81]

Contour maps were generated using the program Surfer 7.0, the results of Rietveld refinement and composition from ICP-OES of 20 different single phase compositions.[152] The first step of the process was to generate a grid of the desired composition space from the data sets. The topographical grids were developed with the xy plane representing the composition and the z axis the a or c lattice parameter. Kriging gridding methods were used to produce the grids.[153] The grids were then used to generate a contour map of the a or c lattice parameters in the composition space. The line spacing used in the contour maps was 0.005 Å for both a and c. The contour maps were then positioned onto the ternary structure-composition diagram and cropped to the limits of the single phase layered region. Figure 6.12 shows the a and c axis contour plots in the single phase layered region of the structure-composition ternary diagram of Li-Ni-Mn oxides.

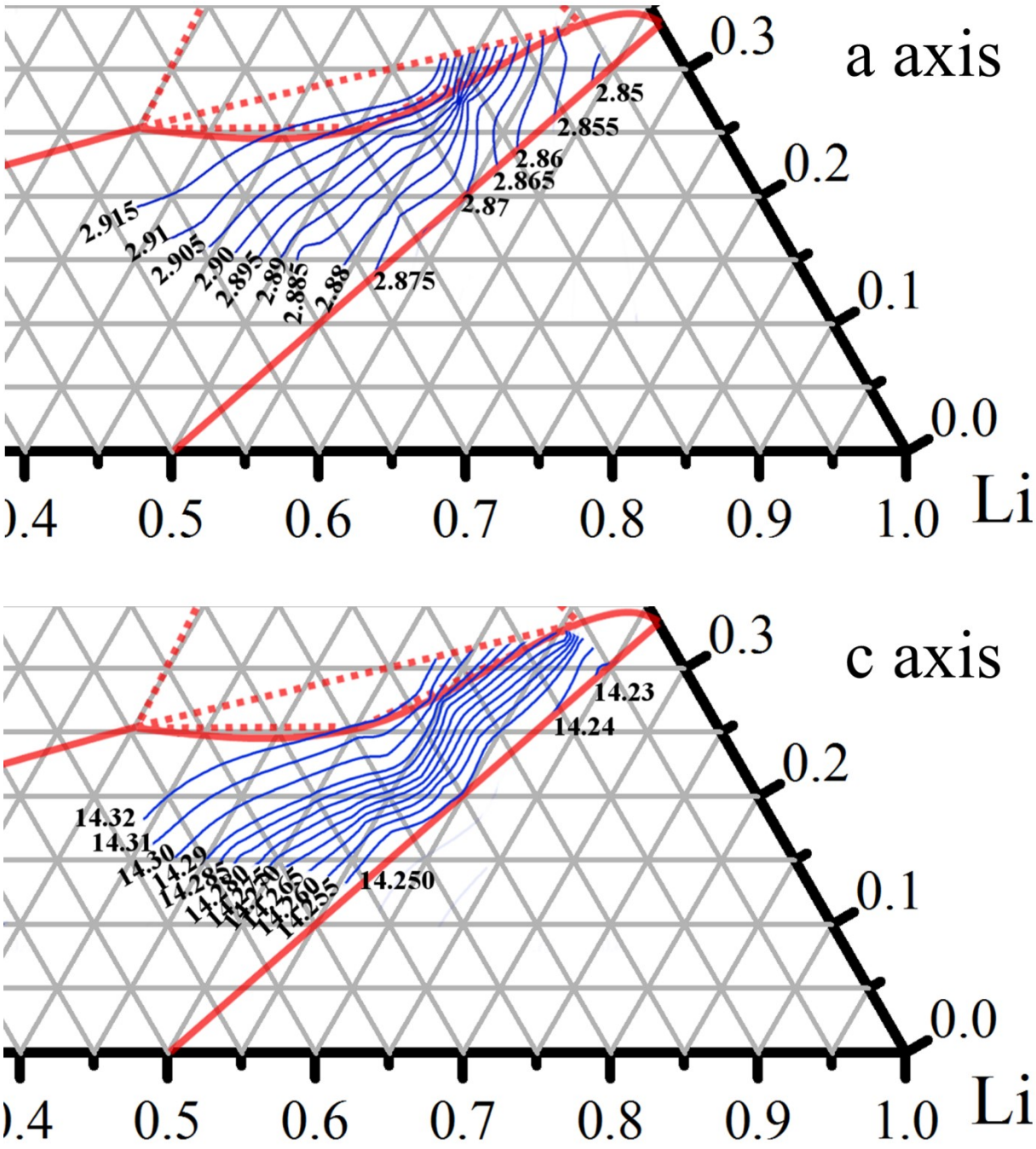

Figure 6.12 Contour plots of the a and c axes within the single phase layered region of the structure composition diagram shown in Figure 2.1. Reproduced from the Journal of the Electrochemical Society, open-source article.[140]

The general trends in the lattice constants are as lithium content increases the c-axis shrinks and as nickel content increases the a-axis increases. The contour plots and lattice parameters from the Rietveld refinements were used to estimate the composition of the core and shell phases. Positioning was accomplished by stacking the a and c-axis contour maps on top of each other with different colours for each set of lines. The coloured stack map was then used with data digitizing software to determine the coordinates of the intersection of the a and c axis for the core and shell phases. Contour lines in Figure 6.12 were shown mostly in 0.05 Å increments, so for samples between contour lines, visual interpolation was used to position the sample. Figure 6.13 shows the core and shell positions of samples listed in Table 6.3. Numbers 1 to 5 in Figure 6.13 represent the core and shell composition for samples S6-46C to S6-46G or S6-47C to S6-47G with C = 1, D = 2, etc.

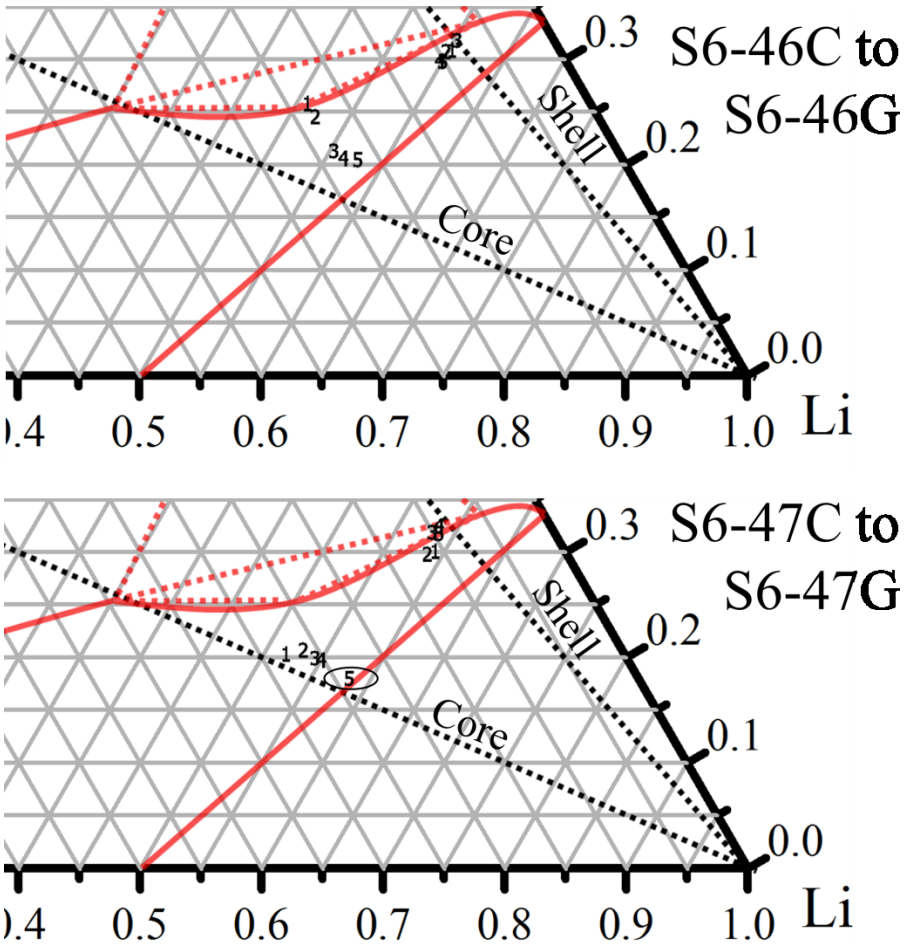

Figure 6.13 Results of positioning procedure using contour maps and Rietveld refinement results of S6-46C to S6-46G & S6-47C to S6-47G on the Li-Ni-Mn oxide structure-composition diagram. In the top diagram points labeled 1 represents the core and shell composition of S6-46C, 2=D 3=E, 4=F & 5=G. Bottom panel shows samples S6-47C to S6-47G with the same numbering scheme. Ellipse around core point "5" in bottom panel represents the accuracy of the fitting method. Reproduced from the Journal of the Electrochemical Society, open-source article.[140]

An ellipse was drawn around the core point "5"in the bottom panel of Figure 6.13 to represent the accuracy of the fitting method. The radii of the ellipse were determined by measuring the average spacing between contour lines in Figure 6.12 in the direction parallel and perpendicular to the lithium-nickel edge. The line spacing, cm/Å, was then multiplied by the Rietveld refinement accuracy to determine the radii of the ellipse. For

clarity an oval is only shown around point 5 in the bottom panel, but can be assumed to be of similar size around the other points.

In the top panel of Figure 6.13, moving from sample 1 (S6-46C) to sample 5 (S6-46G), the core phase moves towards the lithium corner of the diagram, but the shell phase remained near the upper boundary of the single phase region. The precursor S4-6 being manganese-rich in the core was supported by the shift in core positions right of the target composition line. For samples S6-47C to S6-47G a similar trend was observed. The core moves towards the lithium corner going from 1 to 5 and again the shell remained fixed near the upper boundary of the single phase region. For the precursor S4-7 the sample was much closer to the target core composition than S4-6 and was evident by how close the core compositions were to the target line. Table 6.4 shows the composition of the core and shell based on the contour plot fitting procedure.

Table 6.4 Composition of core and shell for DA6-46 & 47C-G determined from contour plot fitting routine.

		Core			Shell			Overall		
	Sample	Li	Ni	Mn	Li	Ni	Mn	Li	Ni	Mn
1	S6-46C	0.51	0.23	0.25	0.60	0.09	0.31	0.54	0.18	0.27
2	S6-46D	0.52	0.24	0.24	0.60	0.09	0.30	0.55	0.19	0.26
3	S6-46E	0.56	0.23	0.22	0.60	0.08	0.32	0.57	0.18	0.25
4	S6-46F	0.57	0.23	0.21	0.60	0.10	0.30	0.58	0.18	0.24
5	S6-46G	0.58	0.22	0.20	0.60	0.10	0.29	0.59	0.18	0.23
1	S6-47C	0.52	0.28	0.20	0.60	0.11	0.29	0.54	0.24	0.22
2	S6-47D	0.53	0.26	0.21	0.59	0.12	0.29	0.54	0.23	0.22
3	S6-47E	0.55	0.25	0.20	0.58	0.10	0.32	0.55	0.22	0.22
4	S6-47F	0.55	0.25	0.20	0.59	0.09	0.32	0.56	0.22	0.22
5	S6-47G	0.58	0.24	0.18	0.59	0.09	0.32	0.58	0.21	0.21

Samples were attempted with more lithium than the "G" samples for both series, but the additional lithium resulted in the samples being too hard to break the aggregates apart, suggesting the samples were saturated with lithium. It was interesting that the maximum lithium content of the shell phase was approximately 0.60, very close to the maximum lithium content achieved for the core phase, 0.58. The lithium content of the shell, or more manganese-rich, phase may be limited to the maximum lithium content of the other phase. This concept should be examined by future researchers by making additional samples in the Li-Ni-Mn oxide system with different core and shell transition metal compositions. It may be possible to control the lithium content of the core and shell phases by synthesizing the precursor with intermediate layers between the core and shell.

Single phase materials of the target core and shell composition of S4-6 and S4-7 were also synthesized. Appropriate lithium contents were selected at equal intervals across the single phase region. Table 6.5 shows the target composition for single phase materials of S4-6 and S4-7 core and shell target transition metal composition.

Table 6.5 Lattice parameters of single phase materials of target core and shell transition metal composition in S4-6 and S4-7.

Sample	Li	Ni	Mn	a (Å)	c (Å)
Core-1	0.50	0.30	0.20	2.894	14.293
Core-2	0.52	0.29	0.19	2.888	14.282
Core-3	0.54	0.28	0.18	2.884	14.275
Core-4	0.56	0.26	0.18	2.881	14.268
Core-5	0.58	0.25	0.17	2.877	14.261
Core-6	0.60	0.24	0.16	2.872	14.250
Core-7	0.62	0.23	0.15	2.868	14.237
Core-8	0.65	0.21	0.14	2.868	14.237
Shell-1	0.60	0.08	0.32	2.861	14.258
Shell-2	0.61	0.08	0.31	2.858	14.254
Shell-3	0.63	0.08	0.30	2.855	14.247
Shell-4	0.64	0.07	0.29	2.854	14.246
Shell-5	0.65	0.07	0.28	2.853	14.243
Shell-6	0.67	0.07	0.26	2.851	14.234

The smallest c lattice parameter obtained for the shell phase in the core-shell materials was 14.257, significantly larger than that observed for the single phase shell composition materials, 14.234 Å. If Shell-6 was positioned on the phase diagram with the contour plots, like the core-shell samples, it would have a lithium concentration of about 0.65, significantly more than the lithium concentration of the shell in the core-shell samples. ICP-OES was conducted on Shell-6 which had a lithium concentration of 0.635. For the core phase, the minimum c lattice parameter in the core-shell was 14.239 Å, very similar to what was obtained for the single phase sample Core-8, 14.237 Å. This shows that in the core-shell samples the core phase could achieve the same saturated lithium concentration as reported in single-phase samples, while the manganese-rich shell phase could not.

6.4 Core-Shell Materials with Cobalt

Electrolyte free, dry pouch cells manufactured by LiFun (Zhuzhou City, China) with a graphite negative electrode and a core-shell positive electrode were shipped to the laboratory at Dalhousie in the fall of 2014 for other studies involving electrolyte additives. The positive electrode in these cells was synthesized with a target core composition of $LiNi_{0.67}Mn_{0.37}O_2$ and a shell composition of $Li_{1.15}[Ni_{0.17}Co_{0.17}Mn_{0.66}]_{0.85}O_2$, the core to shell mass ratio was reported as 2:1. The positive electrode from these cells was removed and used to make half-type coin cells. The target core and core-shell compositions were synthesized at Dalhousie and were also made into coin cells. Both the core and core-shell were studied with the Ultra High Precision Chargers to examine the impact the shell coating has on lifetime. The electrochemical results will be discussed in Chapter 7.

Figure 6.14 shows the EDS false-colour composition maps for the precursor synthesized at Dalhousie and the electrode from the LiFun cell. The positive electrode in the LiFun cell was scraped from its current collector and the recovered powder encased in epoxy similar to all other EDS measurements.

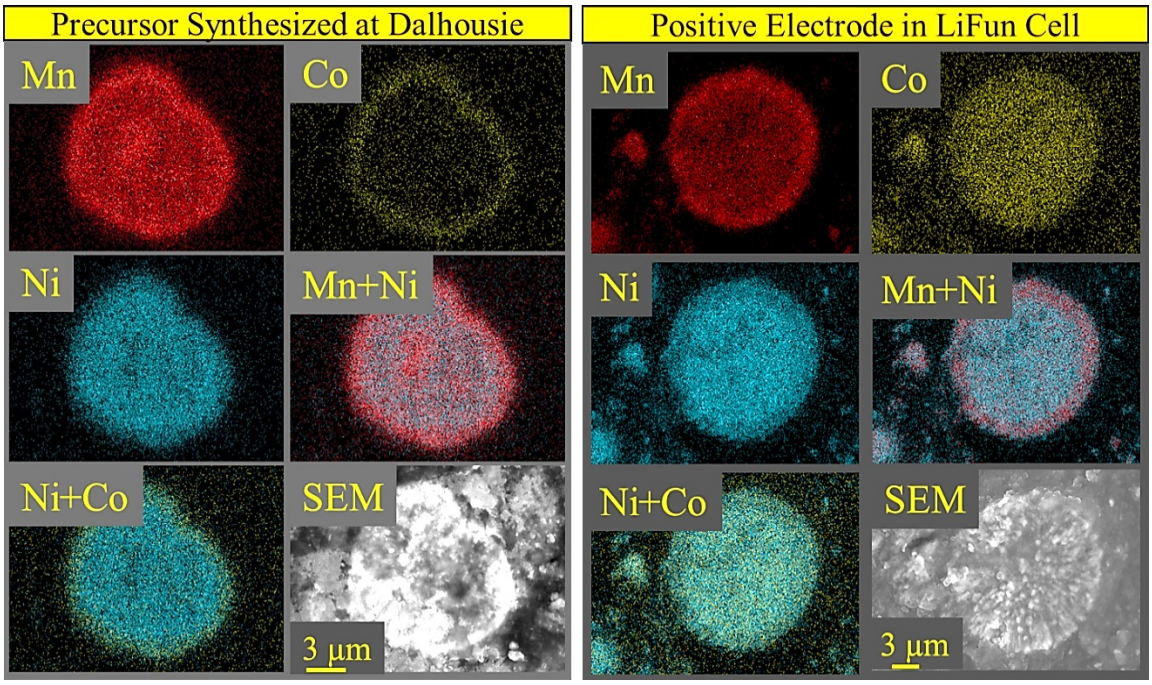

Figure 6.14 False-colour EDS composition maps of cobalt containing precursor synthesized at Dalhousie and active material from the positive electrode of the LiFun pouch cell. In stacked maps (Mn+Ni) colour-scale of individual element signal is same as in their respective individual maps.

In Figure 6.14 the precursor particles contained cobalt only in the shell. The active material extracted from the positive electrode of the LiFun cell showed cobalt throughout the particle, but was still a two-phase core-shell as evident in the stacked Mn + Ni composition map. The Dalhousie precursor was mixed with lithium carbonate and heated similarly to the other samples discussed in this chapter. The EDS composition maps of the heated Dalhousie precursor were virtually the same as the LiFun sample; cobalt present throughout the particles, but still maintaining a contrasting nickel and manganese concentration in the core and shell.

Cobalt appears to be much more mobile than nickel and manganese during the sintering process. Diffusion studies should be completed on cobalt containing materials to better understand the rate of diffusion. If the rate of diffusion was well known one could anticipate it. One could develop the precursor with the cobalt content in the core and shell different than the target composition, after heating the diffusion of cobalt between the two phases would result in the desired cobalt content in the core and the shell. It may also be possible to prevent cobalt diffusion by using a bi-layered shell. A second, thin shell layer between the core and the shell that is permeable to lithium, but impermeable to cobalt would prevent cobalt diffusion. Such compatible materials may not exist.

6.5 Chapter 6 Conclusions

In this chapter several Li-Ni-Mn oxide core-shell powders were synthesized. Using EDS it was determined that the samples were two-phase and that nickel and manganese diffusion during high temperature sintering was small. XRD was used to determine the lattice parameters of the core and shell phases in the samples. Due to the similarities of the core and shell phases, higher resolution diffraction patterns, which required a longer sample acquisition time, were required to resolve the diffraction peaks of the two phases. Rietveld refinement using a two-phase sample model was used to determine the lattice parameters of the core and shell phases in the lithiated core-shell samples.

Contour maps of the a and c lattice parameters were developed from 20 single-phase samples. These contour maps were used with the lattice parameters of the core-shell samples to position the core and shell on the structure-composition diagram.

After positioning the samples on the phase diagram, it was observed that the core phase would accept additional lithium, while the shell phase maintained its composition near the upper boundary of the single phase region on the structure composition diagram. It was not determined why the shell phase would not accept more lithium in the core-shell samples even though it did in single-phase samples. This interesting complexity to the core-shell materials should be further investigated by future researchers.

A core-shell material with cobalt was also investigated. In this material the target composition was to have cobalt in the shell and no cobalt in the core phase. From EDS measurements it was determined that cobalt diffused into the core and was approximately homogeneous throughout the particle. This result was confirmed in a second sample of the same target composition that was synthesized at Dalhousie. Cobalt mobility may present a challenge to core-shell materials.

The sintering process of core-shell materials presents several obstacles that need to be further addressed. First, crystallization and volume expansion may result in core and shell separation or delamination of the shell from the core during heating. It may be possible to overcome this issue by adjusting sintering conditions, although some ratios of core to shell and composition combinations may simply be impossible to synthesize. Second, there is limited control over lithium content in the two phases. A bi-layer shell may be able to overcome such issues. Finally cobalt was shown to be highly mobile during sintering; again bi-layer shells or other diffusion barrier methods may be useful in limiting

cobalt diffusion. It may also be possible to synthesize a material with cobalt contents in the core and shell different than that desired, but selected so that after sintering and cobalt diffusion, the cobalt concentration is the desired amount in the core and shell phases.

The recovered products after the sintering were not as simple to understand as the precursor materials. This was due to complications, such as diffusion and phase equilibria, that occurred because the core-shell structure was already formed and in close proximity. One cannot simply pick a target Li, Ni, Co and Mn composition for the core and the shell and expect the final product to be exactly that. It may be possible to achieve the desired core and shell composition by forming the core-shell structure at a different point in the synthesis process. A lithiated core could be synthesized and then placed into a tank reactor to be coated with hydroxides of the shell, followed by lithiation and sintering again. This process is less economical than a single precursor step presented in this thesis, but should be explored as it may allow for a greater flexibility in the choice of materials and compositions.

Chapter 7. Electrochemical Analysis of Core-Shell Materials

7.1 Expectations of Electrochemical Analysis of Core-Shell Materials

Some of the materials synthesized in Chapter 6 were studied in coin-cells. This was done to understand the impact the shell coating has on lifetime and capacity. Chapter 1 showed the charge endpoint capacity slippage of several NMC layered structure materials. UHPC and standard battery chargers were used to study the core-shell materials to determine if the charge endpoint slippage and coulombic efficiency were improved in the core-shell materials compared to the core phase only materials. It was also of interest to determine if the structural analysis of the core and shell phases in Chapter 6 could be used to compare the voltage versus capacity plot of the core-shell to core and shell single phase materials.

7.2 Core-Shell Materials in Coin Cells

Samples S6-46C to S6-46F, S6-47D to S6-47G, Core-1 to Core-4 and Shell-2 to Shell-5 were tested in half-coin cells. 1 M $LiPF_6$ EC:DEC 1:2 volume ratio without any additives was used as the electrolyte in the half cells. The LiFun core-shell positive electrode material and its target core composition $Li[Ni_{0.67}Mn_{0.33}]O_2$, which was synthesized at Dalhousie, were also studied in half cells with the same additive-free electrolyte. UHPC and standard chargers were used to study these materials. The UHPC study of the LiFun materials was started prior to the EDS measurements on the LiFun core-shell material being collected. The core analog material was selected based on the target

cobalt-free composition, instead of the cobalt containing core composition observed in EDS measurements.

For all cells, the cycling protocol was 2 charge-discharge cycles, charging to 4.8 V and discharging to 2.5 V. This was called the activation step. After activation, the cells were charge-discharge cycled for up to 50 cycles between 2.5 and 4.6 V. Cells were placed in temperature controlled boxes during cycling at 40. ± 0.1°C for the LiFun materials and at 30. ± 0.1°C for all others. Cells were cycled using a constant current of 10 mA/g between the upper and low voltage limits. For materials synthesized at Dalhousie, the active-material: binder: carbon black weight ratio was 90: 5: 5. The LiFun electrodes were manufactured elsewhere and reported to be 96 *wt*% active material.

7.2.1 Voltage Curves of S6-46 and S6-47 Core-Shell Materials

Figure 7.1 shows a plot of voltage versus specific capacity of the first cycle for the materials from S6-46 and S6-47 that were studied in coin cells.

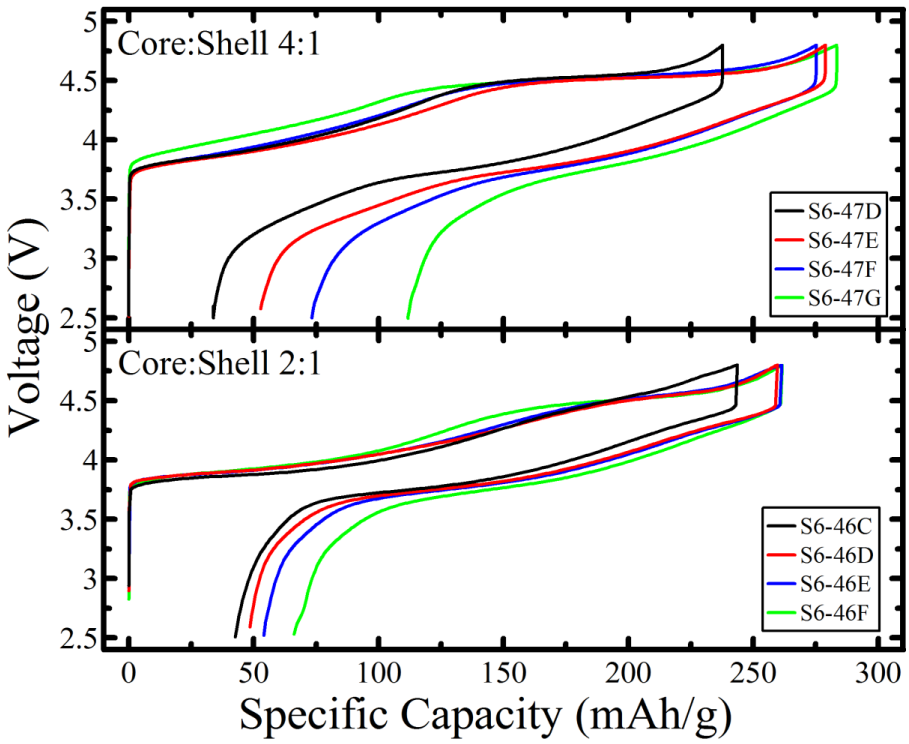

Figure 7.1 Plot of voltage versus specific capacity for the first cycle of samples from S6-46 and S6-47.

In the samples from S6-46, samples D, E and F showed nearly identical charge capacities, with sample C showing slightly less. In the voltage curve of sample S6-46C there is not a clear plateau during charge at 4.5 V that is in the other 3 samples. This suggests that for sample C the shell phase, which has a well-defined activation plateau (Figure 7.2), may not have formed the desired layered phase. It is possible that sample C was slightly lithium deficient and lies in a two phase layered-layered region described by McCalla.[74,85] In this region, samples are a composite of two layered phases, a "M" manganese-rich phase and a "N" nickel-rich phase. McCalla reported the lattice parameters of M, a = 2.854 Å and c = 14.291 Å and N, a = 2.909 Å and c = 14.30 Å. The lattice parameters of the "M" and "N" phases are extremely similar to the values obtained

from the two-phase refinement of S6-46C. McCalla reported the electrochemistry of the layered-layered composite region to be extremely poor.

In samples with more lithium than S6-46C, the shell phase was no longer a layered-layered composite and the anticipated plateau at 4.5 V was observed. Adding additional lithium beyond S6-46D increased the irreversible capacity and the length of the activation plateau. This was most likely due to the core phase being synthesized with more trivalent nickel to accommodate the excess lithium.

Samples from the series S6-47 showed similar first charge and discharge curves. Sample S6-47D showed significantly less charge capacity than the samples with more lithium. Unlike S6-46C which showed virtually no high voltage plateau, S6-47D showed a plateau at 4.5 V which suggests the issue with this sample is not in the shell phase, but rather in the core-phase. For sample S6-47D, the Rietveld refinement reached its optimal fit with 11% of the lithium-layer sites occupied with nickel. For sample S6-47E only 7% of the lithium-layer sites were occupied with nickel in the optimized Rietveld refinement. The low capacity in S6-47D may have been due to cation disorder reducing the capacity from the core phase. Increasing the lithium concentration in S6-47E and F, the first charge capacity increased slightly, but less than the increase in irreversible capacity. The cross-sectioned particle micrograph of S6-47C in Figure 6.5 showed large rocksalt like primary particles which may also have been present in S6-47D.

Figure 7.2 shows the voltage versus capacity plot of the first charge and discharge of the core and shell single phase materials listed earlier in this chapter.

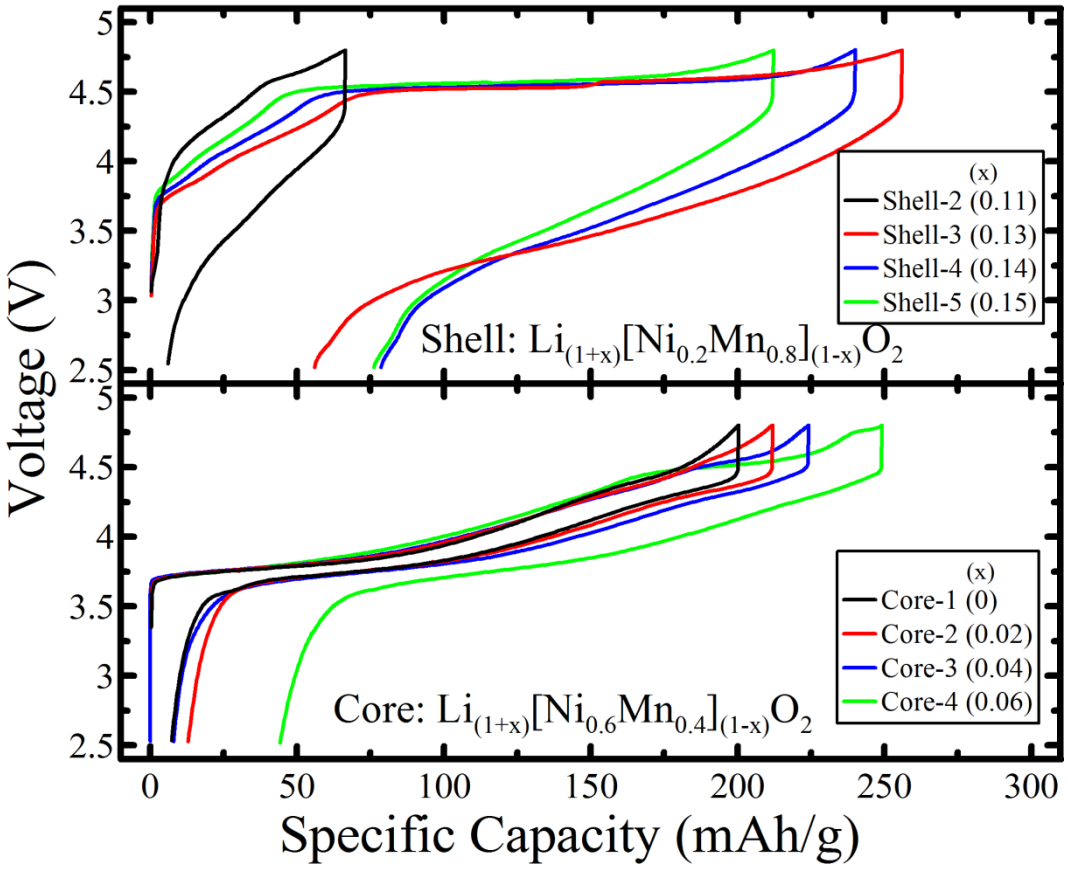

Figure 7.2 Plot of voltage versus specific capacity of various core and shell single phase materials.

The bottom panel of Figure 7.2 shows the voltage versus specific capacity plot of a few of the single phase core materials. Table 7.1 shows the first change (q_c) and discharge capacity (q_d), the irreversible capacity (IRC) and length of the 4.5 V plateau for the materials shown in Figure 7.2. Comparing Core-1, Core-2 and Core-3, the discharge capacity increases with lithium content, where the value of x in the composition is shown next to each samples label in the legend. This is most likely due to a reduction in cation disorder in the core of these materials. Sample Core-4 was the only core material that showed an appreciable 4.5 V plateau. Core-4 had an increased first charge capacity compared to the other Core samples, but less discharge capacity and larger irreversible

capacity than Core-3. For the shell materials, sample Shell-2 was a composite "M" and "N" layered-layered material described earlier in this section. Shell-3 has enough lithium to lie outside the composite region of the structure-composition diagram (Figure 2.1) and thus shows much higher capacity. Shell-4 and Shell-5 had a shorter q_c, q_d and larger IRC compared to Shell-3.

Table 7.1 q_d, q, IRC and activation plateau length for materials from Core and Shell series.

Sample	q_d (mAh/g)	q_c (mAh/g)	IRC (mAh/g)	Plateau (mAh/g)
Core-1	193	200	7	0
Core-2	205	212	7	0
Core-3	211	224	13	12
Core-4	206	250	44	51
Shell-2	60	66	6	0
Shell-3	200	255	55	146
Shell-4	161	239	78	156
Shell-5	136	212	76	126

The irreversible capacities of the samples from S6-46 were less than those of S6-47. In samples from S6-47, the large irreversible capacity may be due to the core being overlithiated, exhibiting behavior similar to Core-4. Comparing the lattice parameters in Tables 6.3 and 6.5, the core phase in S6-47F and G are similar to that of Core-4. In the series S6-46, the c-axis lattice parameter was larger than Core-4 suggesting the lithium content in the core phase was less than Core-4.

Figure 7.3 shows a plot of the differential capacity, dq/dV, versus voltage for samples S6-46E, S6-47D, Core-3 and Shell-4. The first cycle after the activation step is shown in blue and the 20^{th} cycle is highlighted in red with intermediate cycles shown in black. In sample Shell-4 an increase in capacity in the low voltage region was observed

with cycling. For Core-3, there were virtually no changes in the differential capacity curve in the first 20 cycles. The core-shell sample, S6-46E showed elements of both the core and shell phases with some low voltage capacity growth, but far less than Shell-4.

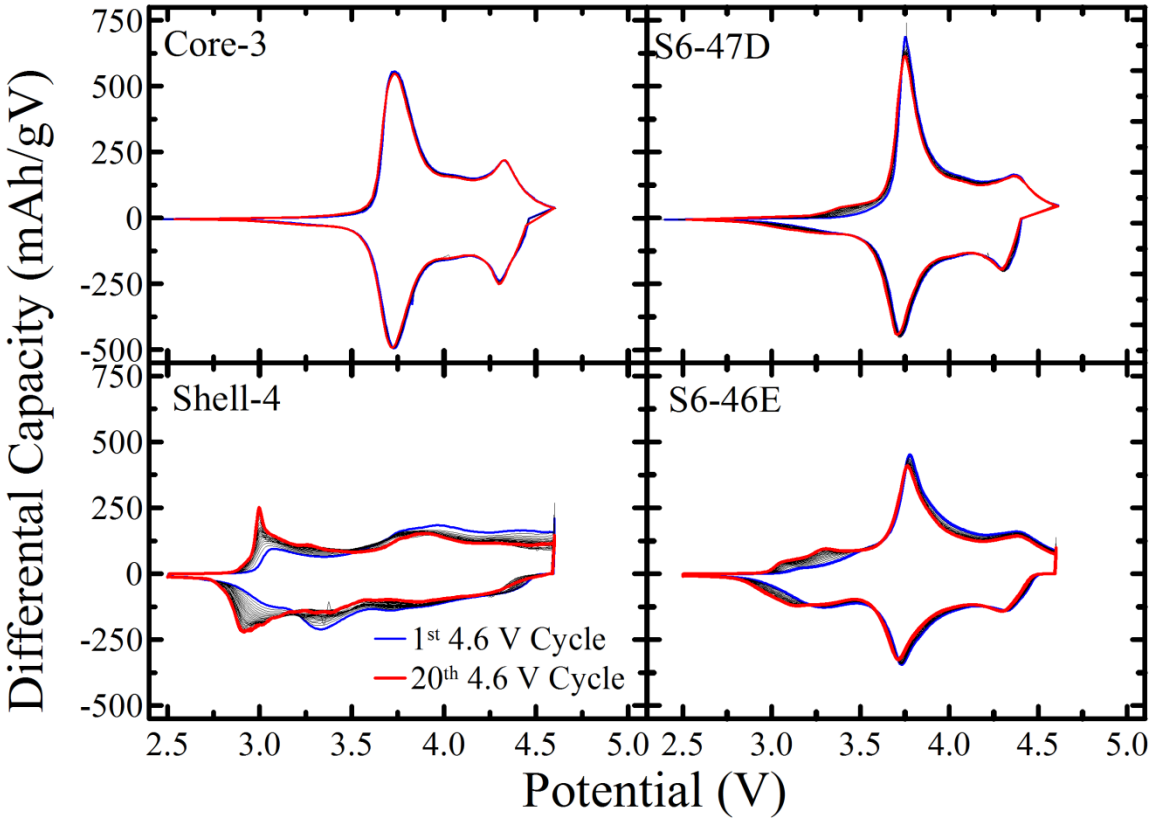

Figure 7.3 Plot of differential capacity (dq/dV) versus potential for various core, shell and core-shell materials. All panels are drawn with the same scale, red cycle is the 20th cycle, blue is the first cycle after activation and intermediate cycles shown in black. Reproduced from the Journal of the Electrochemical Society, open-source article.[140]

Sample S6-47D showed less low voltage capacity than S6-46E and showed more capacity in the 3.5 to 4.0 V region. Sample S6-47D has more core phase than S6-46E, so it was expected that more of the capacity would be derived from the core. Capacity below 3.5 V that increased with cycling was observed in Shell-4 and not Core-3. The electrochemistry of the core-shell materials was similar to that of a composite of discrete

particles of core phase and shell phases. Two lithium diffusion pathways are plausible for the core phase in a core-shell material; solid-state diffusion via vacancies in the shell or direct contact with the electrolyte. It may be possible to better understand the diffusion pathway for lithium by exploring the rate capabilities of the core-shell materials compared to the core-only materials. If the diffusion is only via small pores in the shell than at high specific currents, core capacity should decrease more in the core-shell material than in core-only materials.[154] These experiments were not done, but should be explored.

Figure 7.4 shows the specific discharge capacity versus cycle number for the samples shown in Figures 7.1 and 7.2. In Figure 7.4, the discharge capacity of each material is shown for cycling between 2.5 and 4.6 V, two sister-cells are shown for each material.

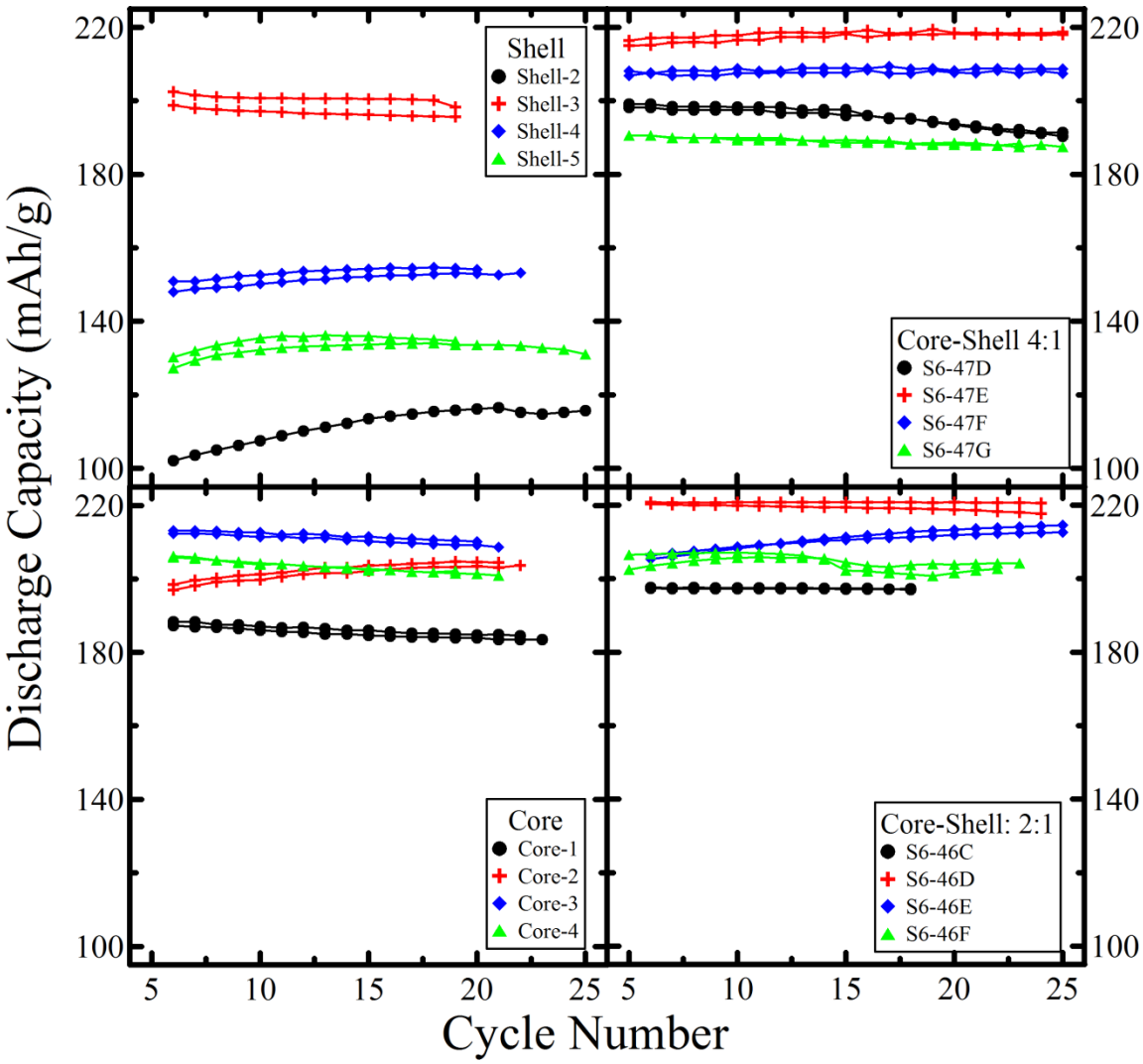

Figure 7.4 Plot of Specific discharge capacity versus cycle number for various samples of S6-46, S6-47, core and shell series. Cycles shown are charge and discharge cycling between 2.5 and 4.6 V with a specific current of 10 mA/g. Reproduced from the Journal of the Electrochemical Society, open-source article.[140]

Samples S6-46D and S6-47E showed the highest reversible capacity of all the materials shown in Figure 7.4. It was unexpected that the capacity of the core-shell materials was higher than the best core or shell material. It was expected that the capacity of the core-shell materials would be a linear combination of the core and shell phases' capacities. In samples S6-46 the composition of the core was slightly manganese rich of

the target and core-series samples. This small change in composition may have resulted in a material with a higher specific capacity than the target core composition. For samples from S6-47, the core phase composition was much close to the target transition metal composition compared to S6-46; see Figure 6.13. For samples S6-47E and F, the capacity was higher than the best core, Core-3. Comparing the lattice constants of S6-47E and F to the materials in Table 6.5, the core is similar to Core-3 and the shell phase is similar to Shell-3. The extra capacity in the core-shell materials may be due to less cation disorder in the core-phase of the core-shell samples compared to Core-3; for sample Core-3, 6.6% of lithium layer sites were occupied with nickel, compared to 4.2 % in S6-47E and 3.7% in S6-47F.

7.2.2 Ultra High precision Charger Results of Core-Shell Materials

Samples S6-46D, S6-46E, S6-47D, S6-47E, Shell-3 and Core-3 were studied with UHPC. Figure 7.5 shows the charge endpoint capacity slippage versus cycle number normalized to the first 4.6 V charge cycle. The data points for each sample are the average of two sister cells, with error bars representing one standard deviation of the sister cells. Sample S6-46D showed the smallest charge endpoint slippage after 20 cycles. Sample Shell-3 showed a much larger charge endpoint capacity slippage than the core-shell sample. In Chapter 3 a similar manganese-rich composition was shown to have a very small charge endpoint capacity slippage. The difference in charge endpoint capacity slippage between the sample in Chapter 3 and Shell-3 may be due to the vacancies that were present in the Chapter 3 sample.

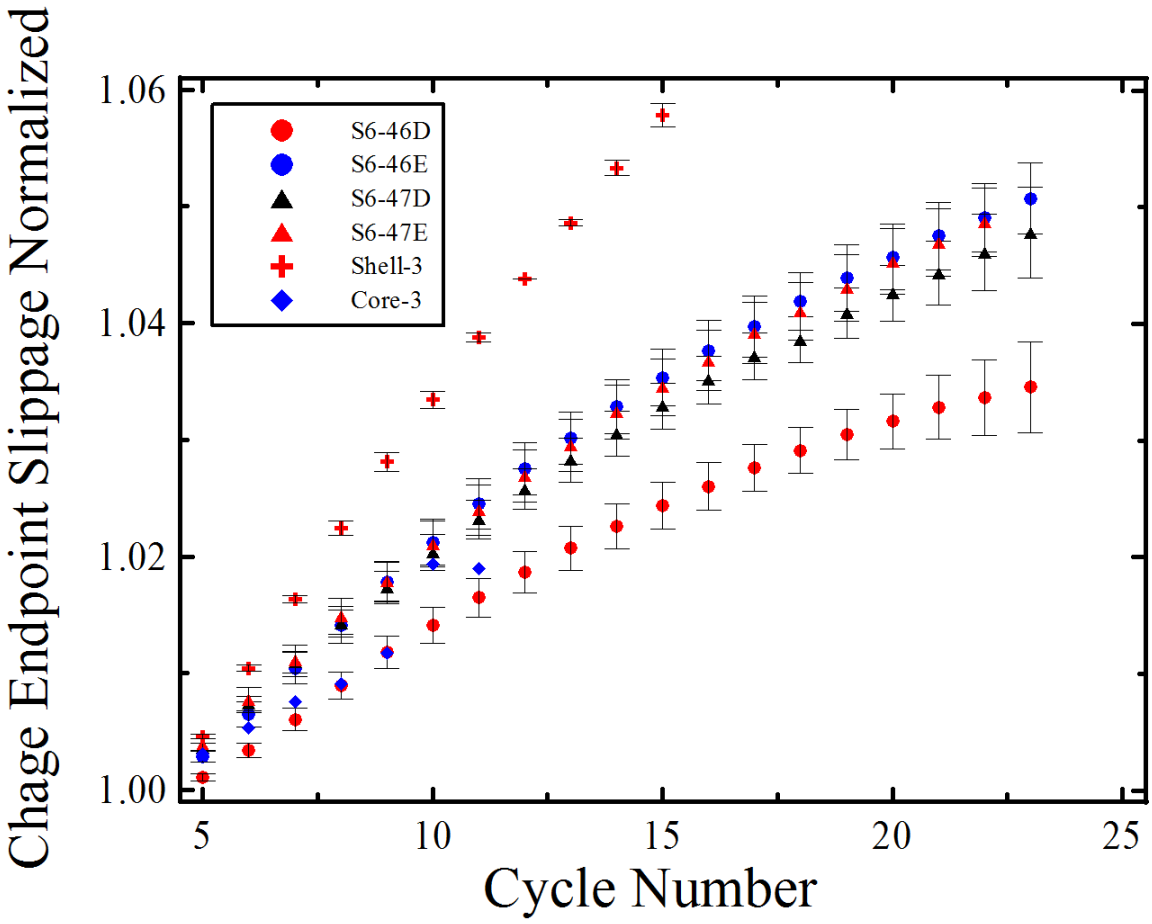

Figure 7.5 Charge endpoint capacity slippage, normalized to cycle 3, versus cycle number of various materials from S6-46, S6-47, Core and Shell series.

Sample S6-46D showed the smallest charge endpoint slippage of all the materials in Figure 7.5. The slope of the charge endpoint slippage was fit for the last 3 cycles for each cell shown in Figure 7.5. Table 7.2 shows the slope of the charge endpoint slippage for these cells. The slope of the charge endpoint slippage for all of the core-shell materials was smaller than Core-3 and Shell-3. This suggests that less electrolyte was oxidized at the positive electrode surface in the core-shell materials than Core-3 and Shell-3.

Table 7.2 Slope of charge endpoint capacity slippage of last 3 cycles for cells in Figure 7.5

	Slope
S6-46D	0.00086
S6-46E	0.0016
S6-47D	0.0017
S6-47E	0.0017
Shell-3	0.0041
Core-3	0.0036

The core-shell materials had higher capacity and less charge endpoint capacity slippage than the Core or Shell series materials. Although this UHPC study only explored a few materials it showed that the core-shell structure impacted the charge endpoint capacity slippage, suggesting decreased electrolyte oxidation. A more complete study is necessary as the optimal lithium content for lifetime considerations may not have been studied on the UHPC for the Core and Shell series materials.

7.3 Ultra High Precision Charger Results of Cobalt containing Materials

The LiFun positive electrodes were studied using the UHPC. The LiFun positive electrode was compared to the target core composition synthesized at Dalhousie. Figure 7.5 shows the voltage versus specific capacity for several cycles of the LiFun core-shell material and the target core material after the formation process.

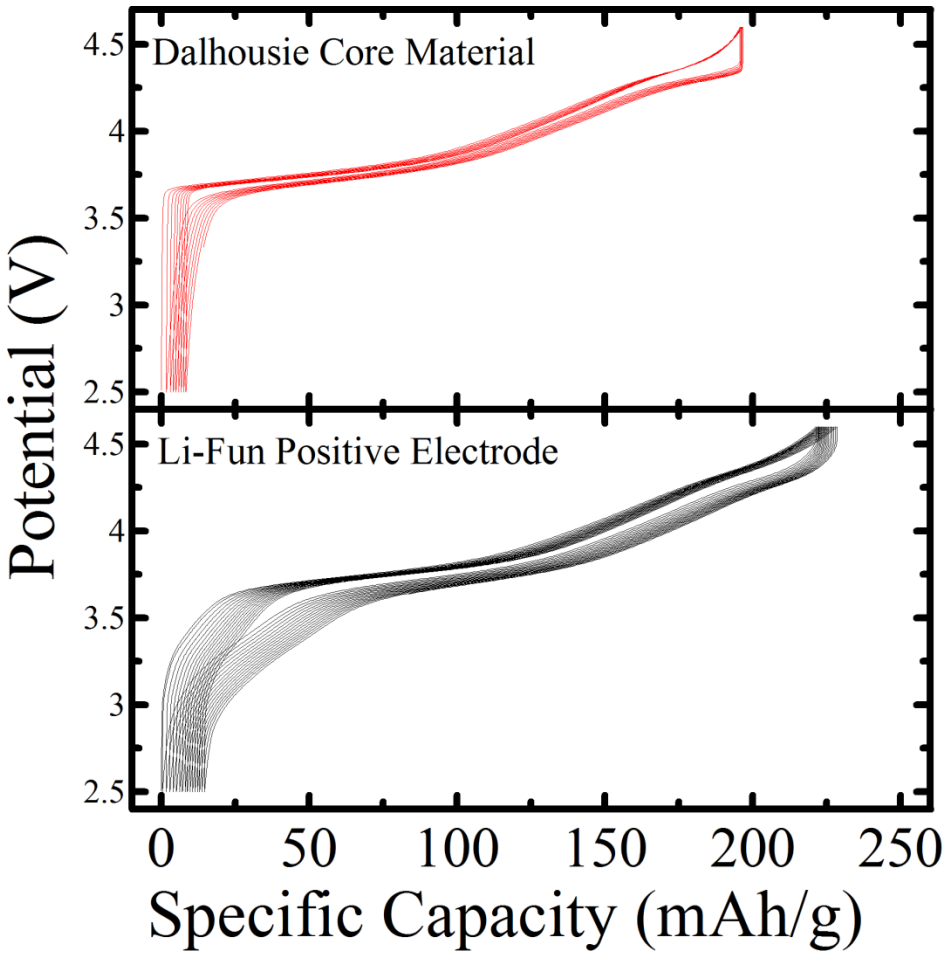

Figure 7.6 Plot of voltage versus specific capacity for LiFun core-shell material and its target core composition, synthesized at Dalhousie. Plots show cycling after two charges to 4.8 V to complete activation process.

In Figure 7.6, the LiFun positive electrode material showed more low voltage capacity growth than the Dalhousie core material. This was expected since the LiFun shell phase was a manganese-rich composition. A greater overpotential was observed in the LiFun cells in the 3.7 to 4.0 V region of the voltage curve compared to the core-only material. The increased overpotential may be due to the differences in the lithium diffusion pathway between the two materials. Outside of the 3.7 to 4.0 V region it is difficult to

determine overpotential, due to the hysteresis in the manganese-rich materials lithium insertion and removal that was discussed in Chapter 3.

Figure 7.7 shows the specific capacity and coulombic inefficiency per hour (CIE/h) versus cycle number of the LiFun core-shell and Dalhousie core material. CIE/h was determined from the CE and discharge time in hours ($t_{discharge}$),

$$CIE/_h = \frac{1-CE}{t_{discharge}}. \quad (7.1)$$

CIE/h was used in place of CE since the time the two materials were exposed to high voltage was not the same because of capacity and capacity fade rate differences in the two materials being compared. By plotting CIE/h versus cycle number the measurement is effectively independent of time allowing for a simpler comparison of the materials.[26]

Charge endpoint capacity slippage was not plotted for these cells, although it is one of the best metrics for determining if the shell was impacting electrolyte oxidation. Figure 7.6 showed that for the core material the charge endpoint slippage was effectively zero and was larger for the LiFun core-shell material. The near zero slippage of the Dalhousie core material was due to capacity fade in the core material. In Figure 7.7, the capacity of the core material was fading very quickly compared to the core-shell material. The capacity fade resulted in the charge endpoint effectively not moving, but instead the discharge endpoint slipping to the right only. For the core-shell material which showed less capacity fade, the voltage curve showed the expected slippage to the right at the top of charge. Figure 1.8 showed the charge endpoint slippage normalized to capacity of the 20th cycle for various NMC layered material. If the LiFun material was added to Figure 1.8 its charge

endpoint slippage at cycle 20 would be 1.012, which is better than most other materials in this figure.

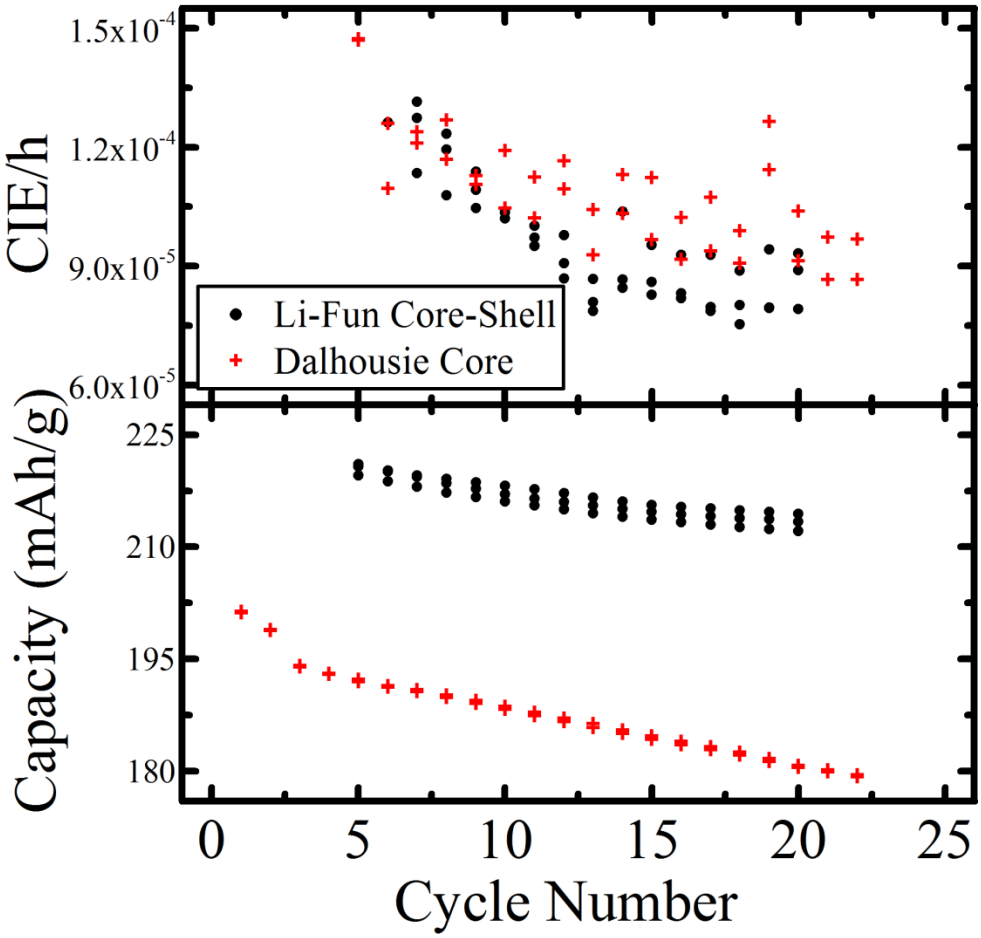

Figure 7.7 CIE/h and discharge capacity versus cycle number of the LiFun core-shell material and Dalhousie core material.

In Figure 7.7 the discharge capacity of the core-shell material was more than the core material. The core-shell material's shell phase was manganese-rich with a higher specific capacity than the core phase so it was expected that the core-shell phase would have more capacity than the core phase. The difference in capacity may also be due to differences in the lithium content of the core phases in the two materials or cobalt diffusion

in the LiFun material. Only one lithium content was explored for the Dalhousie core material which may not be the optimized lithium concentration for high energy density.

The CIE/h of the core-shell material was slightly better than the core-only material. The core-shell material in the LiFun cell showed excellent charge endpoint capacity slippage compared to the materials in Figure 1.8, high specific capacity and a low CIE/h. It also showed less capacity fading than the core only material. Although the LiFun example should not be considered a thorough analysis comparing a core-shell material to its core it shows that core-shell materials may provide lifetime benefits without a significant loss of energy density.

7.4 Chapter 7 Conclusions

Samples from the series S6-46 and S6-47 were studied with traditional battery chargers. The electrochemical data showed structural information that was not apparent with diffraction or EDS experiments. In sample S6-46C the shell phase may be a composite of "M" and "N" phases as described by McCalla. The lattice parameters of "M" and "N" are very similar to the expected core and shell compositions and thus diffraction could not distinguish this. Electrochemically, core-shell materials behave very similar to composite electrodes. Future work is necessary to better understand rate capabilities of core-shell materials which may provide insight into the diffusion pathway for lithium-ions from the core; solid-state via the shell or direct electrolyte contact.

The LiFun core-shell material was examined with UHPC and compared to the target core composition. The core-shell material showed higher capacity and better CIE/h than the core-only material. Charge endpoint capacity slippage analysis could not be completed on the core material since it showed capacity fading that masked the charge endpoint capacity slippage. The LiFun material had a charge slippage normalized to the 20^{th} cycle of 1.012, which was as good as the best material shown in Figure 1.7. A true head to head comparison of the LiFun core-shell to its true core composition could not be made due to diffusion of cobalt. Future researchers should be interested in doing a complete electrochemical comparison of a core-shell material to its core and a composite of the core and shell phases. It needs to be shown with UHPC that the core-shell structure has a smaller charge endpoint slippage (electrolyte oxidation) compared to the same composite and core-only material. Due to the diffusion of cobalt and the lack of contour plots and thorough understanding of the composition space, this may be best accomplished on Li-Ni-Mn layered oxide core-shell materials.

Chapter 8. Conclusions and Future Work

8.1 Conclusions on Synthesis of Core-Shell Materials

Precursors with a core-shell structure were synthesized with the desired core and shell composition. The ratio of the two phases was easily controlled by changing the ratio of dispensing time for the core composition metal sulfate and the shell composition metal sulfate solutions. Fine control over composition was demonstrated, allowing for virtually any NMC hydroxide precursor to be synthesized. It was necessary to adjust parameters such as pH, stir rate and gas flow rate to improve morphology. pH was critical in ensuring the shell phase formed a coating on the core particles. In general, as manganese concentration increased, it was necessary to reduce to pH to induce more precipitation-dissolution.

Synthesis of lithium transition metal oxides from the core-shell precursors was demonstrated in Chapter 6. It was shown in Chapter 6 that lithium uptake in the two phases of the core-shell material was not straightforward. Sintering at 900°C for 10 h did not result in appreciable diffusion of nickel and manganese; however cobalt was extremely mobile at this temperature. EDS measurements on the LiFun composition core-shell precursor and sintered product demonstrated it was possible to synthesize a core-shell precursor with cobalt present in only one of the phases, but after sintering cobalt was approximately homogeneous throughout the particle.

Lithium concentration in the core and shell phases was difficult to control. For the samples studied in this thesis, the shell-phase would not achieve the same saturation of lithium in the core-shell material as was possible in a single-phase sample of the shell

phase. The core-phase in the core-shell sample could achieve similar lithium saturation as its single phase core-phase analog. It was important that several lithium concentrations were attempted for the core-shell material. By making samples from the upper to lower boundary of the single phase layered region of the structure composition diagram, a better understanding of lithium uptake in the two phases was found. It was also useful to make multiple lithium concentrations to better understand the changes observed in the diffraction patterns. If only a single lithium concentration was selected one might have discerned from diffraction experiments that the core-shell samples were single phase.

8.2 Conclusions on Characterization Techniques of Core-Shell Materials

It was demonstrated that powder X-ray diffraction, SEM and EDS are all necessary to develop a thorough understanding of the core-shell powders. It is insufficient to use only a single technique, but rather is best to collect all three at minimum. For the precursors XRD showed clearly the presence of two unique hydroxide phases in the samples, but it did not show if the sample was a composite of discrete secondary particles or a true core-shell sample. For the lithiated products it was necessary to confirm the core-shell structure was maintained with EDS due to less separation in diffraction peaks of the core and shell phases in the lithiated products. False-colour maps of cross-sectioned particles were an effective qualitative method for verifying the core and shell phases had unique transition metal compositions. With optimized scanning parameters it was possible to observe two layered lithium transition metal oxide phases with XRD. Rietveld refinement further confirmed that the samples were indeed two phases.

The two phase Rietveld refinement results were used with the contour maps of the lattice parameters to determine the composition of the core and shell phases in the core-shell samples. This technique showed a unique method for characterization of composite sample.

Absorption of X-rays in diffraction experiments was shown to be an effective method for estimating the shell thickness. The spherical model shown in Chapter 5 estimated the shell thickness in agreement with what was observed in EDS. The spherical model was simple to use, requiring two diffraction patterns and a micrograph to estimate the shell thickness.

8.3 Review of Thesis Scope

In section 1.4 several points were listed as the scope of this thesis, those points were:

1. During precursor synthesis how can one ensure that the shell is forming a closed coating around the core particles?
2. What methods can be used to determine the ratio of the core and shell phases and the thickness of the shell coating?
3. Do transition metals diffuse during the sintering process?
4. Lithium cannot be detected with EDS methods so how can the lithium content in the core and shell phases be individually determined?
5. Is the core-shell structure maintained during charging and discharging of the material in a cell?

6. Does the core-shell material provide a lifetime benefit in coulombic efficiency and charge endpoint capacity slippage?

Items 1, 2 & 4 were well addressed in this thesis in chapters 4, 5 & 6. Item 3, diffusion of transition metals should be further explored. The stability of the core-shell structure during cycling in a cell needs to be better explored with post-mortem analysis with XRD and SEM of materials cycled until cell death (80% of reversible capacity). Item 6 was explored briefly in chapter 7, but the results are not definitive and only completed on half-cells. Full-cell testing of coin-cell materials with and without electrolyte additives is necessary to better understand their impact on lifetime.

8.4 Future Work

In this thesis the choice of core and shell phases was selected based on availability of reference data, such as the structure composition diagram in Figure 2.1 and the ease of synthesis. There are many alternative compositions and phases that may be of interest to study both for a fundamental scientific understanding and in the quest to develop better lithium-ion positive electrode materials.

There are also various characterizations that could be completed that may provide more understanding of the products and the synthesis process.

8.4.1 Alternatives to Layered-Layered Core-shell Materials

It would be interesting to do a similar analysis on Li-Ni-Mn spinel systems since the voltage curves of the mixed spinel, $Li[Ni_{0.5}Mn_{1.5}]O_4$ and manganese spinel $LiMn_2O_4$

are very different. The spinel system may be a simpler system to study for fundamental understanding of core-shell structure, due to its cubic crystal structure and smaller single phase composition region. A previous study of core-shell spinel structures by Sun *et al.* could be used as a starting point for such a study.[155] Dahn *et al.* developed a software package to fit dV/dq curves of composite electrodes.[156] It may be possible to adapt these methods for core-shell samples to determine the phase ratio and shell thickness in the sintered products. This procedure may also be possible on layered-layered core-shell materials when a greater different exist between the core and shell phase than the materials presented in this work.

Similar to spinel-spinel core-shell materials, olivine-olivine core-shell materials should also be explored. $LiCoPO_4$ and $LiFePO_4$, are two possible materials to study as core-shell olivine materials. It would be interesting to determine the differences in the mobility of cobalt in an olivine structure versus a layered or spinel structure. While these materials may be of little commercial interest, they may provide a better understanding of the nature of core-shell materials.

8.4.2 NMC Layered-Layered Core-Shell Materials

Cobalt containing core-shell materials are more likely to be commercialized than cobalt-free materials. There are many cobalt containing lithium-rich materials that have been previously studied that have very high energy density and low irreversible capacity.[132,157] These materials should be explored as the core in core-shell materials. It is difficult to simply pick a shell material since a complete UHPC analysis of many NMC

materials has yet to been completed. It is not entirely necessary that a UHPC analysis of a shell material is completed prior to attempting a core-shell. Materials can be studied with traditional chargers and when an exceptional material is found it should be further explored with UHPC.

Diffusion of cobalt during sintering needs to be further understood. Quantitative EDS measurements may aid in determining the diffusion constants for cobalt. It may also be possible to use an intermediate barrier layer between the core and shell to limit cobalt diffusion.

Bi-layer shells and gradient compositions need to be further explored. Bi-layer shells were proposed in Chapter 6 as a possible method to control lithium content in the core and shell phases. Bi-layers may also prevent cobalt diffusion from the core to shell. There may not be such a material that lithium can diffuse through, but cobalt cannot, in addition to all the other necessary properties such as being able to form a hydroxide in the tank reactor, surviving sintering and not having adverse effects in an electrochemical cell.

It may also be of interest to explore precursors other than hydroxides, such as carbonates. The relationship between morphology and composition in carbonate precursors is different than that of hydroxide precursors. It may be possible to exploit the best morphologies of carbonates and hydroxides by synthesizing the core as a hydroxide and synthesizing the shell as a carbonate. Other influences such as surfactants or additives in the tank reactor solution should be explored as methods to improve morphology and shell coatings. Other synthetic routes to form the core-shell morphology should also be explored. One method proposed in Chapter 6 was to form a hydroxide of the core, lithiate and sinter it and then place that product back into the tank reactor to coat with hydroxide,

then lithiated and sinter again. While this process is economically a disaster for commercial materials, it may provide further insight into the cobalt diffusion, lithium saturation points and other properties of core-shell materials. This methodology would also potential open up new phases for core-shell materials such as a layered core with a spinel shell or olivine core with a layered shell. Again these materials may be nonsense for commercial lithium-ion applications, but they may be of great value in other fields where protective barriers are necessary.

8.4.3 Future Characterization Experiments

In the fall of 2014 a proposal was submitted to the Australian Synchrotron to complete *in-situ* diffraction experiments while sintering core-shell samples from Chapter 6. The proposal was to examine the changes in lattice parameters with time and temperature during the sintering process to better understand why the shell phase in the core-shell structure could not achieve the same saturation of lithium as the single phase sample. It was also of interest to determine if transition metal diffusion occurred early in the sintering process or during the extended hold at high temperature. This experiment was not approved for the cycle it was submitted for, but future diffraction experiments with a synchrotron should be explored, both *in-situ* and *ex-situ*. The reduced instrument broadening a synchrotron provides and the tunable energy may allow for more information to be extracted from diffraction patterns. It may also be of interest to use neutron diffraction to better determine where lithium is in the structure.

Alternative spectroscopic techniques such as Electron Energy Loss Spectroscopy (EELS) may provide a more direct measurement of lithium concentration in the core and shell phases of the core-shell structures.[158] It may not be necessary to use such expensive or complex characterization technique for daily analysis, but it would be useful to validate the Rietveld refinement contour map fitting routine. As core-shell research shifts to NMC materials, diagrams like Figure 2.1 are not available, requiring new methods to analyze samples. This thesis showed a lot of the basic characterization of core-shell materials. For future materials it may not be necessary to have such a thorough analysis of materials; instead the focus should be on electrochemical performance. This thesis lacks significant evidence of the lifetime benefits the core-shell structure is proposed to provide. It is of upmost importance that in the near future those working on core-shell materials validate this claim. Otherwise, many people may pursue these materials in the hope of improved performance that does not exist.

8.4.4 Electrolyte Additives with Core-Shell Materials

In this thesis, electrolyte additives were not extensively examined. Core-shell materials need to be studied with electrolyte additives in a similar fashion to how Wang *et al.* have extensively studied additives with NMC-111 and $LiCoO_2$. Wang employed pouch cells in his study of electrolyte additives.[27,159] The pouch cell may not be the proper tool to study core-shell materials since during the activation plateau, oxygen gas is generated. Oxygen scavenging additives may be necessary to prevent oxygen from the activation process from degrading other additives in the electrolyte. Additives that performed well

with NMC-111 or $LiCoO_2$ may not perform well with core-shell materials because the upper cut-off potential for charging is significantly higher for the core-shell materials. Future researchers should start seeking additives for core-shell materials as they most likely will not be commercialized without the aid of electrolyte additives. Since core-shell materials usually contain less cobalt and more manganese than NMC-111 or $LiCoO_2$ the reduced cost in the positive electrode material may allow a more expensive cocktail of additives to be used to further improve the electrochemical performance without impacting the unit cost per cell.

References

(1) Amazon.com: Two Panasonic NCR18650B 3.7V 3400mAh Rechargeable Li-ion Batteries QTY 2: Electronics http://www.amazon.com/Panasonic-NCR18650B-3400mAh-Rechargeable-Batteries/dp/B00DHXY72O (accessed Feb 13, 2015).

(2) Howell, D. EV Everywhere Grand Challenge Battery Status and Cost Reduction Prospects, 2012.

(3) *Linden's Handbook of Batteries*, 4th ed.; Reddy, T. B., Linden, D., Eds.; McGraw-Hill: New York, 2011.

(4) Energy Information Administration; Office of Coal, Nuclear, Electric and Alternate Fuels; U.S. Department of Energ. *Electric Power Monthly June 1996*; DOE/EIA-0226(96/06); 1996; p 171.

(5) Energy Information Administration; Office of Coal, Nuclear, Electric and Alternate Fuels; U.S. Department of Energ. *Electric Power Monthly June 2014*; DOE/EIA-0226(14/06); 2014.

(6) Inflation Calculator | Find US Dollar's Value from 1913-2014 http://www.usinflationcalculator.com/ (accessed Nov 17, 2014).

(7) Regulations & Standards | Fuel Economy | US EPA http://www.epa.gov/fueleconomy/regulations.htm (accessed Nov 15, 2014).

(8) United States Government. *Code of Federal Regulations, Title 10, Energy, PT. 51-199, Revised as of January 1, 2012*; Government Printing Office, 2012.

(9) GENERAL MOTORS COMPANY. *GM U.S. Deliveries for August 2014*; 2014; p 2.

(10) Nissan LEAF Sales Figures - GOOD CAR BAD CAR http://www.goodcarbadcar.net/2011/01/nissan-leaf-sales-figures.html (accessed Nov 15, 2014).

(11) Nissan LEAF® Electric Car: 100% Electric. 100% Fun. http://www.nissanusa.com/electric-cars/leaf/ (accessed Nov 15, 2014).

(12) Tesla Rises After Model S Sales in 2013 Exceed Forecast - Bloomberg http://www.bloomberg.com/news/2014-01-14/tesla-delivered-6-900-cars-in-fourth-quarter-executive-says.html (accessed Nov 15, 2014).

(13) 2014 Nissan Versa Sedan | Nissan Canada http://www.nissan.ca/en/cars/versa-sedan (accessed Nov 15, 2014).

(14) *Marketing Metrics: The Definitive Guide To Measuring Marketing Performance*, 2nd ed.; Farris, P., Ed.; FT Press: Upper Saddle River, N.J, 2010.

(15) 2015 Volt: Electric Cars - Hybrid Cars | Chevrolet http://www.chevrolet.com/volt-electric-car.html (accessed Nov 15, 2014).

(16) Model S | Tesla Motors http://www.teslamotors.com/en_CA/models (accessed Nov 15, 2014).

(17) Bruce, P. G.; Freunberger, S. A.; Hardwick, L. J.; Tarascon, J.-M. *Nat. Mater.* **2011**, *11* (1), 19.

(18) Halifax, NS - Google Maps https://www.google.ca/maps/place/Halifax,+NS/@44.6488625,-63.5753196,566652m/data=!3m1!1e3!4m2!3m1!1s0x4b5a211407dbfac1:0x666be3a6438b2ddc (accessed Nov 15, 2014).

(19) Brodd, R. J. Li-Ion Battery/Cell Manufacturing Cost Comparisons, 2010.

(20) Fathi, R.; Burns, J. C.; Stevens, D. A.; Ye, H.; Hu, C.; Jain, G.; Scott, E.; Schmidt, C.; Dahn, J. R. *J. Electrochem. Soc.* **2014**, *161* (10), A1572.

(21) Smith, A. J.; Burns, J. C.; Xiong, D.; Dahn, J. R. *J. Electrochem. Soc.* **2011**, *158* (10), A1136.

(22) Burns, J. C.; Kassam, A.; Sinha, N. N.; Downie, L. E.; Solnickova, L.; Way, B. M.; Dahn, J. R. *J. Electrochem. Soc.* **2013**, *160* (9), A1451.

(23) Smith, A. J.; Burns, J. C.; Trussler, S.; Dahn, J. R. *J. Electrochem. Soc.* **2010**, *157* (2), A196.

(24) Peled, E. *J. Electrochem. Soc.* **1997**, *144* (8), L208.

(25) Fong, R. *J. Electrochem. Soc.* **1990**, *137* (7), 2009.

(26) Smith, A. A HIGH PRECISION STUDY OF LI-ION BATTERIES. PhD Thesis, Dalhousie University: Halifax, NS Canada, 2012.

(27) Wang, D. Y.; Sinha, N. N.; Petibon, R.; Burns, J. C.; Dahn, J. R. *J. Power Sources* **2014**, *251*, 311.

(28) Aurbach, D.; Gamolsky, K.; Markovsky, B.; Gofer, Y.; Schmidt, M.; Heider, U. *Electrochimica Acta* **2002**, *47* (9), 1423.

(29) Bernard Simon; Jean-Pierre Boeuve. Rechargeable lithium electrochemical cell. US5626981 A. 1997.

(30) Li, S. R.; Sinha, N. N.; Chen, C. H.; Xu, K.; Dahn, J. R. *J. Electrochem. Soc.* **2013**, *160* (11), A2014.

(31) Xu, K. *Chem. Rev.* **2014**, *114* (23), 11503.

(32) Petibon, R.; Rotermund, L.; Nelson, K. J.; Gozdz, A. S.; Xia, J.; Dahn, J. R. *J. Electrochem. Soc.* **2014**, *161* (6), A1167.

(33) Campion, C. L.; Li, W.; Lucht, B. L. *J. Electrochem. Soc.* **2005**, *152* (12), A2327.

(34) Petibon, R.; Henry, E. C.; Burns, J. C.; Sinha, N. N.; Dahn, J. R. *J. Electrochem. Soc.* **2013**, *161* (1), A66.

(35) 4-Fluoro-1,3-dioxolan-2-one 114435-02-8 | TCI America http://www.tcichemicals.com/eshop/en/us/commodity/F0731/ (accessed Nov 17, 2014).

(36) Diethyl Carbonate 105-58-8 | TCI America http://www.tcichemicals.com/eshop/en/us/commodity/C0041/ (accessed Nov 17, 2014).

(37) Ethylene Carbonate 96-49-1 | TCI America http://www.tcichemicals.com/eshop/en/us/commodity/E0076/ (accessed Nov 17, 2014).

(38) Vinylene Carbonate 872-36-6 | TCI America http://www.tcichemicals.com/eshop/en/us/commodity/V0015/ (accessed Nov 17, 2014).

(39) Newman, M. S.; Addor, R. W. *J. Am. Chem. Soc.* **1955**, *77* (14), 3789.

(40) Whittingham, M. S. *Chem. Rev.* **2004**, *104* (10), 4271.

(41) McCalla, E.; Rowe, A. W.; Shunmugasundaram, R.; Dahn, J. R. *Chem. Mater.* **2013**, *25* (6), 989.

(42) Brown, C. Combinatorial Study of the Li-Ni-Mn-Co Oxide Pseudo-Quaternary System for use in Li-ion Battery Materials Research, MsC Thesis Dalhousie University, Halifax, NS Canada, 2014.

(43) Reimers, J. N. *J. Electrochem. Soc.* **1992**, *139* (8), 2091.

(44) Yamada, A.; Chung, S. C.; Hinokuma, K. *J. Electrochem. Soc.* **2001**, *148* (3), A224.

(45) Padhi, A. K. *J. Electrochem. Soc.* **1997**, *144* (4), 1188.

(46) Amine, K. *Electrochem. Solid-State Lett.* **1999**, *3* (4), 178.

(47) Aydinol, M.; Kohan, A.; Ceder, G.; Cho, K.; Joannopoulos, J. *Phys. Rev. B* **1997**, *56* (3), 1354.

(48) Geological Survey (U.S.). *Mineral Commodity Summaries, 2014*; Government Printing Office, 2014.

(49) Zhou, F.; Zhao, X.; van Bommel, A.; Rowe, A. W.; Dahn, J. R. *Chem. Mater.* **2010**, *22* (3), 1015.

(50) McCalla, E.; Carey, G. H.; Dahn, J. R. *Solid State Ionics* **2012**, *219*, 11.

(51) Chen, Z.; Dahn, J. R. *J. Electrochem. Soc.* **2002**, *149* (9), A1184.

(52) Li, H.; Wang, Z.; Chen, L.; Huang, X. *Adv. Mater.* **2009**, *21* (45), 4593.

(53) Chen, Z.; Qin, Y.; Amine, K.; Sun, Y.-K. *J. Mater. Chem.* **2010**, *20* (36), 7606.

(54) Wang, Z.; Wu, C.; Liu, L.; Wu, F.; Chen, L.; Huang, X. *J. Electrochem. Soc.* **2002**, *149* (4), A466.

(55) Cho, J.; Kim, Y. J.; Park, B. *Chem. Mater.* **2000**, *12* (12), 3788.

(56) Rowe, A. W.; Camardese, J.; McCalla, E.; Dahn, J. R. *J. Electrochem. Soc.* **2014**, *161* (9), A1189.

(57) Gummow, R. J.; de Kock, A.; Thackeray, M. M. *Solid State Ion.* **1994**, *69* (1), 59.

(58) Joshi, T.; Eom, K.; Yushin, G.; Fuller, T. F. *J. Electrochem. Soc.* **2014**, *161* (12), A1915.

(59) Amine, K.; Chen, Z.; Zhang, Z.; Liu, J.; Lu, W.; Qin, Y.; Lu, J.; Curtis, L.; Sun, Y.-K. *J. Mater. Chem.* **2011**, *21* (44), 17754.

(60) Huggins, R. A. *Energy storage*; Springer: New York, 2010.

(61) Mizushima, K.; Jones, P. C.; Wiseman, P. J.; Goodenough, J. B. *Mater. Res. Bull.* **1980**, *15* (6), 783.

(62) Ohzuku, T.; Makimura, Y. *Chem. Lett.* **2001**, *30* (7), 642.

(63) Lu, Z.; MacNeil, D. D.; Dahn, J. R. *Electrochem. Solid-State Lett.* **2001**, *4* (12), A200.

(64) MacNeil, D. D.; Lu, Z.; Dahn, J. R. *J. Electrochem. Soc.* **2002**, *149* (10), A1332.

(65) Lu, Z.; Beaulieu, L. Y.; Donaberger, R. A.; Thomas, C. L.; Dahn, J. R. *J. Electrochem. Soc.* **2002**, *149* (6), A778.

(66) Armstrong, A. R.; Holzapfel, M.; Novák, P.; Johnson, C. S.; Kang, S.-H.; Thackeray, M. M.; Bruce, P. G. *J. Am. Chem. Soc.* **2006**, *128* (26), 8694.

(67) Van Bommel, A.; Krause, L. J.; Dahn, J. R. *J. Electrochem. Soc.* **2011**, *158* (6), A731.

(68) Croy, J. R.; Kim, D.; Balasubramanian, M.; Gallagher, K.; Kang, S.-H.; Thackeray, M. M. *J. Electrochem. Soc.* **2012**, *159* (6), A781.

(69) Croy, J. R.; Gallagher, K. G.; Balasubramanian, M.; Chen, Z.; Ren, Y.; Kim, D.; Kang, S.-H.; Dees, D. W.; Thackeray, M. M. *J. Phys. Chem. C* **2013**, *117* (13), 6525.

(70) Koga, H.; Croguennec, L.; Ménétrier, M.; Mannessiez, P.; Weill, F.; Delmas, C.; Belin, S. *J. Phys. Chem. C* **2014**, *118* (11), 5700.

(71) Koga, H.; Croguennec, L.; Ménétrier, M.; Mannessiez, P.; Weill, F.; Delmas, C. *J. Power Sources* **2013**, *236*, 250.

(72) Jarvis, K. A.; Deng, Z.; Allard, L. F.; Manthiram, A.; Ferreira, P. J. *Chem. Mater.* **2011**, *23* (16), 3614.

(73) McCalla, E.; Li, J.; Rowe, A. W.; Dahn, J. R. *J. Electrochem. Soc.* **2014**, *161* (4), A606.

(74) McCalla, E. Structural and Electrochemical Studies of the Li-Mn-Ni-O and Li-Co-Mn-O Pseudo-Ternary Systems. PhD Thesis, Dalhousie University, 2013.

(75) Smith, A. J.; Burns, J. C.; Dahn, J. R. *Electrochem. Solid-State Lett.* **2010**, *13* (12), A177.

(76) Rowe, A. W. Structural and Electrochemical Studies of Positive Electrode Materials in the Li-Mn-Ni-O System for Lithium-ion Batteries. PhD Thesis, Dalhousie University: Halifax, NS Canada, 2014.

(77) Park, B.-C.; Bang, H. J.; Amine, K.; Jung, E.; Sun, Y.-K. *J. Power Sources* **2007**, *174* (2), 658.

(78) Sun, Y.-K.; Lee, B.-R.; Noh, H.-J.; Wu, H.; Myung, S.-T.; Amine, K. *J. Mater. Chem.* **2011**, *21* (27), 10108.

(79) Lee, K.-S.; Myung, S.-T.; Moon, J.-S.; Sun, Y.-K. *Electrochimica Acta* **2008**, *53* (20), 6033.

(80) Koenig, G. M.; Belharouak, I.; Deng, H.; Sun, Y.-K.; Amine, K. *Chem. Mater.* **2011**, *23* (7), 1954.

(81) Li, J.; Camardese, J.; Glazier, S.; Dahn, J. R. *Chem. Mater.* **2014**, *26* (24), 7059.

(82) NIST. Composition of Air, Dry (Near Sea Level) http://physics.nist.gov/cgi-bin/Star/compos.pl?matno=104 (accessed Jan 7, 2014).

(83) Wyckoff, R. G. W. *Crystal Structures*, 2nd ed.; Robert E. Krieger Publishing Company: Malabar, Fla, 1986; Vol. 2.

(84) McCalla, E.; Lowartz, C. M.; Brown, C. R.; Dahn, J. R. *Chem. Mater.* **2013**, *25* (6), 912.

(85) McCalla, E.; Li, J.; Rowe, A. W.; Dahn, J. R. *J. Electrochem. Soc.* **2014**, *161* (4), A606.

(86) Carey, G. H.; Dahn, J. R. *ACS Comb. Sci.* **2011**, *13* (2), 186.

(87) Linden, D.; Reddy, T. B. *Handbook of batteries*; McGraw-Hill: New York, 2002.

(88) Lee, D.-K.; Park, S.-H.; Amine, K.; Bang, H. J.; Parakash, J.; Sun, Y.-K. *J. Power Sources* **2006**, *162* (2), 1346.

(89) Lee, M.-H.; Kang, Y.-J.; Myung, S.-T.; Sun, Y.-K. *Electrochimica Acta* **2004**, *50* (4), 939.

(90) Van Bommel, A. Lithium-Rich Transition Metal Oxides as Positive Electrode Materials in Lithium-Ion Batteries. PhD Thesis, Dalhousie University: Halifax, NS Canada, 2010.

(91) Ignasi Puigdomenech. *Medusa*; 2013.

(92) Van Bommel, A.; Dahn, J. R. *Chem. Mater.* **2009**, *21* (8), 1500.

(93) *The Merck index: an encyclopedia of chemicals, drugs, and biologicals*, 11th ed., centennial ed.; Budavari, S., Ed.; Merck: Rahway, N.J., U.S.A, 1989.

(94) Bazhenov, A. A.; Miklushevskii, V. V.; Vatulin, I. I.; Kropacheva, E. N.; Bidylo, A. P. *Russ. J. Non-Ferr. Met.* **2010**, *51* (1), 44.

(95) Marks, T.; Trussler, S.; Smith, A. J.; Xiong, D.; Dahn, J. R. *J. Electrochem. Soc.* **2011**, *158* (1), A51.

(96) Sinha, N. N.; Burns, J. C.; Sanderson, R. J.; Dahn, J. *J. Electrochem. Soc.* **2011**, *158* (12), A1400.

(97) Obrovac, M. N. A model of the electrochemistry of chromium substituted lithium manganese oxides based on photoelectron spectroscopy valence band measurements. MSc Thesis, Dalhousie University, 1997.

(98) Brian Michael Way. Lithium Intercalation in BxC1-x Solid Solution, Simon Fraser University: Burnaby, BC Canada, 1995.

(99) Lux, S. F.; Chevalier, J.; Lucas, I. T.; Kostecki, R. *ECS Electrochem. Lett.* **2013**, *2* (12), A121.

(100) Burns, J. C.; Sinha, N. N.; Jain, G.; Ye, H.; VanElzen, C. M.; Scott, E.; Xiao, A.; Lamanna, W. M.; Dahn, J. R. *J. Electrochem. Soc.* **2013**, *160* (11), A2281.

(101) Burns, J. C.; Sinha, N. N.; Jain, G.; Ye, H.; VanElzen, C. M.; Scott, E.; Xiao, A.; Lamanna, W. M.; Dahn, J. R. *J. Electrochem. Soc.* **2013**, *161* (3), A247.

(102) Warren, B. E. *X-ray diffraction*, Dover ed.; Dover Publications: New York, 1990.

(103) Cullity, B. D.; Stock, S. R. *Elements of x-ray diffraction*; Prentice Hall: Upper Saddle River, NJ, 2001.

(104) Rietveld, H. M. *J. Appl. Crystallogr.* **1969**, *2* (2), 65.

(105) ICDD Products- PDF-4+ http://www.icdd.com/products/pdf4.htm (accessed Jan 7, 2015).

(106) Crystal Impact. *Match!*; Crystal Impact, 2013.

(107) C. T. Chantler; K. Olsen; R. A. Dragoset; J. Chang; A. R. Kishore; S. A. Kotochigova; D. S. Zucker. *X-Ray Form Factor, Attenuation, and Scattering Tables*; National Institute of Standards and Technology, 2001.

(108) B.D. Cullity; S.R. Stock. *Elements of X-ray Diffraction*, 3rd ed.; Prentice Hall, 2001.

(109) Phillips Electronic Instruments. *Norelco Diffractometer Alignment Procedure Instruction Manual*; Philips Electronic Instruments: Mount Vernon, New York USA, 1962.

(110) B. A. Hunter. *Rietica for Windows*; 2007.

(111) Toby, B. H. *Powder Diffr.* **2006**, *21* (01), 67.

(112) Zhou, F.; Zhao, X.; Van Bommel, A.; Rowe, A. W.; Dahn, J. R. *Chem. Mater.* **2009**, *22* (3), 1015.

(113) *Scanning electron microscopy and X-ray microanalysis: a text for biologists, materials scientists, and geologists*; Goldstein, J., Ed.; Plenum Press: New York, 1981.

(114) Dahn, J. R.; Trussler, S.; Hatchard, T. D.; Bonakdarpour, A.; Mueller-Neuhaus, J. R.; Hewitt, K. C.; Fleischauer, M. *Chem. Mater.* **2002**, *14* (8), 3519.

(115) Kimball, S.; Mattis, P. *GIMP*; GIMP Development Team, 2013.

(116) Drouin, D.; Couture, A. R.; Joly, D.; Tastet, X.; Aimez, V.; Gauvin, R. *Scanning* **2007**, *29* (3), 92.

(117) Raynald, G. *CASINO*; Université de Sherbrooke: Québec, Canada, 2003.

(118) Camardese, J.; McCalla, E.; Abarbanel, D. W.; Dahn, J. R. *J. Electrochem. Soc.* **2014**, *161* (5), A814.

(119) Downie, L. E.; Nelson, K. J.; Petibon, R.; Chevrier, V. L.; Dahn, J. R. *ECS Electrochem. Lett.* **2013**, *2* (10), A106.

(120) *The CRC handbook of solid state electrochemistry*; Gellings, P. J., Bouwmeester, H. J. M., Eds.; CRC Press: Boca Raton, Fla, 1997.

(121) Keithley. 220 Programmable Current Source http://www.keithley.com/data?asset=367 (accessed Jan 7, 2015).

(122) Bond, T. M.; Burns, J. C.; Stevens, D. A.; Dahn, H. M.; Dahn, J. R. *J. Electrochem. Soc.* **2013**, *160* (3), A521.

(123) Smith, A. J.; Burns, J. C.; Xiong, D.; Dahn, J. R. *J. Electrochem. Soc.* **2011**, *158* (10), A1136.

(124) Sun, Y.-K.; Chen, Z.; Noh, H.-J.; Lee, D.-J.; Jung, H.-G.; Ren, Y.; Wang, S.; Yoon, C. S.; Myung, S.-T.; Amine, K. *Nat. Mater.* **2012**, *11* (11), 942.

(125) McCalla, E.; Rowe, A. W.; Camardese, J.; Dahn, J. R. *Chem. Mater.* **2013**, *25* (13), 2716.

(126) Dahn, J. R.; Von Sacken, U.; Michal, C. A. *Solid State Ion.* **1990**, *444* (1-2), 87.

(127) Whittingham, M. S. *Chem. Rev.* **2014**, *114* (23), 11414.

(128) Carroll, K. J.; Qian, D.; Fell, C.; Calvin, S.; Veith, G. M.; Chi, M.; Baggetto, L.; Meng, Y. S. *Phys. Chem. Chem. Phys.* **2013**, *15* (26), 11128.

(129) Laoire, C. O.; Mukerjee, S.; Abraham, K. M.; Plichta, E. J.; Hendrickson, M. A. *J. Phys. Chem. C* **2010**, *114* (19), 9178.

(130) Sathiya, M.; Rousse, G.; Ramesha, K.; Laisa, C. P.; Vezin, H.; Sougrati, M. T.; Doublet, M.-L.; Foix, D.; Gonbeau, D.; Walker, W.; Prakash, A. S.; Ben Hassine, M.; Dupont, L.; Tarascon, J.-M. *Nat. Mater.* **2013**, *12* (9), 827.

(131) Rowe, A. W.; Camardese, J.; McCalla, E.; Dahn, J. R. *J. Electrochem. Soc.* **2014**, *161* (9), A1189.

(132) Shunmugasundaram, R.; Senthil Arumugam, R.; Dahn, J. R. *Chem. Mater.* **2015**, *27* (3), 757.

(133) Camardese, J.; Abarbanel, D. W.; McCalla, E.; Dahn, J. R. *J. Electrochem. Soc.* **2014**, *161* (6), A890.

(134) De Wolff, P. *Tech. Phys. Diesnt* **1972**.

(135) Van Bommel, A.; Dahn, J. R. *Chem. Mater.* **2009**, *21* (8), 1500.

(136) Delmas, C.; Tessier, C. *J. Mater. Chem.* **1997**, *7* (8), 1439.

(137) Ramesh, T. N.; Kamath, P. V.; Shivakumara, C. *Acta Crystallogr. B* **2006**, *62* (4), 530.

(138) B. Boucher; R. Buhl; M. Perrin. *J. Phys. Chem. Solids* **1971**, *32*, 2429.

(139) Dahn, J. *Solid State Ion.* **1990**, *44* (1-2), 87.

(140) Camardese, J.; Li, J.; Abarbanel, D. W.; Wright, A. T. B.; Dahn, J. R. *J. Electrochem. Soc.* **2014**, *162* (3), A269.

(141) E Prince. *International Tables for Crystallography, Mathematical, Physical and Chemical Tables*; Springer Science & Business Media, 2004.

(142) Koenig, G. M.; Belharouak, I.; Deng, H.; Sun, Y.-K.; Amine, K. *Chem. Mater.* **2011**, *23* (7), 1954.

(143) Munro, D. H. *Yorick*; Lawrence Livermore National Laboratory: California, USA, 2014.

(144) Von Dreele, R. B.; Suchomel, M. R.; Toby, B. H. Compute X-ray Absorption http://11bm.xray.aps.anl.gov/absorb/absorb.php (accessed Jan 30, 2015).

(145) Marcin Wojdyr. *Fityk*; 2001.

(146) Ham, F. S. *J. Appl. Phys.* **1959**, *30* (10), 1518.

(147) Zener, C. *J. Appl. Phys.* **1949**, *20* (10), 950.

(148) Westsson, E.; Koper, G. *Catalysts* **2014**, *4* (4), 375.

(149) Gadjov, H.; Gorova, M.; Kotzeva, V.; Avdeev, G.; Uzunova, S.; Kovacheva, D. *J. Power Sources* **2004**, *134* (1), 110.

(150) Tarascon, J. .; Wang, E.; Shokoohi, F. K.; McKinnon, W. R.; Colson, S. *J. Electrochem. Soc.* **1991**, *138* (10), 2859.

(151) Dahn, J.; U. von Sacken; C. A. Michal. *Solid State Ion.* **1990**, *44* (1-2), 87.

(152) Golden Software, Inc. *Surfer*; Golden Software, Inc: Golden, Colorado USA, 2000.

(153) Cressie, N. *Math. Geol.* **1990**, *22* (3), 239.

(154) Atlung, S. *J. Electrochem. Soc.* **1979**, *126* (8), 1311.

(155) Cho, Y.; Lee, S.; Lee, Y.; Hong, T.; Cho, J. *Adv. Energy Mater.* **2011**, *1* (5), 821.

(156) Dahn, H. M.; Smith, A. J.; Burns, J. C.; Stevens, D. A.; Dahn, J. R. *J. Electrochem. Soc.* **2012**, *159* (9), A1405.

(157) Thackeray, M. M.; Kang, S.-H.; Johnson, C. S.; Vaughey, J. T.; Benedek, R.; Hackney, S. A. *J. Mater. Chem.* **2007**, *17* (30), 3112.

(158) Qian, D.; Xu, B.; Chi, M.; Meng, Y. S. *Phys Chem Chem Phys* **2014**, *16* (28), 14665.

(159) Wang, D. Y.; Xia, J.; Ma, L.; Nelson, K. J.; Harlow, J. E.; Xiong, D.; Downie, L. E.; Petibon, R.; Burns, J. C.; Xiao, A.; Lamanna, W. M.; Dahn, J. R. *J. Electrochem. Soc.* **2014**, *161* (12), A1818.

Appendix

Copyright Information

The copyright information is outlined in this section, with the permission granted for figures used in this thesis.

Copyright permission for Figure 3.6

ROYAL SOCIETY OF CHEMISTRY LICENSE TERMS AND CONDITIONS

Jan 08, 2015

This is a License Agreement between John Camardese ("You") and Royal Society of Chemistry ("Royal Society of Chemistry") provided by Copyright Clearance Center ("CCC"). The license consists of your order details, the terms and conditions provided by Royal Society of Chemistry, and the payment terms and conditions.

All payments must be made in full to CCC. For payment instructions, please see information listed at the bottom of this form.

License Number	3544321062986
License date	Jan 08, 2015
Licensed content publisher	Royal Society of Chemistry
Licensed content publication	Physical Chemistry Chemical Physics
Licensed content title	Probing the electrode/electrolyte interface in the lithium excess layered oxide Li1.2Ni0.2Mn0.6O2
Licensed content author	Kyler J. Carroll,Danna Qian,Chris Fell,Scott Calvin,Gabriel M. Veith,Miaofang Chi,Loic Baggetto,Ying Shirley Meng
Licensed content date	May 8, 2013
Volume number	15
Issue number	26
Type of Use	Thesis/Dissertation
Requestor type	academic/educational
Portion	figures/tables/images
Number of figures/tables /images	3
Format	print and electronic
Distribution quantity	10
Will you be translating?	no
Order reference number	None
Title of the thesis/dissertation	A study of core-shell materials for lithium-ion batteries
Expected completion date	Apr 2015
Estimated size	250
Total	0.00 CAD

Terms and Conditions

This License Agreement is between {Requestor Name} ("You") and The Royal Society of Chemistry ("RSC") provided by the Copyright Clearance Center ("CCC"). The license consists of your order details, the terms and conditions provided by the Royal Society of Chemistry, and the payment terms and conditions.